EFFECTS OF SURFACE ROUGHNESS ON THE FLOW CHARACTERISTICS IN A TURBULENT BOUNDARY LAYER

A Thesis Submitted to the College of

Graduate Studies and Research

in Partial Fulfillment of the Requirements

for the Degree of Doctor of Philosophy

in the Department of Mechanical Engineering

University of Saskatchewan

Saskatoon

By

Olajide Ganiyu Akinlade

December 2005

PERMISSION TO USE

The author grants permission to the University of Saskatchewan Libraries to make this thesis available for inspection. Copying of this thesis, in whole or in part, for scholarly purposes may be granted by my supervisor, Prof. D. J. Bergstrom, the Head of the Department of Mechanical Engineering, or the Dean of the College of Engineering. It is understood that any copying or publication or use of this thesis or part thereof for financial gain shall not be allowed without my written permission. It is also understood that due recognition to me and the University of Saskatchewan must be granted in any scholarly use which may be made of any material in this thesis.

Request for permission to copy or to make other use of material in this thesis in whole or in part should be addressed to:

Head of the Department of Mechanical Engineering

University of Saskatchewan

57 Campus Drive

Saskatoon, Saskatchewan

S7N 5A9

ABSTRACT

The present understanding of the structure and dynamics of turbulent boundary layers on aerodynamically smooth walls has been clarified over the last decade or so. However, the dynamics of turbulent boundary layers over rough surfaces is much less well known. Nevertheless, there are many industrial and environmental flow applications that require understanding of the mean velocity and turbulence in the immediate vicinity of the roughness elements.

This thesis reports the effects of surface roughness on the flow characteristics in a turbulent boundary layer. Both experimental and numerical investigations are used in the present study. For the experimental study, comprehensive data sets are obtained for two-dimensional zero pressure-gradient turbulent boundary layers on a smooth surface and ten different rough surfaces created from sand paper, perforated sheet, and woven wire mesh. The physical size and geometry of the roughness elements and freestream velocity were chosen to encompass both transitionally rough and fully rough flow regimes. Three different probes, namely, Pitot probe, single hot-wire, and cross hot-film, were used to measure the velocity fields in the turbulent boundary layer. A Pitot probe was used to measure the streamwise mean velocity, while the single hot-wire and cross hot-film probes were used to measure the fluctuating velocity components across the boundary layer. The flow Reynolds number based on momentum thickness, Re_θ, ranged from 3730 to 13,550. The data reported include mean velocity, streamwise and wall-normal turbulence intensities, Reynolds shear stress, triple correlations, as well as

skewness and flatness factors. Different scaling parameters were used to interpret and assess both the smooth- and rough-wall data at different Reynolds numbers, for approximately the same freestream velocity. The appropriateness of the logarithmic law and power law proposed by George and Castillo (1997) to describe the mean velocity in the overlap region was also investigated. The present results were interpreted within the context of the Townsend's wall similarity hypothesis.

Based on the mean velocity data, a novel correlation that relates the skin friction to the ratio of the displacement and boundary layer thicknesses, which is valid for both smooth- and rough-wall flows, was proposed. In addition, it was also found that the application of a "mixed outer scale" caused the velocity profile in the outer region to collapse onto the same curve, irrespective of Reynolds numbers and roughness conditions. The present results showed that there is a common region within the overlap region of the mean velocity profile where both the log law and power law are indistinguishable, irrespective of the surface conditions. For the power law formulation, functional relationships between the roughness shift, ΔU^+, and the power law coefficient and exponent were developed for the transitionally rough flows. The present results also suggested that the effect of surface roughness on the turbulence field depends to some degree on the specific characteristics of the roughness elements and also the component of the Reynolds stress tensor being considered.

In the case of the numerical study, a new wall function formulation based on a power law was proposed for smooth and fully rough wall turbulent pipe flow. The new

formulation correctly predicted the friction factors for smooth and fully rough wall turbulent pipe flow. The existing two-layer $k-\varepsilon$ model realistically predicted the velocity shift on a log-law plot for the fully rough turbulent boundary layer. The two-layer $k-\varepsilon$ model results also showed the effect of roughness is to enhance the level of turbulence kinetic energy and Reynolds shear stress compared to that on a smooth wall. This enhanced level extends into the outer region of the flow, which appears to be consistent with present and recent experimental results for the boundary layer.

ACKNOWLEDGEMENTS

First of all, I give glory to Almighty God for the completion of this program. I would like to express my profound appreciation to my supervisor, Prof. D. J. Bergstrom. You have not only been a supervisor, but a source of inspiration. Thank you so much for everything you have done, even sometimes going out of your way to ensure that my program was a success. My appreciation also goes to the members of my advisory committee, Profs. Jim Bugg, David Sumner, and Rob Sumner for your invaluable suggestions and advices given to me throughout my program. Special thanks goes to Mr. Dave Deutscher for your all round assistance during my experimental studies. Your assistance contributed immensely to the success of this thesis. I am grateful to my external examiner, Prof. Jonathan Naughton, for his comments and suggestions, many of which have been reflected in the thesis.

I would also like to express a very big appreciation to my brother, Dr. Olatunji Akinlade, whom Almighty God used to open the door of opportunity to pursue this program. Thank you to my brothers Fatai, Oladele, and Abiodun and their families for their supports and encouragements throughout my studies. A special thank you also goes to my cousins, Mr. Adeniyi Akanni and Mr. Moruf Adeogun.

My thanks also goes to my mum, Mrs. Akinlade, my parents-in-Law, Mr. & Mrs. P.O. Ojelabi, and my siblings-in-Law, Bola, Jumoke, Sumbo and Jide. Your prayers, encouragements and supports are greatly appreciated. A special acknowledgment goes to

the memory of my brother-in-Law, late Dapo Ojelabi. Although you are not here physically, your memory lies in our hearts.

I cannot but acknowledge and say a big thank you to Dr. & Mrs. Akinbolue and their entire family. Your support towards my self and my family went a long way towards the successful completion of my program. Your gesture will forever be appreciated.

To my numerous friends and well-wishers, thank you all so much. A special thank you to: Dr. Dapo Okeola, Samuel Adaramola, Femi Farinu, Franklin Morlu and Family, Tope Abe, Dr. Oguocha, Dr. Tachie, Bola Tawose, Femi Akosile and Famliy to mention but few. I really appreciate your friendship and support.

Last but not least, a special thank you to my loving wife, Bimpe Akinlade. Thank you for always being there. To our little bundle of joy, Seyitan Akinlade, I thank God for adding you to our family. You have been a source of inspiration and encouragement.

DEDICATION

This thesis is dedicated to the memory of my father, Late Pa Alao Akinlade, for being a father, a friend and a confidant. Daddy, I wish you were here to see your dream for me come true, but I take solace in the knowledge that you showed me.

TABLE OF CONTENTS

LIST OF TABLES

LIST OF FIGURES

NOMENCLATURE

ENGLISH SYMBOLS

A	:	Additive constant in logarithmic law (smooth wall)
B	:	Additive constant in logarithmic law (smooth wall)
C	:	Power law multiplicative factor
C_f	:	Skin friction coefficient
C_i	:	Power law multiplicative factor for inner layer
C_o	:	Power law multiplicative factor for outer layer
D	:	Pipe diameter (m)
E	:	Anemometer voltage output for single-hot wire (Volt)
E_1	:	Anemometer voltage output from channel 1 (Volt)
E_2	:	Anemometer voltage output from channel 2 (Volt)
f_i	:	Dimensionless functional relationship for the inner layer
f_o	:	Dimensionless functional relationship for the outer layer
G	:	Integral shape factor
H	:	Karmán-type shape factor
k	:	Turbulence kinetic energy (m^2/s^2)
k	:	Roughness height (mm)
k^+	:	Roughness Reynolds number (kU_τ / ν)
k_{eq}	:	Equivalent sand grain roughness
k_{eq}^+	:	Equivalent sand grain roughness Reynolds number ($k_{eq}U_\tau / \nu$)
P	:	Mean pressure (Pa)
R	:	Pipe radius (m)

Re	:	Reynolds number based on pipe diameter (UD/ν)
Re_θ	:	Reynolds number based on momentum thickness ($U\theta/\nu$)
S_{ij}	:	Strain rate tensor ($0.5(U_{i,j}+U_{j,i})$)
T	:	Absolute temperature (K)
t	:	Time (sec)
u'	:	Streamwise turbulence intensity (m/s)
U	:	Mean velocity (m/s)
U(y)	:	Mean velocity in wall-normal direction (m/s)
U_e	:	Freestream velocity (m/s)
U_τ	:	Friction velocity (m/s)
$<u_iu_j>$	:	Reynolds stress tensor (m^2/s^2)
v'	:	Wall-normal turbulence intensity (m/s)
x	:	Streamwise coordinate (m)
y	:	Wall-normal coordinate direction (m)
y_o	:	Location of virtual origin (m)

GREEK SYMBOLS

α	:	Power law exponent
Δ	:	Defect thickness (mm)
δ	:	Boundary layer thickness (mm)
δ^*	:	Boundary layer displacement thickness (mm)
δ^+	:	Reynolds number based on boundary layer thickness ($\delta U_\tau/\nu$)

δ_{ij}	:	Kronecker delta
ε	:	Dissipation rate (m^2/s^3)
γ	:	Power law exponent
κ	:	von Karmán constant
μ	:	Dynamic viscosity (Ns/m^2)
υ	:	Kinematic viscosity (m^2/s)
υ_t	:	Eddy viscosity (m^2/s)
Π	:	Wake parameter
θ	:	Boundary layer momentum thickness (mm)
ρ	:	Density (kg/m^3)
τ_w	:	Wall shear stress (N/m^2)

CHAPTER 1

INTRODUCTION

1.1 Turbulent Flow

> *"Because turbulence is complex, its complete analysis and quantification will probably never be achieved. Turbulent flow will be the subject of research in the foreseeable future, ….."*
>
> *Frank White, 1991*

Without exaggeration, one can say there is hardly any branch of fluid mechanics in which the flows of practical relevance are not turbulent. This means that the fluid motion is unsteady (even if the mean flow is steady), three-dimensional (even if the mean flow is only two-dimensional), rotational, dissipative, strongly diffusive, and highly irregular in space and time. The turbulent motion has a wide spectrum of eddy sizes, with large and small eddies coexisting in the same volume of fluid. The largest eddies are associated with low frequency fluctuations and are responsible for most of the momentum transport. The smallest eddies are associated with high frequency fluctuations, and determined by the viscous forces.. For engineers, turbulence is a practical matter with which they have to routinely contend, since it plays an important role in industrial and environmental flow applications.

Despite the challenges encountered, the study of the nature and features of turbulence has received considerable attention over the last two centuries. Due to the aforementioned complexities, turbulent flow is extremely difficult to describe and predict using purely theoretical methods, although the equations describing the turbulent motion of a Newtonian, viscous, incompressible fluid are known – the so-called Navier-Stokes equations. As a result, the fluid mechanics research community has used two main approaches, namely, experimental, and numerical studies (the latter which includes Reynolds-Averaged Navier-Stokes (RANS) methods, direct numerical simulation (DNS), and large-eddy simulation (LES)) to investigate turbulent flows.

The flow within the boundary layer along a wall becomes turbulent when the local Reynolds number becomes sufficiently large. The simplest case of a turbulent boundary layer occurs on a flat plate at zero angle of incidence. This is often referred to as a canonical zero-pressure turbulent gradient boundary layer. The wall surface conditions, such as surface roughness, play an important role in influencing the characteristics of turbulence structure in the near-wall region of the flow. In the following section, an overview of turbulent boundary layers is reported and the classification of surface roughness is discussed. Thereafter, the motivation for rough-wall turbulence research is presented. The Reynolds-Averaged Navier-Stokes equations, which represent the basic equations of motion, are also presented. Finally, the overall objectives and organization of the thesis are outlined.

1.2 Turbulent Boundary Layer

Flow of a viscous fluid over a solid surface encounters frictional forces, which retard the motion of the fluid in a thin layer close to the wall. The development of this layer is a major contributor to flow resistance on streamlined geometries and is of great importance in many engineering problems. The concept of a boundary layer is largely due to Prandtl in 1904, as reported by White (1974), who showed that the effects of friction within the fluid are significant only in a very thin layer close to the surface. The use of boundary layer theory has many important applications, such as the calculation of flow separation and skin friction drag.

Extensive research has been undertaken to study two-dimensional turbulent boundary layer flow over a smooth surface and in the context of a zero pressure gradient because of its simplicity both in terms of physics and geometry. Figure 1.1 presents a schematic showing the growth of a two-dimensional turbulent boundary layer on a smooth flat plate. The existence of the no-slip boundary condition at the wall retards the flow, resulting in a smooth streamwise mean velocity profile $U(y)$ (where y is the wall-normal coordinate direction), which smoothly merges into the external freestream velocity field, U_e. The boundary layer thickness $\delta(x)$ (where x is the streamwise coordinate) is considered to be the location above the surface at which the local mean velocity is 99% of the freestream value. As indicated in Figure 1.1, the boundary layer thickness grows with increasing distance, x , from the leading edge. Apart from the boundary layer thickness, there are two other relevant length scales, namely, the displacement thickness, δ^*, and

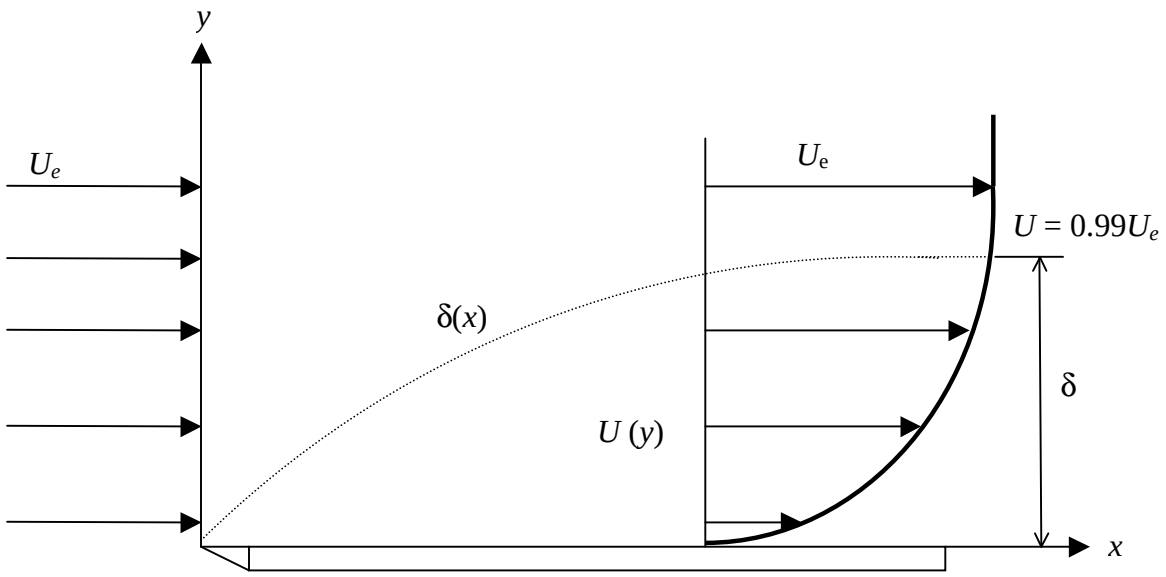

Figure 1.1: Schematic of a typical two-dimensional turbulent boundary layer on a flat plate.

momentum thickness, θ. The displacement thickness is the distance by which the wall would have to be displaced outward in a hypothetical frictionless flow so as to maintain the same mass flux as in the actual flow. The momentum thickness is related to the momentum loss due to the skin friction drag.

1.3 Surface Roughness

According to Perry et al. (1969), roughness elements can be classified into *k*-type and *d*-type, depending on the flow characteristics. For instance, when the roughness shift depends on the roughness height, *k*, it is called *k*-type, while for a *d*-type flow, the cavities between the roughness elements are narrow, and the roughness shift depends on

an outer scale (e.g. pipe diameter). In the present study, only *k*-type roughness is considered. Figure 1.2 shows a schematic of a 2-d generic rough surface. In this figure, *k* is the average roughness height, y_p is the wall-normal distance measured from the top plane of the roughness element, and y_o is the location of the virtual origin. The virtual origin is the distance between y_p and the location where the mean velocity extrapolates to zero. For a rough surface, the effective wall normal distance is expressed as, $y = y_p + y_o$. The location of the virtual origin depends on the geometrical structure of the roughness element (Kays and Crawford, 1993).

Based on the physical geometry of the wall, experimental evidence has shown that three flow regimes exist for turbulent flow over rough surfaces, (hydraulically smooth, transitionally rough and fully rough flows) primarily depending on the size of the roughness elements relative to the viscous sublayer. Following Schlichting (1968), Nikuradse (1932) has shown that, for *k*-type roughness, the equivalent sand grain roughness Reynolds number $k_{eq}^{+} = U_\tau k_{eq} / \nu$ (where U_τ is the friction velocity, k_{eq} is the equivalent sand grain roughness height, and ν is the kinematic viscosity) can be used as an indicator of the rough wall turbulence regime as follows: hydraulically smooth wall for $0 < k_{eq}^{+} \leq 5$, transitionally rough regime for $5 < k_{eq}^{+} < 70$, and completely rough regime for $k_{eq}^{+} \geq 70$.

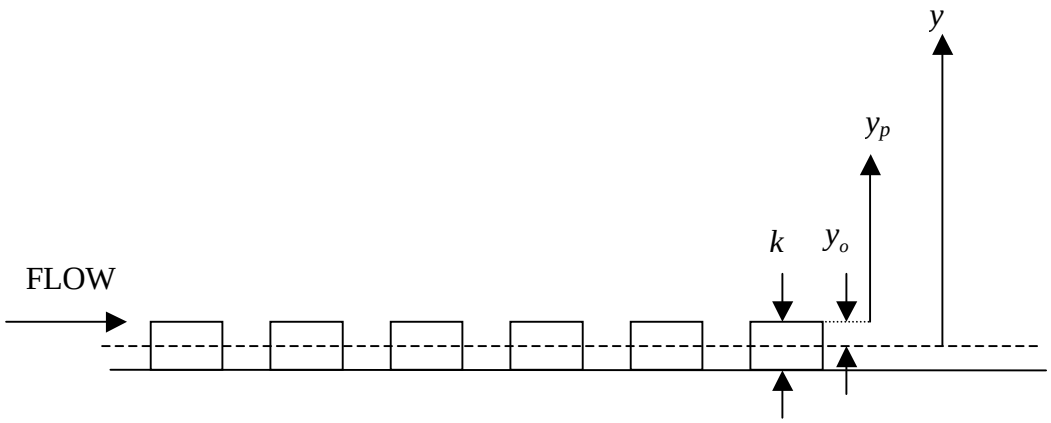

Figure 1.2: Schematic diagram of a 2-d generic rough surface.

1.4 Motivation for Rough Wall Turbulence Research

Turbulent flow over a rough surface occurs in diverse engineering and industrial applications. In many engineering applications (e.g. heat exchangers, turbine blades, ship and submarine hulls, high performance aircraft, and piping systems) surface roughness can significantly affect the skin friction and heat transfer characteristics (Hosni et al., 1993). The turbulent boundary layer over a rough wall has received considerable attention from researchers. Effects arising from the perturbations caused by the roughness elements alter the structure of the boundary layer near the wall. These in turn have significant effects on the momentum, heat and mass transfer rates at the surface, since they are controlled by the turbulent flow structure in the near-wall region. Often the most important parameter required by an engineering or industrial analysis is the skin friction drag. The skin friction drag is also required to determine the friction velocity, U_τ, which is an important scaling parameter in boundary layer theory.

However, for rough surfaces, it is difficult to directly measure the local skin friction values. The interpretation and understanding of the effect of surface roughness on the flow structure depends on how accurately the friction velocity can be measured. Accurate determination of the skin friction on rough surfaces continues to be an important research topic in the near-wall turbulence community (Tachie et al., 2001). The effect of surface roughness on the interactions between the inner and outer regions of the flow is not clearly understood. In addition, understanding the extent of the roughness effect arising from a variety of roughness types would improve modeling and predictive capabilities.

The effects of surface roughness present an additional complexity to similarity analysis of a turbulent boundary layer. Close to the wall itself, the effects of roughness on the velocity field depend on the specific geometry of the roughness elements. However, further from the wall, the effects have often been generalised to consist of an increase in the wall shear stress and an associated roughness shift, ΔU^+, to the logarithmic velocity profile. In contrast to the flow in the immediate vicinity of the roughness elements, often the flow structure in the outer region is assumed to retain a strong similarity to that for a smooth surface. The wall similarity hypothesis of Townsend (1976) confines the effect of surface roughness to the roughness sublayer. This implies that, at sufficiently high Reynolds number, both smooth and rough wall turbulent boundary layers will be structurally similar outside the sublayer when scaled with the friction velocity. However, recent experimental studies, e.g. the boundary layer measurements of Antonia and Krogstad (2001) and Keirsbulck et al. (2002), suggest that

the wall similarity notion may not be valid; instead, roughness effects can be observed to extend into the outer region of a turbulent boundary layer, both in terms of the mean velocity profile (e.g. the strength of the wake) and the fluctuating velocity fields. Even though rough-wall turbulent flow has been much studied using both experimental and more recently, numerical methods, the fundamental issue of how surface roughness affects the near-wall and (possibly) outer regions of the boundary layer has not yet been satisfactorily answered. The ambiguity in the literature can be partly attributed to the lack of data for higher-order moments of the fluctuating component of the velocity field in rough wall flows. Furthermore, the interpretation of rough wall boundary layer data often depends on the choice of scaling parameter.

An immediate question for near-wall computational studies is to what degree the turbulence model reproduces the effects of surface roughness in the outer region of the flow. In recent years, computational models based on both k-ε and more complex closures have made significant progress towards predicting near-wall turbulent flows, even in applications where pressure gradients and surface curvature are present. However, the present capability for numerical simulation of rough wall flows is substantially deficient compared to that for smooth surfaces, especially for high Reynolds number applications. The application of DNS to rough wall turbulence research has been minimal. This can be largely attributed to the additional complexity and computational burden arising from the roughness geometry. As pointed out by Patel (1998), the treatment of rough surfaces by present modeling techniques is still deficient and additional investigations are required.

1.5 Reynolds-Averaged Navier-Stokes Equations

The dynamics of near-wall turbulence is adequately described by the continuity and Navier-Stokes equations. In steady incompressible turbulent flows of a Newtonian fluid, the Reynolds-averaged mass and momentum equations can be concisely written in Cartesian tensor form as,

$$\frac{\partial(\rho U_j)}{\partial x_j} = 0 \tag{1.1}$$

$$\rho U_j \frac{\partial U_i}{\partial x_j} = -\frac{\partial P}{\partial x_i} + \frac{\partial}{\partial x_j}\left(\mu \frac{\partial U_i}{\partial x_j} - \rho < u_i u_j > \right) + \rho g_i \tag{1.2}$$

where U_j and u_j are the jth components of the mean and fluctuating velocities, respectively; P is the mean pressure; $< u_i u_j >$ is the Reynolds stress; x_j denotes coordinate direction; g_i represents gravitational acceleration and ρ and μ are the fluid density and viscosity, respectively. The instantaneous velocity components $\tilde{u}_i$ and the pressure $\tilde{p}$ are decomposed into mean and fluctuating parts as

$$\tilde{u}_i = U_i + u_i, \qquad \tilde{p} = P + p \tag{1.3}$$

where u_i and p are the fluctuating components, and U_i and P are the mean components. The mean value can be obtained using different methods depending on the assumptions adopted. For example, the ergodic hypothesis states that, in statistically steady turbulent flow, the ensemble mean is equal to a time average, whereas in statistically homogeneous turbulence, the ensemble mean is equal to a spatial average (Hinze, 1975). The work in this thesis considers statistically steady turbulence, and the mean value is therefore defined as

$$U = \frac{1}{T}\int_{t}^{t+T} \tilde{u}_i \ (x,t)\mathrm{d}t \tag{1.4}$$

where T is the time period of averaging and t is the time variable.

The problem of modeling turbulent flows arises from the nonlinear convective term of the Navier-Stokes equations that leads to the appearance of time-averaged products of the fluctuating velocities which represent an unknown correlation tensor $< u_i u_j >$ (called the Reynolds stress tensor) in Equation (1.4). The RANS equation set is not closed until a model is provided that links the Reynolds stress tensor $< u_i u_j >$ to the mean velocity U_i and possibly other variables in a physically reasonable manner.

In 1904 Prandtl deduced that a shear layer will be very thin when the Reynolds number is large, so that the following approximations apply: $V << U$; $\partial/\partial x << \partial/\partial y$; $\partial^2 U/\partial x^2 << \partial^2 U/\partial y^2$. Applying these approximations to Eqn. (1.2) yields the Prandtl boundary layer equations as follows:

Momentum along the wall: $$U\frac{\partial U}{\partial x} + V\frac{\partial U}{\partial y} \approx U_e\frac{dU_e}{dx} + \frac{1}{\rho}\frac{\partial}{\partial y}\left(\mu\frac{\partial U}{\partial y} - \rho < uv >\right)$$

The pressure gradient term is assumed to be known in advance from Bernoulli's equation applied to the outer inviscid flow.

The existence of surface roughness in wall-bounded flow can be categorised as a complex boundary condition (Tachie et al., 2004). As mentioned earlier in Section 1.4,

the main effect of surface roughness is to increase the turbulence close to the roughness elements. A primary goal for a turbulence model is therefore to incorporate this effect, in the way that the turbulent shear stresses are modeled by relating this increase directly to the surface roughness. Different approaches have been employed to model the turbulent flow on a rough wall. Detailed information on these approaches is provided in Chapter 2.

1.6 Objectives and Organization of the Thesis

1.6.1 Objectives

Understanding the degree of roughness perturbation for a variety of roughness types would improve modeling and predictive capabilities. However, a clear physical understanding of the effects of surface roughness on both the mean velocity and turbulence fields requires that appropriate scaling laws be employed to analyze the experimental and numerical results. In this case, different scaling parameters, such as the friction velocity and freestream velocity, are used to assess the surface roughness effects on both the mean velocity and turbulence fields.

The overall purpose of the research is to improve the understanding of the effects of surface roughness on both the mean velocity and turbulence fields in a zero-pressure gradient turbulent boundary layer. The specific objectives are:

1. To obtain a large matrix of experimental data for mean velocity and turbulence quantities that encompasses hydraulically smooth, transitionally rough, and fully rough flow regimes;

2. To use different profile fitting techniques to evaluate the skin friction for smooth and rough wall flows;
3. To investigate the appropriateness of different inner and outer scaling parameters proposed for both the mean velocity and turbulence fields, and to examine whether Townsend's wall similarity hypothesis holds for different surface characteristics;
4. To examine the applicability of power laws to describe the mean velocity in the overlap region, and to evaluate the power law constants for rough wall flows.

Another compelling issue is the numerical simulation and prediction of flow fields on a rough surface. Most existing turbulence models for rough-wall flows have been used to predict the effect of surface roughness on the mean velocity field without examining the capability of such models to reproduce the effect of roughness on the turbulence field. Of special interest is to examine the validity of the wall similarity hypothesis in the context of a numerical study.

5. To predict of the mean velocity and turbulence quantities on smooth and rough surfaces using near-wall turbulence models is one of the objectives of this thesis.

In order to achieve the objectives outlined above, experimental data sets were obtained on a hydraulically smooth and ten different rough surfaces created from sand paper, perforated sheet, and woven wire mesh. The physical size and geometry of the roughness elements, and the freestream velocity were chosen to encompass both transitionally rough and fully rough flow regimes. Velocity field measurements were

obtained using a Pitot probe, as well as single- and X-probe hot-film anemometers. In the case of the numerical prediction, both wall function formulation and two-layer k-ε models were employed. The two-layer k-ε models were used to examine the validity of the wall similarity hypothesis, while a new set of equations was proposed for the wall function formulation.

1.6.2 Organization of Thesis

In Chapter 2, the theoretical basis of scaling laws for the mean velocity and turbulence statistics, as well as previous relevant experimental and numerical studies of smooth- and rough-wall turbulent boundary layers, are reviewed. The instrumentation and surface roughness as well as the experimental step-up, are described in Chapter 3. In Chapter 4, the smooth and rough wall data for the mean velocity are reported. The data sets presented in this chapter are used to determine the friction velocity. In addition, the scaling issues, effects of different roughness geometries on the mean velocity in the inner region, and the behaviour of the power law coefficient and exponent for different flow regimes, are all examined in this chapter. Furthermore, the data sets are also used to calibrate the power law coefficient and exponent in transitionally rough flow, and establish a skin friction correlation valid for smooth and rough walls. Outer flow similarity issues for smooth and rough walls are discussed in Chapter 5. In Chapter 6, the effects of surface roughness on Reynolds stresses are assessed using different scaling parameters. The effects of surface roughness on the higher-order moments such as triple velocity products, skewness and flatness factors are discussed in chapter 7. Numerical results of mean velocity profiles on smooth and rough walls using near-wall turbulence

models are presented in Chapter 8. In Chapter 9, a summary, major conclusions, and contributions from the study are presented.

CHAPTER 2

THEORETICAL ANALYSIS AND LITERATURE REVIEW

2.1 Introduction

This chapter contains a review of the theoretical derivation of the scaling laws for the mean velocity and turbulence quantities for a two-dimensional flat-plate turbulent boundary layer. A description of the overlap region of the mean turbulent boundary layer, the scaling laws proposed by the classical theories, and power law formulations are carefully considered. The determination of surface drag using different experimental methodologies is also described. Some previous and current experimental and numerical studies of turbulent boundary layers are reviewed.

2.2 Scaling of Mean Velocity in Turbulent Boundary Layers

The interpretation of experimental measurements of the mean velocity depends on the choice of appropriate scaling laws. In a turbulent boundary layer, two flow regions have been identified, i.e., the inner and outer regions, each of which exhibits a distinct scaling as indicated in Figure 2.1. Matched asymptotic expansions by Millikan (1938) suggested that an overlap region exists between the inner and outer layers for sufficiently high Reynolds numbers. In the following subsections, the description of the scaling laws for the inner and outer regions, as well as the overlap region, is presented.

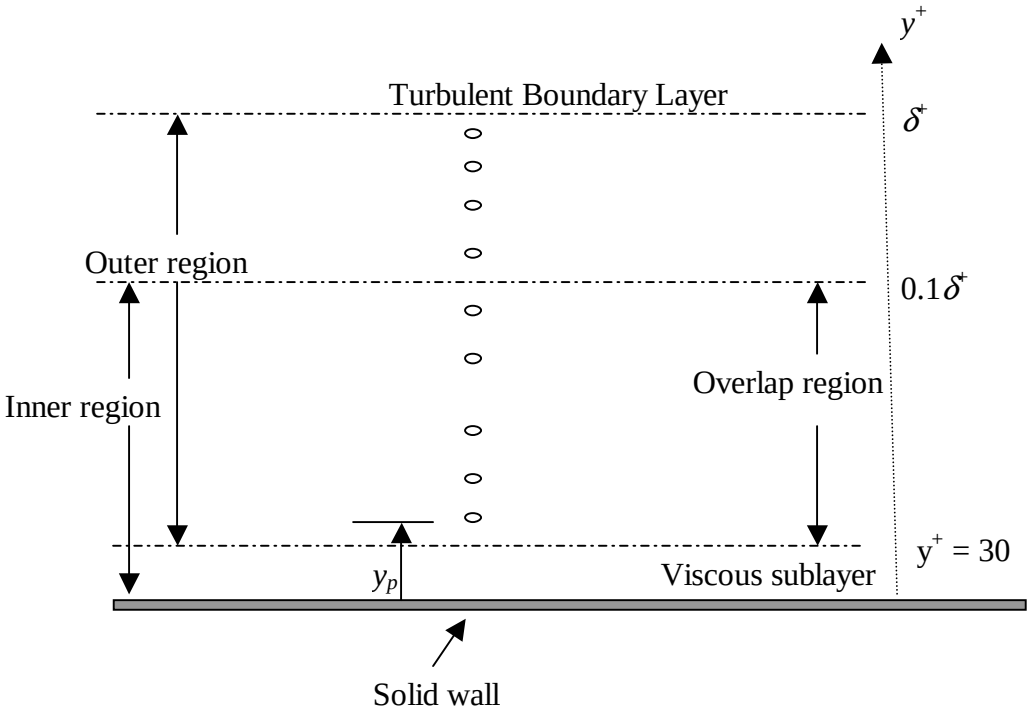

Figure 2.1: Schematic showing different regions within a turbulent boundary layer.

2.2.1 The Law of the Wall and Defect Law

According to Prandtl (1932), the viscosity and wall shear stress are the significant parameters which influence the mean velocity profile in the inner region, so that

$$U = f_i(y, \tau_w, \nu, \rho) \tag{2.1}$$

In the outer region, at sufficiently high Reynolds numbers, the energy-containing motions are independent of viscosity, so that the velocity profile is scaled as

$$U_e - U = f_o(y, \delta, u_o) \tag{2.2}$$

where u_o is the velocity scale in the outer region. Following Rotta (1962), as proposed originally by Prandtl (1932), dimensional analysis of Eqns. (2.1) and (2.2) leads to the

following scaling of the mean velocity profile in the inner and the outer regions, respectively:

$$U^+ = f_i(y^+) \tag{2.3}$$

and

$$\frac{U_e - U}{u_o} = f_o(\eta) \tag{2.4}$$

where $U^+ = U/U_\tau$, $y^+ = yU_\tau/\nu$, $U_\tau\ (=\tau_w/\rho)^{1/2}$ is the friction velocity, f_i and f_o are the dimensionless functional parameters in the inner and outer functions, respectively, and $\eta = y/\delta$. Equation (2.3) is the classical "Law of the Wall" for the inner region, which implies complete similarity (Reynolds number independence) in the inner region. Equation (2.4) is also known as the "Defect Law", which expresses complete similarity in the outer region.

For the outer region, the mean velocity profile is often presented in defect form. Three different velocity scales have been proposed for u_o in the outer region. According to classical theories, the friction velocity, U_τ, was proposed as the outer scale for the mean velocity defect. Based on their own similarity analysis, George and Castillo (1997) concluded that the outer velocity scale was proportional to the freestream velocity, U_e. Recently, Zagarola and Smits (1998) introduced an outer velocity scale which is proportional to the mass flux deficit in the boundary layer. They proposed the following outer velocity scale for a smooth wall turbulent boundary layer:

$$u_o = U_e \int_0^1 \left(1 - \frac{U}{U_e}\right) d\left(\frac{y}{\delta}\right) = U_e \frac{\delta^*}{\delta} \tag{2.5}$$

where δ^* is the boundary layer displacement thickness. This outer velocity scale has been used to successfully collapse the mean velocity defect profiles on both smooth (Castillo and Walker, 2002) and rough surfaces (Seo, 2003).

2.2.2 Scaling Laws for the Overlap Region

In wall-bounded turbulent flows, the choice of an appropriate scaling law to describe the mean velocity profile in the overlap region continues to be a subject of controversy within the turbulence community. Since the inner length scale (ν/U_τ) and the outer length scale (δ) are presumably too small and too large, respectively, the dynamics of the flow in the overlap region is independent of all length scales except the distance from the wall (Tennekes and Lumley, 1972). Different theories have been advanced regarding the form of the mean velocity profile which exists in the overlap region. Figure 2.2 presents a schematic diagram of the inner, outer and overlap regions of a turbulent boundary layer. The classical theories propose a logarithmic law for both ducts and turbulent boundary layers (Millikan, 1938; Clauser, 1954; Panton, 1990). Due primarily to inconsistencies in fitting the experimental data to log law relations, several researchers have investigated alternatives (Barenblatt, 1993; George and Castillo, 1997; Afzal, 2001). Based on different similarity analyses, they propose power laws as an alternative formulation for the overlap region in the limit of finite Reynolds numbers, as are often encountered in the turbulence measurements in the laboratory.

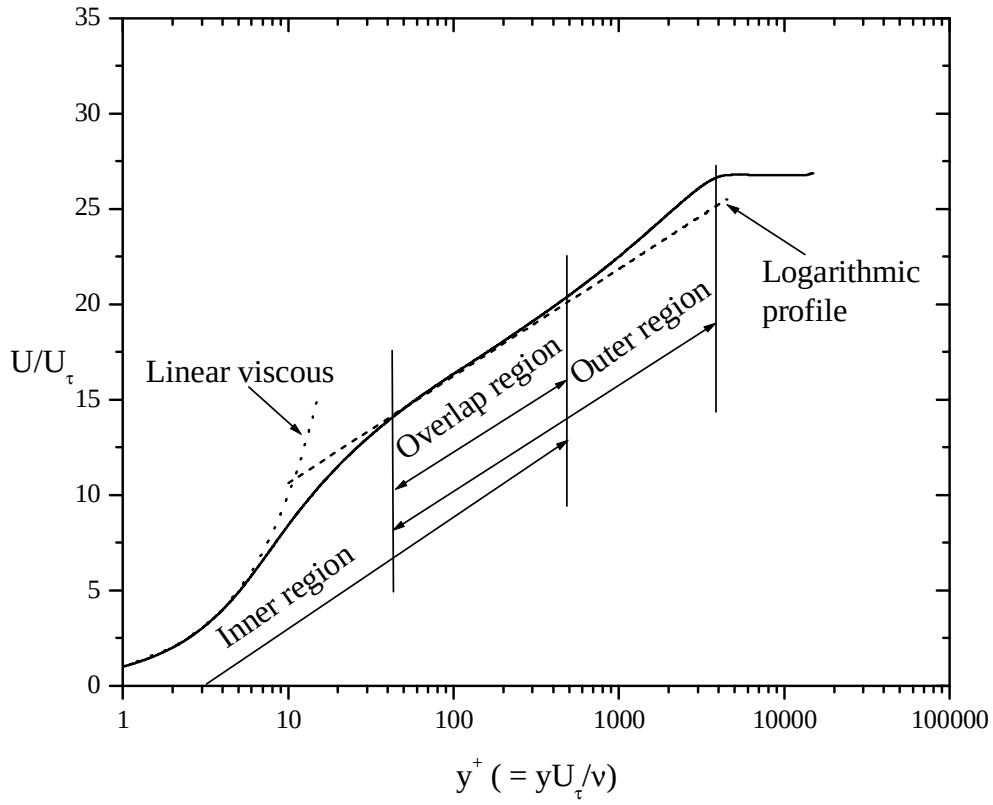

Figure 2.2: Schematic diagram of the inner, outer, and overlap regions of a turbulent boundary layer.

Theoretical and experimental arguments continue to consider both the power law and log law. For example, the boundary layer measurements reported by Österlund et al. (2000) provide evidence in support for a log law; however, reconsideration of the same data by Barenblatt et al. (2000) suggests that they are better described by a power law. In an attempt to resolve the log law versus power law issue, Zagarola et al. (1997) studied turbulent pipe flow over a range of Reynolds numbers. They proposed that the mean velocity consists of two distinct regions: a power law region for $50 \le y^+ \le 500$ or $0.1R^+ (= U_\tau R/\nu$, where R is the pipe radius, the upper limit being dependent on

Reynolds number), and a log law region for $500 < y^+ < 0.1R^+$. Panton (2000) concluded in his study that the log law and the power law apply to different regions of the boundary layer; more specifically, that a power law extends into the inner part of the wake region whereas a log law does not. Panton (2002) also evaluated the Barenblatt-Chorin-Prostokinshin power law for turbulent boundary layers and found that the method was very sensitive, and could produce profiles that did not closely match the data. Buschmann and Gad-el-Hak (2003) recently examined the extent to which logarithmic and power law profiles describe the mean velocity profile in the overlap region of a smooth wall boundary layer. They showed that there exists a region in the overlap layer that can be described by both power law and logarithmic profiles.

2.2.2.1 Logarithmic Law

According to classical theories, the mean velocity profile in the overlap region is best described by the logarithmic law. Clauser (1954), following Millikan (1938), matched the Law of the Wall and Defect Law to obtain a logarithmic velocity profile for a smooth wall to describe the outer part of the inner region as

$$U^+ = \frac{1}{\kappa} \ln y^+ + B \tag{2.6}$$

and the inner part of the outer region as

$$\frac{U_e - U}{U_\tau} = -\frac{1}{\kappa} \ln\left(\frac{y}{\delta}\right) + A \tag{2.7}$$

where κ is the von Karman constant, and A and B are the additive constants. The constants are assumed to be universal and independent of Reynolds number. The values

of the constants (κ = 0.41, B = 5.0, and $A \approx 2.5$) have been found by many researchers to adequately describe the logarithmic velocity profile in the overlap region. Coles (1956) incorporated the wake function into the logarithmic law with the aim of describing both the overlap and outer regions of a smooth wall boundary layer, so that Eqn. (2.6) becomes

$$U^+ = \frac{1}{\kappa}\ln y^+ + B + \frac{2\Pi}{\kappa}\omega(\eta) \tag{2.8}$$

where Π is the Coles wake parameter and $\omega(\eta)$ is the wake function. Based on a curve-fit approximation to experimental data, the wake function expressed as

$$\omega(\eta) \approx 2\sin^2\left(\frac{\pi}{2}\frac{y}{\delta}\right) \tag{2.9}$$

For a rough wall turbulent boundary layer, the mean streamwise velocity distribution across both the overlap and outer regions is given by (Krogstad et al., 1992)

$$U^+ = \frac{1}{\kappa}\ln\frac{(y+y_o)U_\tau}{\nu} + B - \Delta U^+ + \frac{2\Pi}{\kappa}\omega(\frac{y+y_o}{\delta}) \tag{2.10}$$

where y_o is the virtual origin, which represents the virtual location of the wall relative to the nominal top of the roughness elements (see discussion on page 4), and $\Delta U^+ = \Delta U/U_\tau$ is the roughness function, which represents the downward shift of the linear portion of the velocity profile plotted on a logarithmic plot.

2.2.2.2 Power Laws

In spite of the fact that a power law was originally proposed by Nikuradse (1933) about seven decades ago, many researchers have preferred the use of a logarithmic law to

model the velocity profile in wall-bounded turbulent shear flows. The range of y^+ for which the power law fits the velocity profile has been noted to be different from that of the logarithmic law (Buschmann and Meniert, 1999; Panton, 2000). More specifically, the power law allows the lower edge of the wake zone to be fitted, while a small region in the lower part of the logarithmic region is not represented. In general form, a power law can be expressed using inner coordinates as

$$U^+ = C(y^+)^\gamma \tag{2.11}$$

The coefficients, C and γ, are experimental parameters, which depend on the Reynolds number.

In the context of pipe flow, Barenblatt (1993) derived a power law formulation to describe the mean velocity profile in the overlap region. He based his formulation on incomplete similarity, which supports the idea of Reynolds number dependent characteristics of the overlap region. The power law proposed by Barenblatt (1993) can be expressed as

$$U^+ = C(y^+)^\alpha \tag{2.12}$$

where the power law constants are given by the following asymptotic expansions

$$\alpha = \frac{a_1}{\ln \mathrm{Re}} + \frac{a_2}{(\ln \mathrm{Re})^2} + ... \tag{2.13}$$

$$C = c_1 \ln \mathrm{Re} + c_2 + \frac{c_3}{\ln \mathrm{Re}} + ... \tag{2.14}$$

Based on the pipe flow experimental data of Nikuradse (1933) and Barenblatt and Prostokishin (1993), the values of the constants are $a_1 = 3/2$, $c_1 = 1/\sqrt{3}$, and $c_2 = 5/2$,

where only the first term and the first two terms are retained for α and C, respectively. Using the Princeton Superpipe data, which cover a range of $31\times10^3 \le \mathrm{Re} \le 35\times10^6$, Zagarola et al. (1997) recalibrated Barenblatt's power law coefficients to obtain:

$$\alpha = \frac{1.085}{\ln \mathrm{Re}} + \frac{6.535}{\ln \mathrm{Re}^2} \quad \text{and} \tag{2.15}$$

$$C = 0.7053 \ln \mathrm{Re} + 0.3055 \tag{2.16}$$

where Re ($=U_{ave}D/\nu$) is the Reynolds number, U_{ave} is the average velocity, and D is the pipe diameter.

George and Castillo (1997) used the Asymptotic Invariance Principle (AIP) to derive a power law relation for the mean velocity in the overlap region of a zero-pressure gradient boundary layer. They noted that except in the limit of infinite Reynolds number, the overlap region is Reynolds number dependent since the ratio of the inner and outer velocity scales, U_τ/U_e, is Reynolds number dependent. Their form of the power law is defined in terms of $y' = y + a$, so that Eqn. (2.11) becomes

$$U^+ = C_i (y^+ + a^+)^\gamma \tag{2.17}$$

In outer scaling, they also derived a power law form for the mean velocity given by

$$\frac{U}{U_e} = C_o \left(\frac{y + a}{\delta} \right)^\gamma \tag{2.18}$$

Similar to Coles' proposal, George and Castillo (1997) incorporated a wake term to obtain the following expression that describes the overlap region and outer region of the boundary layer,

$$\frac{U}{U_e} = C_o\left(\frac{y+a}{\delta}\right)^{\gamma} + (1-C_o)\frac{y}{\delta}\sin\left(B\frac{y}{\delta}\right) \tag{2.19}$$

The multiplicative coefficients, C_i and C_o, as well as the exponent γ, are dependent on the Reynolds number, $\delta^+ (= U_\tau \delta/\nu)$. The second term on the right hand side represents a wake function, where *B* attains a value of 2.03 as recommended by George and Castillo (1997). In the above equations, *a* represents a shift in the origin for measuring *y* associated with the growth of the mesolayer region ($30 \le y^+ \le 300$) and the value of $a^+ = -16$ is adopted. It should be noted that the origin shift, *a*, was not derived, but rather introduced on the basis of additional arguments. George and Castillo (1997) looked for similarity solutions of the following forms:

$$U - U_\infty = U_{so}(x)\, f_o(\bar{y}, \delta^+) \tag{2.20}$$

$$-<uv> = R_{so_{uv}}(x) r_o(\bar{y}, \delta^+) \tag{2.21}$$

$$<u^2> = R_{so_{u^2}}(x) k_u(\bar{y}, \delta^+) \tag{2.22}$$

$$<v^2> = R_{so_{v^2}}(x) k_v(\bar{y}, \delta^+) \tag{2.23}$$

where U_{so}, $R_{so_{uv}}$, $R_{so_{u^2}}$, and $R_{so_{v^2}}$ are the outer velocity scale and the outer Reynolds stress scales which depend only on x. Note that these scales are initially unknown and are determined from the boundary layer equations only. The arguments inside the similarity functions (f_o, r_o, k_u, k_v) represent the wall normal distance normalized by the outer similarity length scale, $\bar{y} = y/\delta$, and the Reynolds number, δ^+.

Porporato and Sordo (2001) modified the coefficients in the power law relations proposed by Barenblatt (1993) for turbulent pipe flow to include the effect of surface roughness for sand grain type roughness. In their study, the coefficients, C and α, are modified for fully rough flow as follows:

$$\alpha_r = 0.455\left(\frac{D}{2k_s}\right)^{-0.225} \quad \text{and} \quad C_r = \frac{c}{\mathrm{Re}^{\alpha_r}} \tag{2.24}$$

where the subscript 'r' indicates the fully rough regime, k_s is the characteristic sand grain roughness height, and a value of c = 35.6 was obtained from curve fitting to experimental data for sand grain roughness.

The power law formulation of George and Castillo (1997) has also been used to describe the mean velocity profile on a rough wall. The first attempt to modify the power law formulation for a rough wall was done by Kotey *et al*. (2003). Based on semi-empirical arguments, they re-write Eqn. (2.17) as:

$$U_R^+ = \frac{C_i}{E}(y^+ + a^+)^{\gamma+\xi} \tag{2.25}$$

where the subscript R represents the rough wall, E (≥ 1) is a parameter introduced to reproduce the downward shift caused by the roughness effect in the overlap region, and ξ (≥ 0) accounts for the increase in the wake parameter due to surface roughness.

Seo (2003) also incorporated the surface roughness effect into the original power law proposed by George and Castillo (1997). She modified the power law coefficients,

C_i, C_o, and γ, to account for the effects of surface roughness, and obtained complex expressions as follows:

$$\tilde{C}_i(\delta^+, k^+) = \left(\frac{C_{i\infty}}{1 + 0.0355(k^+)^{0.88647}} \right) \left(1 + 0.283\exp(-0.00598\delta^+)\right) \exp\left(\frac{-(1+\alpha)A}{(\ln \delta^+)^{\alpha}} \right) \quad (2.26)$$

$$\tilde{\gamma}(\delta^+, k^+) = \gamma_\infty + 0.0065(k^+)^{0.60126} + \frac{\alpha A}{(\ln \delta^+)^{1+\alpha}} \quad (2.27)$$

$$\tilde{C}_o(\delta^+, k^+) = C_{o\infty}(1 + 0.00576(k^+)^{0.517})(1 + 0.283\exp(-0.00598\delta^+) \quad (2.28)$$

where k^+ is the roughness Reynolds number. The numerical values of the power law constants are given as follows: $C_{i\infty}$ = 55, $C_{o\infty}$ = 0.897, γ_∞ = 0.0362, A = 2.90, and α = 0.46. If k^+ = 0, Eqns. (2.26) to (2.28) reduce to the original expressions given by George and Castillo (1997).

2.2.3 Determination of Skin Friction

Accurate determination of the skin friction on smooth and rough surfaces continues to be important. Many reliable techniques for estimating the skin friction (or wall shear stress) have been developed for a smooth wall turbulent boundary layer including use of the momentum integral equation, correlations based on total pressure measurements at the surface (i.e. using a Preston tube), and oil-film interferometry. Indirect methods based on fitting to the mean velocity profile have also been employed to determine the skin friction. These include the 'classical' Clauser technique, and fitting profiles based on either a defect law or power law. Using either direct or indirect methods, a number of correlations (e.g., Schultz-Grunow, 1941; Coles, 1962; Osaka et al., 1998; Tachie et al.,

2001) have been developed to allow the prediction of skin friction on a smooth surface for practical applications.

Analyzing smooth- and rough-wall boundary layer flows using profile-fitting methods requires some assumption regarding the mean velocity profile. Probably the most common plotting technique for determining the friction velocity, U_τ, is that of Clauser, in which a logarithmic profile is fitted to the experimental data for the mean velocity in the overlap region to obtain U_τ, which can then be used to determine the skin friction coefficient, $C_f = 2(U_\tau / U_e)^2$, where U_e is the freestream velocity. Eqn. (2.10) shows that description of a measured velocity profile on a rough wall requires the determination of four parameters, i.e., U_τ, ΔU^+, Π, and y_o. Perry et al. (1969) noted that due to the additional roughness parameters $(\Delta U^+, y_o)$ the Clauser plot technique for determining the friction velocity can be inaccurate. Bandyopadhyay (1987) also argued that only a few data points in the logarithmic region could be accommodated by the Clauser technique. For a turbulent boundary layer, other factors such as freestream turbulence intensity and pressure gradient, can also influence the skin friction characteristics.

As an alternative to the Clauser technique, Hama's formulation is a commonly used defect form for the velocity distribution in zero pressure-gradient boundary layers on smooth and rough surfaces. For small values of y/δ, the defect profile is dominated by the logarithmic term and is written as

$$\frac{U_e - U}{U_\tau} = -\frac{1}{\kappa}\ln\left(\frac{yU_\tau}{\delta^* U_e}\right) - 0.6 \text{, where } \left(\frac{yU_\tau}{\delta^* U_e} \le 0.045\right) \tag{2.29}$$

For larger values of y/δ, the wake contribution dominates and Hama proposed the function

$$\frac{U_e - U}{U_\tau} = 9.6\left(1 - \left(\frac{10yU_\tau}{3\delta^* U_e}\right)\right)^2 \text{, where } \left(\frac{yU_\tau}{\delta^* U_e} > 0.045\right) \tag{2.30}$$

In both cases, the displacement thickness δ^* is used as the reference length scale. A smooth connection exists between Eqns. (2.29) and (2.30) at $y/\delta = 0.15$. Bandyopadhyay (1987) suggests that the Hama profile could be fitted to obtain a reliable estimate of friction velocity irrespective of surface condition. The distinct advantage of Hama's formulation over the Clauser technique is that the profile covers virtually the entire boundary layer region.

The experimental evidence from some studies of the near-wall turbulent flows (e.g. Bandyopadhyay, 1987; Perry et al., 1987; Krogstad et al., 1992) revealed that the friction velocity, U_τ, obtained from the Hama formulation is consistently higher than that obtained from either a momentum balance or by extrapolating the Reynolds stress to the wall. Bradshaw (1987) pointed out that this may due to the lower value of the strength of the wake prescribed in the Hama formulation. Recent experimental results have shown that the strength of the wake depends on Reynolds number, Re_θ, roughness effects, and the streamwise turbulence level.

As an alternative to the Hama formulation, Finley et al. (1996) proposed to use the velocity defect law in terms of a formulation that does not implicitly fix the strength of the wake, Π, but rather allows its value to be optimized while ensuring a reliable determination of the friction velocity. This method was used by Granville (1976) and Krogstad et al. (1992). In this case, the mean defect profile is given by

$$\frac{U_e - U}{U_\tau} = \frac{2\Pi}{\kappa}\left[w(1) - w\left(\frac{y}{\delta}\right)\right] - \frac{1}{\kappa}\ln\left(\frac{y}{\delta}\right) \tag{2.31}$$

The wake function used in Eqn. (2.26) is expressed as

$$w\left(\frac{y}{\delta}\right) = \frac{1}{2\Pi}\left[(1+6\Pi) - (1+4\Pi)(y/\delta)\right]\left(\frac{y}{\delta}\right)^2 \tag{2.32}$$

A distinct advantage of using the defect profile, especially for high Reynolds number flows, is that velocity data outside the inner layer can be included.

Both Barenblatt (1993) and George and Castillo (1997) used their proposed power law formulations to derive skin friction relations. Barenblatt (1993) obtained the following skin friction relation:

$$C_f = 2\left(\frac{U_\tau}{U_e}\right)^2 = 2\left(\frac{1}{\exp(3/2)}\left(\frac{\exp(3/2\alpha}{C}\right)^{1/(1+\alpha)}\right)^2 \tag{2.33}$$

In the case of the power law proposed by George and Castillo (1997), the skin friction relation is expressed as

$$C_f = 2\left(\frac{U_\tau}{U_e}\right)^2 = 2\left(\left(\frac{C_o}{C_i}\right)^{1/(1+\gamma)}\left(\frac{U_e\delta}{\nu}\right)^{-\gamma/(1+\gamma)}\right)^2 \tag{2.34}$$

Djenidi et al. (1997) also found the use of a power law in determining the friction velocity in a low Reynolds number turbulent boundary layer to be reliable. The values of the skin friction obtained from these formulations have shown to be comparable to the values obtained by other reliable techniques (Tachie et al., 2001). The friction velocities obtained from these methods were shown to be within ± 4 %.

2.2.3.1 Skin Friction Correlation

The empirical relationships between C_f and Re_θ in two-dimensional incompressible boundary layers over a smooth surface have a long history. Fernholz and Finley (1996) argued that many empirical correlations were curve fits to measurements without theoretical justification. White (1974) obtained a power law approximation for C_f on a smooth wall turbulent boundary layer as follows:

$$C_f \approx 0.012\,\mathrm{Re}_\theta^{-1/6} \approx 0.018\,\mathrm{Re}_\delta^{-1/6} \approx 0.0128\,\mathrm{Re}_{\delta^*}^{-1/6} \approx \frac{0.455}{\ln^2(0.06\,\mathrm{Re}_x)} \qquad (2.35)$$

Fernholz et al. (1995) proposed a correlation for the skin friction on a smooth wall as

$$C_f = 0.32(1.77 + \ln(\mathrm{Re}_\theta))^{-2} \qquad (2.36)$$

In their re-examination of the Reynolds number effect on the mean flow quantities, Osaka et al. (1998) proposed an empirical expression for the skin friction given by

$$\frac{1}{C_f} = 20.03(\log \mathrm{Re}_\theta)^2 + 17.24(\log \mathrm{Re}_\theta) + 3.71 \qquad (2.37)$$

Tachie et al. (2001) developed a skin friction correlation for smooth wall in an open channel flow, given by

$$C_f = 4.13\times10^{-2} - 2.68\times10^{-2}(\log \mathrm{Re}_\theta) + 6.528\times10^{-3}(\log \mathrm{Re}_\theta)^2 - 5.54\times10^{-4}(\log \mathrm{Re}_\theta)^3 \tag{2.38}$$

For a rough-wall turbulent boundary layer, based on the experimental data of Nikuradse (1933) for sand-roughened plates, Schlichting (1979) proposed a skin friction correlation as follows:

$$C_f = \left(2.87 + 1.58\log_{10}(x/k)\right)^{-2.5} \tag{2.39}$$

Acharya et al. (1986) proposed a skin friction correlation given by,

$$\sqrt{\frac{2}{C_f}} = \frac{1}{\kappa}\ln\left(\frac{\delta^*}{k}\sqrt{\frac{2}{C_f}}\right) + A \tag{2.40}$$

which requires a linear relationship between $\sqrt{2/C_f}$ and $\ln((\delta^*/k)\sqrt{2/C_f})$, and A is a constant. Seo (2003) also proposed a skin friction correlation as follows;

$$C_f = 2\left(\frac{C_{o\infty}(1+C_{ok})(1+C_{ik})}{C_{i\infty}}\right)^2 \delta^{+-(\gamma_\infty+\gamma_k)} \exp\left(\frac{2A}{(\ln(\delta^+))^\alpha}\right) \tag{2.41}$$

where $C_{ok} = 0.00576k^{+0.517}$, $C_{ik} = 0.03551k^{+0.88647}$, and $\gamma_k = 0.0065k^{+0.60126}$.

Recall that Clauser (1954) showed that a boundary layer with a constant turbulence equilibrium parameter could be scaled with a single parameter. He defined a thickness parameter for equilibrium flow, also known as the defect thickness, Δ, where

$$\Delta = \int_0^\infty \frac{U_e - U}{U_\tau}\,dy = \delta^*\lambda \tag{2.42}$$

and $\lambda = \sqrt{2/C_f}$ is related to the local skin friction. The self-similar velocity profiles were then scaled with y/Δ. An integral shape factor, *G*, which remains constant in an equilibrium boundary layer, was defined as follows:

$$G = \frac{1}{\Delta}\int_o^\infty \left(\frac{U_e - U}{U_\tau}\right)^2 dy \tag{2.43}$$

where *G* is related to the ordinary Kármán-type shape factor, *H*, by the following expression

$$H = \frac{\delta^*}{\theta} = \left(1 - \frac{G}{\lambda}\right)^{-1} \tag{2.44}$$

and θ is the momentum thickness. Eqn. (2.38) can be re-arranged as follows:

$$C_f^{1/2} = \frac{\sqrt{2}}{\Delta}\delta^* \tag{2.45}$$

Multiplying the right-hand side by δ/δ leads to the following equivalent expression:

$$C_f^{1/2} = \sqrt{2}\left(\frac{\delta}{\Delta}\right)\left(\frac{\delta^*}{\delta}\right) \tag{2.47}$$

Zagarola and Smits (1998) noted that, at high Reynolds numbers, $C_f^{1/2} \sim \delta^*/\delta$ for a smooth wall turbulent boundary layer. In view of this observation, one might conjecture that the ratio δ/Δ is invariant for general classes of turbulent boundary layer flows. In the present study, this hypothesis will be explored further for both smooth and rough surfaces.

2.3 Scaling of Turbulence Quantities

The appropriate scaling parameter for the Reynolds stress components in turbulent boundary layers also continues to be a subject of debate. Classical arguments support the use of the friction velocity, U_τ, as the scaling parameter for the Reynolds stresses on a smooth wall (Tennekes and Lumley, 1972). However, some researchers have indicated that scaling the streamwise Reynolds stress with the friction velocity, U_τ, does not obtain a universal profile in the overlap and outer regions of the flow (e.g. George and Castillo, 1997; DeGraaff and Eaton, 2000). They attribute the failure of the friction velocity to collapse the streamwise Reynolds stress to its dependence on the Reynolds number. A review by Gad-el-Hak and Bandyopadhyay (1994) also indicated that since Reynolds number effects are present, inner variable scaling alone is insufficient.

In view of the above, alternative scaling parameters have been proposed which would collapse streamwise turbulent stress data for a smooth wall at different Reynolds numbers onto a single curve. For example, based on their own similarity analysis, George and Castillo (1997) concluded that the proper scaling parameter for the streamwise and wall-normal Reynolds stress components is the freestream velocity, U_e, while the shear stresses were shown to scale on the friction velocity, U_τ. Based on their experimental data, DeGraaff and Eaton (2000) proposed a new mixed scaling, $U_\tau U_e$, with the aim of collapsing the streamwise Reynolds stress onto a universal curve, while the wall-normal and shear stresses were shown to scale on the friction velocity, U_τ. The justification for their mixed scaling came from the turbulence kinetic energy balance of

the boundary layer, in which the total rate of energy dissipation by the turbulence depends on both U_e and U_τ.

For higher-order turbulent statistics, specifically, the triple correlations, the use of the friction velocity as the scaling parameter is the prevailing approach in the literature. However, according to the analysis of George and Castillo (1997), the proper scaling parameter is the mixed velocity scale, $U_e U_\tau^2$.

2.4 Previous Studies and Current Status

2.4.1 Experimental Studies of Turbulent Boundary Layers

Since Prandtl's mixing length theory proposed over 70 years ago, the turbulent boundary layer has been extensively investigated. Many issues such as Reynolds number dependency, initial conditions, pressure gradient, elevated freestream turbulence, and roughness effects have continued to be important research topics. In this thesis, attention is focused on the effects of surface roughness on the mean velocity and turbulence fields. The review of previous studies on this topic issue is presented in the following subsections.

2.4.1.1 Surface Roughness Effects

Extensive research has been performed to investigate the features of a zero-pressure-gradient two-dimensional turbulent boundary layer over a rough surface (e.g. Furuya and Fujita, 1967; Perry et al., 1969; Antonia and Luxton, 1971; Acharya et al., 1986; Bandyopadhyay and Watson, 1988; Raupach et al., 1991; Tachie et al., 2000; Antonia

and Krogstad, 2001; Bergstrom et al., 2001; Schultz and Flack, 2003; Flack et al., 2005). The review by Raupach et al. (1991) surveyed surface roughness research performed in zero pressure gradient turbulent boundary layers for both meteorological and engineering flows. In wind tunnel roughness experiments, different surface geometries have been investigated with the aim of elucidating the effect of surface roughness on both mean velocity and turbulence quantities. Popular roughness elements typically used in wind tunnel experiments include the following: (i) sandgrain (Nikuradse, 1933; Bergstrom et al., 2001), (ii) sand paper (Andreopoulos and Bradshaw, 1981; Song and Eaton, 2002; Schultz and Flack, 2003), (iii) wire mesh (Perry and Li, 1990; Krogstad and Antonia, 1999; Bergstrom et al., 2001), and (iv) arrays of rods (Krogstad and Antonia, 1999). Recall that Perry et al. (1969) classified all the aforementioned rough surfaces above as *k*-type roughness, since the roughness shift depends on the roughness height.

The global effects of surface roughness on the mean flow are fairly well documented in the literature. These effects have often been generalized to consist of an increase in the wall shear stress and an associated roughness shift, ΔU^+, to the logarithmic velocity profile. A most contentious issue is the wall-normal extent of the effect of surface roughness within the boundary layer. Various experimental studies have attempted to support or contradict the wall similarity hypothesis of Townsend (1976), which confines the effect of surface roughness to the roughness sublayer. This hypothesis suggests that at sufficiently high Reynolds number, both smooth and rough wall turbulent boundary layers are structurally similar outside the roughness sublayer.

For example, the results of Raupach et al. (1991), George and Simpson (2000), Song and Eaton (2002), Schultz and Flack (2003) and Flack et al. (2005) support the notion that the effect of surface roughness is confined to the roughness sublayer. The recent DNS study of Ashrafian et al. (2004) on turbulent flow in a rod-roughened channel also indicated that the effect of surface roughness on the turbulence structure is confined within the roughness sublayer. On the other hand, Krogstad et al. (1992), Antonia and Krogstad (1999), Keirsbulck et al. (2002), and Tachie et al. (2003) concluded that surface roughness modifies the turbulent stresses, and that this effect extends into the outer region of the boundary layer. This observation is in disagreement with the wall similarity hypothesis. In general, the transport mechanisms related to this effect are still not well-understood.

In his recent review of rough wall flows, Jimenez (2004) suggested that the Reynolds number based on boundary layer thickness, δ^+, should be greater than 4000 as a condition for a well-defined rough wall turbulent boundary layer. The other criterion considered by Jimenez (2004) was that the blockage ratio, k/δ, be sufficiently small, i.e. $k/\delta < 0.025$ for similarity laws to be expected. Flack et al. (2005) reported measurements of mean velocity and turbulence quantities on a smooth wall and rough surfaces having blockage ratio $k_{eq}/\delta < 0.025$ (where k_{eq} is the equivalent sand grain roughness height). They selected a woven wire mesh roughness, which has been previously studied by Krogstad et al. (1992) with contrasting results related to the extent of roughness effects in the boundary layer. They concluded that, for roughness with a

blockage ratio $k_{eq}/\delta < 0.025$, significant similarity in the turbulence structure could be expected outside the roughness sublayer. However, for roughness with blockage ratio $k_{eq}/\delta < 0.025$, turbulence modifications might be anticipated to extend well into the outer layer.

The interpretation of rough wall boundary layer data often depends on the choice of scaling parameter. The use of the friction velocity, U_τ, as the scaling parameter for assessing the effect of surface roughness on the mean velocity and turbulence fields is often adopted in the literature. However, some researchers have indicated that scaling the Reynolds stress components with U_τ does not result in a universal profile in the overlap region of the flow (e.g. George and Castillo, 1997). At the present time, various scaling laws have been proposed based on theoretical approaches that incorporate different assumptions. For example, based on their own similarity analysis, George and Castillo (1997) concluded that the proper scaling parameter for both streamwise and wall-normal Reynolds stresses is the freestream velocity, U_e. Seo et al. (2004) employed the freestream velocity, U_e, as the scaling parameter for the Reynolds stresses in turbulent boundary layers over a smooth wall at high Reynolds number for the same upstream conditions. They observed a relatively small Reynolds number dependence in the distribution of the streamwise Reynolds stress when scaled with the freestream velocity. Tachie et al. (2003) examined roughness effects in a low Reynolds number open-channel turbulent boundary layer and used the freestream velocity as the scaling parameter for the turbulence quantities. They observed that the effects of surface

roughness are much more pronounced when the turbulence quantities are scaled with the freestream velocity, U_e. Based on their experimental data, DeGraaff and Eaton (2000) proposed a new mixed scaling, $U_\tau U_e$, with the aim of collapsing the streamwise Reynolds stress onto a universal curve. The justification for their mixed scaling came from the turbulence kinetic energy balance of the boundary layer, in which the total rate of energy dissipation by the turbulence depends on both U_e and U_τ. The study of Schultz and Flack (2003) found that the mixed scale, $U_\tau U_e$, did not collapse the streamwise Reynolds stress profiles for different sand paper roughness as effectively as did the friction velocity.

The higher-order moments contain valuable statistical information which relates to the turbulent flux of the Reynolds stress. Antonia and Krogstad (2001) noted that the velocity triple products are expected to be a more sensitive indicator of the effect of surface roughness than second-order moments. However, relatively few rough wall studies have presented these statistics in the literature (e.g. Andreopoulos and Bradshaw (1981), Bandyopadhyay and Watson (1988), Antonia and Krogstad (2001), Kiersbulck et al. (2002), Tachie et al. (2003), and Flack et al. (2005)). Assessing the effect of surface roughness on the velocity triple products has led to different conclusions. While Antonia and Krogstad (2001), Kiersbulck et al. (2002), and Tachie et al. (2003) concluded that the effect of surface roughness influenced the triple velocity products in both the inner and outer regions, Flack et al. (2005) disagreed with that conclusion. They observed the influence of surface roughness to be restricted to $y < 5k_s$. Recall that

Raupach et al. (1991) identified the roughness sublayer as that region within a rough-wall turbulent boundary layer which extends from the wall to about 5 roughness heights.

2.4.2 Numerical Studies of Rough-Wall Flows

Two main modelling approaches have been advanced for numerical calculations of rough-wall flows: the equivalent sandgrain roughness models and topographic form-drag models. Van Driest (1956) proposed the earliest equivalent sandgrain roughness model as follows:

$$\nu_t = (F\kappa y)^2\left(\frac{\partial U}{\partial y}\right) \tag{2.47}$$

$$F = 1-\exp\left(-\frac{y^+}{26}\right)+\exp\left(-2.3\frac{y^+}{k_{eq}^+}\right) \tag{2.48}$$

where ν_t is eddy viscosity and F is the damping function. Rotta (1962) modified the van Driest (1956) model to account for the roughness effect by adding a shift Δy^+ to the distance from the wall. Cebeci and Chang (1978) employed this model to perform some of the earliest numerical calculations of boundary layers on rough walls. Granville (1985) reviewed all the models related to van Driest damping function in which the roughness effect is incorporated. Krogstad (1991) suggested another version of the mixing length model for sandgrain roughness given as

$$F = 1-\exp\left(-\frac{y^+}{26}\right)+\exp\left(-\frac{y^+}{26}\left(\frac{70}{k_{eq}^+}\right)^{3/2}\right)\sqrt{1+\exp\left(-\frac{70}{k_{eq}^+}\right)} \tag{2.49}$$

Patel (1998) noted that various mixing length models differ in the way in which the roughness effect is introduced. In general, the mixing length model cannot account for the effect of surface roughness on the turbulence quantities.

The two-equation turbulence model (k-ε) has been employed to incorporate both the equivalent sandgrain roughness models and topographic form-drag models. In the following subsection, a brief description of two-equation turbulence models as well as different types of near-wall treatment for the boundary conditions for rough wall flows is presented.

2.4.2.1 Two-Equation Model Approach

In the standard $k-\varepsilon$ model (Launder and Spalding, 1974), the Reynolds stress is modeled as

$$-\rho < u_i u_j >= -\frac{2}{3}\rho\, k\delta_{ij} + 2\mu_t S_{ij} \tag{2.50}$$

The eddy viscosity μ_t is related to the turbulence kinetic energy k and its dissipation rate ε as follows:

$$\mu_t = \rho\, C_\mu \frac{k^2}{\varepsilon} \tag{2.51}$$

and the strain tensor, S_{ij}, is given by $S_{ij} = \frac{1}{2}(U_{ij} + U_{ji})$. Eqn. (2.46) represents a linear relationship between the turbulent stress and the rate of strain, and forms the basis for all linear two-equation models.

The distributions of turbulence kinetic energy, k, and its dissipation rate, ε, are determined from their modeled transport equations, which, respectively, for steady flow are given by:

$$\frac{\partial(\rho U_i k)}{\partial x_i} = \frac{\partial}{\partial x_i}\left[\left(\mu + \frac{\mu_T}{\sigma_k}\right)\frac{\partial k}{\partial x_i}\right] - \rho < u_i u_j > \frac{\partial U_j}{\partial x_i} - \rho\varepsilon \tag{2.52}$$

$$\frac{\partial(\rho U_i \varepsilon)}{\partial x_i} = \frac{\partial}{\partial x_i}\left[\left(\mu + \frac{\mu_T}{\sigma_\varepsilon}\right)\frac{\partial \varepsilon}{\partial x_i}\right] - C_{1\varepsilon}\frac{\varepsilon}{k}\rho < u_i u_j > \frac{\partial U_j}{\partial x_i} - C_{2\varepsilon}\rho\frac{\varepsilon^2}{k} \tag{2.53}$$

Typical values of the model coefficients are as follows: $C_\mu = 0.09$; $\sigma_K = 1.0$; $\sigma_\varepsilon = 1.3$; $C_{\varepsilon 1} = 1.44$; and $C_{\varepsilon 2} = 1.92$. Different near-wall treatments can be used in combination with the aforementioned turbulence models. These include wall functions, two-layer formulations, and low Reynolds number formulations. Each of these formulations is further modified to account for the effect of surface roughness on the mean velocity and turbulence quantities.

2.4.2.1.1 Standard Wall Functions

A standard wall function is usually employed to treat the boundary conditions for velocity and other transported variables in the near-wall flows at high Reynolds numbers. In this approach, the viscous sublayer and blending region are bridged by employing empirical formulae to provide near-wall boundary conditions for the mean flow and turbulence transport equations. This allows placement of the first grid node in the overlap region in fully turbulent flow. This approach has two major advantages: the first is the ability to escape the need to extend the computations right to the wall, while the second advantage is that it circumvents the need to account for specific near-wall

and viscous effects in the turbulence model. The wall function formulation can be expressed as follows (Launder and Spalding, 1974):

$$\frac{U_p}{u_\tau} = \frac{1}{\kappa}\ln\left(E\frac{y_p u_\tau}{\nu}\right); \qquad k_p = \frac{u_\tau^2}{\sqrt{C_\mu}}; \qquad \varepsilon_p = \frac{u_\tau^3}{\kappa y_p} \tag{2.54}$$

where U_p is the absolute value of the velocity component parallel to the wall at the first grid node, $E = 9.0$ for a smooth surface, τ_w is the shear stress at the wall, y_p is the normal distance to the wall, k_p is the turbulence kinetic energy, and ε_p is the dissipation rate at the first grid node. For a fully rough surface, an approximate relation is $E = b/k_{eq}^+$ (where b = 29.7) (Jayatillaka, 1969). Although they involve major assumptions, wall functions as a near-wall treatment for smooth and rough surfaces still play a major role in commercial CFD codes used for industrial applications. However, the wall function formulation has no direct effect on the turbulence quantities.

2.4.2.1.2 Two-Layer $k-\varepsilon$ Model

The two-layer $k-\varepsilon$ models resolve the viscosity-affected regions close to the wall with a one-equation model, while the outer core flow is solved from the standard $k-\varepsilon$ model. In the one-equation model (Baldwin and Barth, 1990; Rodi and Mansour, 1990; Spalart and Allmaras, 1994), the eddy viscosity is made proportional to a velocity scale and a length scale as follows:

$$\mu_t = \rho\, C_\mu \sqrt{k} l_\mu \tag{2.55}$$

The distribution of the length scale, l_μ is prescribed algebraically while the velocity scale is determined by solving the k- equation. The dissipation rate, ε, appearing as a

sink term in the k- equation is expressed in terms of k and a dissipation length scale, l_ε, which is also prescribed algebraically. The dissipation rate is expressed as follows:

$$\varepsilon = \frac{k^{3/2}}{l_\varepsilon} \tag{2.56}$$

In the outer region of the flow, the eddy viscosity is determined from eqn. (2.51).

Patel and Yoon (1995) attempted an extension of the Chen and Patel (1988) model to incorporate Rotta's (1962) formulation of the roughness effect on the length scale in the wall region. Durbin et al. (2001) also modified the two-layer k-ε model closure of Chen and Patel (1988) to use a hydrodynamic roughness length y_o to implement the effects of roughness on the mean velocity and turbulence field at the wall. Their model includes a calibration curve for the relationship between y_o and the equivalent sand grain roughness height, based on the sand grain pipe flow data of Nikuradse.

2.4.2.1.3 Low-Reynolds-Number Formulation

In many engineering applications, low-Reynolds number k-ε models are used to predict near-wall flows. The low Reynolds number formulations have the ability to integrate the models down to the solid boundary. The formulations are generally derived from the high Reynolds number models by incorporating damping functions or extra non-linear terms to account for the effect of the wall on turbulence (e.g. Craft et al., 1996; Iacovides and Raise, 1999). Both the equivalent sandgrain roughness and topographic form-drag models have been incorporated into the low-Reynolds number formulation.

Zhang at al. (1996) incorporated the equivalent sand grain roughness into a low Reynolds number k-ε model closure to account for the log-law shift in the mean velocity profile. Although their model was demonstrated to give the approximately correct skin friction behaviour in various rough wall flows, details of predictions for the mean velocity and turbulence kinetic energy profiles were not provided.

In the case of the topographic models, Taylor et al. (1985, 1988) used the discrete element roughness model which incorporates the surface roughness form drag and blockage effects into the momentum equations. Tarada (1990) also employed the topographic model in his low Reynolds number formulation, in which sink and source terms are added to the momentum equations. Zhang et al. (1996) noted that the complexity arising from characterizing stochastic roughness makes the topographic models difficult to use in many engineering applications.

2.5 Summary

In the previous sections of this chapter, the scaling laws for mean and turbulence quantities were reviewed. Some of the widely used skin friction relations were summarized. The existing experimental and numerical studies on rough-wall flows were briefly reviewed.

In spite of extensive research efforts, the present state of knowledge regarding the extent of the effects of surface roughness on the turbulence structure is contradictory.

In addition, the existing rough wall literature indicates that accurate measurement of skin friction still poses a challenge to experimentalists.

Numerical prediction of rough-wall flows has also received considerable research attention over the past two decades. Both mixing length and eddy viscosity approaches have been used to predict the characteristics of mean velocity over rough walls. However, the present state of knowledge indicates that the ability to accurately predict the turbulence quantities in rough wall turbulent flow is deficient compared to the success achieved in modeling turbulent flows over a smooth wall.

CHAPTER 3

EXPERIMENTAL SET-UP AND INSTRUMENTATION

3.1 Introduction

This chapter describes the experimental set-up and instrumentation used in the present study. The wind tunnel facility is described in the first section (3.2) and this is followed by a description of the smooth and rough surfaces (3.3 and 3.4). The detailed information on the instrumentation (3.5) as well as the calibration of the constant temperature anemometry probes is presented in the following section (3.6). In the final sections, the measurement procedure (3.7) and uncertainty (3.8) is discussed.

3.2 The Wind Tunnel

The experiments were performed in a closed-return low-speed wind tunnel at the University of Saskatchewan, shown in Figure 3.1. The wind tunnel contains two test sections, the Low-Speed Test Section (LSTS) and High-Speed Test Section (HSTS). The airflow is driven by a 75-kW variable-pitch fan. As indicated in Figure 3.1, the air flow generated by the fan passes through a diffuser where it is expanded. Thereafter, it passes through two sets of turning vanes located at the top and bottom corners where it is redirected through 180 degrees.

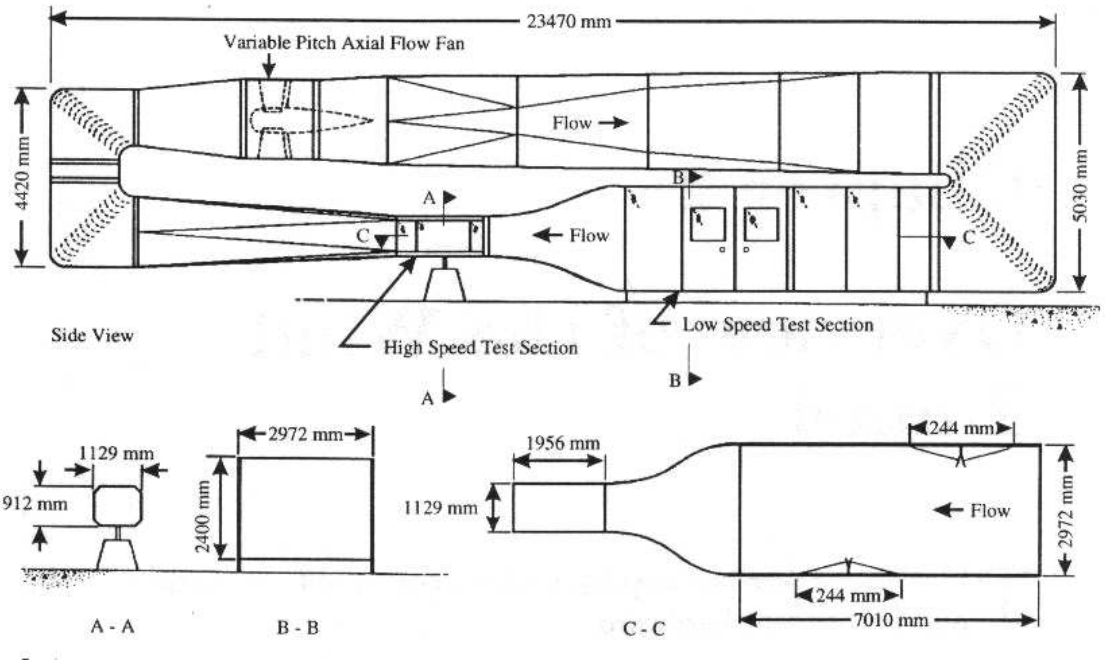

Figure 3.1: Schematic of Wind Tunnel

Two turbulence reduction screens are located at the exit of the turning vanes. The screens reduce the turbulence intensity of the air by eliminating the large-scale vortices created by the fan. The flow then enters the LSTS which has a large cross-sectional area and acts as a large settling chamber. The flow enters the HSTS from the low-speed test section through a 7:1 contraction. The contraction also reduces the variations of axial velocity over the cross-section thereby reducing the freestream turbulence intensity to acceptable values (Bradshaw, 1970). After the HSTS, the air flow then re-circulates to the fan as indicated in Figure 3.1.

The experiments described in this thesis were performed in the HSTS which is 1.12 m x 0.91 m in cross-section, and approximately 2.00 m long. The side-walls are made of Plexiglas to facilitate visual inspection of probe positions, model configurations and flow behaviour during experiments. The ground plane in the test section is a rectangular plate 1.82 m long, 0.95 m wide, and 0.025 m thick. Streamlined risers are used to maintain a 0.040 m spacing between the bottom of the ground plane and the floor of the HSTS. At the rear of the HSTS are sets of vents that prevent static pressure drift as the air heats up during a test (Bradshaw, 1970). The traversing wing, which is used to position the measurement probe, is located inside the test section. The velocity range that can be attained in this section is 5 – 60 m/s. The longitudinal freestream turbulence intensity was approximately 0.4 % for the entire range of velocities, and the non-uniformity of the freestream mean velocity field outside the test section wall boundary layers was less than 0.5 %. The nominal longitudinal static pressure gradient

was – 10 Pa/m. The flow exits the HSTS through a diffuser and is then redirected by two additional turning vanes before finally entering the fan section to be re-circulated.

3.3 Description of Smooth Surface

The smooth surface (SM) was created on of a Medium Density Fibre (MDF) board, for which the large-scale deviation is less than ± 0.5 mm from the horizontal plane. The MDF board was screwed onto the top of the Plexiglas ground plane. Based on ISO – JIS specifications and a 12.5-mm cut of length, the arithmetic mean deviation of the surface profile, R_a, for the MDF board was found to be 3.82 μm. As will be shown later, this roughness was sufficiently small to qualify the MDF board as hydraulically smooth. The board is 1.68 m long, 1.02 m wide and 0.019 m thick. The leading edge was carefully rounded to achieve an elliptic profile in order to improve the quality of the flow.

3.4 Description of Roughness Elements

The rough surfaces were made from sandpaper of different grit, steel perforated sheet of different sheet thickness and circular hole diameter, and stainless steel woven wire mesh of different diameter and openness ratio. The following ten roughness elements were used in the present study:

($a1$) 120d-grit (SGS) with a roughness height of 0.18 mm;

($a2$) 80d-grit (SGM) with a roughness height of 0.30 mm;

($a3$) 60d-grit (SGML) with a roughness height of 0.37 mm;

($a4$) 40d-grit (SGL) with a roughness height of 0.48 mm.

(b1) A 0.76-mm-thick perforated steel sheet (PS) with circular holes 1.2 mm in diameter spaced 3.4 mm between centres giving an openness ratio of 22%;

(b2) A 0.9-mm-thick perforated steel sheet (PM) with circular holes 1.6 mm in diameter spaced 2.43 mm between centres giving an openness ratio of 41%;

(b3) A 0.9-mm-thick perforated steel sheet (PL) with circular holes 2 mm in diameter spaced 2.81 mm between centres giving an openness ratio of 45%;

(c1) A stainless steel woven wire mesh (WMS) consisting of 0.36 mm diameter wire laid out 1.68 mm on centre to give an openness ratio of 44%;

(c2) A stainless steel woven wire mesh (WMM) consisting of 0.58-mm-diameter wire laid out 1.77 mm on centre to give an openness ratio of 30%;

(c3) A stainless steel woven wire mesh (WML) consisting of 1.04-mm-diameter wire laid out 3.68 mm on centre to given openness ratio of 35%.

Note that each surface is described by a specific acronym which indicates the type of surface and the size, e.g. PS for perforated sheet with small holes.

The sandpaper was primarily made with aluminium oxide, and was graded according to the size of the grains. The grains, which are of the same nominal diameter, were evenly distributed to achieve a homogenous rough surface. The grains constitute the roughness elements on the sandpaper. Due to protrusion of the roughness elements into the flow in the vicinity of the wall, the roughness elements act as “local blockage” to the near-wall flow. This will lead to flow disturbance in the near-wall region. One of the objectives of the present research is to examine and document the extent of the impact of these “local blockages” on the near-wall region of the flow.

In the case of the perforated sheet shown in Figure 3.2, staggered hole patterns were created on a smooth stainless steel sheet. The perforated holes, which are uniform with equal centre-to-centre spacing, are three-dimensional. The presence of the perforated hole introduced another flow phenomenon that is distinguished from that on a hydraulically smooth surface. The flow in the vicinity of the wall will interact with the cavities of the perforated sheet. A complete understanding of the extent of the interactions produced by different sizes of these cavities in the boundary layer is also one of the motivations for the present research.

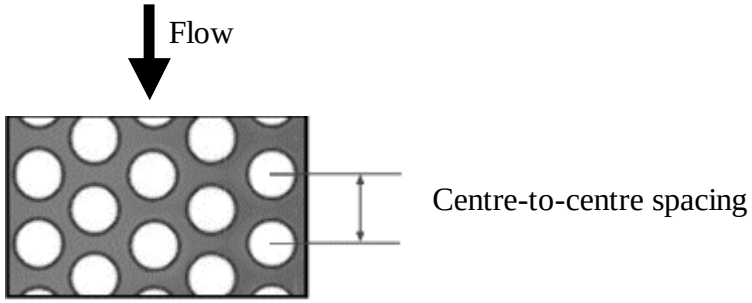

Figure 3.2: A typical staggered perforated sheet

The wire mesh roughness, shown in Figure 3.3, was created by interlacing the strips of wires with equal diameters. Apart from the cavities created within the mesh, one wire was also placed at the top of another at the point of the interlacing. From the perspective of this geometrical layout, the flow in the vicinity of the wall interacts with the cavities within the mesh. In addition, the wires at the point of the interlacing will act as “local blockage” to the upcoming flow adjacent to the wall. Of interest is the impact

of these interactions on the turbulence structure in the inner and outer regions of the boundary layer.

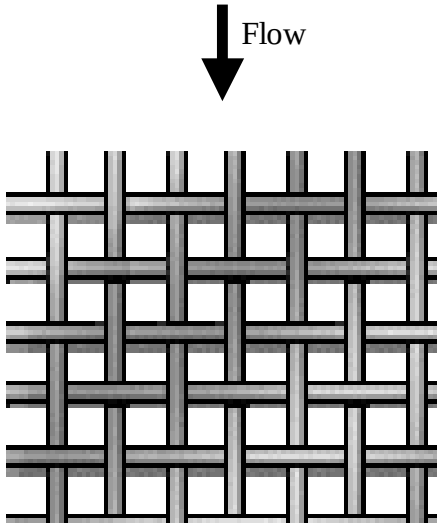

Figure 3.3: A typical woven wire mesh roughness

Photographs of three selected surfaces are shown in Figure 3.4. The thickness of the perforated plate and the diameter of the wire mesh were used as the roughness height, k. For example, the 0.9-mm-thick perforated sheet has a roughness height of k = 0.9 mm, while the woven wire mesh with a wire diameter of 1.04 mm has a roughness height of k = 2.08 mm, which is equal to twice the diameter of the wire following Furuya and Fujita (1967). Note that the choice of roughness height is somewhat arbitrary and possibly ambiguous; it should not be confused with the equivalent sand grain roughness, k_{eq}, calculated from the roughness shift. Each rough surface was attached

onto the MDF board using double-sided tape. Before each experiment, a level was placed on the attached rough surface to ensure that it was flat.

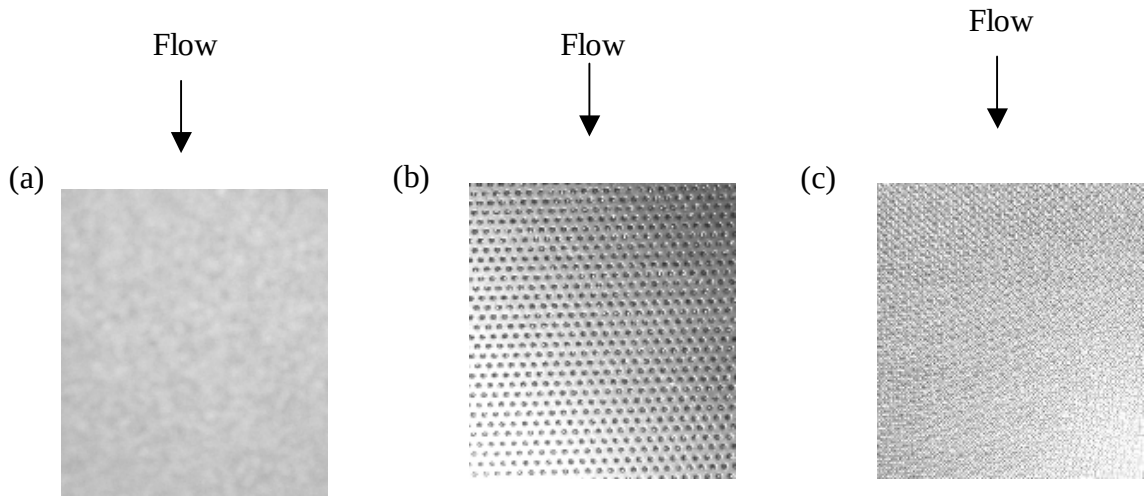

Figure 3.4: Photographs of different surface roughness conditions used in the experiment (a) Sand paper; (b) Perforated plate; (c) Woven wire mesh

3.5 Instrumentation

3.5.1 Data Acquisition System

The wind tunnel data were acquired using a computer with a 1.8 GHz Intel Pentium 4 processor and a data acquisition card. National Instruments LabVIEW software was used for data acquisition and control of the instruments. The LabVIEW software has the advantage of sampling different parameters using different channels. For example, for each data point, four channels were sampled corresponding to the freestream dynamic pressure, freestream static pressure, air temperature, and the Pitot probe stagnation pressure. The data acquisition card was a National Instruments PCI – 6031E 16-bit multifunction board.

3.5.2 Pressure and Temperature Monitoring System

The freestream conditions were obtained with a Pitot-static probe (United Sensor, 3.2-mm outer diameter). The probe was inserted into the side-wall of the HSTS, located 400 mm from the contraction exit and 340 mm above the ground plane, and extending 270 mm into the HSTS. The static port of the Pitot-static probe was connected to a Datametrics Barocell absolute pressure transducer. It was also connected to a Datametrics Barocell differential transducer which has the ability to achieve a thermal stability of 50 ppm/^{o}C and an accuracy of 0.05% of full scale. The stagnation port of the Pitot-static probe was connected to a Datametrics Barocell differential pressure transducer. It is a 10-inch H_2O transducer with a thermal base to reduce zero drift. It is based on the variable capacitance principle, which assures the utmost in zero stability and performance. A modified United Sensor boundary layer Pitot probe (BA-.025-12-C-11-.650), with an outer diameter of d_p = 0.60 mm as shown in Figure 3.5, clamped in the traversing wing was used to measure the stagnation pressure across the boundary layer. In order to measure dynamic pressure across the boundary layer, the Pitot probe was connected to a Validyne Differential Pressure Sensor and the reference static pressure port of the wall-mounted Pitot-static probe.

The temperature was measured with a Copper-Constantan thermocouple (type T) which was placed in the flow at the downstream end of the test section. This thermocouple was connected to the main control box of the wind tunnel and the analog output fed to the data acquisition card. The uncertainty in the temperature measurement

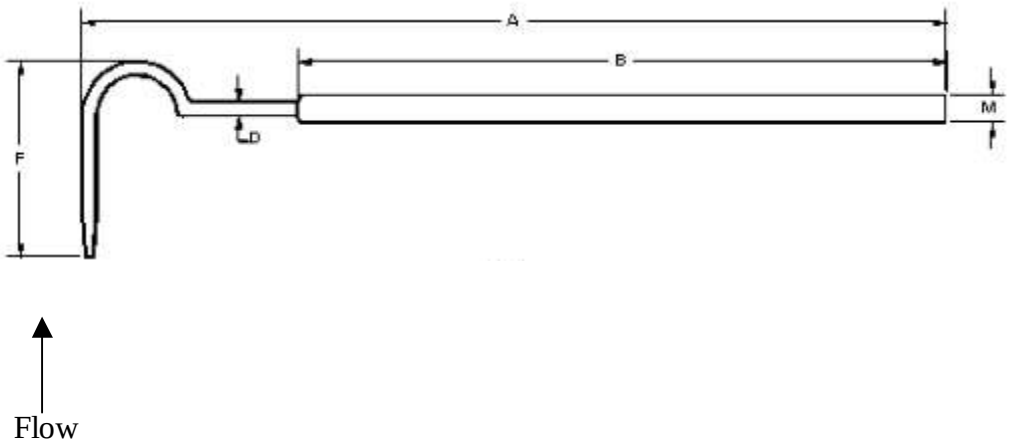

Figure 3.5: United Sensor boundary layer Pitot probe (A = 304.8 mm, B = 2.8 mm, D = 0.6 mm, F = 16.5 mm, M = 3.1 mm)

was ± 0.33°C. The absolute pressure is used together with the air temperature to calculate the air density using the ideal gas equation as follows:

$$\rho = \frac{P_\infty}{RT} \tag{3.1}$$

where R = 287 J/kg K is the gas constant for air. The kinematic viscosity is calculated using the Sutherland correlation as follows,

$$\nu = 1.458\times10^{-6}\frac{T^{3/2}}{\rho(T+110.4)} \tag{3.2}$$

3.5.4 Measurement Probe Traversing Mechanism

The traversing wing allows 3-D placement of measurement probes in the HSTS. The traversing system, which can position a thermal probe or Pitot tube at any (*x*, *y*, *z*) position, is controlled by the stepper motor. The operation of the stepper motor uses the LabVIEW software on the computer, which has a National Instruments PCI-7344

motion control board. The signal from the computer is sent through the Universal Motion Interface (UMI 7764) to the Intelligent Motion System (IMS 1007) micro-stepping drivers. Each micro-stepping driver can be adjusted from 400 to 51,200 steps per revolution. The signal from IMS controls the stepper motor, which has a movement of 1.8^{o} per step. The stepper motor has a resolution of 0.0006 mm in the x-direction (streamwise), 0.0128 mm in the y-direction (wall-normal), and 0.0125 mm in the z-direction (spanwise). Using the LabVIEW software, the position of the measurement probe could be achieved by setting a reference position when the tip of the measurement probe is positioned on the test surface. Given the desired range and number of grid points as input, the program automatically moves the probe and stores its current position in a file together with the measured parameters sampled at each location.

3.6 Thermal Anemometry Instrumentation

3.6.1 The Thermal Probes

A TSI model – T1.5 constant-temperature single hot-wire probe and a TSI model 1243-20 boundary layer cross flow (X) hot-film probe were operated with a TSI IFA-100 anemometer at an overheat ratio of 1.8. The Intelligent Flow Analyzer (IFA) has three channels, which enables voltage output from three wires simultaneously. In the case of the single hot wire, the probe was connected to the first channel of the IFA. The recommended operating resistance and bridge compensation were set on the IFA as given by TSI. Figure 3.6a shows a typical boundary layer single-hot wire probe. The

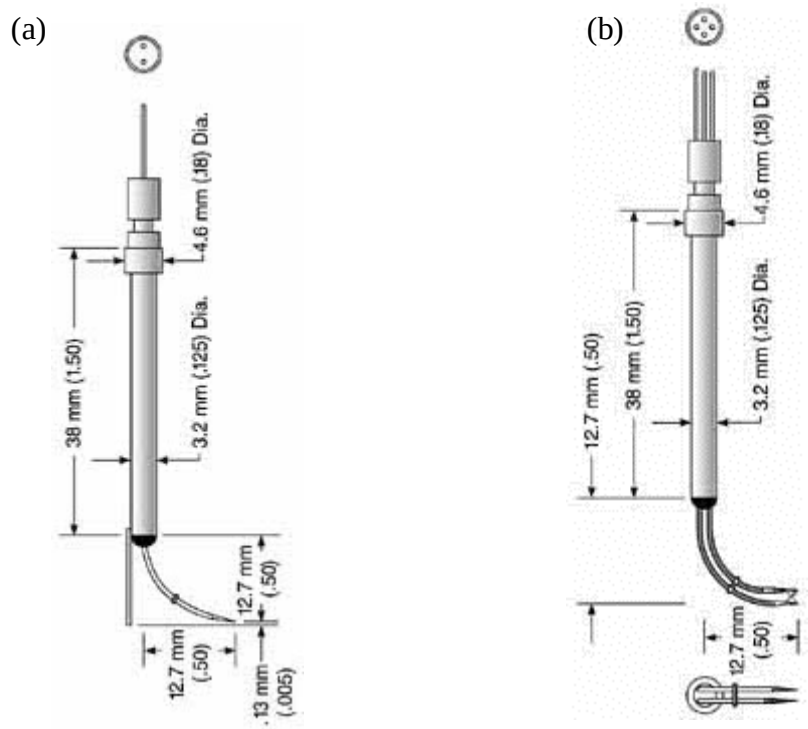

Figure 3.6: Thermal probes and probe holder: (a) single hot wire; (b) cross hot-film (TSI catalogue)

sensor of the hot-wire probe, made of platinum-plated tungsten wire, had a diameter of 3.8 μm and a length-to-diameter (l/d) ratio of about 335, which is large enough to avoid conduction errors. The sensing length (l) of the wire was 1.27 mm, which gives $l^+ = 75$ for the $\mathrm{Re}_\theta = 5680$ case, and $l^+ = 122$ for the $\mathrm{Re}_\theta = 10360$ on a smooth surface. The distance between the supports was 1.52 mm.

For the cross hot-film, the probe was connected to two channels of the IFA. For each channel, the recommended operating resistance and bridge compensation were set on the IFA as given by TSI. A typical boundary layer cross flow (X) hot-film probe is

shown in Figure 3.6b. The sensors of the cross hot-film probe, made of platinum wire, have a diameter of 50.8 μm and 1.02 mm sensing length (l), which gives l^+ = 83 for the Re_θ = 7720 case on a smooth surface. The distance between its supports was 1.65 mm. Ligrani and Bradshaw (1987) also recommended that $l^+ < 20 - 25$ for the thermal probes to resolve the peak of the streamwise turbulence intensity in the near-wall region. Comparison between the present values of l^+ and the recommended value by Ligrani and Bradshaw (1987) shows that the thermal probes used in the present study would not resolve the near-wall peak of the streamwise Reynolds stress component. However, the thermal probes used in the present study provide meaningful and insightful information of the Reynolds stress components in the overlap and outer regions of the boundary layer.

3.6.2 Probe Calibration

3.6.2.1 Single Wire Probe Calibration

The single wire probe was calibrated in situ against a Pitot-static probe over a range of 24 freestream velocities outside the boundary layer. The voltage signal from the anemometer was stored together with the freestream velocity. The calibration curve used for the experiment was a fourth-order polynomial expressed as follows:

$$U = c_1 + c_2 E + c_3 E^2 + c_4 E^3 + c_5 E^4 \tag{3.3}$$

where U is the mean velocity, c_1 to c_5 are constants to be determined and mean E is the voltage output from the anemometer. The mean velocity, U, was determined through the relationship

$$p_{tot} - p = \frac{1}{2}\rho U^2 \tag{3.4}$$

using a Pitot-static probe to measure the dynamic pressure, where p_{tot} is the total pressure, p is the static pressure, and ρ is the density of air. The density could be determined accurately by measuring the static pressure and temperature. A typical single-wire calibration curve is shown in Figure 3.7.

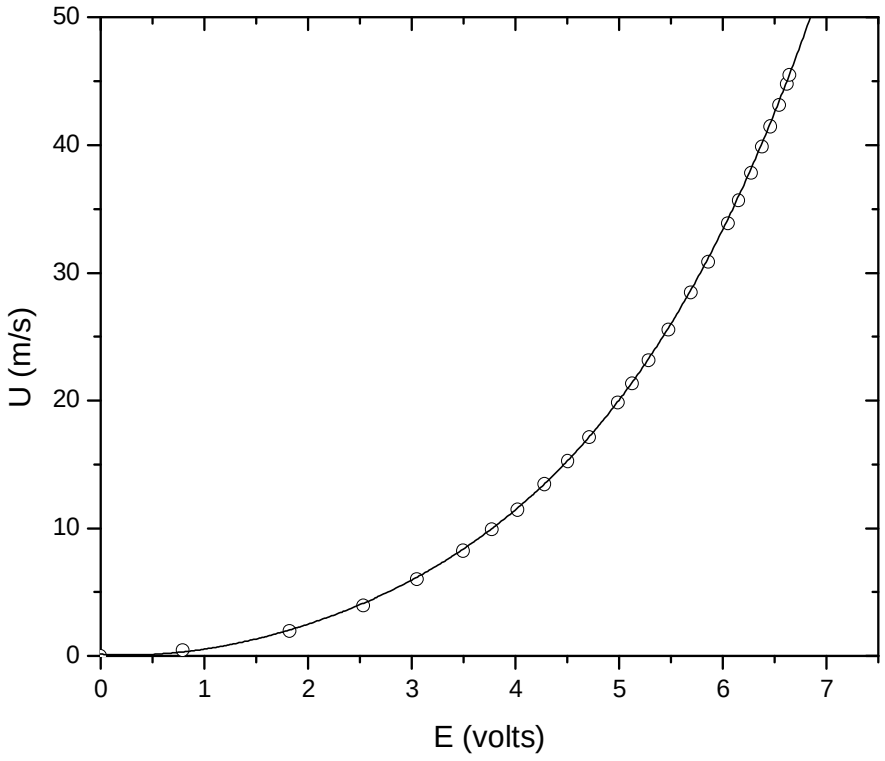

Figure 3.7: Calibration curve for a single hot-wire probe

3.6.2.1 Cross-Film Probe Calibration

The calibration of the cross-film probe involves variation of both the velocity and probe yaw angle. The probe was calibrated in situ over a range of different wind-tunnel speed settings in the core region of the HSTS using a Pitot-static probe (United Sensor, external diameter of 3.2 mm) and an automated variable-angle calibrator **(**Sumner, 2002**)**. One stepping motor was used to position the probe in yaw. The calibrator has an angular resolution of 0.9 degrees. For each velocity/yaw – angle pair (U_o, α), shown in Figure 3.8, a unique voltage pair (E_1, E_2) is obtained. The probe is oriented such that the binormal velocity component (W), i.e. the velocity component perpendicular to both wires, equals to zero. The angles α_1 and α_2 are both equal to 45^o. At a fixed freestream velocity, the angular position of the probe was varied between – 32.4 and +32.4 degrees at a constant increment of 8.1 degrees. This procedure was repeated at 9 different freestream velocities. The in-situ calibration eliminates any uncertainty caused by differences between the test conditions and the calibration flow conditions. Two-dimensional third-order polynomials were fitted to the voltage data to give response equations for the velocity magnitude and the yaw angle, similar to the method of Österlund (1999). A typical cross-film probe calibration map is shown in Figure 3.9. The streamwise and wall-normal velocities were obtained from the equations

$$U = U_o \cos\alpha \tag{3.5}$$

$$V = U_o \sin\alpha \tag{3.6}$$

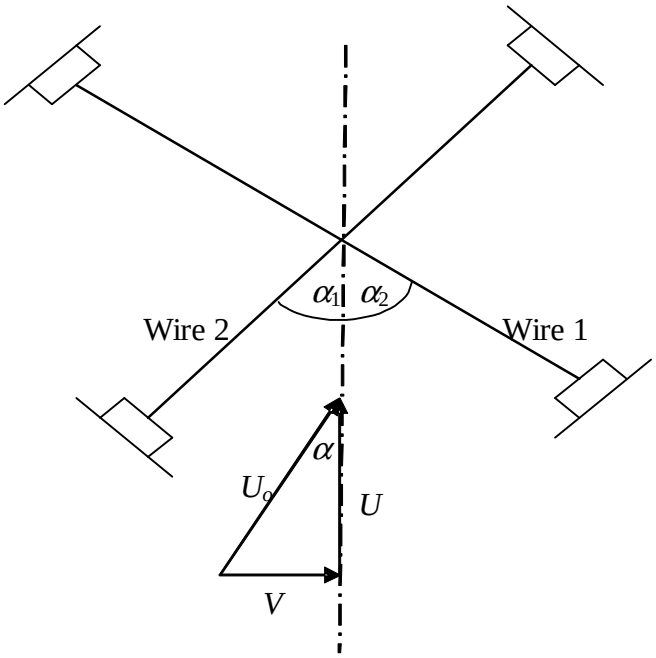

Figure 3.8: The definition of the yaw angle in the plane of the prong.

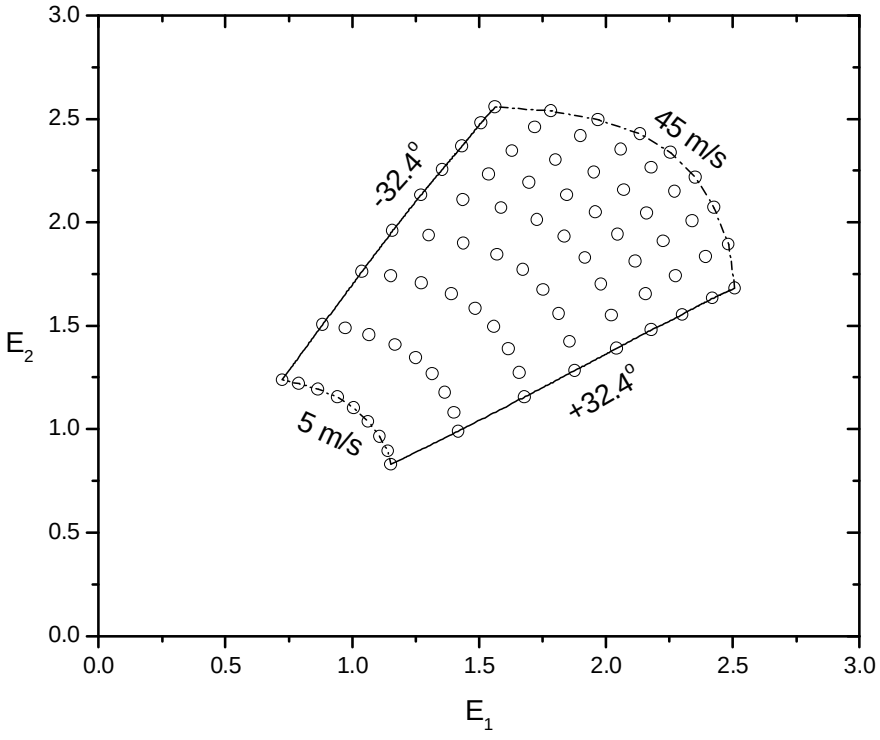

Figure 3.9: Calibration map for a cross hot-film probe

where U and V are the streamwise and wall-normal velocity components, respectively, and α is the probe angle of attack. Two variables, x and y (not representing coordinates), denoting the streamwise and cross stream velocity components, are determined from the wire voltages E_1 and E_2 as follows

$$x = E_1 + E_2 \tag{3.7}$$

$$y = E_1 - E_2 \tag{3.8}$$

The two variables are then used to obtain two two-dimensional third-order polynomials, given by

$$U_o = a_1 + a_2 x + a_3 y + a_4 x^2 + a_5 xy + a_6 y^2 + a_7 x^3 + a_8 x^2 y + a_9 xy^2 + a_{10} y^3 \tag{3.9}$$

$$\tan\alpha = b_1 + b_2 x + b_3 y + b_4 x^2 + b_5 xy + b_6 y^2 + b_7 x^3 + b_8 x^2 y + b_9 xy^2 + b_{10} y^3 \tag{3.10}$$

The above equations were solved using a least square method, to determine the coefficients a_1 to a_{10} and b_1 to b_{10}. The coefficients are then stored and used in the experiments to determine the instantaneous velocities, U and V.

3.7 Description of Experiment

The experiments were conducted in the HSTS of the wind tunnel. The major objective of these experiments was to examine scaling issues for the three different flow regimes, namely, hydraulically smooth, transitionally rough, and fully rough. The MDF board, which was screwed onto the ground plane, served as the hydraulically smooth surface. The ten different rough surfaces used in the present study were attached to the MDF board. The physical size and geometry of the roughness elements and freestream

velocity were chosen to encompass both transitionally rough and fully rough flow regimes. A trip strip made of sand paper (36-d grit) was placed across the width of the plate; the trip strip was 75 mm wide and located 15 mm from the leading edge. The trip ensured an early transition to turbulence, and was used in all the experiments in order to maintain consistent development of the turbulent boundary layer. The use of a strip of roughness was also shown by Klebanoff and Diehl (1951) to provide effective boundary layer thickening and a fairly rapid self-similarity.

Three different probes, namely, a Pitot probe, single hot-wire, and cross hot-film, were used to measure the velocity fields in the turbulent boundary layer. A Pitot probe was used to measure the mean streamwise velocity, while the single hot-wire and cross hot-film probes were used to measure the fluctuating velocity components across the boundary layer at a section 1300 mm (downstream) from the leading edge. The Pitot probe was carefully aligned using an angle bar to the flow to eliminate any errors caused by yaw. The pressure signal was digitized using a 16-bit A/D converter at a sampling frequency of 500 Hz; 10,000 samples were taken at each normal position. Corrections were applied to the data following MacMillan (1956), in which the value of $0.15d_p$ was added to the y-coordinate. However, as noted by Perry et al. (2001), for viscous distances from the wall greater than $y^+ = 100$, the corrections tend to be insignificant. In our own case, only a very few data points fall within $30 < y^+ < 100$ for both smooth and rough wall flows, indicating that MacMillan's correction had little impact on the overall results. In the case of the thermal anemometer probes also aligned with flow, the analog output signal of the probe was filtered (low pass) at 10 kHz to minimize any

contamination from high frequency electronic noise, and then offset and amplified to give an output bounded by ± 5 V. The sampling frequency of the cross flow (X) hot-film probe was determined using oscilloscope and found to be 10 kHz. Different sampling times of 5, 10, and 15 seconds at the sampling frequency of 10 kHz were used to investigate the convergence of the statistics. It was observed that the Reynolds shear stress and triple velocity products required 10 seconds sampling time to achieve convergence, while other variables examined in this study required lesser sampling time to converge. In view of this, the sampling frequency used was 10 kHz, and a sampling time of 10 seconds was used to obtain convergence of the statistics. For the Pitot probe measurements, four different Reynolds numbers were obtained for each surface by varying the freestream velocity, U_e, from approximately 15 to 45 m/s. The mean velocity data obtained from the Pitot probe were used to identify the three flow regimes, namely, hydraulically smooth, transitionally rough, and fully rough. With this information, flows over some selected surfaces that exhibited these flow regimes were used to obtain the fluctuating velocity components using both the single hot-wire and cross hot-film probes. Three different Reynolds numbers were achieved by varying the freestream velocity, U_e, from approximately 25 to 45 m/s in the case of the single hot-wire probe. This provides opportunity to assess the Reynolds number effects on the streamwise turbulence intensity data for different surface conditions. For the cross hot-film probe, the freestream velocity used range from 25 to 35 m/s. The positions of the cross hot-film probe relative to the smooth and rough surfaces were obtained using a measuring tape. In the present study, the velocities measured across the boundary layer over smooth and rough surfaces using the hot-wire/film probes fall within the calibration

map. The experimental results focus on the Reynolds stress components profiles in the region $y/\delta > 0.05$. In view of this, the issue of the drop-outs and rectification does not arise in the present measurements. Each experimental run was completely controlled by the computer and the data acquisition system.

Table 3.1 presents a summary of the test conditions for the smooth surface: U_e is the freestream velocity, Re_θ is Reynolds number based on momentum thickness, δ is the boundary layer thickness, δ^* is the displacement thickness, θ is the momentum thickness, and H is the shape factor for the smooth surface (SM). The boundary layer thickness δ was considered to be the location above the surface at which the local mean velocity was 99% of the freestream value. For both the displacement and momentum thicknesses, they are obtained using the Eqns. (3.1) and (3.2):

$$\text{Boundary displacement thickness, } \delta^* = \int_0^\delta \left(1 - \frac{u}{U_e}\right) dy \tag{3.1}$$

$$\text{Momentum thickness, } \theta = \int_0^\delta \frac{u}{U_e}\left(1 - \frac{u}{U_e}\right) dy \tag{3.2}$$

The shape factor, H, does not vary significantly with increasing Reynolds number, this observation is similar to that of Gad-el Hak and Bandyopadhyay (1994).

A summary of the test conditions for the perforated sheet, sand grain, and wire mesh is given in Tables 3.2, 3.3, and 3.4, respectively. In these tables, k/δ is the blockage ratio, which is the ratio of the roughness height to the boundary layer

thickness. A criterion considered by Jimenez (2004) was that the blockage ratio, k/δ, be sufficiently small, i.e. $k/\delta < 0.025$ for similarity laws to be expected, and perhaps $k/\delta < 0.0125$ for the mechanisms of normal wall turbulence to prevail. In the present case, for the fully rough flows, the sand grain roughness (SGL) approximately meets the second criterion, while the wire mesh does not. Recall that for the wire mesh, the roughness height, k , was equal to twice the wire diameter which may tend to exaggerate the blockage ratio. As observed in the smooth surface, the shape factor, H, does not vary significantly with increasing Reynolds number. A similar conclusion was drawn by Furuya and Fujita (1967) and Schultz and Flack (2003).

Table 3.1: Summary of the test conditions for a smooth surface

	U_e (m/s)	Re_θ	δ (mm)	δ^* (mm)	θ (mm)	H
SM1	15.4	3730	36.9	5.40	4.06	1.33
SM2	25.5	5680	33.7	4.91	3.72	1.32
SM3	35.9	7720	33.0	4.68	3.57	1.31
SM4	44.2	10360	32.5	4.50	3.49	1.29

Table 3.2: Summary of the test conditions for the perforated sheet experiments

		$U_e(m/s)$	Re_θ	δ (mm)	δ^* (mm)	k/δ	θ (mm)	H
PS	PS1	15.3	4030	38.2	6.26	0.020	4.46	1.41
	PS2	25.5	5870	35.3	5.34	0.022	3.81	1.39
	PS3	36.5	8080	34.0	5.22	0.022	3.72	1.39
	PS4	44.5	9130	32.7	4.86	0.023	3.52	1.38
PM	PM1	15.2	3840	35.8	6.04	0.025	4.25	1.43
	PM2	25.4	6030	33.5	5.78	0.027	3.99	1.45
	PM3	36.2	8130	31.8	5.45	0.028	3.79	1.44
	PM4	44.3	10280	31.3	5.58	0.029	3.88	1.44
PL	PL1	15.4	4600	39.4	7.90	0.023	5.00	1.58
	PL2	25.2	6780	34.7	7.26	0.026	4.65	1.56
	PL3	35.1	9190	34.6	6.83	0.026	4.40	1.55
	PL4	44.2	11460	34.4	6.63	0.026	4.31	1.54

Table 3.3: Summary of the test conditions for the sand grain experiments

		$U_e(m/s)$	Re_θ	δ (mm)	δ^* (mm)	k/δ	θ (mm)	H
SGS	SGS1	15.8	3810	35.6	5.56	0.005	3.96	1.41
	SGS2	26.0	5670	32.1	5.23	0.006	3.70	1.41
	SGS3	36.1	8030	31.7	5.35	0.006	3.76	1.42
	SGS4	45.3	10360	32.0	5.45	0.006	3.79	1.42
SGM	SGM1	16.1	3960	34.6	5.90	0.009	4.06	1.45
	SGM2	25.0	6000	33.3	5.80	0.009	4.00	1.45
	SGM3	35.5	8700	33.7	5.89	0.009	4.05	1.45
	SGM4	44.4	10930	33.5	5.99	0.009	4.14	1.45
SGML	SGML1	15.5	4150	36.7	6.77	0.010	4.49	1.51
	SGML2	25.2	6530	34.2	6.37	0.011	4.33	1.49
	SGML3	35.3	9320	33.7	6.51	0.011	4.36	1.48
	SGML4	45.1	11920	34.0	6.40	0.011	4.35	1.47
SGL	SGL1	15.4	4670	39.3	7.91	0.012	5.01	1.58
	SGL2	25.5	7000	37.8	7.44	0.013	4.68	1.57
	SGL3	35.6	9790	35.2	7.24	0.014	4.67	1.55
	SGL4	44.1	12140	35.7	7.33	0.013	4.71	1.56

Table 3.4: Summary of the test conditions for the wire mesh experiments

		$U_e(m/s)$	Re_θ	δ (mm)	δ^* (mm)	k/δ	θ (mm)	H
WMS	WMS1	15.6	4670	38.5	7.85	0.019	5.07	1.55
	WMS2	25.6	7250	36.9	7.68	0.020	4.93	1.56
	WMS3	35.6	9570	34.8	7.43	0.021	4.75	1.56
	WMS4	44.8	12110	33.8	7.08	0.021	4.63	1.53
WMM	WMM1	16.0	4950	39.6	8.25	0.029	5.24	1.57
	WMM2	25.7	7560	36.4	7.80	0.032	4.96	1.57
	WMM3	36.6	10090	35.5	7.35	0.033	4.71	1.56
	WMM4	44.7	12260	34.8	7.34	0.033	4.74	1.55
WML	WML1	15.4	5040	39.6	9.01	0.053	5.42	1.66
	WML2	25.6	7840	36.7	8.44	0.057	5.11	1.65
	WML3	35.6	10630	36.8	8.41	0.056	5.11	1.65
	WML4	44.7	13550	37.4	8.43	0.056	5.10	1.65

The two-dimensionality of the flow was checked by measuring the boundary layer velocity profiles at a number of transverse and streamwise locations. There were no systematic spanwise variations. Clauser (1954) proposed an expression for the equilibrium pressure gradient parameter as $\beta = (\delta^* / \tau_w) dp/dx$. In the present study, the pressure gradient corresponded to a Clauser equilibrium parameter of approximately -0.015, -0.012, -0.013, and -0.012 for the highest Reynolds number data on smooth (SM4), perforated sheet (PL4), sand paper (SGL4), and wire mesh (WML4) surfaces, respectively. In addition, the acceleration parameter $\left(\mathrm{K} = \nu (dU_e/dx)/U_e^2\right)$ (Moretti and Kays, 1965) for the experiment ranged between 1.5×10^{-8} and 4.5×10^{-8}, indicating that the acceleration is insignificant. Based on these values, it was concluded that the pressure-gradient measured in the wind tunnel for all experiments was negligible.

3.8 Uncertainty Estimates

In order to estimate the 95% precision and bias confidence limits, the procedure given by Coleman and Steele (1999) was adopted. Precision uncertainty estimates for the velocity measurements were made through repeatability tests. Four replicate velocity profiles were taken on both a smooth and a rough surface. The systematic error, which represents the bias uncertainty, was obtained from the instrumentation used in the measurements, which includes a Datametrics 600A-1000T-S13-H21X-4 absolute pressure transducer, Datametrics 590D-10W-V1X-4D differential pressure transducer, TSI IFA-100 anemometer, copper-constantan thermocouple (Type T), and data acquisition board. The estimated bias errors were combined with the precision

uncertainties to calculate the overall uncertainties for the measured quantities. A complete uncertainty analysis is presented in Appendix B. The absolute accuracy in hot-film measurements is very difficult to analyse. One factor which directly influences the accuracy in the measurements is the number of independent samples at each point. The integral time scale was estimated with aim of determining the independent samples. Details are presented in Appendix B. Table 3.5 summarizes the uncertainty estimates of both measured and derived quantities. The uncertainty in wall-normal position (y) was ± 0.05 mm. The estimated uncertainty in both δ was $\pm 5\%$. Very close to the wall, the

Table 3.5: Summary of uncertainty estimates

Parameter	Uncertainty estimate
Wall-normal position (y)	± 0.05 mm
Dynamic pressure (P_{dyn})	± 1.04 %
Absolute pressure (P)	± 0.99 %
Absolute temperature (T)	± 0.33 ^{o}C
Density (ρ)	± 1.08 %
Dynamic viscosity (μ)	± 0.25 %
Freestream velocity (U_e)	± 0.75 %
Friction velocity (U_τ)	± 3 % for smooth surface ± 5 % for rough surface
Skin friction (C_f)	± 5 % for smooth surface ± 9 % for rough surface
Reynolds number (Re_θ)	± 6 %
Boundary layer thickness (δ)	± 5 %
Displacement thickness (δ^*)	± 5 %
Momentum thickness (θ)	± 5 %
Streamwise turbulence intensity <u>	± 4 %
Wall-normal turbulence intensity <v>	± 8 %
Reynolds shear stress <uv>	± 11 %
Triple correlations (<u^3>, <v^3>, <u^2v>, <uv^2>)	± 10 – 15 %

uncertainty in the local velocity was approximately $\pm 2\%$, while the estimated uncertainty in the freestream velocity was $\pm 0.75\%$. For the hot-wire/film anemometer probes, standard error estimates were obtained using the independent data.

CHAPTER 4

INNER SCALING OF MEAN FLOW ON SMOOTH AND ROUGH SURFACES

4.1 Introduction

As earlier mentioned in Chapter 2, the mean velocity profile consists of an inner layer (viscous shear dominates) and an outer layer (turbulent shear dominates), as well as an immediate overlap (both types of shear important) between the two. This chapter focuses on the scaling issues for the overlap region of the mean velocity profile obtained for a two-dimensional zero-pressure gradient turbulent boundary layer on smooth and rough surfaces. Recall that there is still a debate on whether the classical logarithmic law or power law is a better scaling law to model the overlap region of the mean velocity profile. The capabilities of these scaling laws to describe the overlap region of the mean velocity profile, as well as to determine the friction velocity for both the smooth and rough wall data using profile fitting techniques, are reported. The effects of surface roughness on the mean velocity are investigated for three flow regimes, namely, hydraulically smooth, transitionally rough, and fully rough. The behaviour of the power law coefficient and exponent on different surfaces, as well as the calibration of the power law coefficient and exponent for transitionally rough flow, is presented. In the final section of this chapter, the logarithmic law and power law formulations are

compared in terms of their extent to which they describe the overlap region, as well as the friction velocity obtained from both formulations. A new skin friction correlation valid for smooth- and rough-wall turbulent boundary layers is proposed.

4.2 Scaling of the Mean Velocity using a Logarithmic Profile

4.2.1 Determination of Friction Velocity and Strength of the Wake

As previously mentioned in Chapter 2, the description of a measured velocity profile on a rough wall requires the determination of four parameters, i.e., U_τ, ΔU^+, Π, and y_o Within our research group, previous rough-wall boundary layer studies have used the profile fitting method of Krogstad et al. (1992) to determine the friction velocity (e.g. Tachie et al., 2000; Bergstrom et al., 2002). It assumes the existence of a log-law and a functional form of the wake, but it allows the strength of the wake to vary. This method was employed to determine the friction velocity on smooth and rough surfaces. The method originally used by Krogstad et al. (1992) also involved an optimization for the virtual origin, y_o, which represents the virtual location of the wall relative to the nominal top of the roughness elements.

Figure 4.1 shows the defect profile fitting of Eqn. (2.26) (represented by the broken lines) for some representative experimental data. In this figure, the friction velocity and the strength of the wake, Π, are determined for both the smooth and rough surfaces. The defect profiles are mentioned in this chapter because they are fitted to experimental data to estimate the friction velocity. More discussion on the defect profiles for smooth and rough surfaces will be presented in Chapter 5. An assessment of

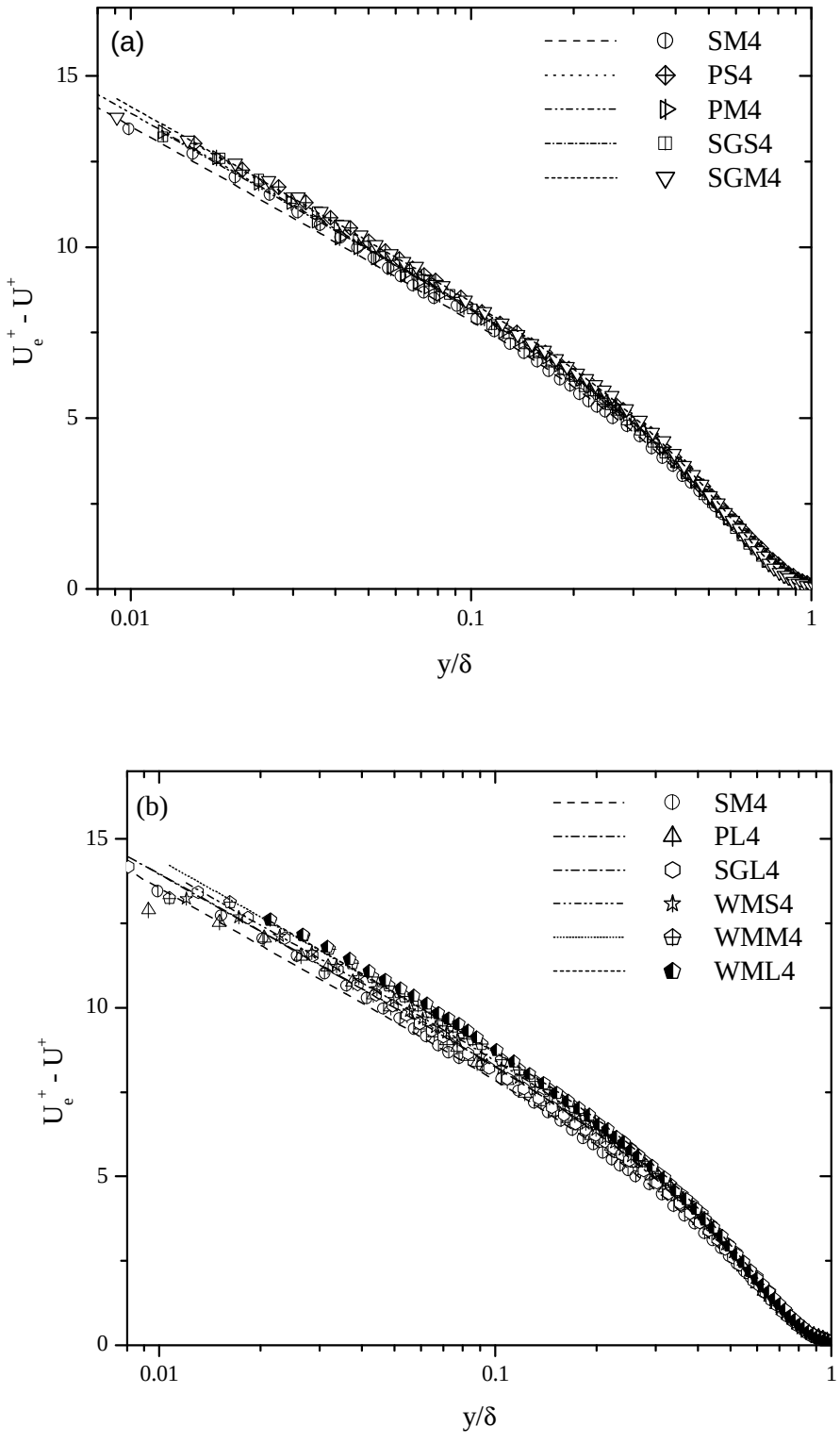

Figure 4.1: Mean velocity defect profiles using inner coordinates: (a) smooth and transitionally rough; (b) smooth and fully rough.

Table 4.1: Summary of skin friction coefficient and flow conditions for a smooth surface

	U_e (m/s)	Re_θ	δ^+	U_τ (m/s)	$C_f \times 10^3$	Π
SM1	15.4	3730	1350	0.610	3.16	0.490
SM2	25.5	5680	1940	0.970	2.90	0.501
SM3	35.9	7720	2830	1.321	2.71	0.520
SM4	44.2	10360	3400	1.580	2.56	0.525

goodness-of-fit using a Chi-square distribution at a 95 percent confidence level was obtained within the region $0.1 \leq y/\delta \leq 1$. When the value of the friction velocity, U_τ, obtained from the defect profile was used to fit a log-law to the experimental data, the velocity profile tended to become slightly concave near the wall as the surface became rougher. In order to eliminate this anomaly, the log-law was enforced for the data points nearest the wall by increasing the wall datum shift. For the roughness elements considered in this study, the maximum value of y_o^+ was estimated to be 82. Although this method is somewhat arbitrary in its forcing of a log law at the bottom of the inner layer, it had the advantage of yielding C_f values for fully rough flow that exhibited minimal variation with Re_θ. Table 4.1 presents a summary of the freestream velocity, Reynolds number based on momentum thickness, friction velocity, skin friction coefficient, and strength of the wake for the smooth surface. The friction velocity obtained from the smooth surface at the highest Reynolds number was used to estimate a roughness Reynolds number, k^+, which was 0.37. This estimate was based on the average roughness height, R_a, for the MDF board, and qualifies the MDF board as a hydraulically smooth surface. The values

Table 4.2: Summary of skin friction coefficient and flow conditions for the perforated sheets.

		U_e (m/s)	Re_θ	δ^+	U_τ (m/s)	$C_f \times 10^3$	Π	ΔU^+	k^+	k_{eq}^+
PS	PS1	15.3	4030	1470	0.640	3.62	0.511	2.0	29	9
	PS2	25.5	5870	2080	1.040	3.34	0.541	2.2	48	10
	PS3	36.5	8080	2930	1.450	3.15	0.590	2.4	66	11
	PS4	44.5	9130	3390	1.710	2.96	0.592	2.5	78	12
PM	PM1	15.2	3840	1400	0.660	3.75	0.530	2.4	36	11
	PM2	25.4	6030	2290	1.148	4.09	0.535	4.4	62	26
	PM3	36.2	8130	3020	1.610	3.95	0.540	4.8	87	30
	PM4	44.3	10280	3830	1.950	3.87	0.550	5.4	105	38
PL	PL1	15.4	4600	1930	0.815	5.58	0.540	7.2	44	79
	PL2	25.2	6780	2620	1.303	5.35	0.555	7.7	70	97
	PL3	35.1	9190	3500	1.801	5.26	0.557	8.3	96	127
	PL4	44.2	11460	4380	2.253	5.19	0.560	8.7	122	149

Table 4.3: Summary of skin friction coefficient and flow conditions for the sand grain.

		U_e (m/s)	Re_θ	δ^+	U_τ (m/s)	$C_f \times 10^3$	Π	ΔU^+	k^+	k_{eq}^+
SGS	SGS1	15.8	3810	1430	0.661	3.50	0.500	2.0	7	9
	SGS2	26.0	5670	2080	1.100	3.59	0.534	3.4	12	17
	SGS3	36.1	8030	2910	1.552	3.70	0.536	4.4	17	26
	SGS4	45.3	10360	3800	1.970	3.78	0.540	5.3	22	37
SGM	SGM1	16.1	3960	1490	0.715	3.98	0.500	3.5	13	18
	SGM2	25.0	6000	2270	1.140	4.15	0.535	5.0	21	33
	SGM3	35.5	8700	3240	1.592	4.02	0.580	5.5	29	40
	SGM4	44.4	10930	3910	1.960	3.91	0.590	5.9	36	47
SGML	SGML1	15.5	4150	1640	0.746	4.65	0.512	5.3	17	37
	SGML2	25.2	6530	2420	1.184	4.40	0.571	6.2	27	53
	SGML3	35.3	9320	3310	1.623	4.24	0.590	6.6	37	63
	SGML4	45.1	11920	4260	2.061	4.18	0.620	7.0	46	74
SGL	SGL1	15.4	4670	1900	0.820	5.65	0.540	7.5	24	89
	SGL2	25.5	7000	2700	1.334	5.46	0.548	8.3	38	124
	SGL3	35.6	9790	3600	1.834	5.31	0.551	8.5	52	137
	SGL4	44.1	12140	4430	2.245	5.18	0.556	9.0	64	169

Table 4.4: Summary of skin friction coefficient and flow conditions for the wire mesh

		U_e (m/s)	Re_θ	δ^+	U_τ (m/s)	$C_f \times 10^3$	Π	ΔU^+	k^+	k_{eq}^+
WMS	WMS1	15.6	4670	1870	0.818	5.60	0.551	7.3	35	82
	WMS2	25.6	7250	2700	1.331	5.42	0.589	8.5	56	134
	WMS3	35.6	9570	3510	1.840	5.35	0.595	9.1	78	177
	WMS4	44.8	12110	4360	2.301	5.28	0.595	9.3	99	186
WMM	WMM1	16.0	4950	2010	0.854	5.68	0.577	7.8	59	101
	WMM2	25.7	7560	2900	1.355	5.55	0.604	8.8	94	156
	WMM3	36.6	10090	3940	1.890	5.33	0.625	9.2	133	183
	WMM4	44.7	12260	4560	2.283	5.22	0.645	9.4	156	191
WML	WML1	15.4	5040	2150	0.889	6.64	0.589	9.8	111	229
	WML2	25.6	7840	3120	1.460	6.49	0.627	10.5	185	314
	WML3	35.6	10630	4130	2.010	6.37	0.642	11.0	249	382
	WML4	44.7	13550	5280	2.506	6.29	0.650	11.6	314	488

of the strength of the wake Π did vary with increasing Reynolds number for the smooth surface.

For the rough surfaces, the roughness shift, ΔU^+, roughness Reynolds number, k^+, and the equivalent sand grain roughness Reynolds number, k_{eq}^+, are given in Tables 4.2, 4.3, and 4.4. The equivalent sand grain roughness Reynolds number, k_{eq}^+, was obtained from the relation used by Raupach et al. (1991). As indicated in Table 4.3, values of the roughness Reynolds number, k^+, for sand grain roughness are not equal to the equivalent sand grain roughness Reynolds number, k_{eq}^+, for the same Reynolds number. This can be attributed to the fact that the present sand grains were created from aluminium oxide, which has a different texture than real sand grain. This observation suggests that the texture of the surface roughness has significant effect on the roughness

shift, ΔU^+, produced. The values of Π for the rough surfaces are typically larger than for the smooth surface, and for each rough surface, the value of Π is observed to increase as the roughness shift increases. This is one example of the effect of surface roughness extending into the outer region.

Based on the values of k_{eq}^+, transitionally rough flows were obtained for two perforated sheets (PS and PM) and three sand grain roughnesses (SGS, SGM, and SGML 1, 2, and 3), while fully rough flow was achieved for one perforated sheet (PL), two sand grain roughnesses (SGML 4 and SGL), and all three woven wire mesh surfaces used in the experiments. The values of the skin friction coefficient, C_f, obtained for the rough surfaces are also higher than those of the smooth surface as expected. Jimenez (2004) suggested that the Reynolds number based on boundary layer thickness, δ^+, should be greater than 4000 as a condition for a well-defined rough wall turbulent boundary layer. In the present study, the Reynolds numbers based on boundary thickness for all fully rough flows at the highest Reynolds number are greater than 4000.

In this sub-section, the friction velocity is determined using the profile fitting technique, as well as other flow parameters, are reported. In addition, three flow regimes, namely, hydraulically smooth, transitionally rough, and fully rough, have been identified based on the values of k_{eq}^+. As earlier mentioned in Chapter 2, the friction velocity is an important scaling parameter, and is used to assess the effects of Reynolds number and surface conditions. In the next section, the evaluation of the effect of

Reynolds number on the mean velocity profiles on different surface characteristics is presented.

4.2.2 Mean Velocity Profiles for Smooth and Rough Walls in Inner Coordinates

Figure 4.2 presents the mean velocity profiles normalized by friction velocity on a smooth wall for different Reynolds numbers using inner coordinates. As the Reynolds number increases, the extent over which the experimental data collapse onto the logarithmic law in the overlap region increases. The effect of Reynolds number is also observed in the outer region of the flow. For example, there is an increase in the strength of the wake, as indicated in Table 4.1.

Figure 4.3 presents the mean velocity profiles normalized by friction velocity obtained for perforated sheets of different thickness and circular hole diameters for different Reynolds numbers using inner coordinates. The mean velocity profiles obtained for perforated sheet (PS) having a roughness height of 0.76 mm and openness ratio of 22 % for different Reynolds numbers are shown in Figure 4.3a, while those obtained for perforated sheets (PM) with a roughness height of 0.9 mm and openness ratio of 41 % for different Reynolds numbers are presented in Figure 4.3b. Figure 4.3c shows the mean velocity profiles obtained for perforated sheet (PL) with a roughness height of 0.9 mm and openness ratio of 45 %. Based on the values of k_{eq}^{+}, nominal transitionally rough flows are achieved on both the PS and PM, while the fully rough flows are obtained on the PL. For each perforated sheet, the mean velocity profiles on

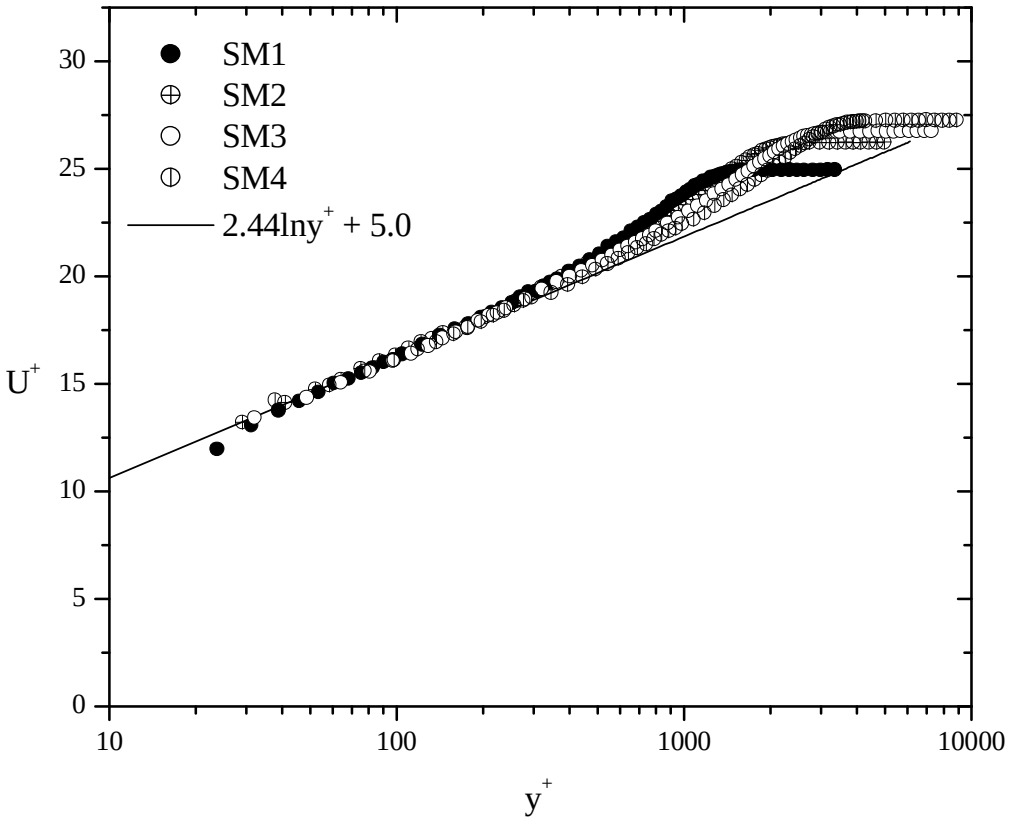

Figure 4.2: Mean velocity profiles on a smooth surface using inner coordinates.

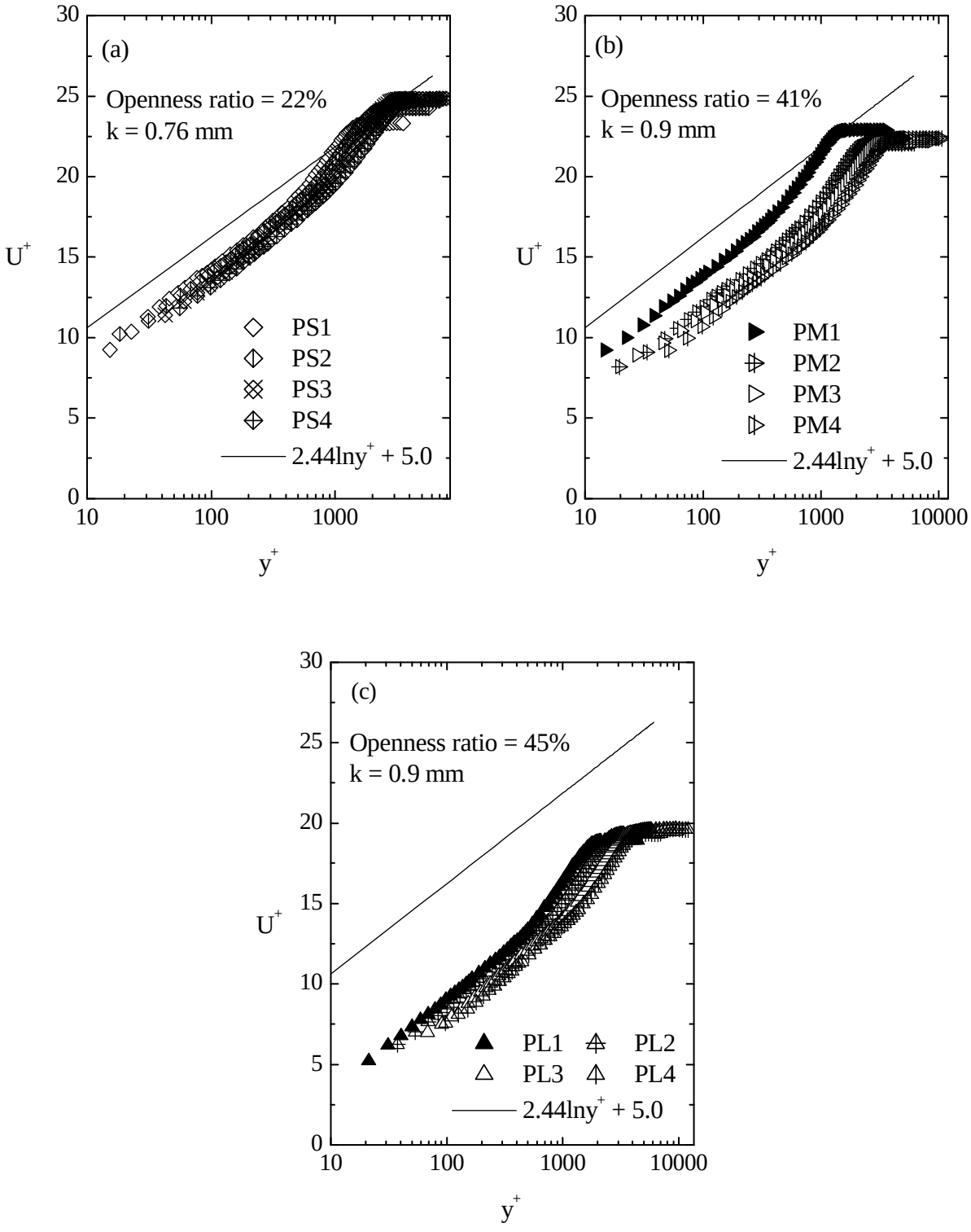

Figure 4.3: Mean velocity profiles on perforated sheets using inner coordinates: (a) transitionally rough; (b) transitionally rough; (c) fully rough.

these rough surfaces exhibit a downward-right shift with respect to the logarithmic law for a smooth surface. For all three perforated sheets, the roughness shift, ΔU^+, increases as the Reynolds number, Re_θ, increases. For instance, the roughness shift, ΔU^+, produced by PS4 (highest Reynolds number) is 25 % higher than that on PS1 (lowest Reynolds number). In the case of the PM, the roughness shift, ΔU^+, obtained for PM4 is 125 % higher than that of PM1, while for the PL, the roughness shift produced by PL4 is approximately 21 % higher than that on PL1. The effects of Reynolds number in terms of the roughness shift produced on PM (transitionally rough) and PL (fully rough) are quite different, despite having the same roughness height but different openness ratio. This observation suggests that the openness ratio of each perforated sheet also contributed in determining the flow regime achievable on each surface with respect to Reynolds number. Comparison among all the perforated sheets (PS, PM, and PL) shows that the Reynolds number effects are more pronounced in the nominal transitionally rough flows than fully rough flows in terms of roughness shift produced. In addition, for all three perforated sheets considered, the evidence of the Reynolds number effect is also observed in the outer region of the boundary layer, as the strength of the wake increases as Reynolds number increases.

Figure 4.4 compares the mean velocity profiles obtained for the perforated sheet for different thickness and openness ratio at the highest Reynolds number. As the openness ratio increases, the flow becomes rougher as indicated by the value of the roughness shift, ΔU^+. For example, note that PM4 and PL4 with the same roughness

height of 0.9 mm produced different roughness shifts. One possible explanation for this behaviour is that the interaction between the flow within the cavities and the bulk flow becomes more significant and pronounced as the openness ratio increases. These experimental results support the conclusion drawn by Furuya and Fijuta (1967) that the roughness height, k, is not the only important parameter in determining the roughness shift, ΔU^+ (although, their conclusion was based on woven wire mesh).

Figure 4.5 presents the mean velocity profiles normalized by friction velocity obtained for different sand grain roughness heights for different Reynolds numbers using inner coordinates. For all the sand grain surfaces considered, the Reynolds number effects generally increase the roughness shift, ΔU^+, produced by each sand grain roughness considered. According to the values of k_{eq}^+, nominal transitionally rough flows are obtained on SGS, SGM, and SGML (1, 2, and 3), while SGML4 and SGL produced fully rough flows. Comparing the Reynolds number effects on the four sand grain surfaces (Figures 4.5a, b, c, and d), it is noted that the roughness shift, ΔU^+, obtained for SGS, SGM, SGML, and SGL at the highest Reynolds number considered are 165 % , 69 %, 32 % , and 20 % higher, respectively, than their counterpart at the lowest Reynolds number. The effects of Reynolds number are also observed in the outer region of the flow where it was noted that the strength of the wake becomes stronger, as shown in Figure 4.5.

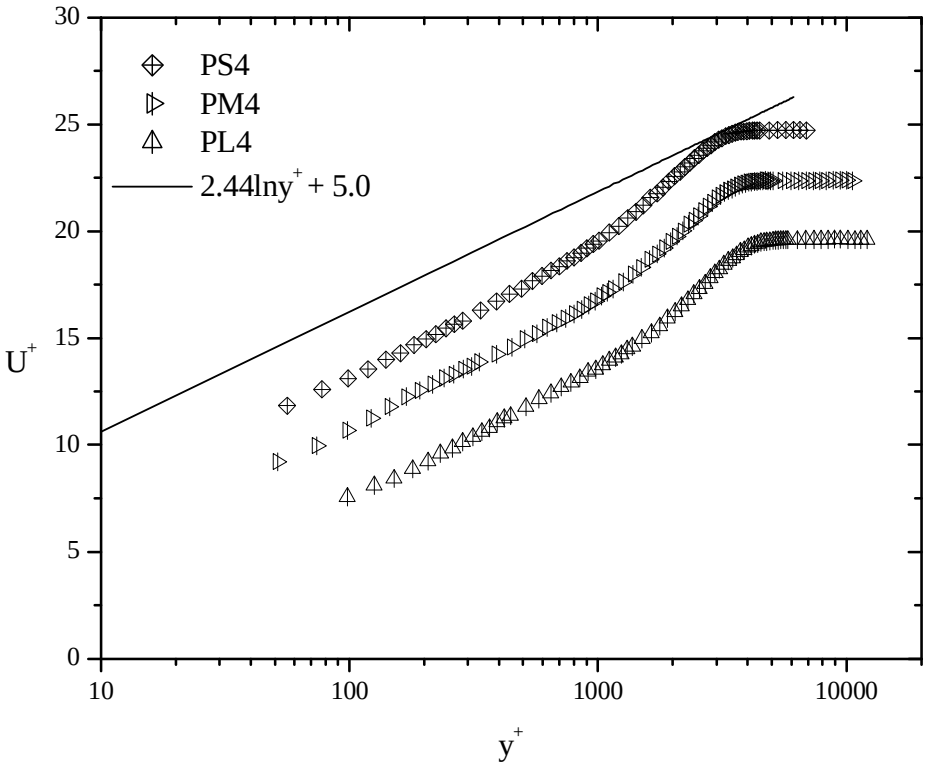

Figure 4.4: Mean velocity profiles on perforated sheets using inner coordinates.

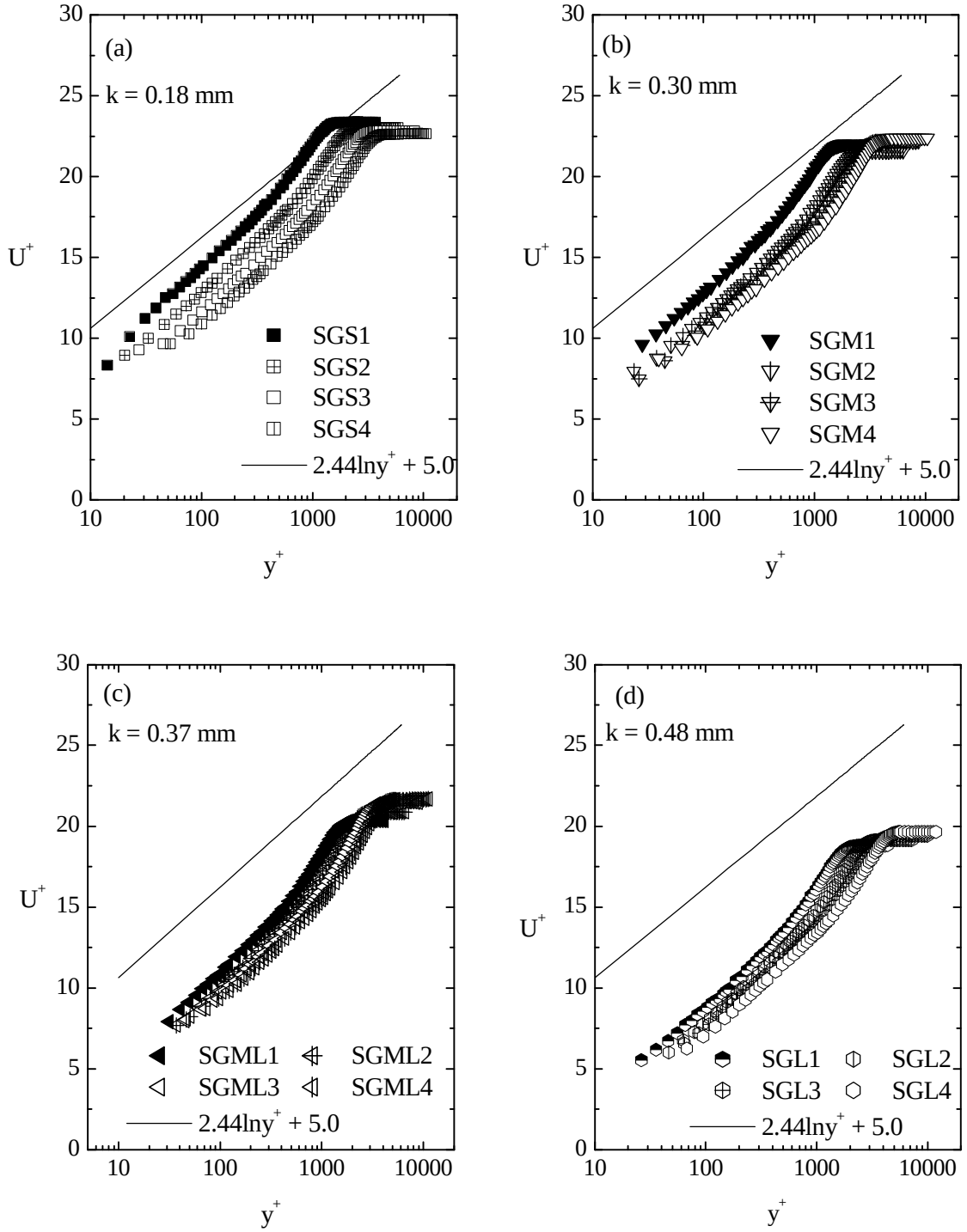

Figure 4.5: Mean velocity profiles on sand grain using inner coordinates: (a) k = 0.18 mm; (b) k = 0.30 mm; (c) k = 0.37 mm; (d) 0.48 mm.

Figures 4.6 compares the mean velocity profiles obtained for the sand grain roughness for different roughness height at the highest Reynolds number. It is observed that the flow becomes rougher as the roughness height, *k*, increases. This is due to the increase in protrusion of the roughness elements into the flow in the vicinity of the wall. Recall that these roughness elements act as "local blockages" to the flow adjacent to the wall. As the roughness height increases the intensity of the vortex shedding process above the viscous layer increases, leading to the gradual destruction of this layer and an increase in the skin friction drag.

Figure 4.7 presents the mean velocity profiles scaled with friction velocity obtained for wire mesh for different diameter and openness ratio for different Reynolds numbers. The mean velocity profiles on all the three wire mesh surfaces show a downward-right shift with respect to the logarithmic law for a smooth surface. Recall that the flows over the wire mesh surfaces (WMS, WMM, and WML) are fully rough. Just as observed in the perforated sheets and sand grain roughness, the roughness shift, ΔU^+, produced by all wire mesh increases as the Reynolds number increases. For example, from the lowest to the highest Reynolds numbers considered, the roughness shifts produced by WMS, WMM, and WML are increased by 27 %, 21 %, and 18 %, respectively. The present experimental results show that the roughness shift obtained for all the surfaces exhibiting fully rough flows show weak dependence on the Reynolds number compared with those on the transitionally rough flows. As indicated in Figures 4.7a, 4.7b, and 4.7c, the strength of the wake increases with increase in the Reynolds number.

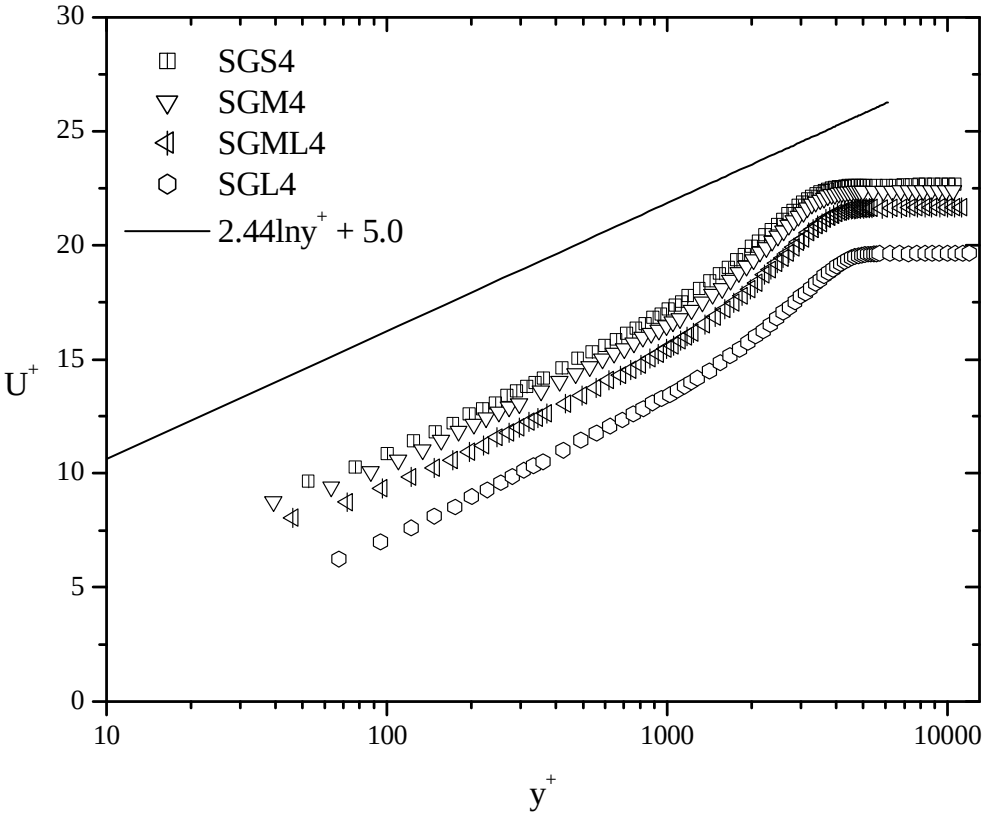

Figure 4.6: Mean velocity profiles on sand grain using inner coordinates.

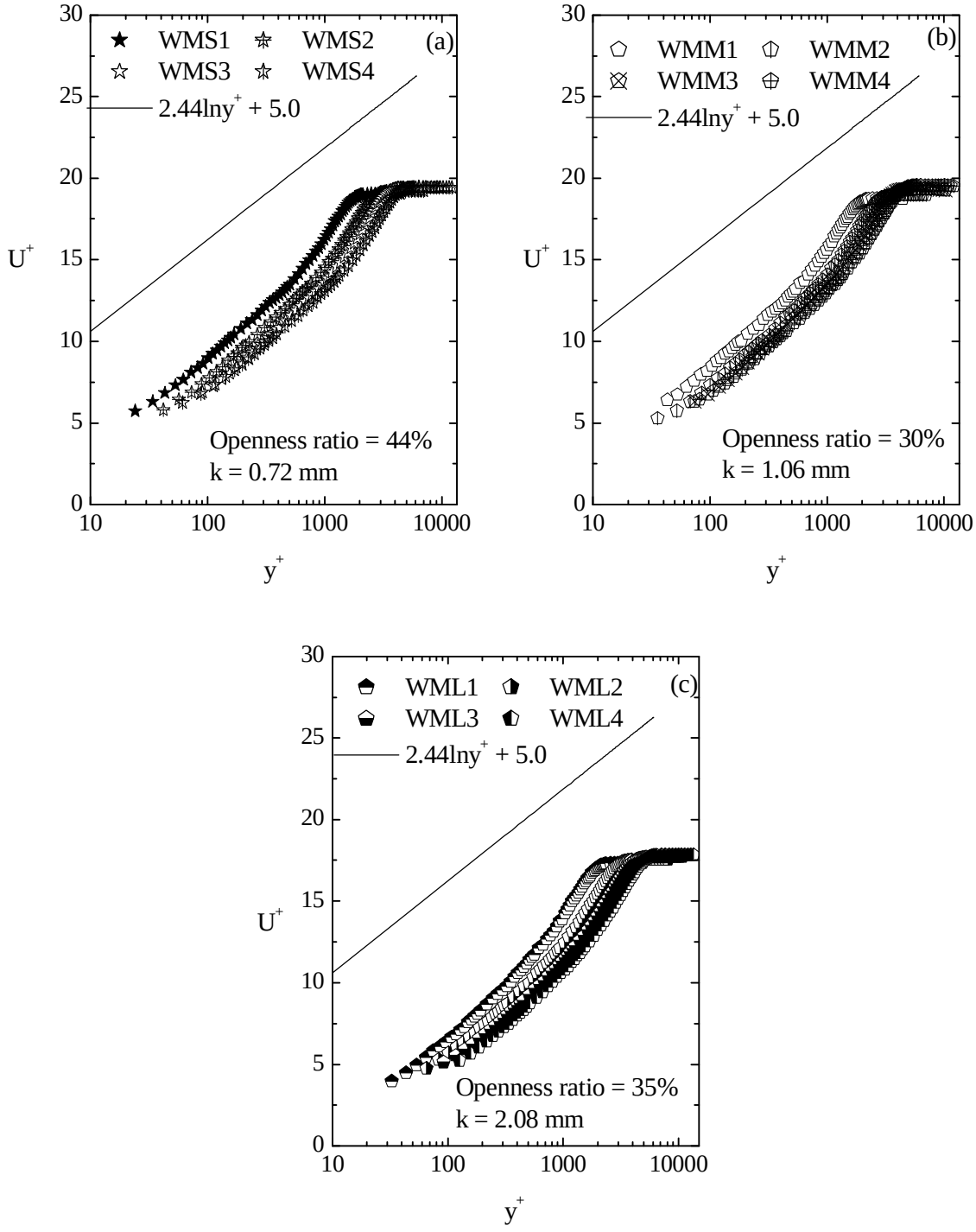

Figure 4.7: Mean velocity profiles on wire mesh roughness using inner coordinates.

Figure 4.8 compares the mean velocity profiles obtained for the wire mesh for different diameter and openness ratio at the highest Reynolds number. Despite their different roughness height MWS4 and WMM4 produced approximately the same roughness shift, ΔU. Recall that the wire mesh WMS4 has a larger openness ratio than that of WMM4. The wire mesh WML4 exhibits the greatest roughness effect compared to the other wire mesh surfaces; although it has the largest roughness height among the wire mesh surfaces considered, but a lower openness ratio than that of WMS4. This observation suggests that the level of roughness effect produced depends on the characteristics of the roughness geometry, which include the roughness height and the openness ratio.

Figure 4.9a compares the mean velocity profiles at the highest Reynolds number for the hydraulically smooth and transitionally rough surfaces using inner coordinates. Figure 4.9b compares the mean velocity profiles obtained for hydraulically smooth and fully rough flows at the highest Reynolds number using inner coordinates. As expected, the effect of surface roughness is to increase the friction velocity resulting in a downward-right shift of the mean velocity profiles. Comparison between Figure 4.9a and 4.9b indicates that the fully rough flow exhibits a significantly larger velocity shift, ΔU^+, than the transitionally rough flow. The present experimental results also indicate that, as the surface roughness increases, the linear region of the overlap region becomes relatively narrow. A similar observation was reported by Bergstrom et al. (2001). As indicated in Figure 4.9, the rough surface

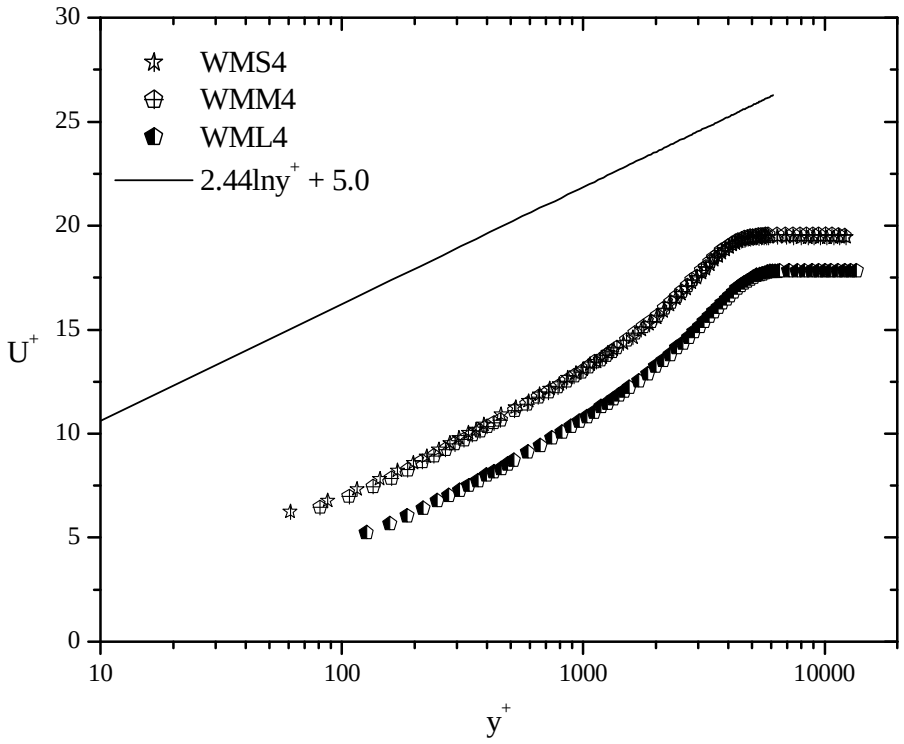

Figure 4.8: Mean velocity profiles on wire mesh roughness using inner coordinates.

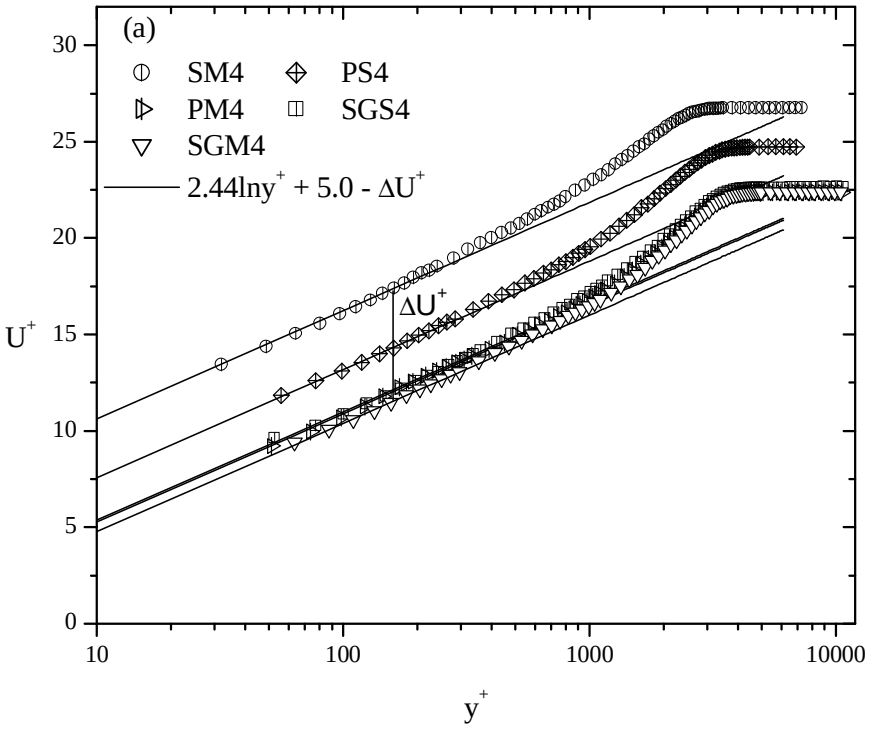

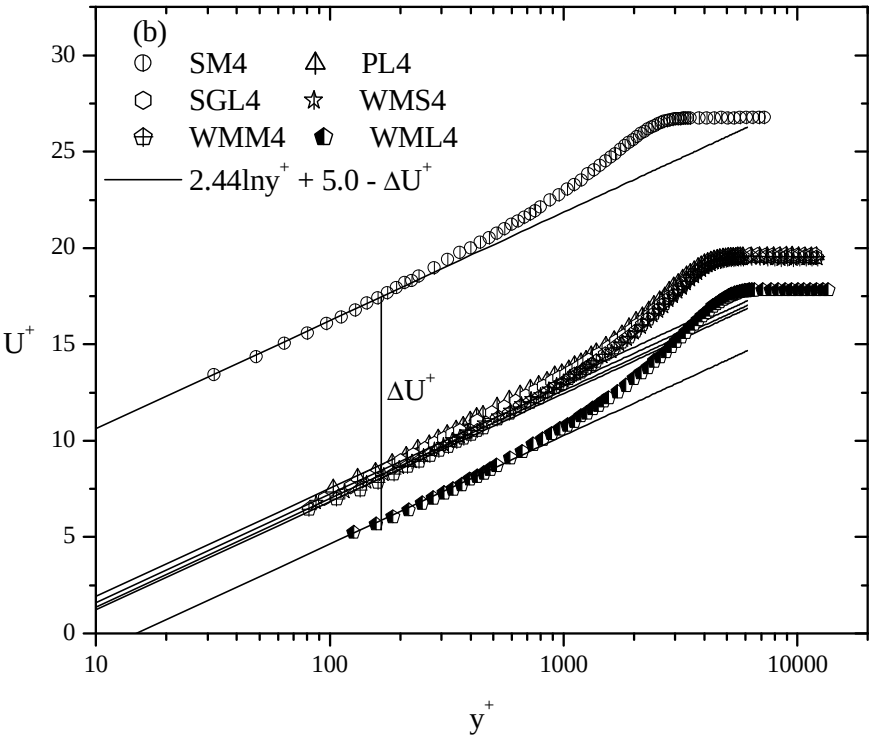

Figure 4.9: Mean velocity profiles using inner coordinates: (a) smooth and transitionally rough; (b) smooth and fully rough.

exhibits a stronger wake component than does the smooth surface. This is evidence that the effect of surface roughness extends into the outer region of the flow. However, the transport mechanisms related to this effect are still not well understood.

4.3 Scaling of Mean Velocity using a Power Law

As noted in Chapter 2, George and Castillo (1997) proposed that a power law profile is more appropriate for describing the mean velocity in the overlap region of the flow over a smooth surface. This scaling law is also used to determine the skin friction (or friction velocity). The determination of the skin friction velocity, U_τ, using the power law proposed by George and Castillo (1997), required the adjustment of three coefficients (C_o, C_i, and γ), as well as the friction velocity, U_τ, as given in Eqn. (2.30). Since the power law in outer coordinates does not contain friction velocity, U_τ, Eqn. (2.19) was fitted to the experimental data to determine C_o and γ, as shown in Figure 4.10 (dotted lines represent fitted Eqn. (2.19)). This approach allows many data points (up to $y = \delta$) to be used in the profile matching. One advantage of this approach is that any uncertainty in the virtual origin y_o would have no effect on the values of C_o and γ, since y_o does not appear in Eqn. (2.19). A value of B = 2.03 as recommended by George and Castillo (1997) was adopted in Eqn. (2.19) for both the smooth and rough walls. Using the determined value of γ, the friction velocity, U_τ, and C_i were then obtained from Eqn. (2.17). Table 4.5 summarizes the values of the coefficients for the power law and the friction velocity obtained for the smooth surface. As the Reynolds number increases, C_i

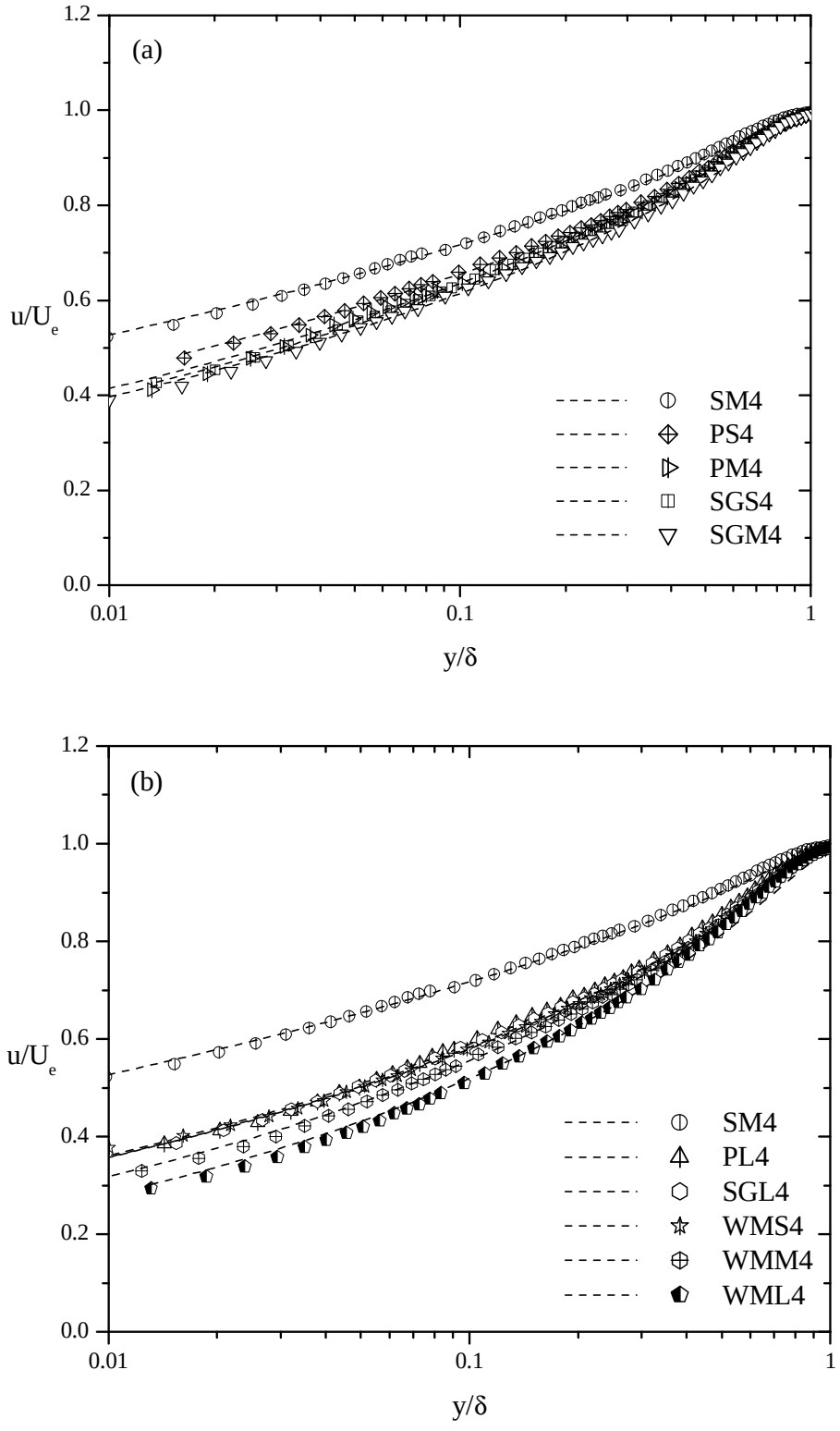

Figure 4.10: Mean velocity profiles using outer coordinates: (a) smooth and transitionally rough; (b) smooth and fully rough.

Table 4.5: Summary of power law constants and friction velocity for smooth surface.

		δ^+	C_i	γ	C_o	U_τ (m/s)	% ΔU_τ
SM	SM1	1350	8.905	0.139	0.960	0.909	0.16
	SM2	1940	8.995	0.136	0.960	0.962	0.83
	SM3	2830	9.009	0.135	0.960	1.320	0.08
	SM4	3400	9.021	0.133	0.950	1.591	0.70

increases and γ decreases. This observation agrees with the behaviour of C_i and γ as proposed by George and Castillo (1997). Kotey *et al.* (2003) also reported a similar behaviour of C_i and γ with the Reynolds number. Comparison of the friction velocity obtained using a logarithmic law and power law shows the value differs within less than 1 %. This observation suggests that both formulations are appropriate for determining the skin friction drag on a smooth wall.

For the rough surfaces, Tables 4.6, 4.7, and 4.8 present the values of the coefficients and exponent for the power law, as well as the friction velocity obtained for the perforated sheet, sand grain roughness, and wire mesh surfaces, respectively. The values of the power law coefficient, C_i, and exponent, γ, are observed to be lower and higher, respectively, than those on the smooth surface. The lower value of C_i can be linked to the increase in drag as a result of surface roughness, which is responsible for the mean velocity profiles for the rough surfaces being 'less full' when compared with those on the smooth surface. The higher value of γ for the rough surface reflects the

Table 4.6: Summary of power law constants and friction velocity for perforated sheets.

		δ^+	C_i	γ	C_o	U_τ (m/s)	$\%\Delta U_\tau$	ΔU^+
PS	PS1	1470	7.321	0.152	0.925	0.639	0.16	2.0
	PS2	2080	6.995	0.157	0.950	1.034	0.58	2.2
	PS3	2930	6.651	0.160	0.985	1.479	2.00	2.4
	PS4	3390	6.535	0.161	0.965	1.762	3.04	2.5
PM	PM1	1400	7.025	0.155	0.924	0.653	1.07	2.4
	PM2	2290	5.581	0.171	0.940	1.140	0.70	4.4
	PM3	3020	5.178	0.178	0.960	1.611	0.06	4.8
	PM4	3830	4.713	0.186	0.975	1.972	1.13	5.4
PL	PL1	1930	3.201	0.231	0.975	0.804	1.37	7.2
	PL2	2620	3.245	0.225	0.959	1.293	0.77	7.7
	PL3	3500	3.289	0.219	0.949	1.776	1.41	8.3
	PL4	4380	3.301	0.215	0.969	2.211	1.90	8.7

Table 4.7: Summary of power law constants and friction velocity for sand grain surfaces.

		δ^+	C_i	γ	C_o	U_τ (m/s)	$\%\Delta U_\tau$	ΔU^+
SGS	SGS1	1430	7.121	0.160	0.960	0.665	0.61	2.0
	SGS2	2080	6.115	0.169	0.950	1.108	0.73	3.4
	SGS3	2910	5.354	0.178	0.960	1.562	0.64	4.4
	SGS4	3800	4.761	0.186	0.970	1.960	0.51	5.3
SGM	SGM1	1490	6.025	0.173	0.960	0.724	1.26	3.5
	SGM2	2270	4.958	0.186	0.960	1.142	0.18	5.0
	SGM3	3240	4.425	0.197	0.960	1.571	1.34	5.5
	SGM4	3910	4.525	0.189	0.947	1.946	0.72	5.9
SGML	SGML1	1640	4.455	0.202	0.970	0.754	1.07	5.3
	SGML2	2420	3.802	0.216	0.976	1.201	1.44	6.2
	SGML3	3310	3.811	0.210	0.986	1.651	1.73	6.6
	SGML4	4260	3.854	0.202	0.945	2.032	1.53	7.0
SGL	SGL1	1900	3.185	0.232	0.975	0.817	0.37	7.5
	SGL2	2700	3.205	0.227	0.960	1.309	1.91	8.3
	SGL3	3600	3.255	0.218	0.960	1.814	1.21	8.5
	SGL4	4430	3.261	0.216	0.946	2.189	2.56	9.0

Table 4.8: Summary of power law constants and friction velocity for wire mesh surfaces.

		δ^+	C_i	γ	C_o	U_τ (m/s)	$\%\,\Delta U_\tau$	ΔU^+
WMS	WMS1	1870	3.121	0.232	0.948	0.798	2.51	7.3
	WMS2	2700	3.161	0.228	0.946	1.293	2.94	8.5
	WMS3	3510	3.221	0.220	0.946	1.798	2.34	9.1
	WMS4	4360	3.231	0.215	0.936	2.243	2.56	9.3
WMM	WMM1	2010	3.121	0.231	0.960	0.852	2.28	7.8
	WMM2	2900	2.004	0.285	0.960	1.328	2.03	8.8
	WMM3	3940	2.015	0.276	0.960	1.874	0.85	9.2
	WMM4	4560	2.115	0.265	0.967	2.238	1.97	9.4
WML	WML1	2150	1.698	0.301	0.976	0.883	0.68	9.8
	WML2	3120	1.758	0.290	0.975	1.422	2.67	10.5
	WML3	4130	1.793	0.277	0.966	1.970	2.03	11.0
	WML4	5280	1.808	0.270	0.956	2.467	1.58	11.6

enhanced level of the strength of the wake, which can be attributed to the effect of surface roughness. It should be noted that the power law coefficient, C_i, and exponent, γ, depend on the experimental data at the upper part of the overlap region and lower end of the wake region, respectively. Previous studies on rough-wall turbulent boundary layers have also concluded that one of the effects of surface roughness is to increase the strength of the wake (e.g. Krogstad et al., 1992; Tachie et al., 2000). By comparing the power law coefficient C_o obtained for smooth and rough surfaces, it is very difficult to make a specific conclusion on the effect of surface roughness on this power law coefficient. This is because the values obtained for different surfaces did not show any particular direction with respect to Reynolds number based on boundary layer thickness. For the transitionally rough flows, indicated in Figure 4.11a, it is observed that as the

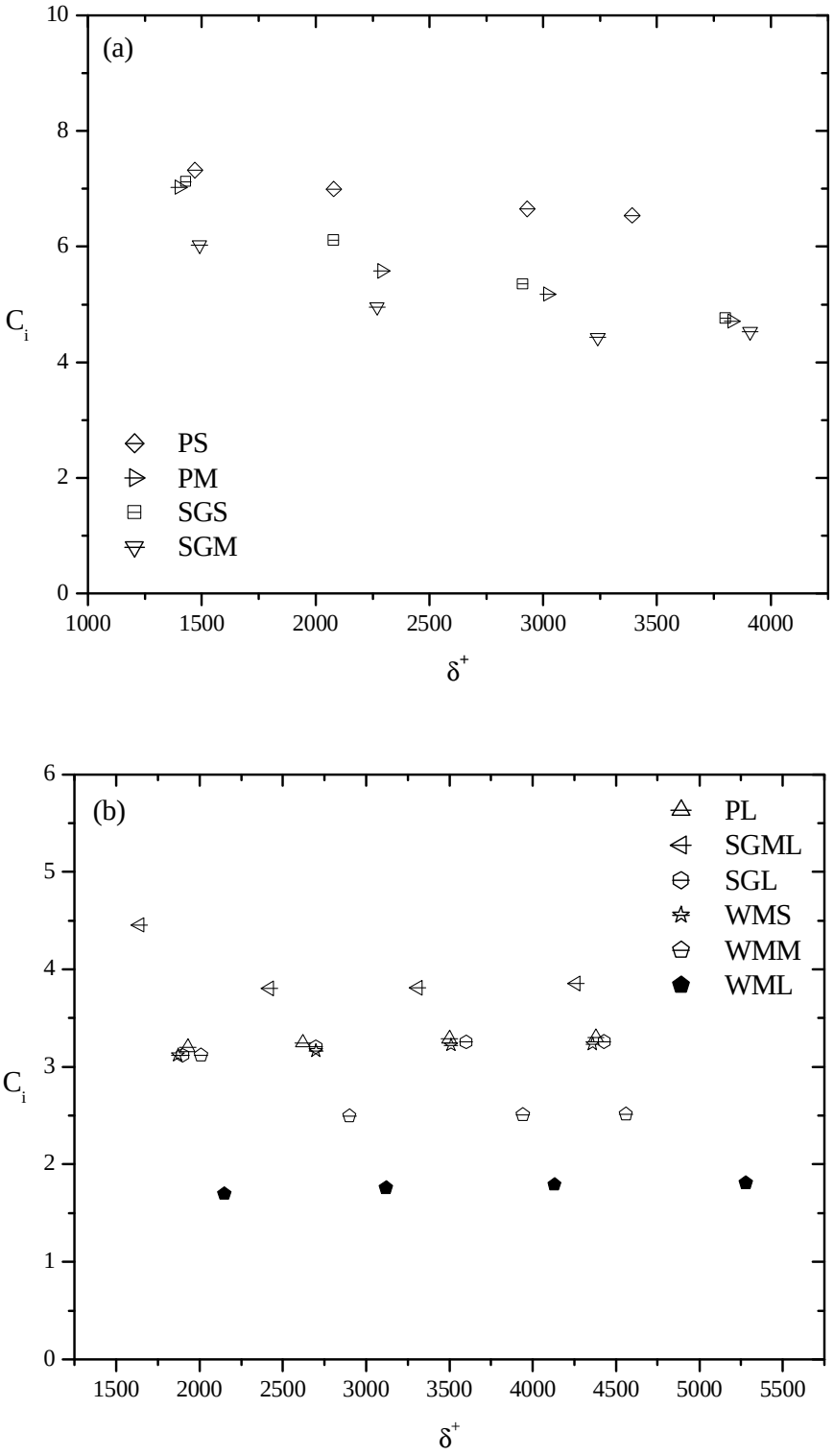

Figure 4.11: Variation of power law coefficient, C_i, with Reynolds number: (a) transitionally rough; (b) fully rough.

Reynolds number, δ^+, increases the power law coefficient, C_i, decreases. This behaviour is in contrast to that on the smooth surface. This is surprising since the characteristics of hydraulic smooth and transitionally rough flows depend on Reynolds number. Recall that δ^+ denotes the ratio of the outer- to inner-layer thickness, and represents the degree of shrinking of the latter. Figure 4.11b shows the distribution of the power law coefficient, C_i, obtained for fully rough flows for different Reynolds numbers. In general, the power law coefficient, C_i, increases as the Reynolds number, δ^+, increases. As shown in Figure 4.12a, the power law exponent, γ, for the transitionally rough flows increases with an increase in Reynolds number. However, for the fully rough flows, the power law exponent, γ, decreases as the Reynolds number increases. This behaviour is quite similar to that on the smooth surface. The behaviour of γ noted for the transitionally rough flows can be attributed to their characteristics which are yet to be fully understood. Overall, comparison between the values of the friction velocity obtained for the rough surfaces through the defect law and the power law profile fitting techniques shows that the values are within $\pm$ 3%.

4.3.1 Comparison between Logarithmic Law and Power Law

Figure 4.13a presents the mean velocity profiles on a smooth surface for four different Reynolds numbers using inner coordinates. Both power law (Eqn. (2.17)) and log law (with κ = 0.41 and B = 5.0) relations are included for comparison. For all four flow

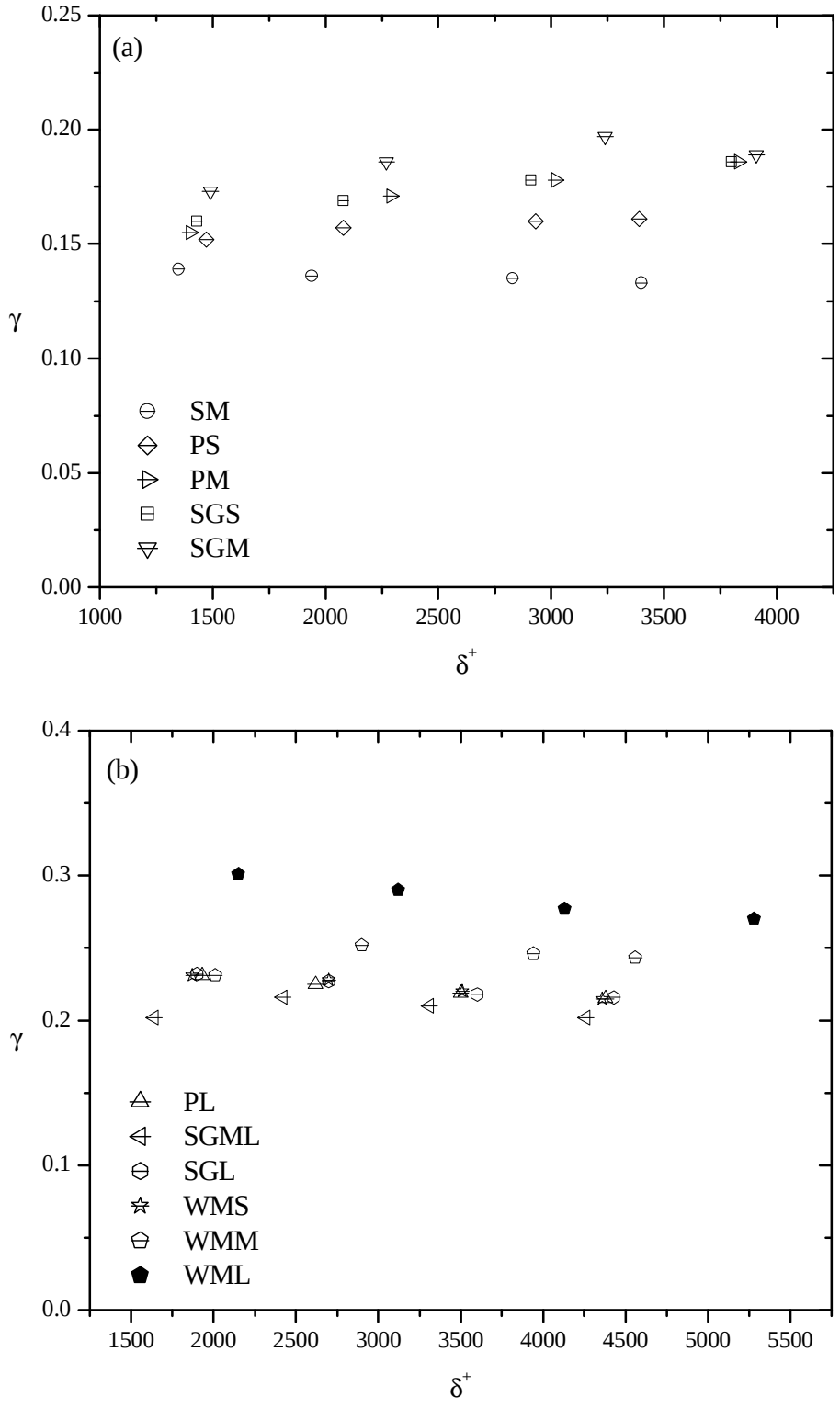

Figure 4.12: Variation of power law exponent, γ, with Reynolds number: (a) transitionally rough; (b) fully rough.

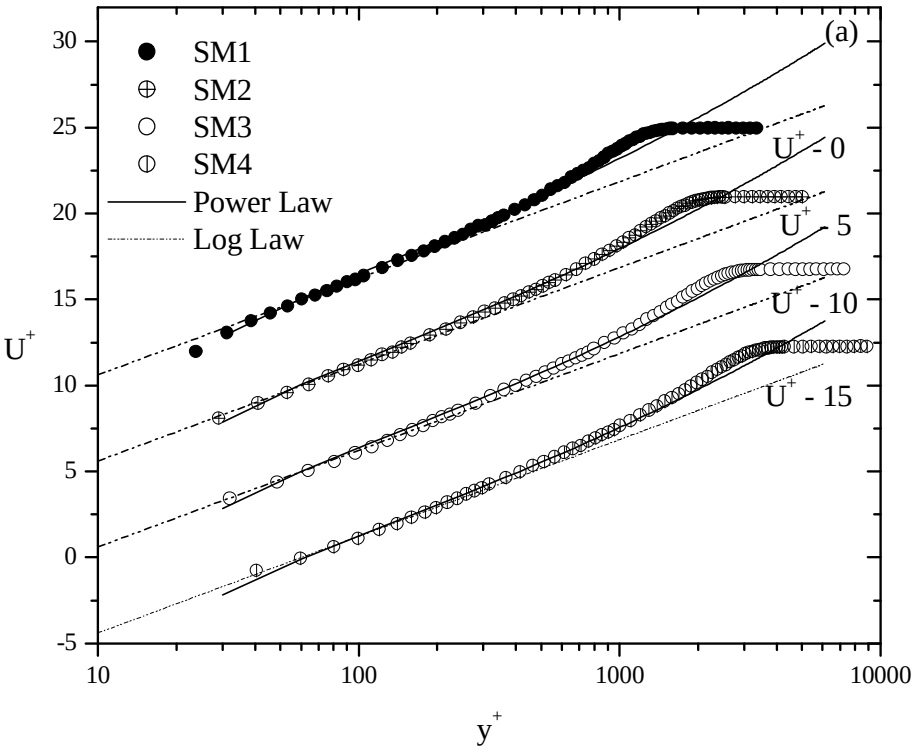

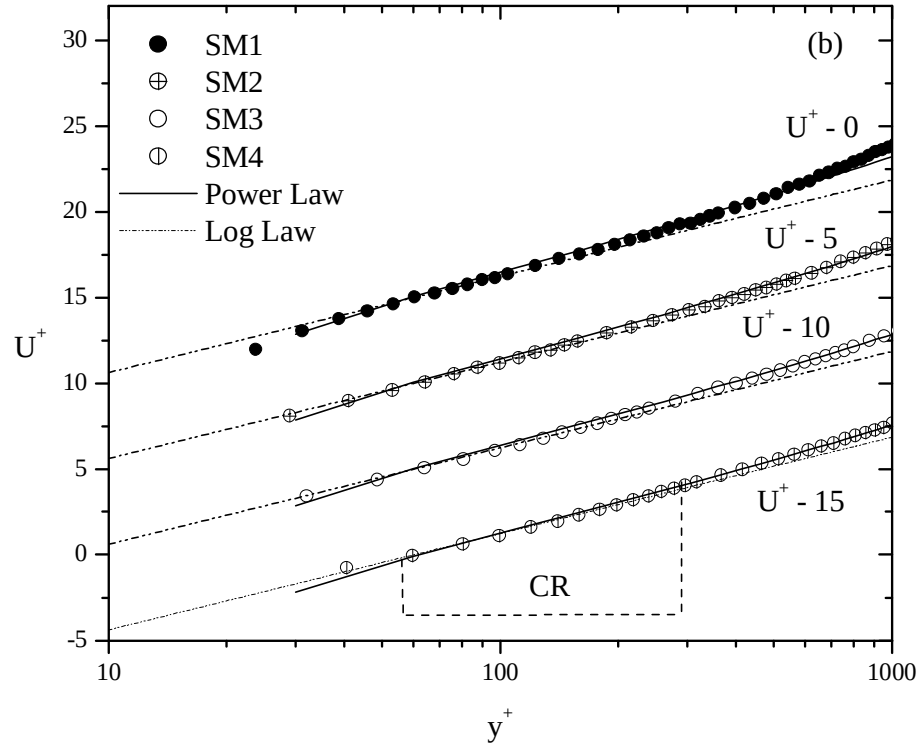

Figure 4.13: Mean velocity profiles for a smooth surface using inner coordinates: (a) overlap and outer regions; (b) overlap region.

conditions considered on the smooth surface (SM1, SM2, SM3, SM4), the lower limits of the power law velocity profiles (shown in Figure 4.13a) were observed to fall slightly below the log-law. Figure 4.13b shows the mean velocity profiles in the overlap region. It should be noted in the lower part of the overlap region, i.e. $50 < y^+ < 70$ (SM1) and $60 < y^+ < 300$ (SM4) in Figure 4.13b, the power and log law profiles are almost indistinguishable from each other. This is a common region (CR) within the overlap region, which is described by both the power law and log law relations. This observation is similar to that of Buschmann and Gad-el-Hak (2003). Evidently the region fitted by the log law is narrower compared to that of the power law. For example, in the case of SM4, the log law fitted the experimental data in the overlap region within $30 < y^+ < 300$, while the power law fitted within $60 < y^+ < 1000$. The extent of the common region increases as the Reynolds number increases. The mean velocity profiles for the highest Reynolds numbers using inner coordinates are shown in Figures 4.14a, 4.15a, and 4.16a for the perforated sheet, sand grain, and wire mesh surfaces, respectively. These figures demonstrate that the power law formulation describes the velocity profile in the overlap region over a wider range than the log law. In general, the velocity profile becomes more concave as the roughness increases at the lower part of the wake region. This characteristic can likely make the log law less suitable for estimating the skin friction on rough surfaces. The lower limits of the power law velocity profile for the nominal transitionally rough surfaces (PS4, PM4, SGS4, and SGM4) fall slightly below the log-law, which is similar to what observed on the smooth wall, whereas in the case of the fully rough surfaces, the lower limits fall on top of the log-law. It is interesting to note

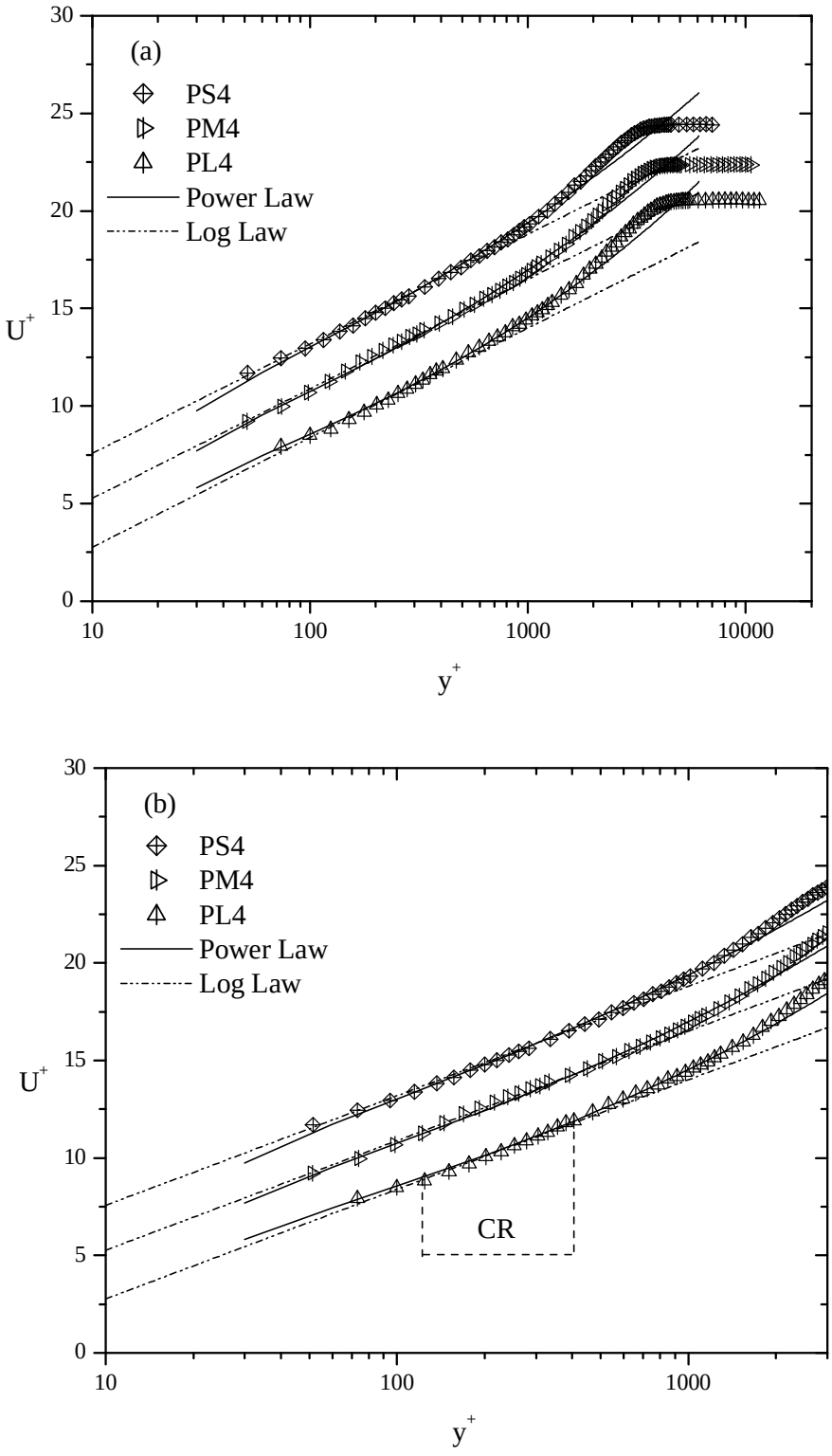

Figure 4.14: Mean velocity profiles for different perforated sheets using inner coordinates: (a) overlap and outer regions; (b) overlap region.

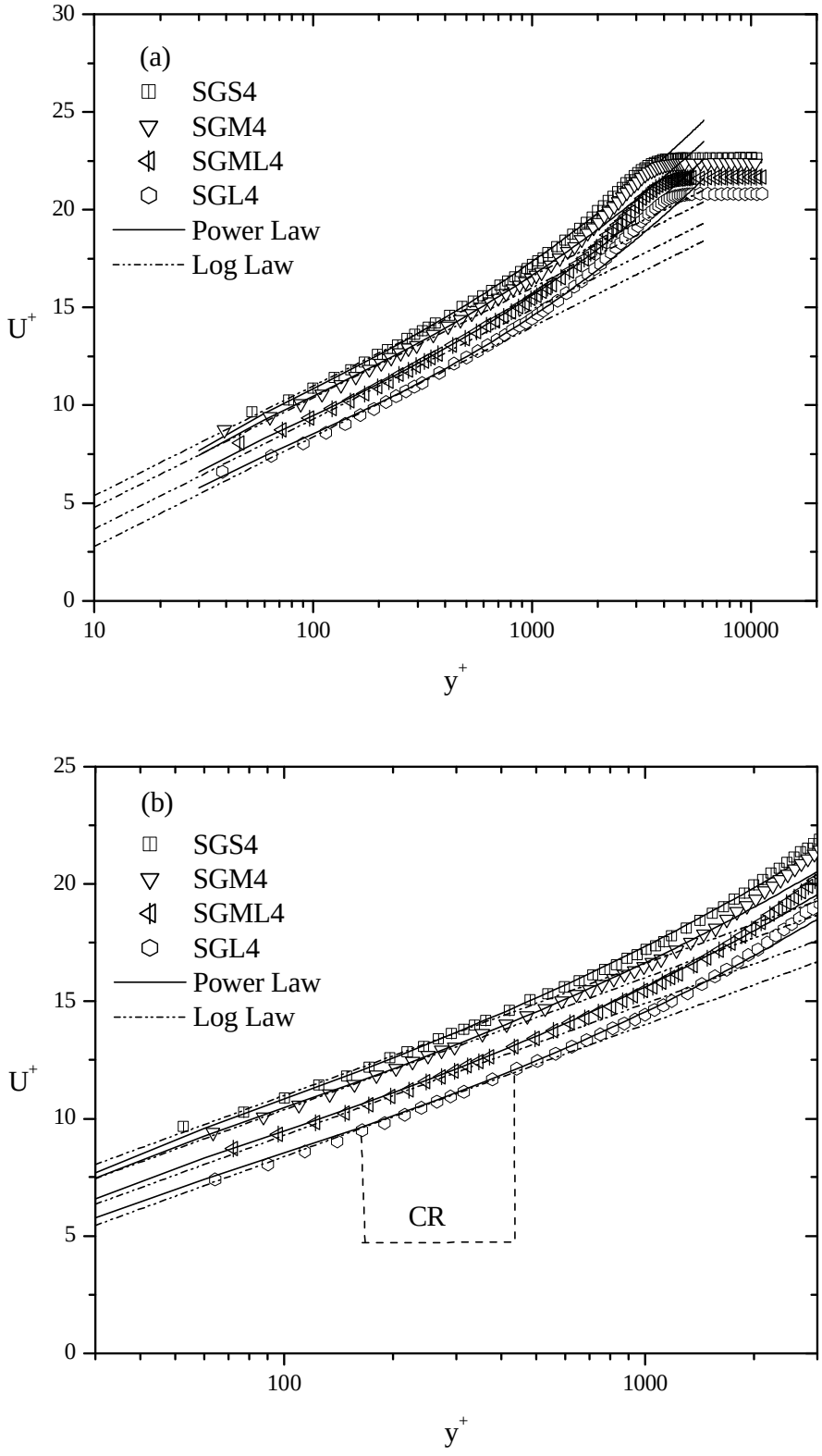

Figure 4.15: Mean velocity profiles for different sand paper grits using inner coordinates: (a) overlap and outer regions; (b) overlap region.

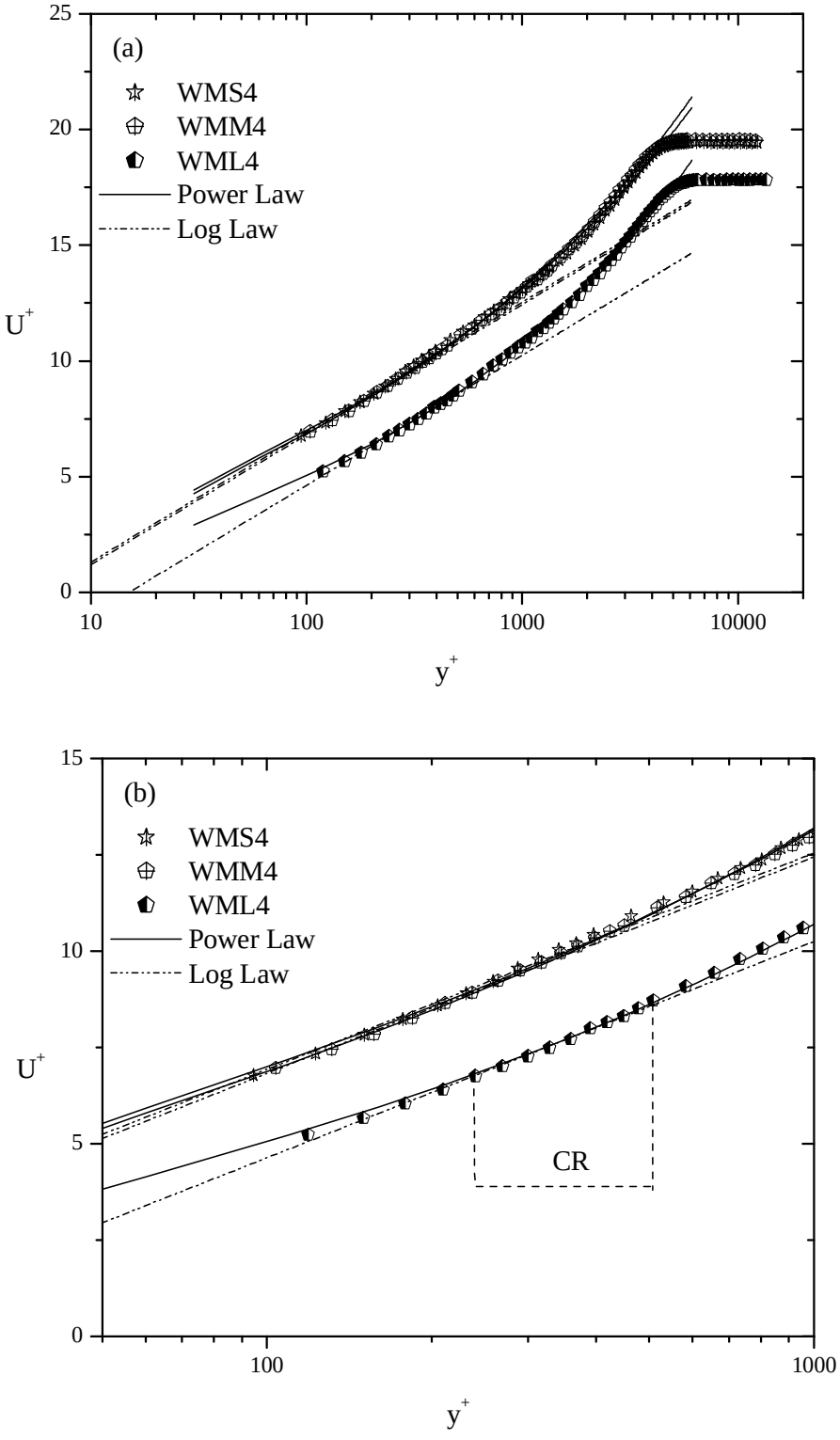

Figure 4.16: Mean velocity profiles for different wire mesh using inner coordinates: (a) overlap and outer regions; (b) overlap region.

that as the roughness shift increases, the lower limit of the power law becomes more concave (Figure 4.16). Figures 4.14b, 4.15b, and 4.16b show the mean velocity profiles in the overlap region for the perforated sheet, sand grain, and wire mesh surfaces, respectively. As noted in the case of a smooth surface, there is also a common region (CR) within the overlap region of the mean velocity profile on the surfaces, which is well described by both the power law and log law.

Figure 4.17a compares the mean velocity profiles on the smooth and rough surfaces at the highest Reynolds numbers using inner coordinates. The power law is able to adequately represent the velocity in the overlap region for all surfaces considered up to the inner region of the wake. This is consistent with the observation of Panton (2000) that power laws can extend into the inner region of the wake. Figure 4.17b shows the mean velocity profiles in the overlap region for hydraulically smooth (SM4), transitionally rough (SGS4), and fully rough (PL4 and WML4) flows. The roughness shift, ΔU^+, is determined at the location within the overlap layer that is described by both a power law and log law.

4.3.2 Behaviour of Power Law Coefficients on Different Surfaces

Figure 4.18a presents the variation of the power law coefficient, C_i, with the roughness shift in the nominal transitionally rough flow. Except for SGM, the values of the coefficient, C_i, for transitionally rough flow generally decrease as the roughness shift. The values of the coefficient, C_i, for different surfaces with approximately the same

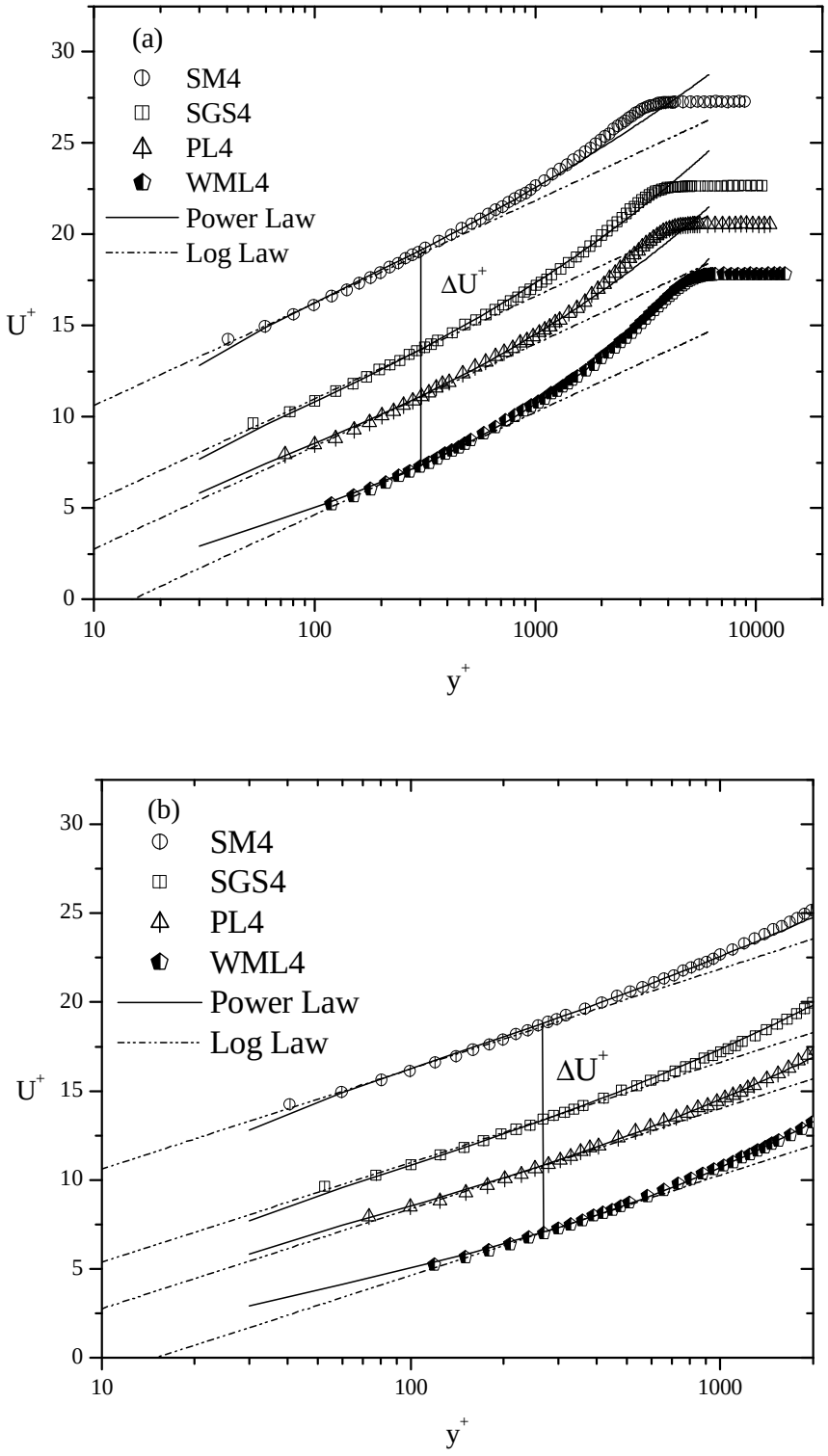

Figure 4.17: Mean velocity profiles for smooth and rough surfaces using inner coordinates: (a) overlap and outer regions; (b) overlap region.

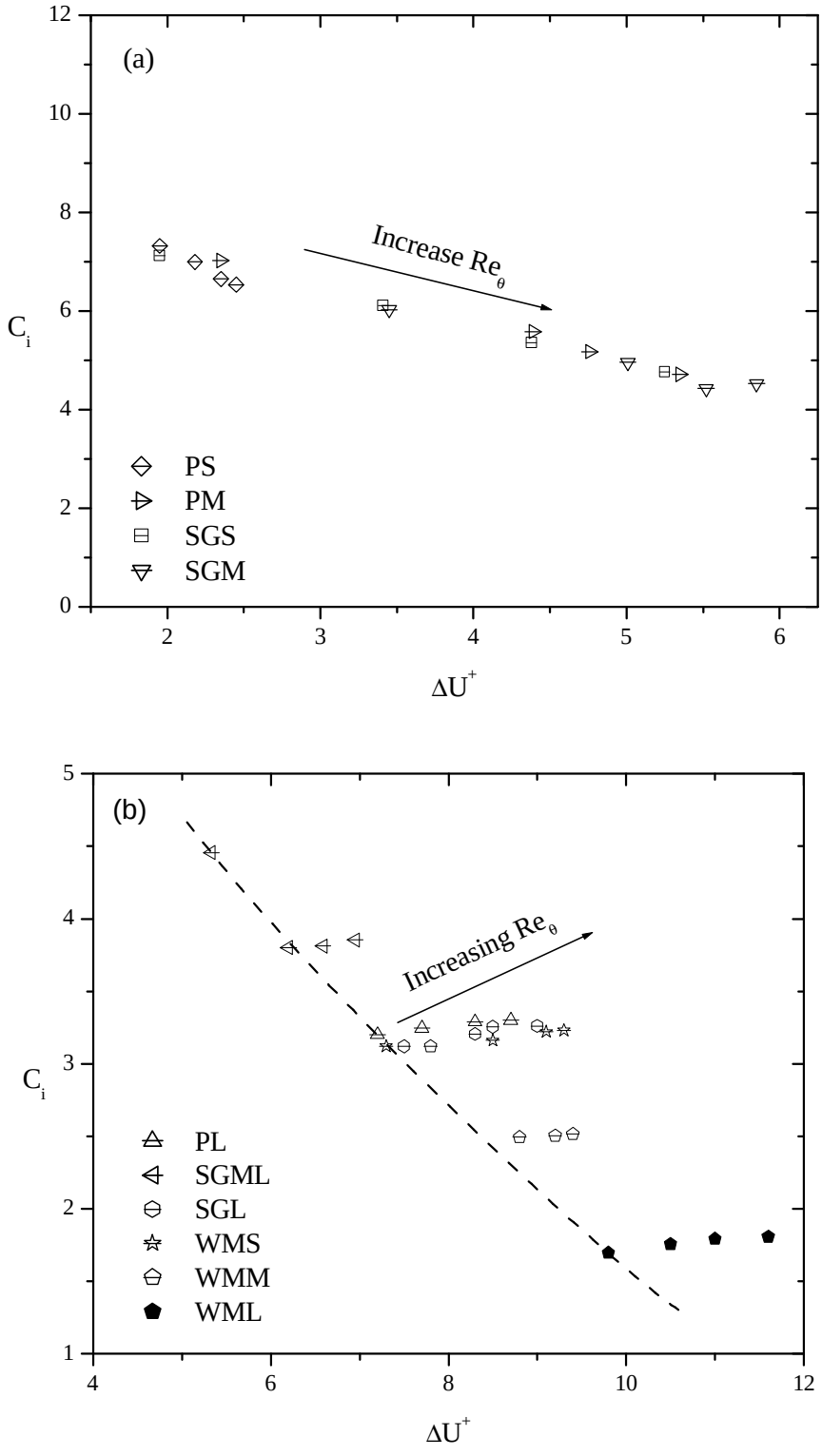

Figure 4.18: Variation of power law coefficient, C_i, with roughness shift: (a) transitionally rough; (b) fully rough.

roughness shift are approximately the same. Figure 4.18b shows the behaviour of the power law coefficient, C_i, with the roughness shift in the fully rough flow. The values of the coefficient, C_i, for SGML are included in Figure 4.18b, even though it only becomes fully rough at the highest Reynolds number. Although the k_{eq}^{+} values would classify it as nominally transitionally rough, the overall variation appears to better match that of the fully rough surfaces. For both the SGML and WMM, the values of the coefficient, C_i, initially decrease by 15% and 20%, and thereafter increase slightly with roughness shift. The values of the coefficient, C_i, for rough surfaces with approximately the same roughness shift are also found to be approximately the same. This observation further suggests that the value of the coefficient, C_i, for different surfaces having similar roughness shift is approximately the same, irrespective of surface geometry. In general, as the roughness shift increases, the coefficient, C_i, in the fully rough flow is observed to be slightly increasing. A careful examination on the dependence of C_i on the roughness shift shows that the increase of C_i for individual fully rough flow ranges between 0.8% and 6%. As such, the C_i values do vary over the range of roughness shift studied. As indicated in Figure 4.18b, C_i generally decreases as the roughness shift produced by different rough surfaces increases, suggesting the presence of an envelope at the lowest roughness shift for each surface considered.

Figure 4.19a presents the variation of the power law exponent, γ, with the roughness shift in the nominal transitionally rough flow. The values of γ generally increase as the roughness shift increases. This behaviour is quite opposite to the observation noted for hydraulically smooth and fully rough flows. As observed in the case of the coefficient, C_i, in the nominal transitionally rough flows, the values of γ for different rough surfaces with almost the same roughness shift are also approximately the same. Figure 4.19b shows the variation of the power law exponent, γ, with the roughness shift for the fully rough flow condition. In contrast to the behaviour of the transitionally rough flow, and SGML and WMM for which the exponent γ initially increases by 7% and 9%, respectively, the value of γ systematically decreases as the roughness shift increases. This behaviour is similar to that on the smooth surface. Kotey et al. (2003) reported similar observations for γ for hydraulically smooth and fully rough flows. The maximum variation for γ in each fully rough flow ranges between 3% and 11%. It is difficult to draw a definite conclusion as to whether the variation will continue to increase as the flow becomes rougher (i.e. for a higher roughness shift). From this present study, the variation suggests that the values of γ do vary with roughness shift. However, more experimental data are required to expand the range of γ and ΔU^+ in order to fully explore the variation of γ with an increase in rough shift, ΔU^+. The present experimental results show that, as flows over different rough surfaces become rougher, the power law exponent, γ, increases, suggesting an envelope at the lowest roughness shifts obtained for different rough surfaces considered, as indicated by the dashed line in Figure 4.19b.

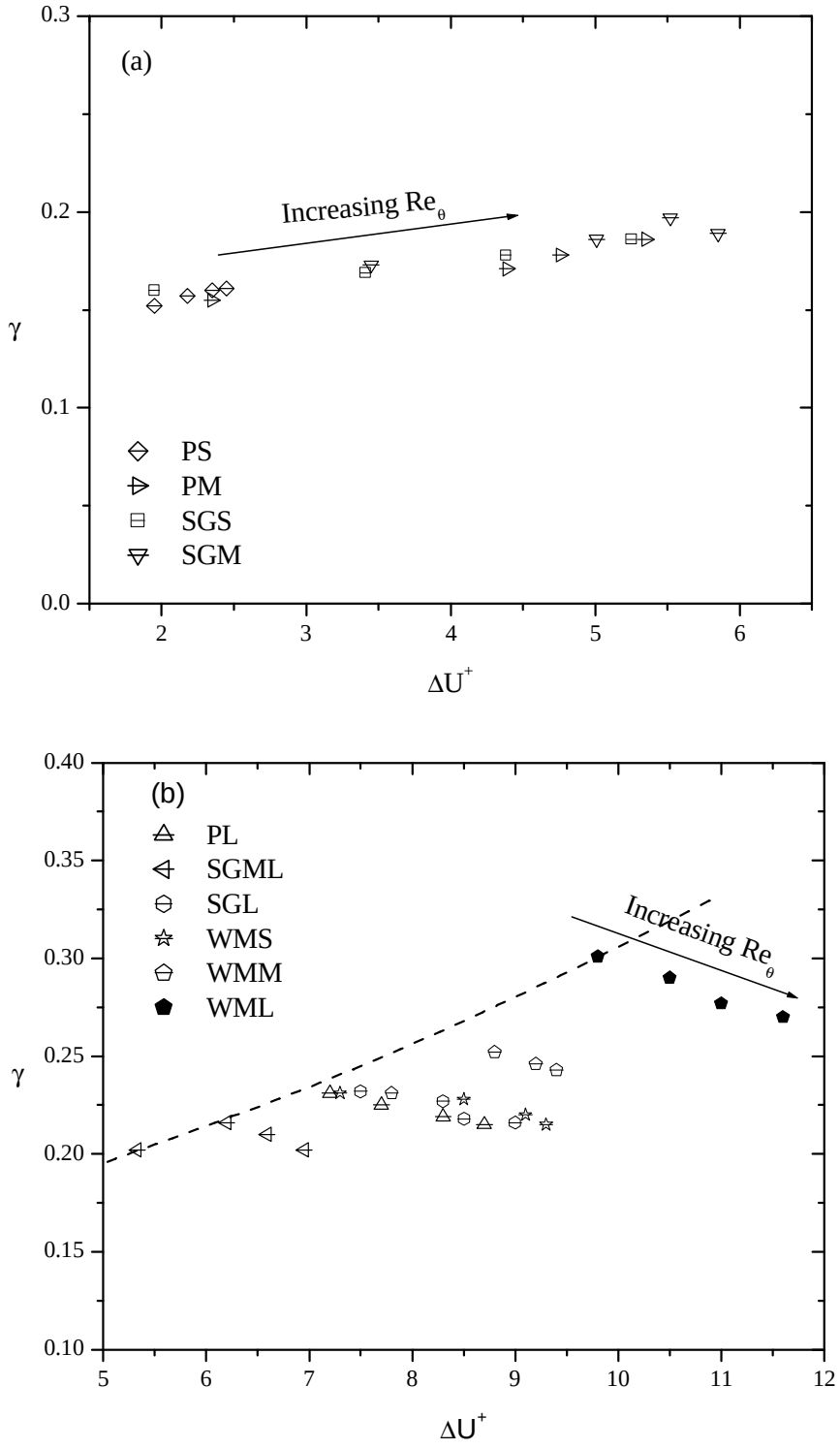

Figure 4.19: Variation of power law exponent, γ, with roughness shift: (a) transitionally rough; (b) fully rough.

4.3.3 Calibration of Power Law Coefficients for Transitionally Rough Flows

For the transitionally rough flow regime, the C_i and γ data sets for each surface appear to almost collapse onto a single curve as shown in Figures 4.20 and 4.21, respectively. In light of this, the following correlations are proposed for the transitionally rough flow regime:

$$C_i = -0.711(\Delta U^+) + 8.544 \tag{4.1}$$

and

$$\gamma = 0.0094(\Delta U^+) + 0.136 \tag{4.2}$$

An assessment of goodness-of-fit using a Chi-squared distribution at a 95 percent confidence level indicates that Eqs. (4.1) and (4.2) do an excellent job of correlating the experimental data over a Reynolds number range of $3810 \le \mathrm{Re}_\theta \le 10930$. The above correlations imply that the values of C_i and γ can be estimated from the knowledge of the roughness shifts for a wide range of Reynolds number and different surfaces exhibiting transitionally rough conditions. In the case of the fully rough flow regime, more experimental data sets for C_i, and γ are still required to establish the complete behaviour of the coefficients at the higher roughness shift, ΔU^+. The present study does suggest C_i remains approximately constant, and γ will continue to decrease, for a given surface as the roughness shift, ΔU^+, increases.

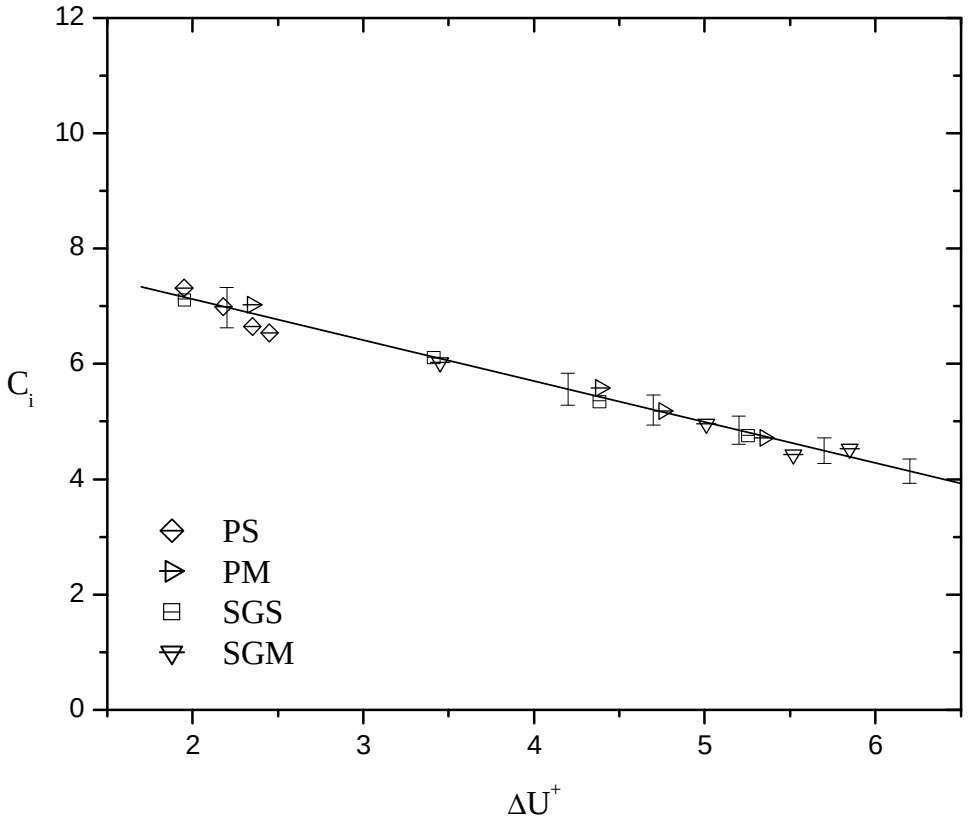

Figure 4.20: Relationship between the coefficient C_i and the roughness shift ΔU^+ in transitionally rough flows (solid line represents Eq. (4.1)).

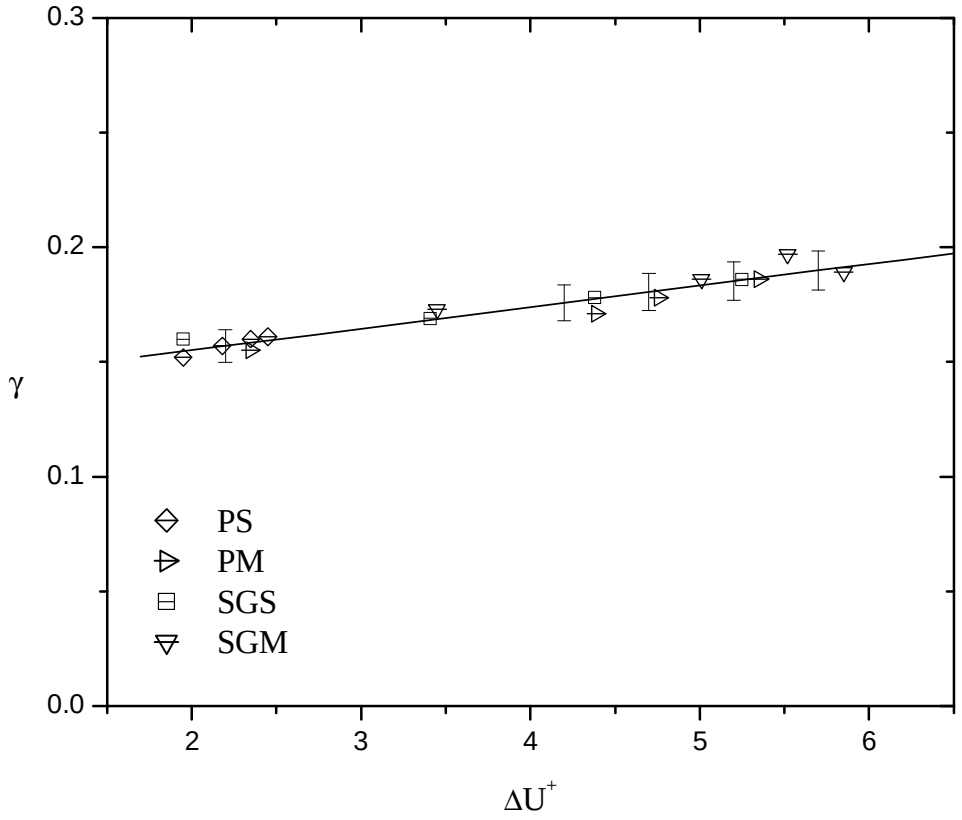

Figure 4.21: Relationship between the coefficient γ and the roughness shift ΔU^+ in transitionally rough flows (solid line represents Eq. (4.2)).

4.4 Skin Friction Correlation for Smooth and Rough Surfaces

Figure 4.22 compares the skin friction coefficient obtained for a smooth wall with the correlation proposed by Osaka et al. (1998) and the somewhat older but still widely used correlation of Coles (1962). Also included are the skin friction data of Purtell et al. (1981) and DeGraaff and Eaton (2000) obtained in a zero pressure gradient turbulent boundary layer at $460 \le \mathrm{Re}_\theta \le 5100$ and $1430 \le \mathrm{Re}_\theta \le 13000$, respectively. A comparison shows that the present skin friction values are in good agreement with the correlation of Osaka et al. (1998) as well as the experimental data of Purtell et al. (1981) and DeGraaff and Eaton (2000). At lower values of Re_θ, the correlation of Coles (1962) tends to be higher than the experimental data, although still just within the experimental uncertainty. It appears unlikely that the present data would trend up with increasing Re_θ to the same degree as that of DeGraaff and Eaton (2000).

In order to assess the friction velocity obtained by fitting to the defect profile, the relation between the shape factor and skin friction is presented in Figure 4.23. Both Bandyopadhyay (1987) and Furuya and Fujita (1967) used this method to indirectly check the skin friction obtained from a profile fitting technique. Furuya and Fujita (1967) plotted the relation between the shape factor, *H*, and skin friction as given in Eqn. (2.39); they used the value of G = 6.3 for a smooth surface and G = 7.0 for a rough surface. For these values of G, Eqn. (2.39) is plotted in Figure 4.23, together with the experimental data for smooth and rough wall flows. As clearly shown, the measurements closely align with each of the curves based on Eqn. (2.39). This gives confidence that the profile fitting technique performs correctly for both smooth and rough surfaces.

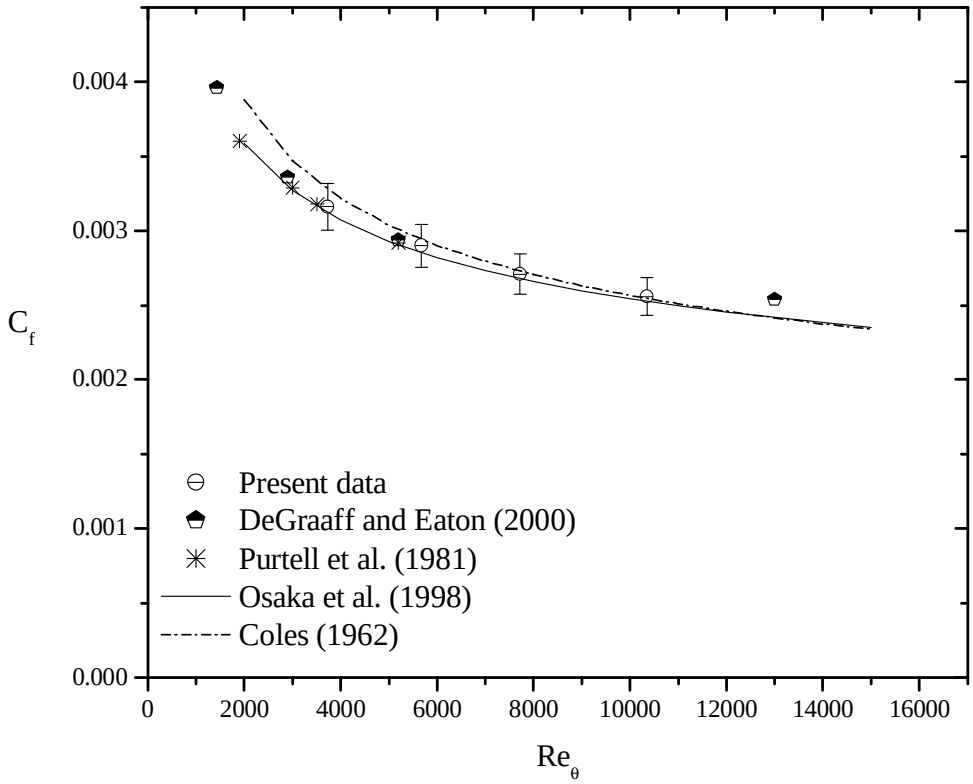

Figure 4.22: Variation of skin friction coefficient for a smooth surface with Reynolds number.

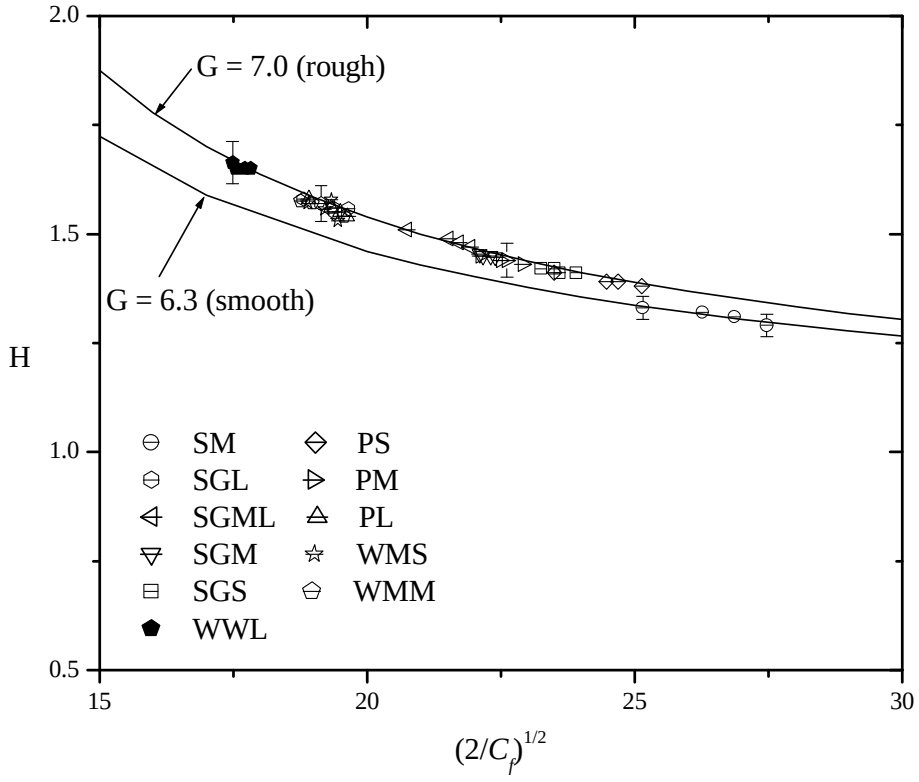

Figure 4.23: Relation of shape factor to skin friction coefficient.

Figure 4.24 presents the variation of the skin friction coefficient, C_f, for smooth and rough surfaces with Reynolds number. Figure 4.24a shows the behaviour of the skin friction coefficient, C_f, for the hydraulically smooth and nominal transitionally rough flows. In the latter case, the skin friction can be as much as 55% higher than that on the smooth surface. The behaviour of the skin friction on surfaces that exhibited a nominal transitionally rough flow regime varied. For example in the case of PS, the value of C_f decreased with Reynolds number, which is the same as for the hydraulically smooth surface. However, the C_f values for PM and SGM initially increase by 9% and 4%, respectively, and thereafter decrease as the Reynolds number increases. In the case of SGS, the skin friction coefficient, C_f, increases throughout with increasing Reynolds number although by a minimal amount. Given the measurement uncertainty of approximately ± 9%, the C_f values for PM, SGS, and SGM do not vary significantly over the range of Re_θ considered, whereas for PS a systematic decrease with Reynolds number is observed. The behaviour observed for PS can be linked to the small openness ratio, which enables it to show characteristics indicative of a hydraulically smooth surface.

Figure 4.24b presents the skin friction coefficient, C_f, for the hydraulically smooth and fully rough flows at different Reynolds numbers. Also included in Figure 4.24b is the skin friction coefficient data for SGML, which only becomes fully rough at

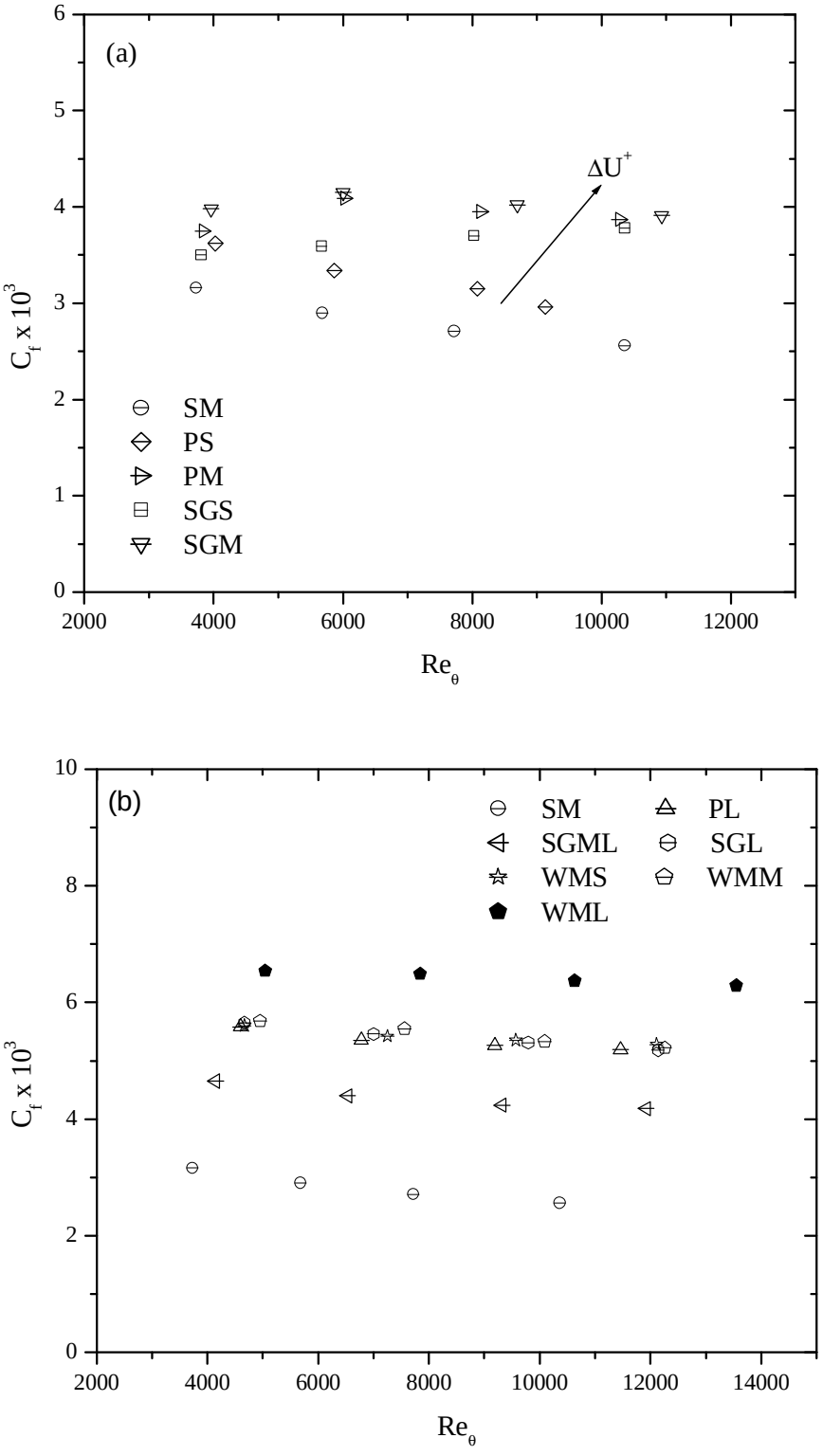

Figure 4.24: Variation of skin friction coefficient with Reynolds number: (a) smooth and transitionally rough; (b) smooth and fully rough.

the highest Reynolds number. Even though the k_{eq}^{+} values would classify it as nominal transitionally rough, the overall variation appears to better match that of the fully rough surfaces. The wire mesh (WML) exhibits the largest increase in C_f over the range of Reynolds numbers considered, almost 146% higher than that on the smooth surface. Again, the maximum variation in C_f for each surface is within or close to the experimental uncertainty. For the fully rough flows, each surface exhibits minimal variation of C_f with Reynolds number, although C_f varies greatly among the different surfaces.

Figure 4.25 presents the variation of the modified skin friction coefficient, $C_f^{1/2}/(\delta^*/\delta)$, with Reynolds number for the flows summarized in Tables 4.1 – 4.4. Also included are the skin friction coefficient data of DeGraaff and Eaton (2000) on a smooth surface, as well as that of Antonia and Krogstad (1993) on a wire mesh for Reynolds numbers ranging from 3120 to 22860. One immediately observes that the modified skin friction coefficient data for all the surfaces considered are confined within a narrow range of values, irrespective of Reynolds number. A possible explanation for the contribution of δ^*/δ will be given Chapter 5. Recalling Eqn. (2.41), the behaviour observed in Figure 4.25 implies that for the zero-pressure-gradient turbulent boundary layers considered, the ratio δ/Δ is approximately independent of both Reynolds number and surface roughness.

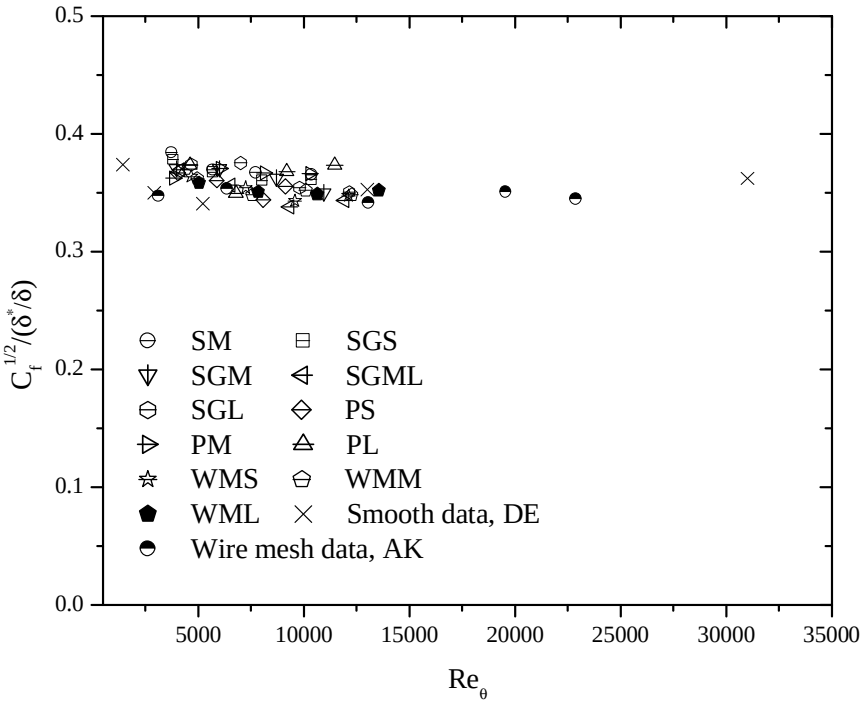

Figure 4.25: Variation of mixed skin friction coefficient for smooth and rough surfaces with Reynolds number (DE and AK denote DeGraaf and Eaton (2000) and Antonia and Krogstad (1993), respectively).

If this approximation is made, i.e. that δ/Δ is approximately constant and $C_f^{1/2}$ varies in a linear manner with δ^*/δ, and the experimental data are plotted for all surface conditions and Reynolds numbers, the behaviour shown in Figure 4.26 is obtained. In general, as roughness increases the value of the ratio δ^*/δ, the skin friction similarly increases. The skin friction coefficient data sets for each surface appear to collapse onto a linear curve for which the following correlation is proposed

$$c_f^{1/2} = (0.360 \pm 0.025)\left(\frac{\delta^*}{\delta}\right) \tag{4.3}$$

An assessment of goodness-of-fit using a Chi-squared distribution at a 95 percent confidence level indicates that Eqn. (4.3) does an excellent job of correlating the experimental data over a Reynolds number range of $1430 \le \mathrm{Re}_\theta \le 31000$. Note that the multiplicative constant in Eqn. (4.3) equals the average value of $C_f^{1/2}/(\delta^*/\delta)$ in Figure 4.24. The smooth wall skin friction data of DeGraaff and Eaton (2000), as well as the rough wall data of Antonia and Krogstad (1993), are also included in Figure 4.24, and show good agreement with the proposed correlation within the experimental uncertainty. The above correlation implies that the skin friction can be estimated from knowledge of the displacement and boundary layer thicknesses for a wide range of Reynolds number and different surface conditions.

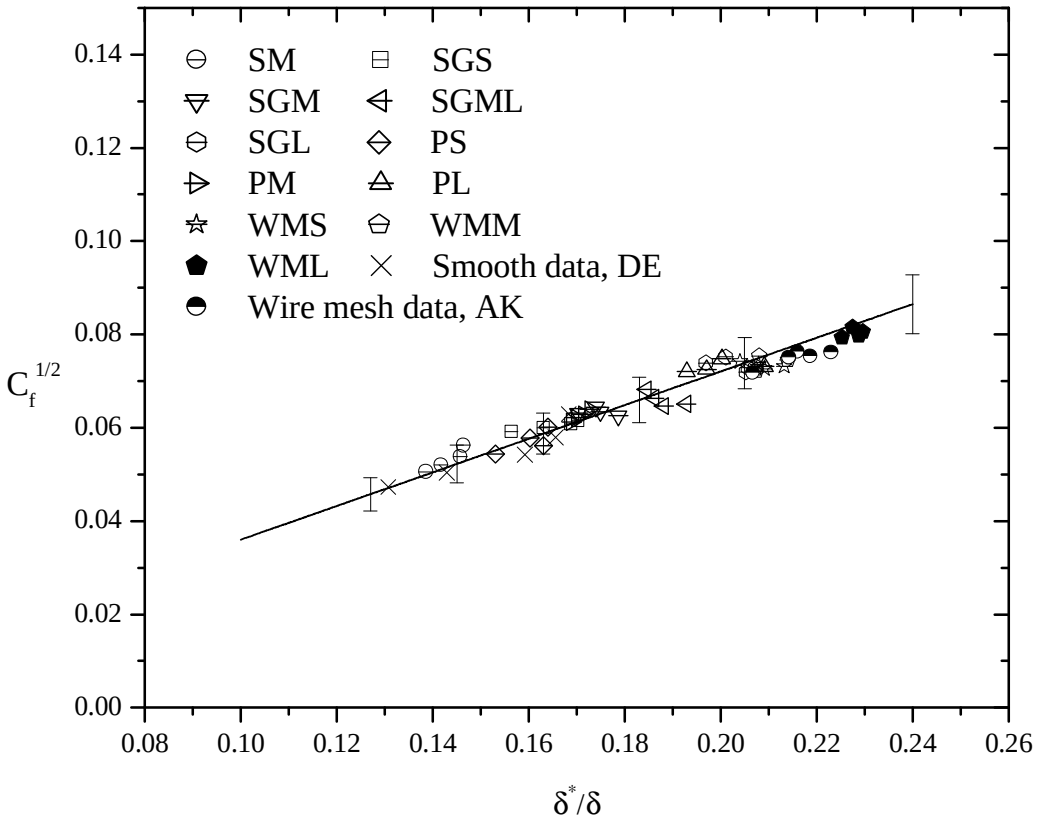

Figure 4.26: Variation of skin friction coefficient for smooth and rough surfaces with length scale ratio.

4.5 Summary

In this chapter, the experimental data for mean velocity obtained for smooth- and rough-wall turbulent boundary layers were reported. The physical size and geometry of the roughness elements and freestream velocity were chosen to encompass both transitionally rough and fully rough flow regimes. For both the smooth and rough surfaces, the velocity defect profile was fitted to the experimental data to determine the friction velocity and the strength of the wake. The power law proposed by George and Castillo (1997) was also employed to determine the friction velocity on the smooth and rough surfaces. The values of the friction velocity obtained from the skin friction laws derived from the power law were in good agreement with the corresponding values obtained from the velocity defect profile fitting technique. The value of the strength of the wake was observed to vary with roughness elements. The observations are at variance with the wall similarity hypothesis, which suggests that effects of the surface roughness should be confined to the roughness sublayer.

The present study identified a common region (CR) within the overlap region described by both the power law and log law. The power law formulation was able to fit the experimental data for smooth and rough surfaces over a greater extent than the logarithmic law. For both the hydraulically smooth and fully rough surfaces, it was observed that the power law coefficient, C_i , increases and exponent, γ, decreases as the Reynolds number increases. However, the situation is quite different for the transitionally rough flow regime, where C_i decreases and γ increases as the Reynolds number increases. The correlations for the coefficient C_i and exponent γ in the power

law relations for transitionally rough, which are based on roughness shift, are proposed. For the case of the fully rough, the correlations for the C_i and γ are left for future consideration.

A new skin friction correlation for zero pressure gradient turbulent boundary layers is proposed. The correlation has the advantage of predicting the skin friction in hydraulically smooth, transitionally rough, and fully rough flows. The length scale ratio, δ^*/δ, was employed to account for the effects of Reynolds number and surface roughness, such that the skin friction coefficient data collapse onto a single curve. This result is a further evidence of the special role of the length scale ratio δ^*/δ in scaling the velocity field in turbulent boundary layers. A more comprehensive assessment of the validity of the correlation requires further investigation using other types of surface geometries and a wider range of Reynolds number based on boundary layer thickness.

CHAPTER 5

OUTER SCALING OF MEAN FLOW ON SMOOTH AND ROUGH SURFACES

5.1 Introduction

In the previous chapter, scaling laws for the overlap region of the mean velocity profile were carefully examined. In this chapter, attention is now turned to the scaling of the mean velocity in the outer region of a turbulent boundary layer, within the context of achieving self-similarity for smooth and rough surfaces. Different scaling parameters, namely, the friction velocity, U_τ, freestream velocity, U_e, and a mixed outer scale, $U_e\delta^*/\delta$, are used to examine the effects of Reynolds number and surface roughness on the mean defect profiles obtained for hydraulically smooth, transitionally rough, and fully rough flow regimes using different surface geometries. The behaviour of the length scale ratios, δ^*/δ and θ/δ, with respect to the equivalent sand roughness Reynolds number, k_{eq}^+, are also examined. Finally, assessment of the effect of surface roughness on the mean flow in the outer region using the scaling parameters noted above is discussed.

5.2 Mean Velocity Profiles in Outer Coordinates

Figure 5.1 presents the mean velocity profiles obtained for a smooth surface at different Reynolds numbers using outer coordinates. The mean velocity profile for SM4 is about 2 % deviated from the SM3 in the overlap region. Figures 5.2a, 5.2b, and 5.2c show the mean velocity profiles obtained for perforated sheets of different sheet thickness and circular hole diameter at different Reynolds numbers using outer coordinates. Recall that both PS and PM exhibit nominal transitionally rough flows, while fully rough flows are obtained on PL. The flows over all perforated sheets appear to be independent of Reynolds number. Figure 5.2d compares the mean velocity profiles at approximately the same freestream velocity for perforated sheets with different surface roughness at the highest Reynolds number using outer coordinates. It is observed that, as the roughness density increases, the mean velocity profile becomes “less full”. Note that the mean velocity profiles for PM4 and PL4 fail to collapse onto each other, even though they have the same roughness height. This observation further shows that not only roughness height, but other geometrical factors are important in determining of the effect of the roughness on the mean flow.

Figures 5.3a, 5.3b, and 5.3c present the mean velocity profiles for the sand grain surface with different roughness heights and different Reynolds numbers using outer coordinates. The mean velocity profiles on the SGS and SGM appear to be independent of Reynolds number. This observation is surprising since the characteristics of transitionally rough flows depend on both Reynolds number and the equivalent sand

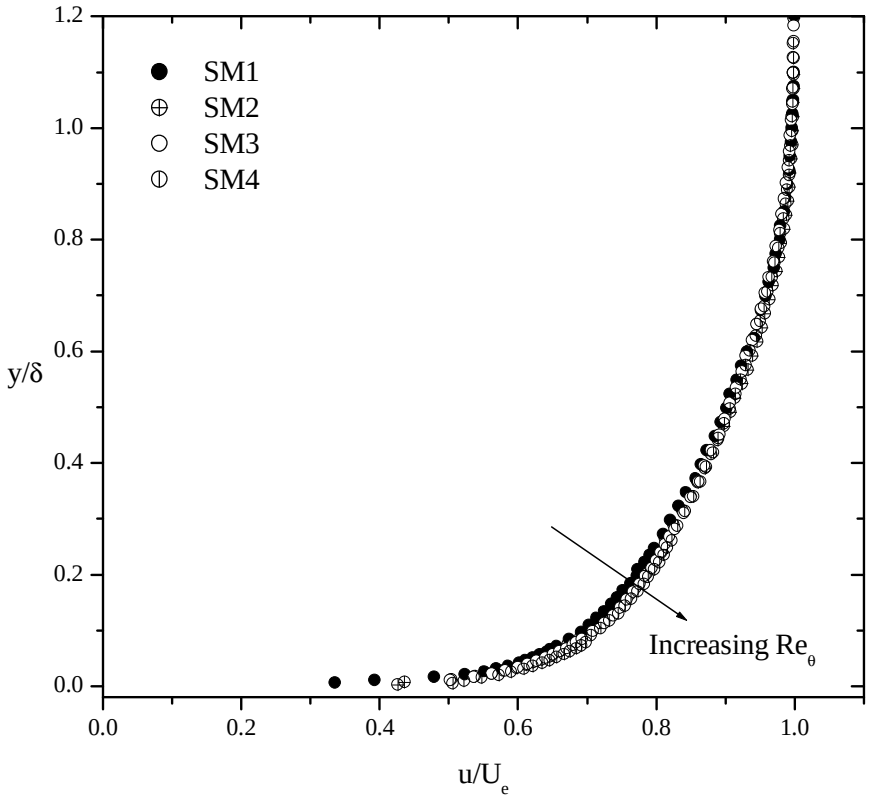

Figure 5.1: Mean velocity profiles for a smooth surface using outer coordinates.

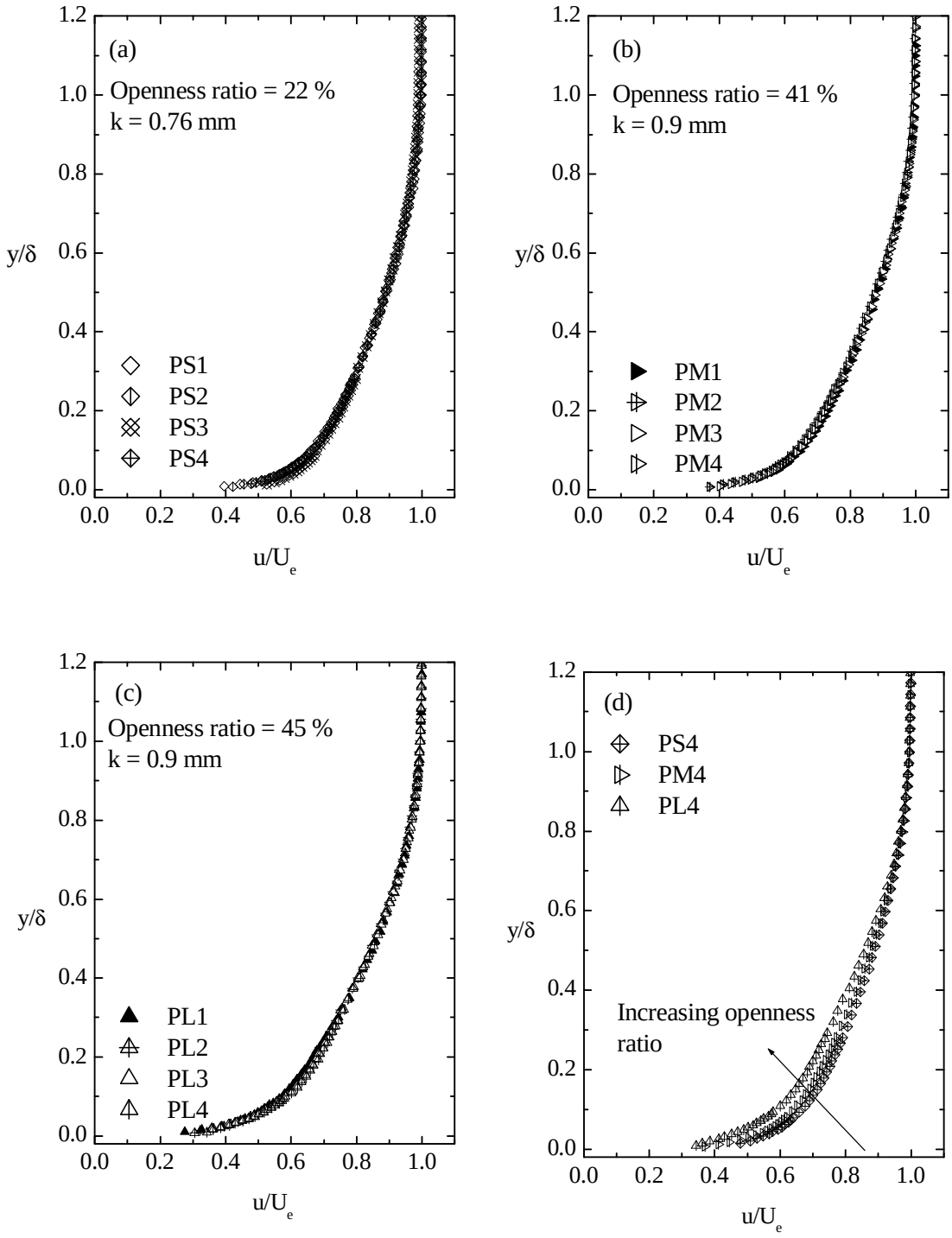

Figure 5.2: Mean velocity profiles on perforated sheet in outer coordinates

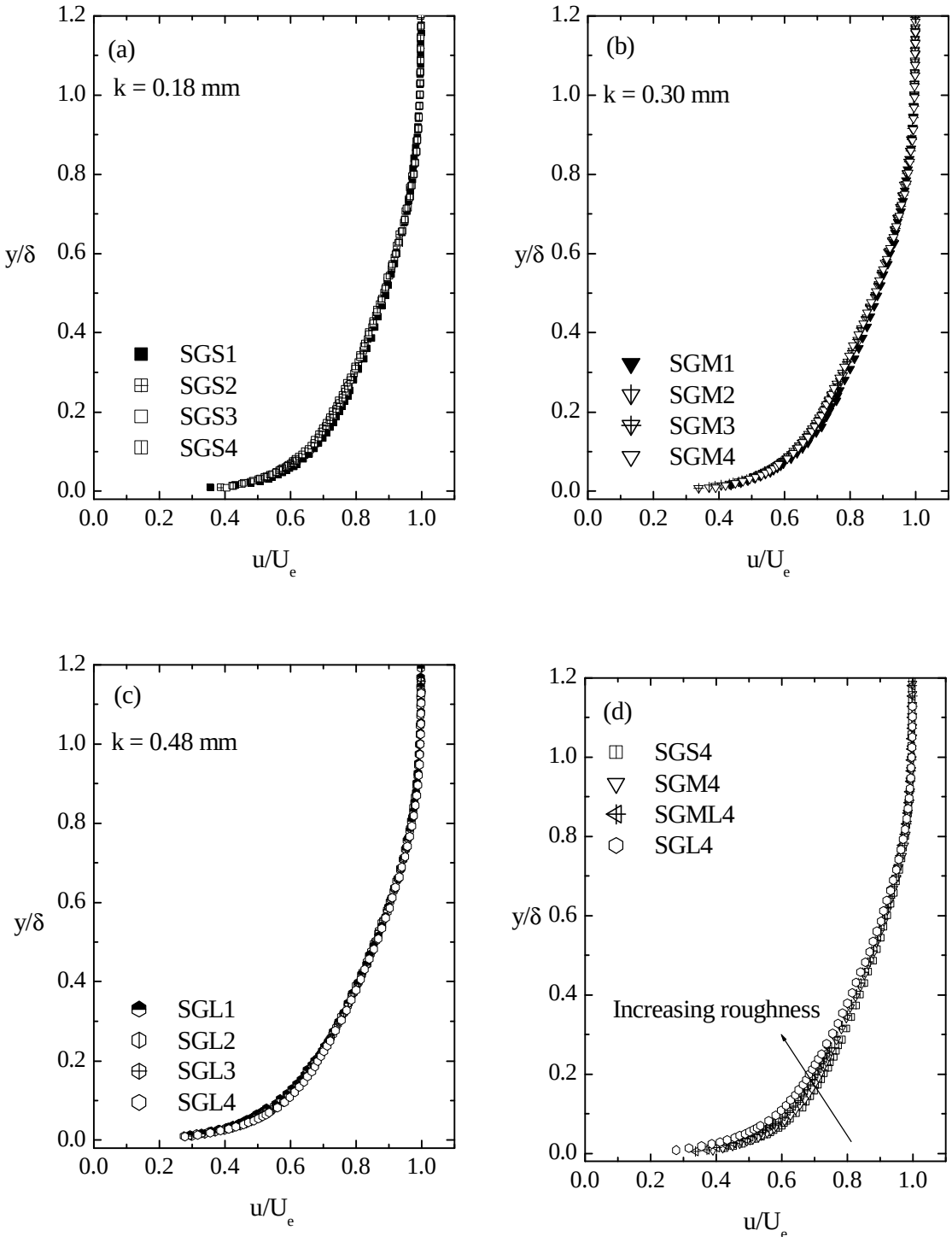

Figure 5.3: Mean velocity profiles on sand grain surfaces in outer coordinates

roughness Reynolds number, k_{eq}^{+}. Recall that the flows on both SGS and SGM are nominal transitionally rough. For the flows on SGL, which are fully rough, the mean velocity profiles appear to collapse onto each other, indicating they are independent of the Reynolds number. Figure 5.3d compares the mean velocity profiles at approximately the same freestream velocity for sand grain surfaces with different roughness height at the highest Reynolds number in outer coordinates. It is noted that as the roughness height increases, the mean velocity profile becomes "less full".

Figures 5.4a, 5.4b, and 5.4c show the mean velocity profiles for the wire mesh surfaces for different diameter and openness ratio at different Reynolds numbers using outer coordinates. Recall that the flows over all the wire mesh surfaces considered are fully rough. Any effect of Reynolds number is minimal as all the mean velocity profiles appear to collapse onto a single curve. Figure 5.4d compares the mean velocity profiles at approximately the same freestream velocity for wire mesh of different surface density at the highest Reynolds number using outer coordinates. Again, as the roughness shift increases, the mean velocity profile becomes "less full".

Figures 5.5a and 5.5b present the mean velocity profiles for smooth and rough surfaces at the highest Reynolds number using outer coordinates. Figure 5.5a shows the mean velocity profiles for smooth and nominal transitionally rough flows (based on k_{eq}^{+} values), while fully rough flows are presented in Figure 5.5b. The effect of surface

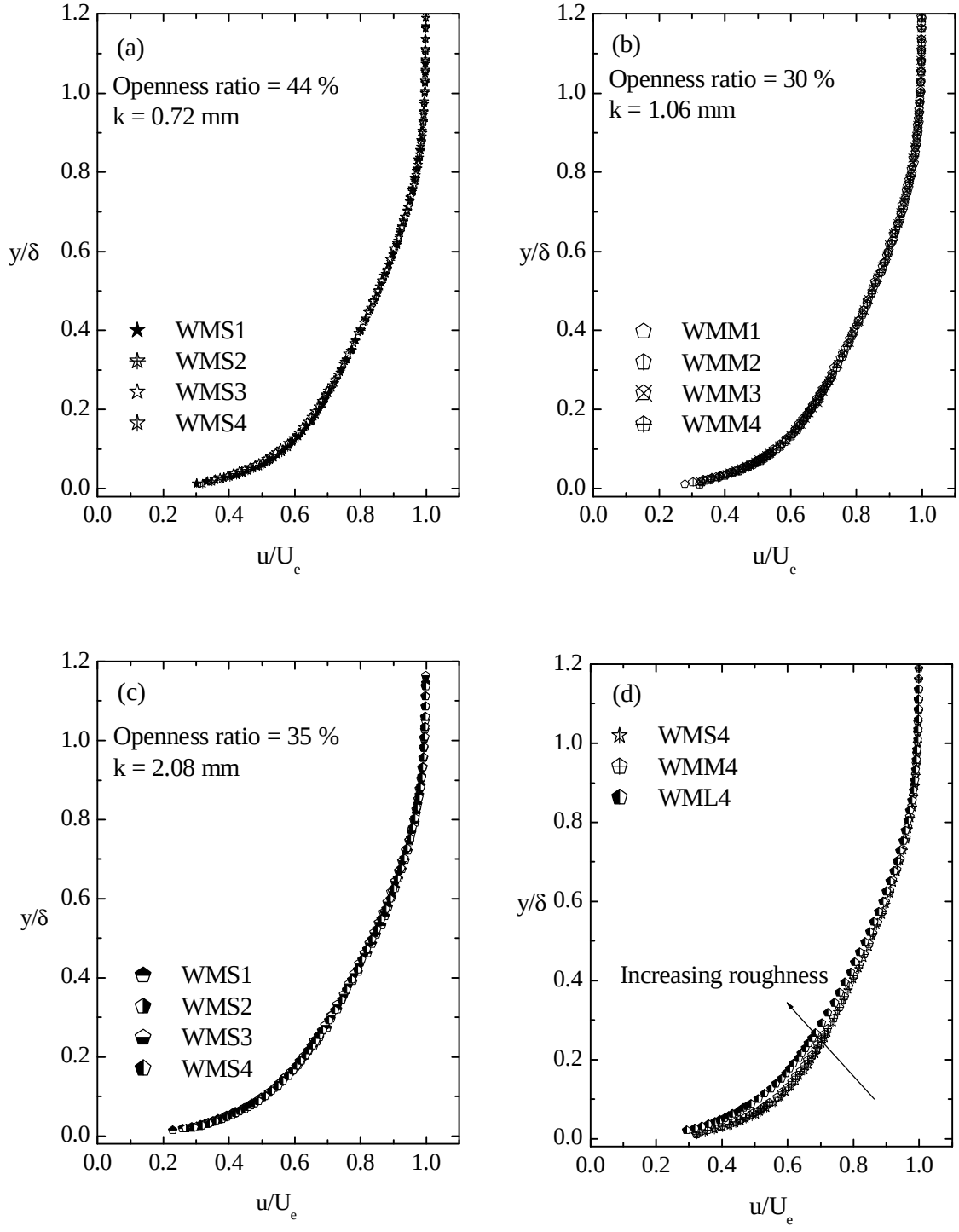

Figure 5.4: Mean velocity profiles on wire mesh surfaces in outer coordinates

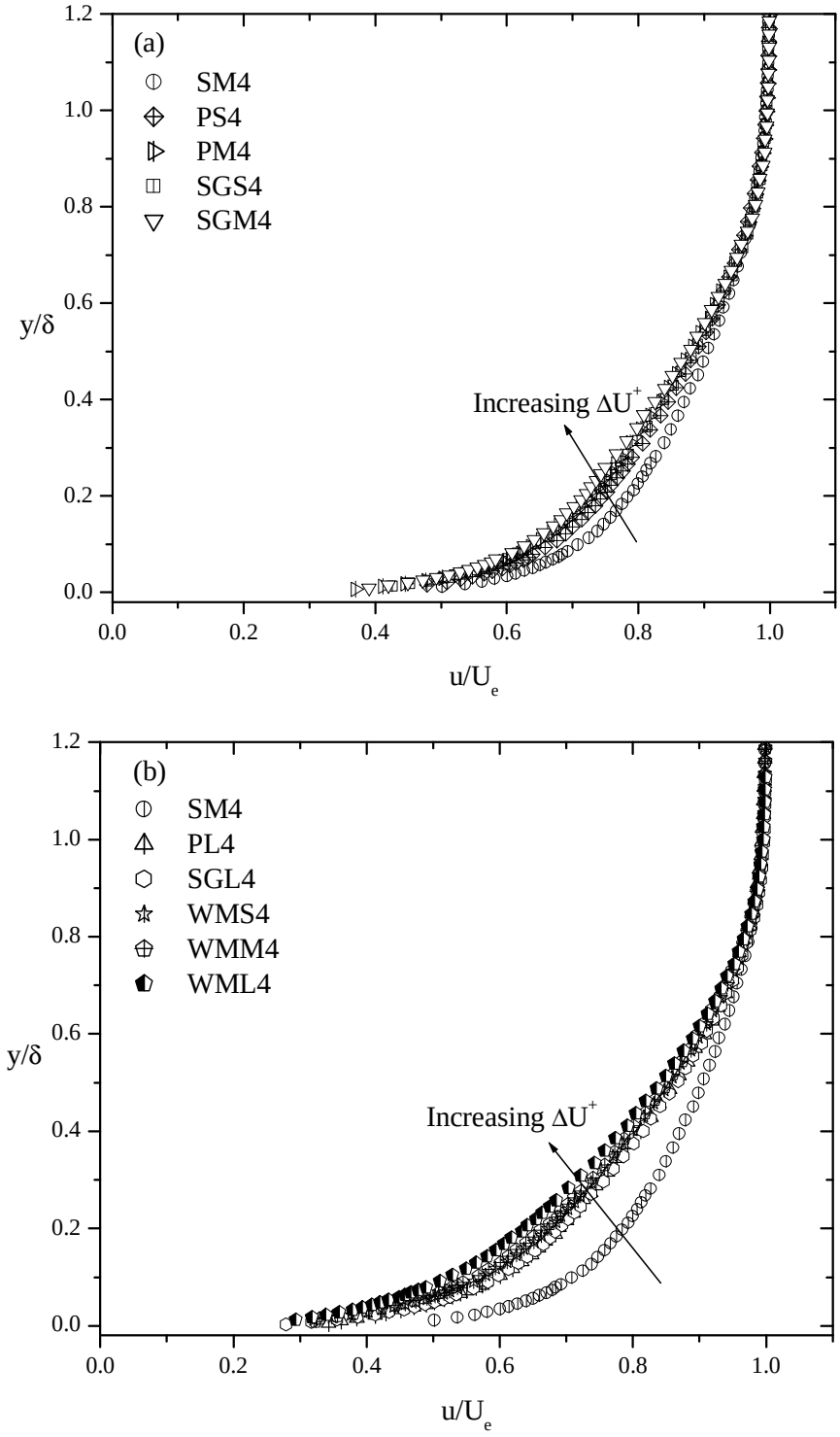

Figure 5.5: Mean velocity profiles using outer coordinates: (a) smooth and transitionally rough; (b) smooth and fully rough.

roughness increases the skin friction drag, which causes the mean flow on a rough surface to be more retarded when compared to that on a smooth surface. As indicated in Figures 5.5a and 5.5b, the fully rough flow exhibits a higher deviation from the smooth profile than the transitionally rough flow.

5.3 Effects of Reynolds Number and Surface Roughness on Mean Velocity Defect Profiles

As previously mentioned in the introduction, for the outer layer, the presence of the wall causes the retardation of the flow, leading to a reduction of the local velocity below the freestream velocity in a manner independent of viscosity but dependent upon wall shear stress, boundary layer thickness, and freestream pressure gradient. In light of this, the mean velocity profile is characterized by the velocity defect $(U_e - U)$ due to the momentum loss. In this section, the use of these three velocity scales, i.e. the friction velocity, U_τ , freestream velocity, U_e , and mixed outer velocity scale, $U_e\delta^*/\delta$, are critically examined to collapse the mean velocity data in the outer region of a turbulent boundary layer for hydraulically smooth, transitionally rough and fully rough flow regimes. The effectiveness of each scaling is evaluated both with respect to Reynolds number and surface condition.

5.3.1 Scaling with Friction Velocity

Figure 5.6 presents the mean velocity defect profiles for hydraulically smooth conditions, where the friction velocity, U_τ, and the boundary layer thickness, δ, are used to scale the velocity and wall-normal distance, respectively. The mean velocity defect

profiles at different Reynolds numbers appear to approximately collapse onto each other, as shown in Figure 5.6. This suggests that Reynolds number similarity can be achieved for the mean velocity defect profiles on a smooth wall when scaled with the friction velocity.

Figures 5.7a, 5.7b, and 5.7c present the mean velocity defect profiles obtained for perforated sheet surfaces of different sheet thickness and circular hole diameter at different Reynolds numbers. As observed in the case of a smooth surface, for each perforated sheets, the mean velocity defect profiles at different Reynolds numbers approximately collapse onto each other with maximum deviation of approximately 2 % observed for PS case. This observation supports of the use of the friction velocity as a scaling parameter for Reynolds number similarity. Figure 5.7d compares the mean velocity defect profiles at approximately the same freestream velocity obtained on perforated sheet surfaces of different surface roughness at the highest Reynolds number. The effect of surface roughness is not noticeable as the defect profiles approximately collapse onto a single curve.

Figures 5.8a, 5.8b, and 5.8c show the mean velocity defect profiles for the sand grain surfaces with different roughness heights at different Reynolds numbers. Based on the equivalent sand grain roughness Reynolds number, k_{eq}^{+}, both SGS and SGM exhibit nominal transitionally rough flows, while fully rough flows were achieved on SGL. For the SGL, the mean velocity defect profiles at different Reynolds numbers approximately

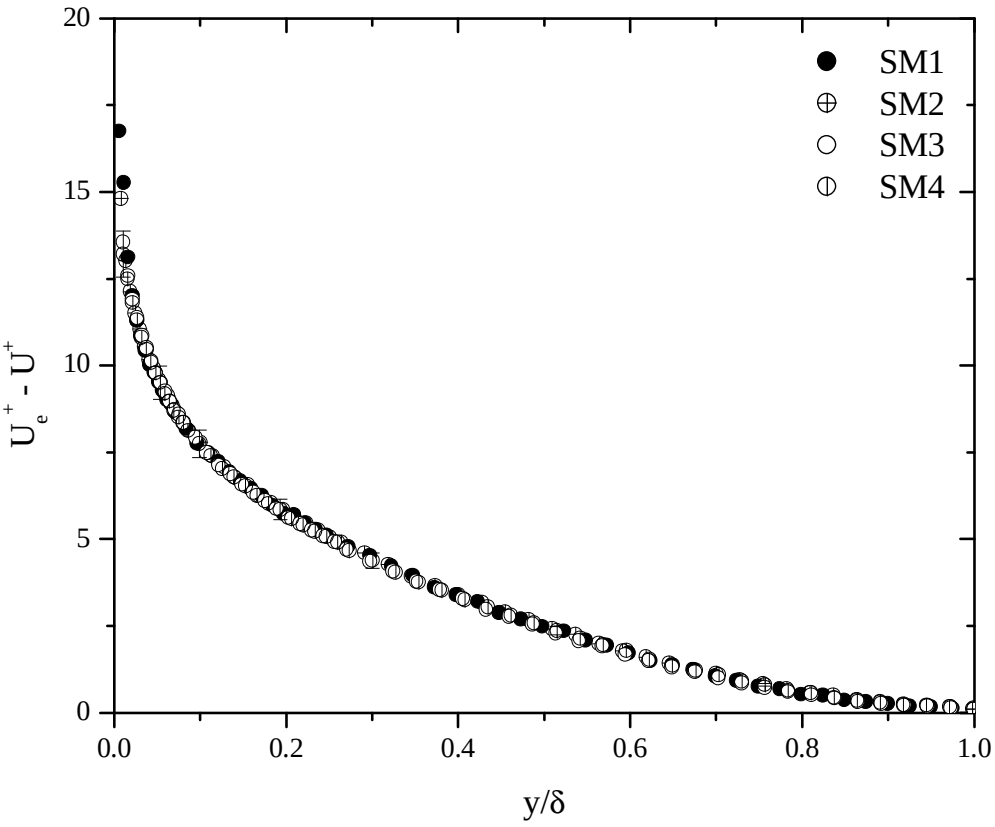

Figure 5.6: Mean velocity defect profiles scaled with friction velocity on a smooth surface.

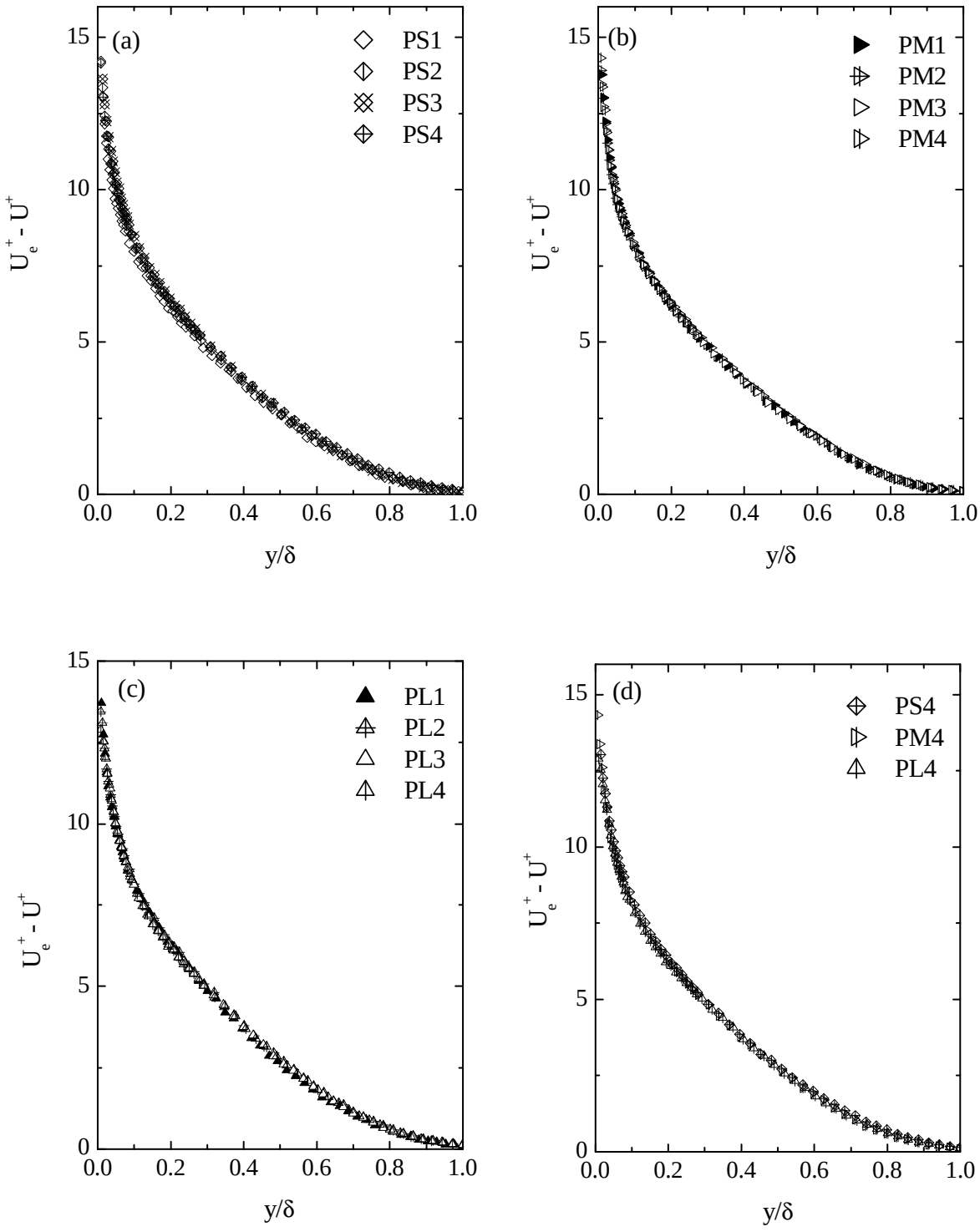

Figure 5.7: Mean velocity defect profiles scaled with friction velocity on perforated sheets.

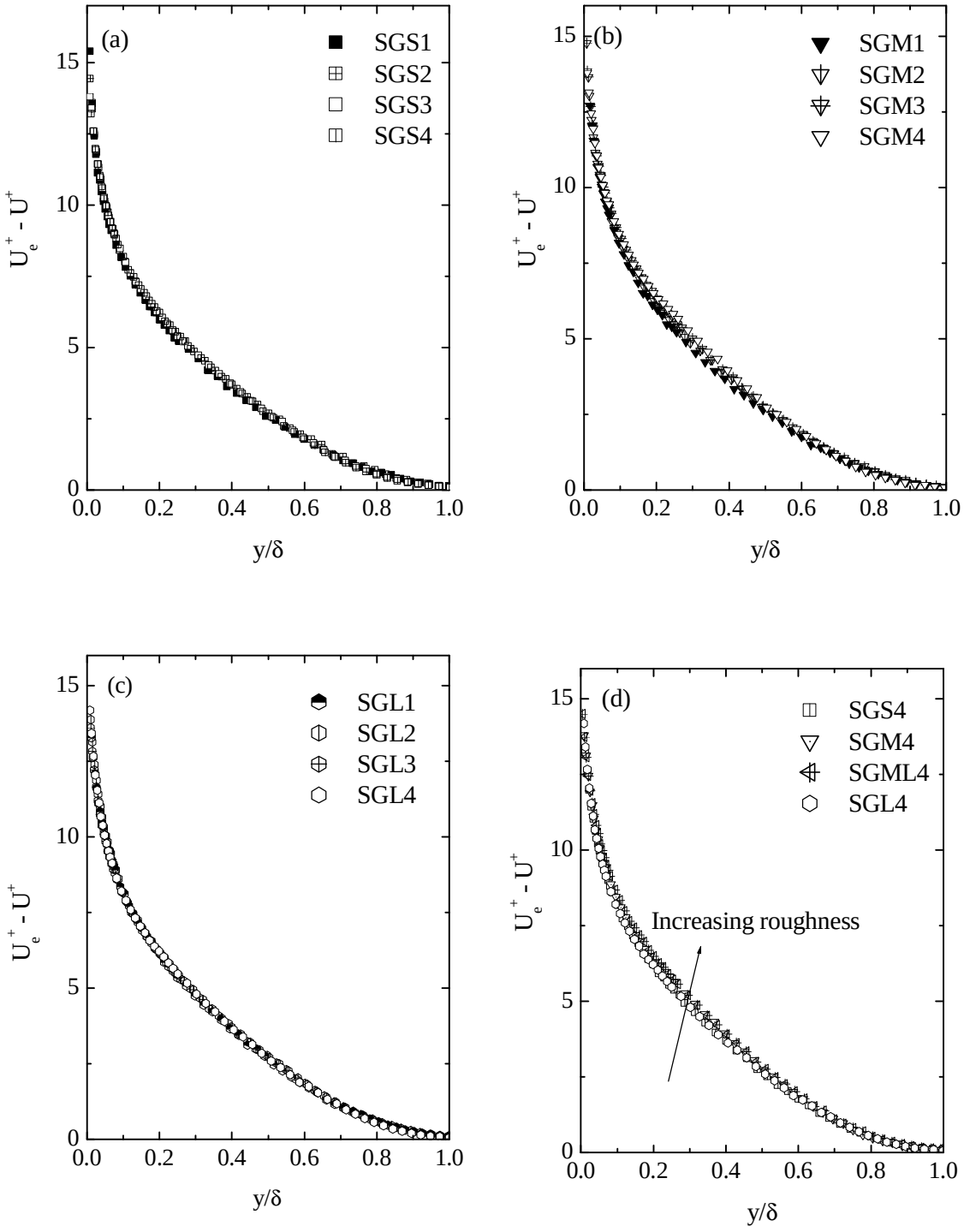

Figure 5.8: Mean velocity defect profiles scaled with friction velocity on sand grain roughness.

collapse onto each other, suggesting that flows over this surface exhibit Reynolds number similarity. Bergstrom et al. (2002) reported similar observations for fully rough flows obtained on sand grain roughness. However, this observation is not noticed for SGS and SGM, for which some Reynolds number dependency is noted in the defect profiles. Figure 5.8d compares the mean velocity defect profiles at approximately the same freestream velocity for each sand grain roughness considered at the highest Reynolds number. Unlike the perforated sheets, the defect profiles exhibit a non-negligible effect of surface roughness, represented by a small upward displacement of the profile as the flow becomes rougher.

Figures 5.9a, 5.9b, and 5.9c present the mean velocity defect profiles for wire mesh surfaces of different diameter and openness ratio at different Reynolds numbers. Self-similar flows are observed on all of the wire mesh surfaces considered, i.e. the mean velocity defect profiles at different Reynolds numbers collapse onto a single curve. This observation further confirms the Reynolds number independent characteristic of fully rough flow. A similar observation was reported by Bergstrom et al. (2002). Figure 5.9d compares the mean velocity defect profiles at approximately the same freestream velocity obtained for each wire mesh surface at the highest Reynolds number. The mean velocity defect profiles appear to collapse onto each other, and no systematic surface roughness effects arising from different wire mesh geometries are observed.

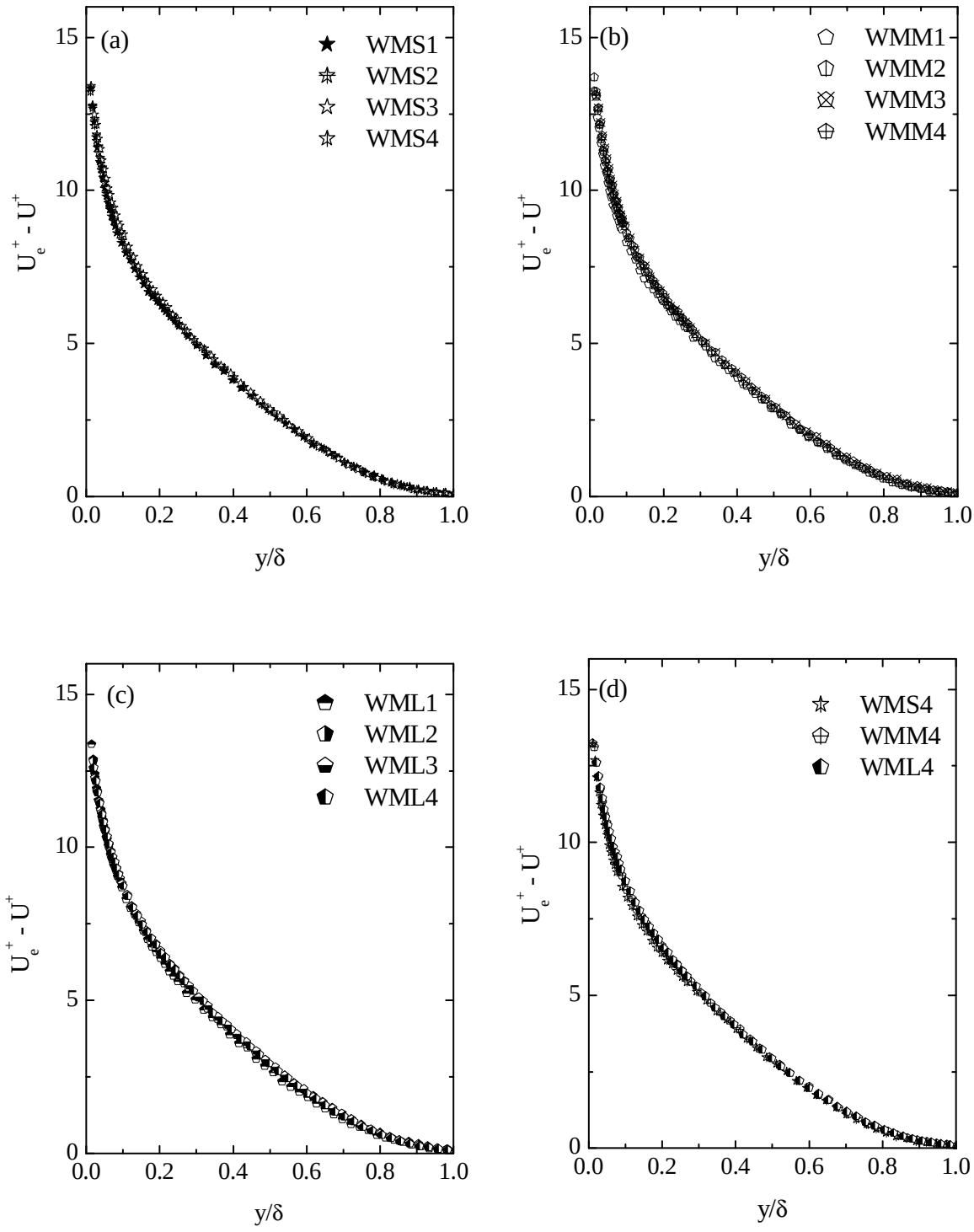

Figure 5.9: Mean velocity defect profiles scaled with friction velocity on wire mesh surfaces.

5.3.2 Scaling with Freestream Velocity

Attention is now turned to the scaling of the mean velocity defect profile with freestream velocity which is the implicit comparison to the friction velocity. Figures 5.10, 5.11, 5.12, and 5.13 present the mean velocity defect profiles for different surface conditions scaled with the freestream velocity, U_e, as proposed by George and Castillo (1997). Figure 5.10 shows the data obtained on the smooth surface at four different Reynolds numbers. The defect profiles for the smooth surface exhibit some Reynolds number dependence. The defect profile decreases slightly as the Reynolds number increases, which is consistent with the observation of Kotey (2001). Figures 5.11a, 5.11b, and 5.11c show the data for perforated sheets with different thickness and circular hole diameter over a range of Reynolds numbers. Unlike the smooth surface, the defect profiles for each perforated sheet collapse onto each other. Figure 5.11d compares the defect profiles at approximately the same freestream velocity for each perforated sheet at the highest Reynolds number. Using the freestream velocity, U_e, each sheet retains a distinct defect profile; as the roughness shift increases the upward displacement of the profile increases.

Figures 5.12a, 5.12b, and 5.12c show the defect profiles for the sand grain surfaces with different roughness at different Reynolds numbers. The defect profiles on both SGS and SGM exhibit some Reynolds number dependence. Figure 5.12d compares the defect profiles at approximately the same freestream velocity obtained for each of the sand grain surfaces considered at the highest Reynolds number. As for the perforated

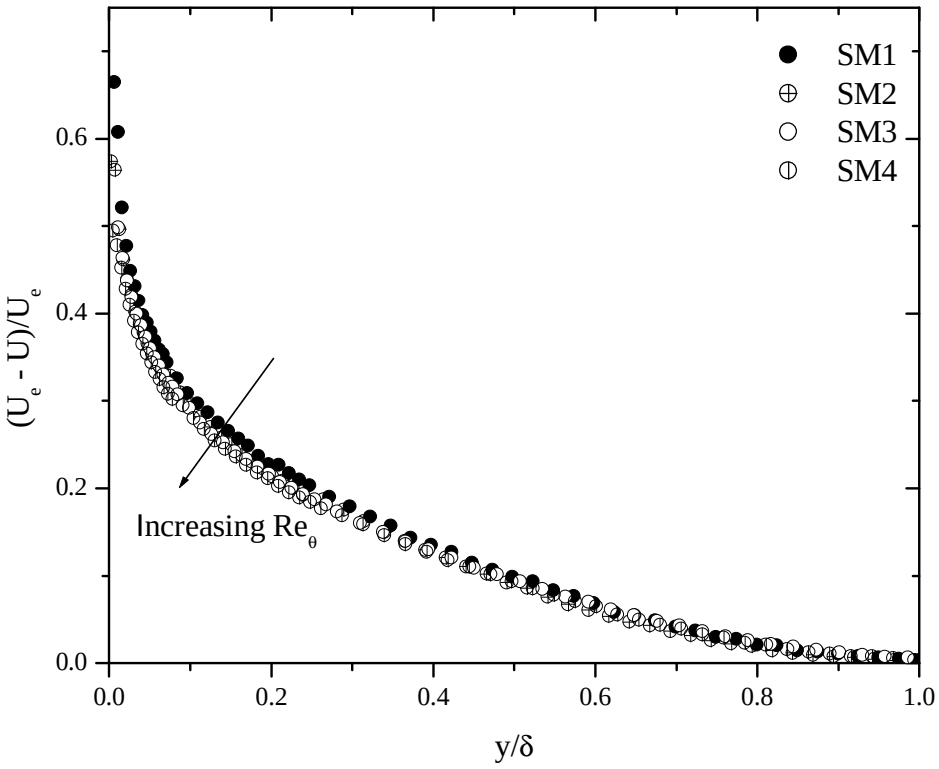

Figure 5.10: Mean velocity defect profiles normalized by freestream velocity for a smooth surface.

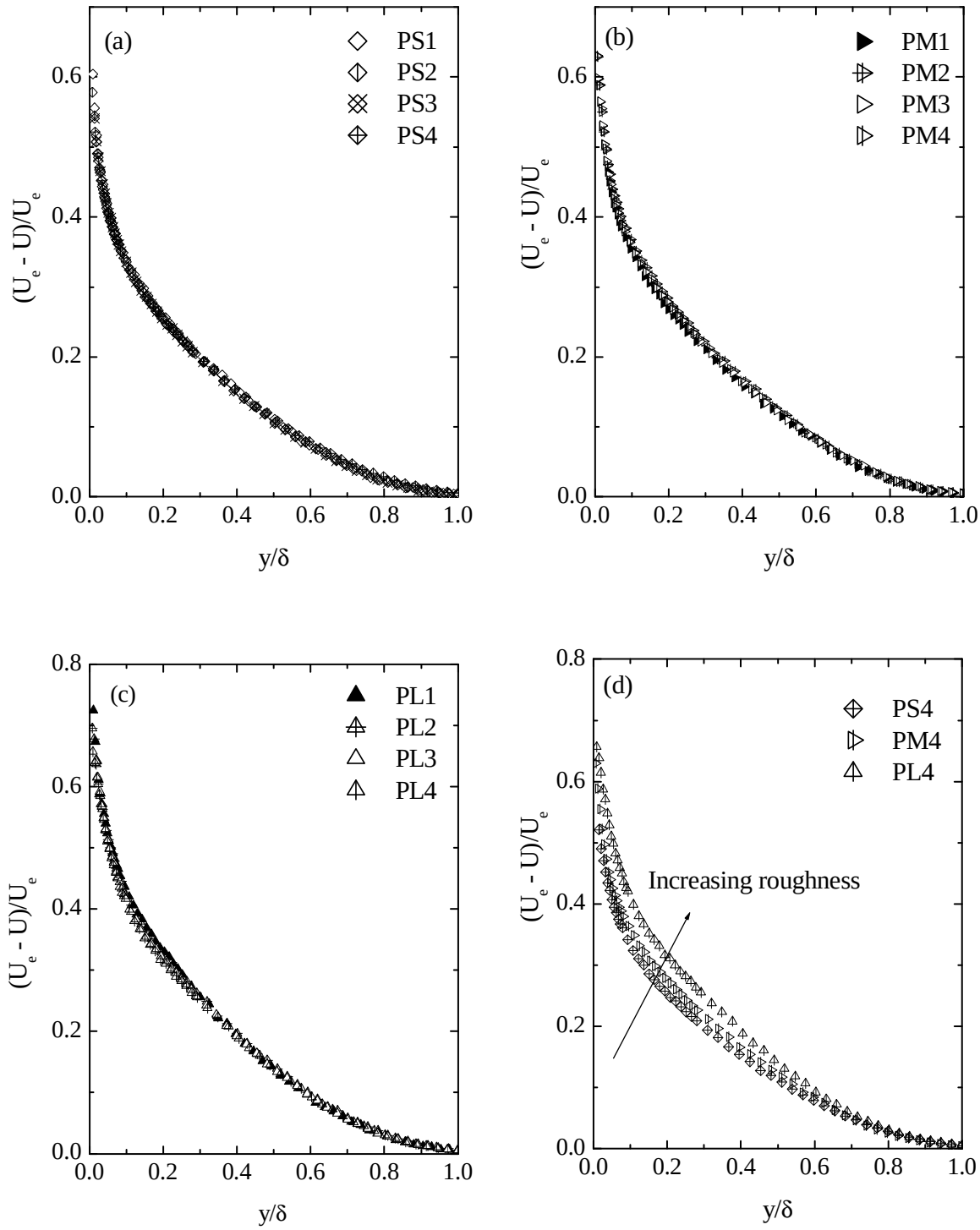

Figure 5.11: Mean velocity defect profiles scaled with freestream velocity for perforated sheets.

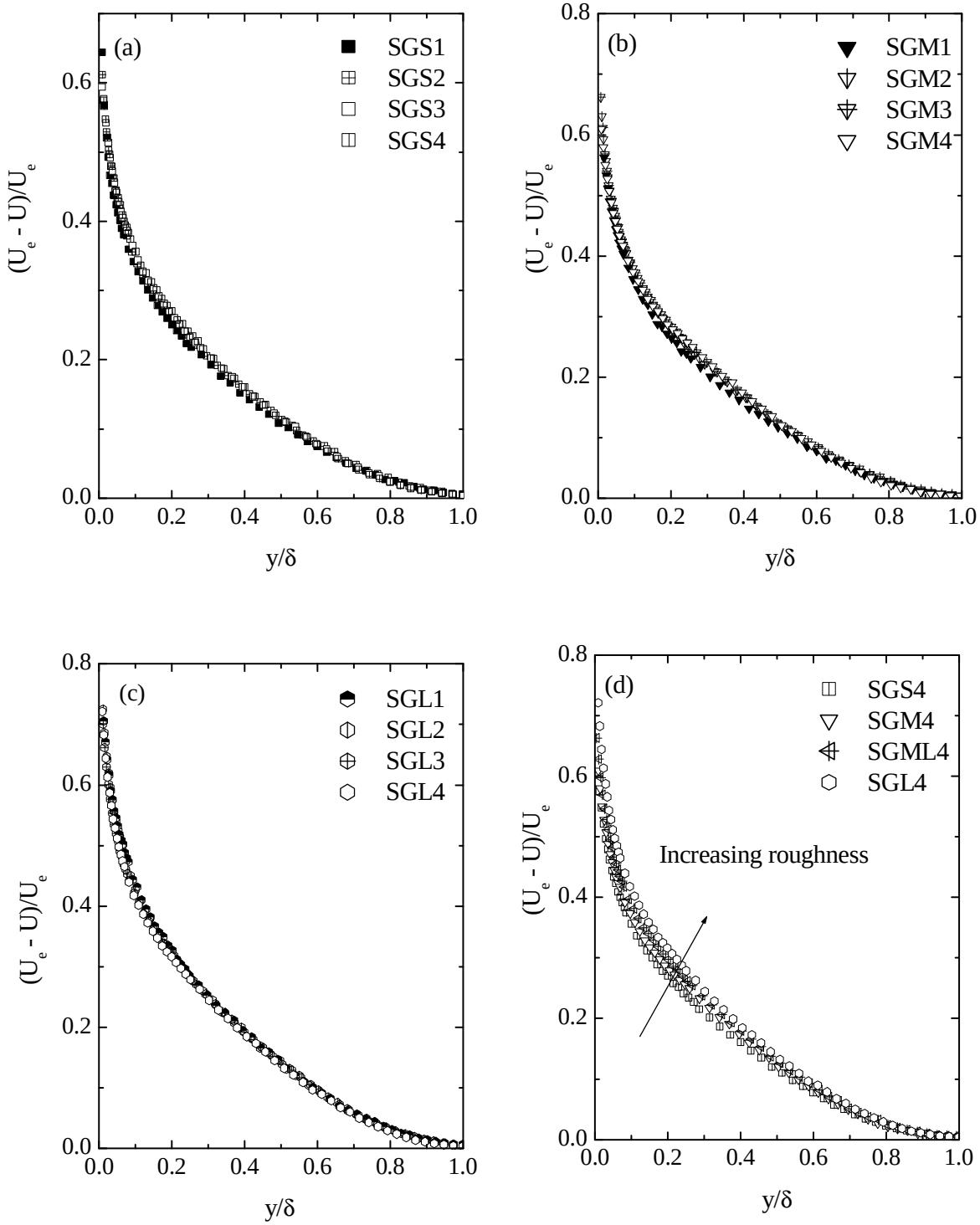

Figure 5.12: Mean velocity defect profiles scaled with freestream velocity for sand grain surfaces

sheet, each sand grain surface retains a distinct shape, with the profile shifting upward as the roughness height increases.

Figures 5.13a, 5.13b, and 5.13c show the mean velocity defect profiles for the wire mesh with different diameter and openness ratio at different Reynolds numbers. The defect profiles on each of the wire mesh surfaces at different Reynolds numbers collapse onto a single curve. Bergstrom et al. (2002) reported similar observation for the wire mesh surfaces. Figure 5.13d compares the defect profiles at approximately the same freestream velocity obtained for each of the wire mesh surfaces at the highest Reynolds number. One characteristic advantage of the freestream velocity as a scaling parameter for the defect profile is that it distinguishes between roughness effects arising from surfaces with similar structure but different surface roughness.

5.3.3 Scaling with Mixed Outer Scale

Figures 5.14, 5.15, 5.16, and 5.17 present the mean velocity defect profiles for different surface conditions scaled with the mixed outer scale, $U_e\delta^*/\delta$, respectively. For each surface, the defect profiles at different Reynolds numbers approximately collapse onto each other. Figures 5.15d, 5.16d, and 5.17d compare the defect profiles at approximately the same freestream velocity obtained for each perforated sheet, sand grain, and wire mesh surface at the highest Reynolds number, respectively. Unlike the previous velocity scales, the defect profile scaled with the mixed outer scale shows no significant effect of surface roughness and Reynolds number. These results are consistent with those of

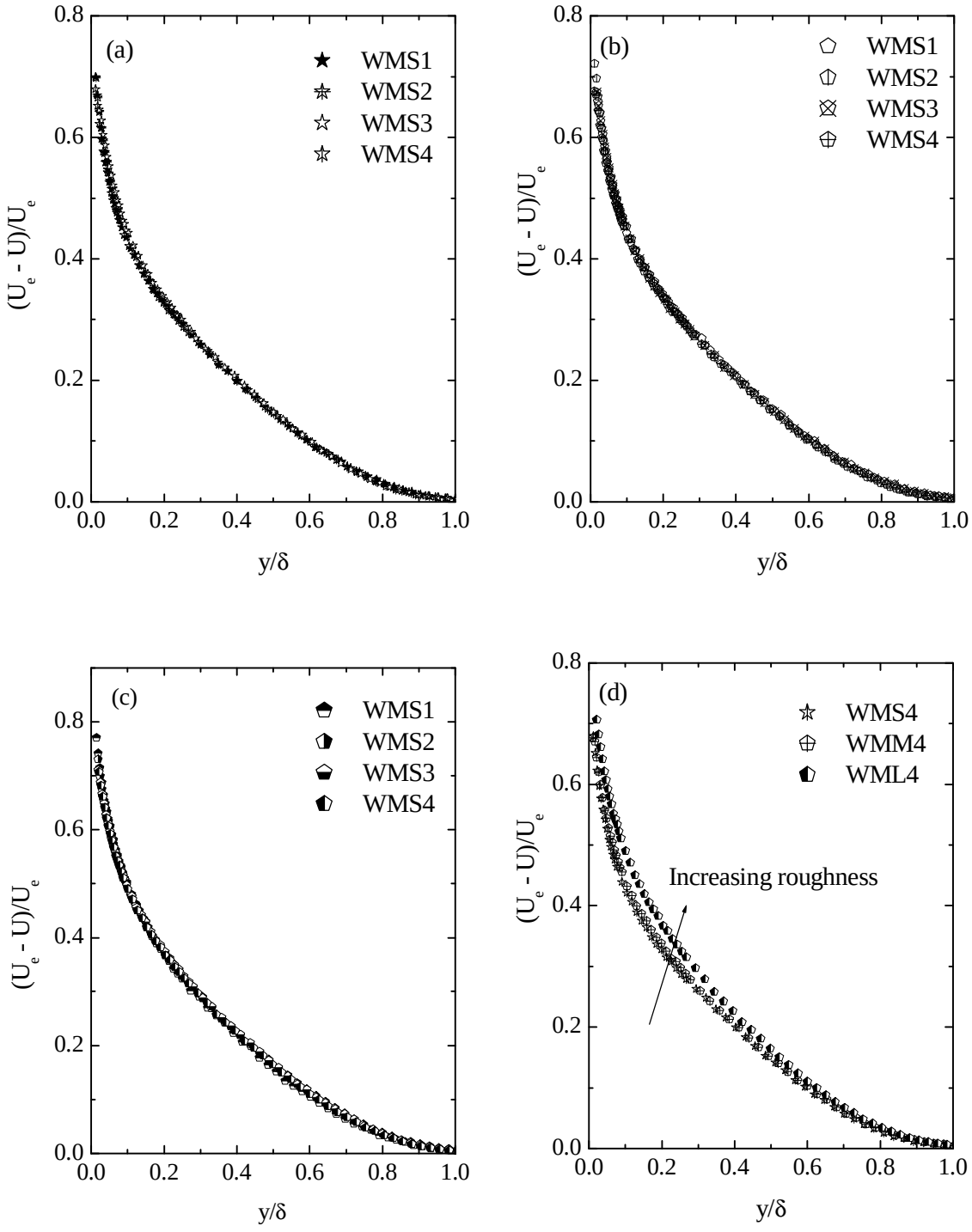

Figure 5.13: Mean velocity defect profiles scaled with freestream velocity for wire mesh surfaces.

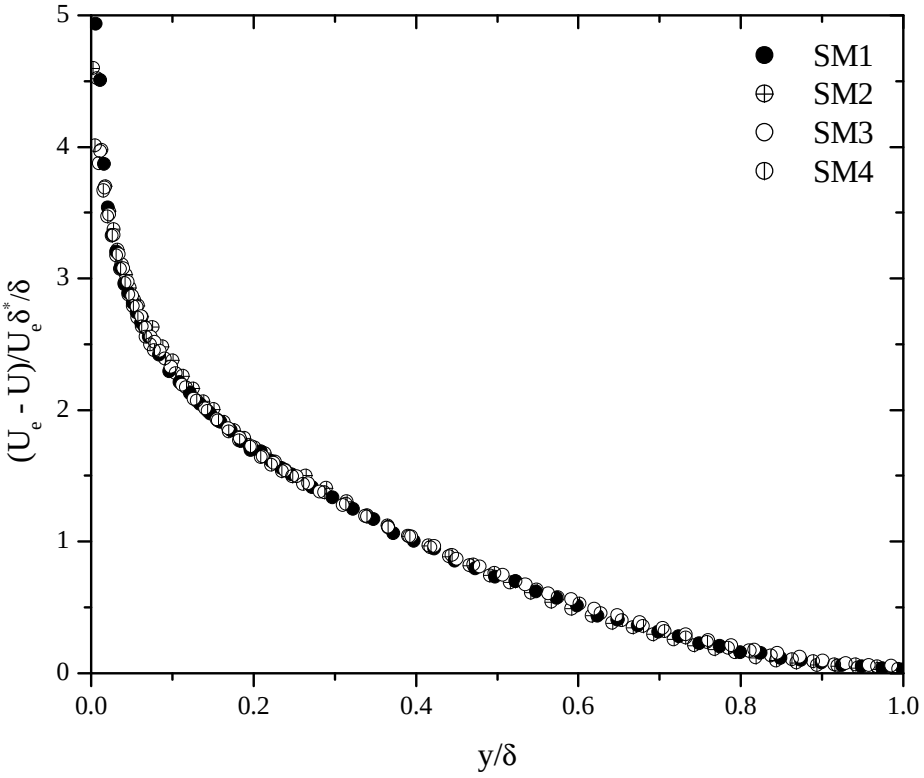

Figure 5.14: Mean velocity defect profiles for a smooth surface using mixed outer scale.

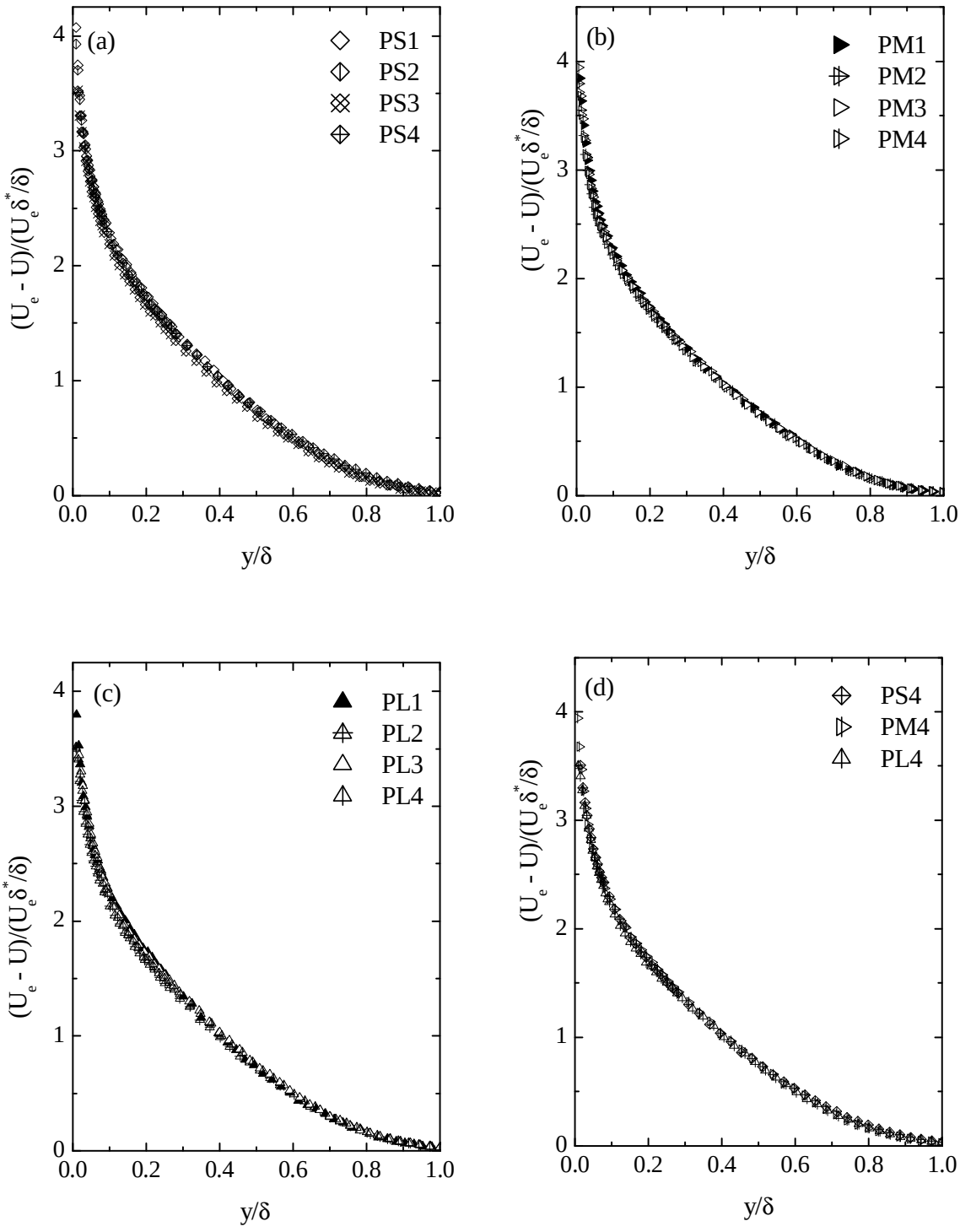

Figure 5.15: Mean velocity defect profiles for perforated sheets using mixed outer scale.

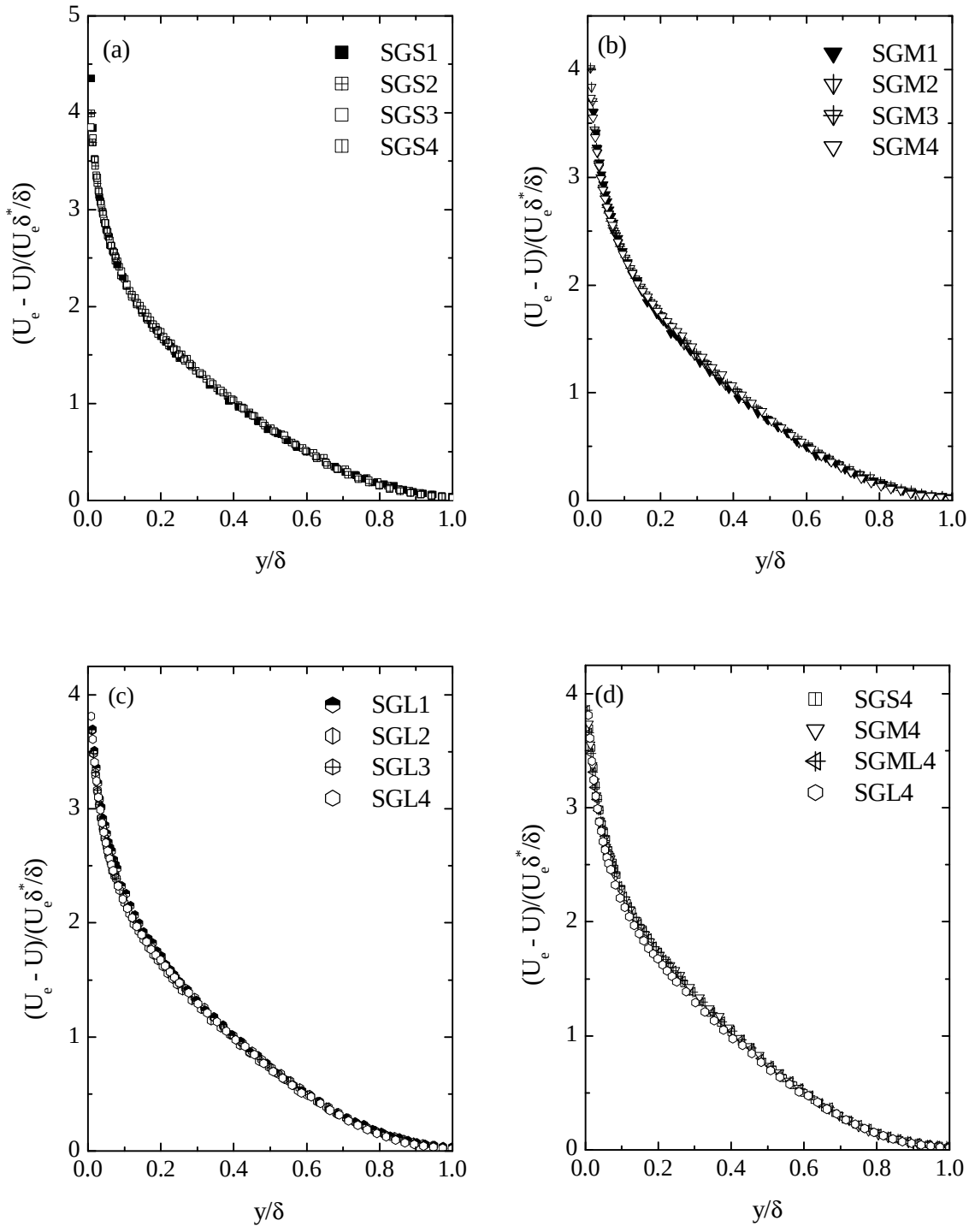

Figure 5.16: Mean velocity defect profiles for sand grain surfaces using mixed outer scale.

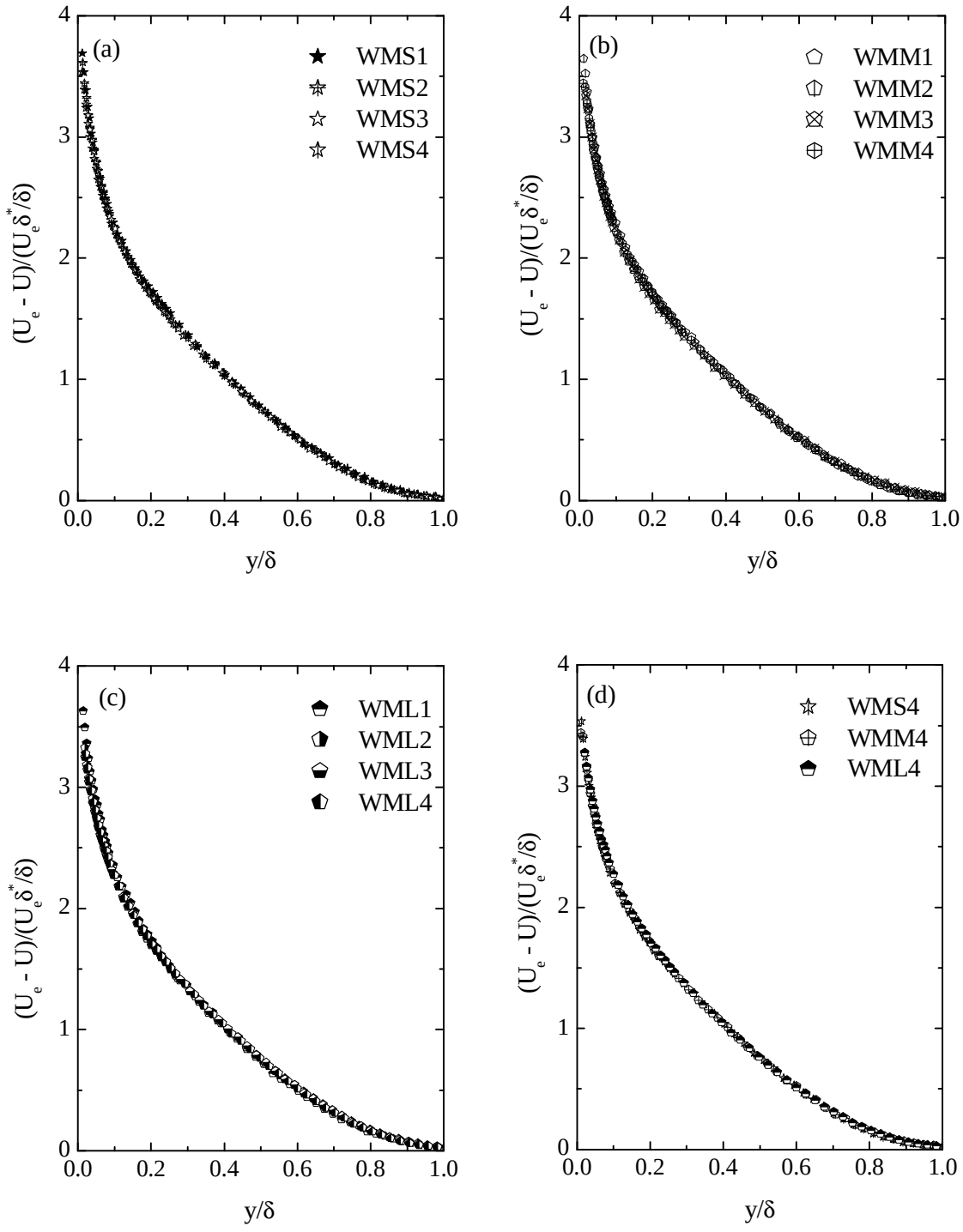

Figure 5.17: Mean velocity defect profiles for sand grain surfaces using mixed outer scale.

Castillo and Walker (2002) in the case of a smooth surface, and Seo et al. (2004) in the case of a fully rough flow. All of the profiles collapse onto each other to form a single curve and, in this sense, use of the mixed outer scale results in a self-similar profile for the mean defect profile, irrespective of surface condition.

The behaviour of the length scale ratio, δ^* / δ, which is used together with the freestream velocity to collapse the defect profiles for different surfaces onto a single curve, is now examined, as well the behaviour of the ratio of momentum thickness to boundary layer thickness, θ / δ. Figure 5.18a compares the boundary layer displacement thickness, δ^*, for different surfaces with respect to Reynolds number. In Figure 5.18a, surface roughness significantly influences the values of the displacement thickness. For example, the flows on WML, which have the highest values of roughness shift, also exhibit the highest values of the displacement thickness. Figure 5.18b compares the variation of length scale ratio, δ^* / δ and θ / δ, with respect to the equivalent sand grain Reynolds number, k_{eq}^+. Note that in the present study, a zero value of k_{eq}^+ is assigned for the smooth surface. It is noted that value of δ^* / δ for the smooth surface increases slightly as the Reynolds number, Re_θ, increases. Based on the values of k_{eq}^+, the flows on PS, PM, SGS, SGM, and SGML (1, 2 and 3) exhibit nominal transitionally rough flow regimes. The values of the length scale ratio, δ^* / δ, for these surfaces increase as k_{eq}^+ increases. However, as roughness increases, the values of the length scale ratio, δ^* / δ, appear to approach an approximately asymptotic level. This observation requires

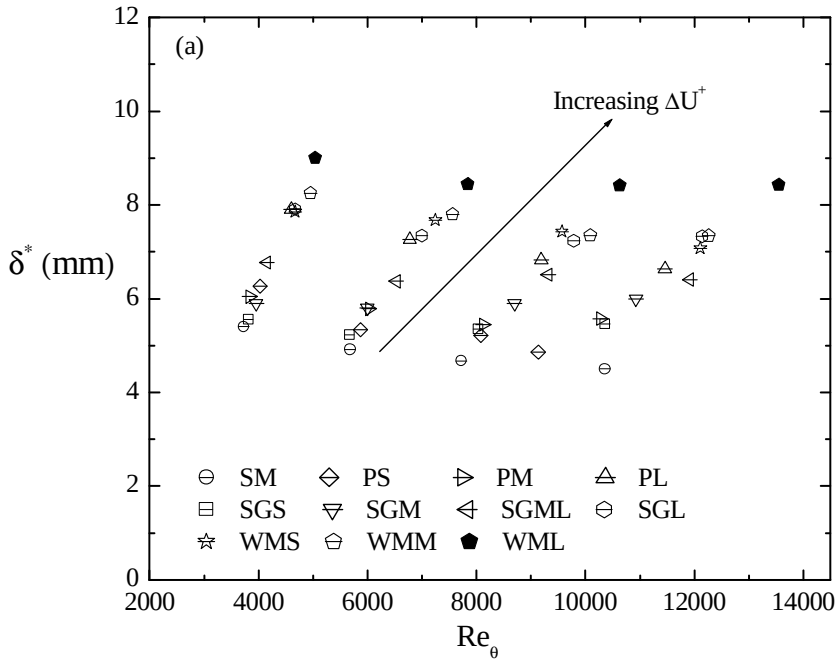

Figure 5.18a: Variation of displacement thickness with Reynolds number for different surfaces

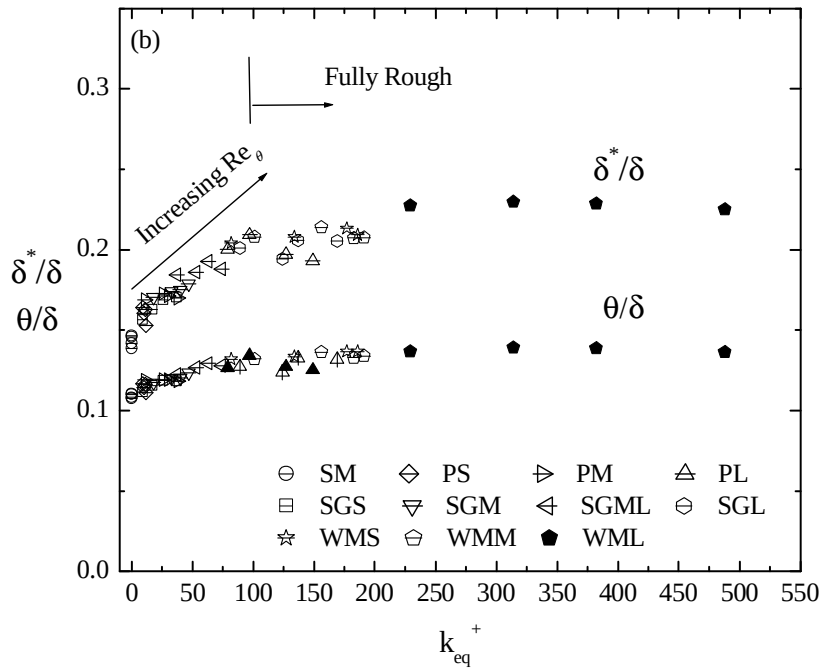

Figure 5.18b: Variation of length scale ratio with equivalent sand grain roughness Reynolds number.

more experimental data for fully rough flows before a final conclusion can be drawn. In the case of θ/δ, the transition between hydraulically smooth and transitionally rough flows is much more gradual. This observation may explain why the length scale, θ/δ, combined with the freestream velocity fails to collapse the mean velocity defect. The ratio θ/δ also appears to attain an asymptotic value as roughness increases.

5.4 Outer Flow Similarity for Smooth and Rough Walls

5.4.1 Scaling with Friction Velocity

Figures 5.19a and 5.19b present the mean velocity defect profiles for the smooth and rough surfaces at the highest Reynolds number, where the friction velocity, U_τ, and the boundary layer thickness, δ, are used to scale the velocity and wall-normal distance, respectively. The defect profile is somewhat higher for the rough surfaces, with a maximum deviation of approximately 7 % and 10 % obtained for the sand grain (SGM4) and wire mesh (WML4), respectively. Similar to the conclusions of Krogstad et al. (1992) and Tachie et al. (2000), the velocity profiles for the different surfaces are distinct from each other not only in the wall region but also over a significant part of the outer region of the boundary layer.

5.4.2 Scaling with Freestream Velocity

Figures 5.20a and 5.20b compare the mean velocity defect profiles for the smooth and rough surfaces at the highest Reynolds number using the outer scaling, and indicate the inability of U_e to collapse profiles for different roughness conditions. The inability of the outer velocity scale to collapse the velocity defect profiles on different surfaces could be

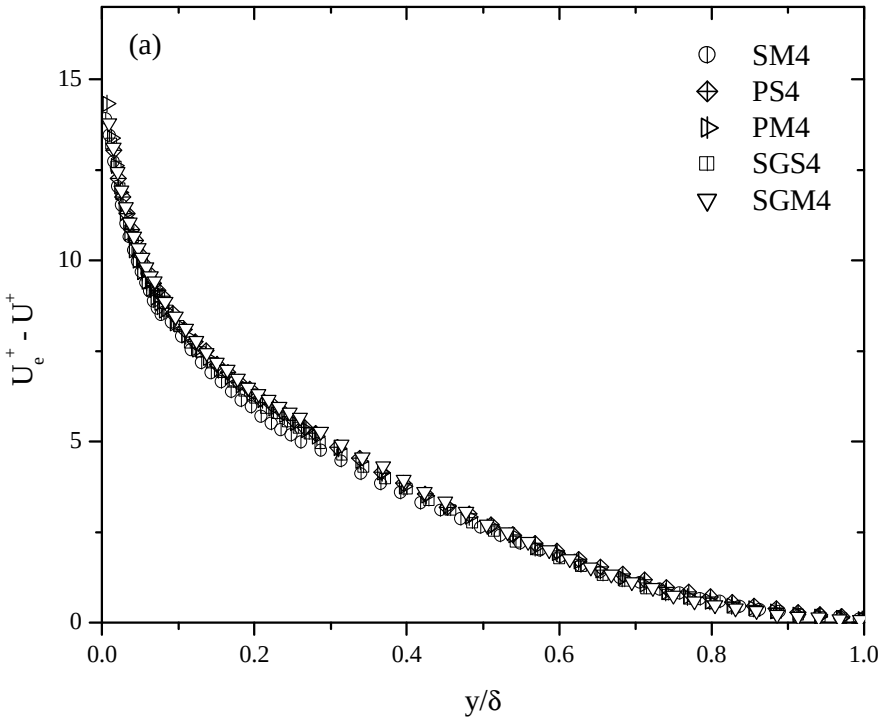

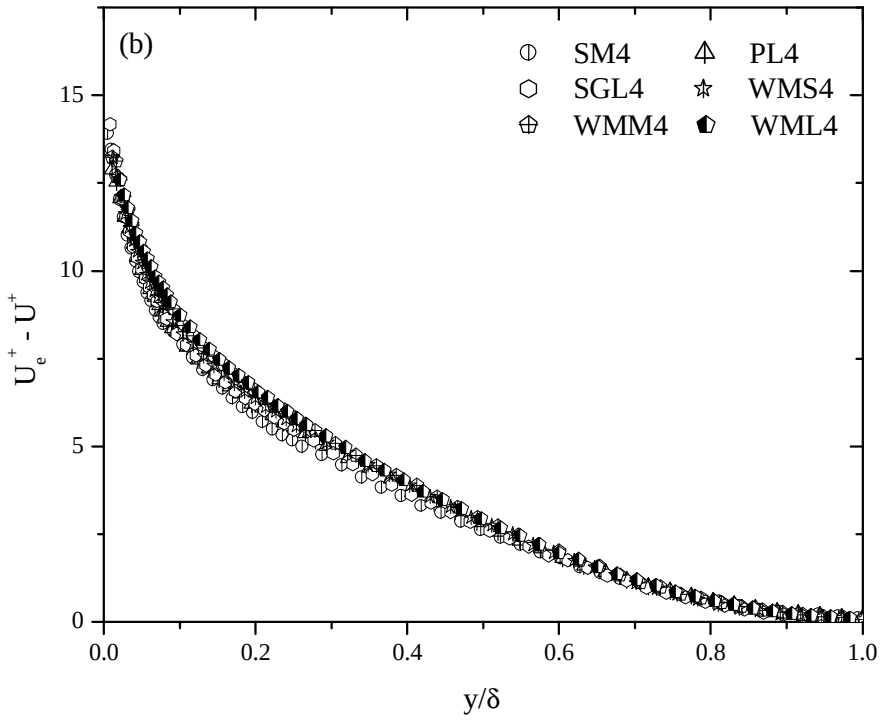

Figure 5.19: Mean velocity defect profiles using inner coordinates: (a) smooth and transitionally rough; (b) smooth and fully rough.

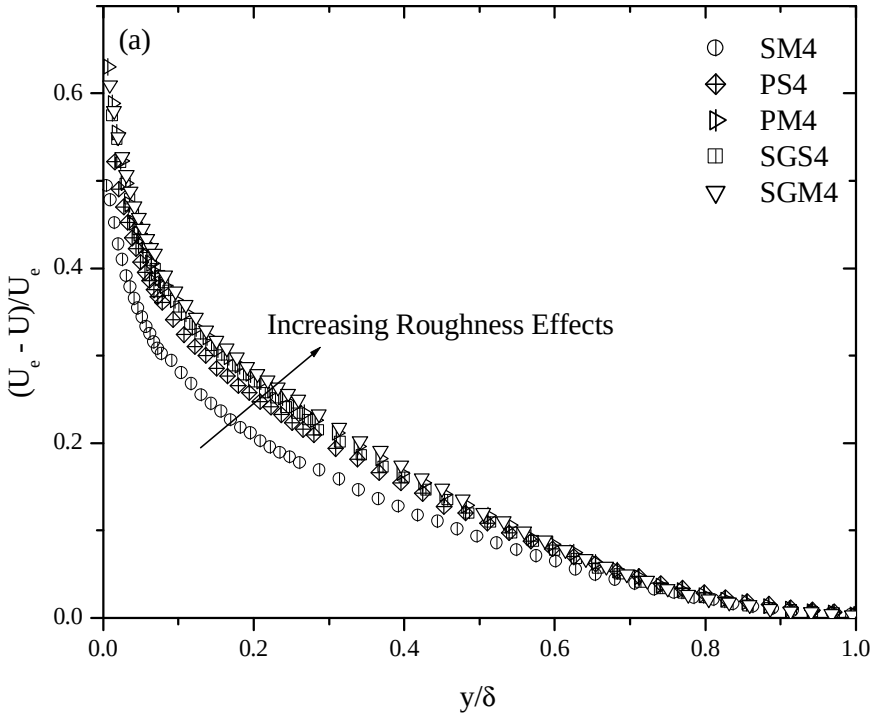

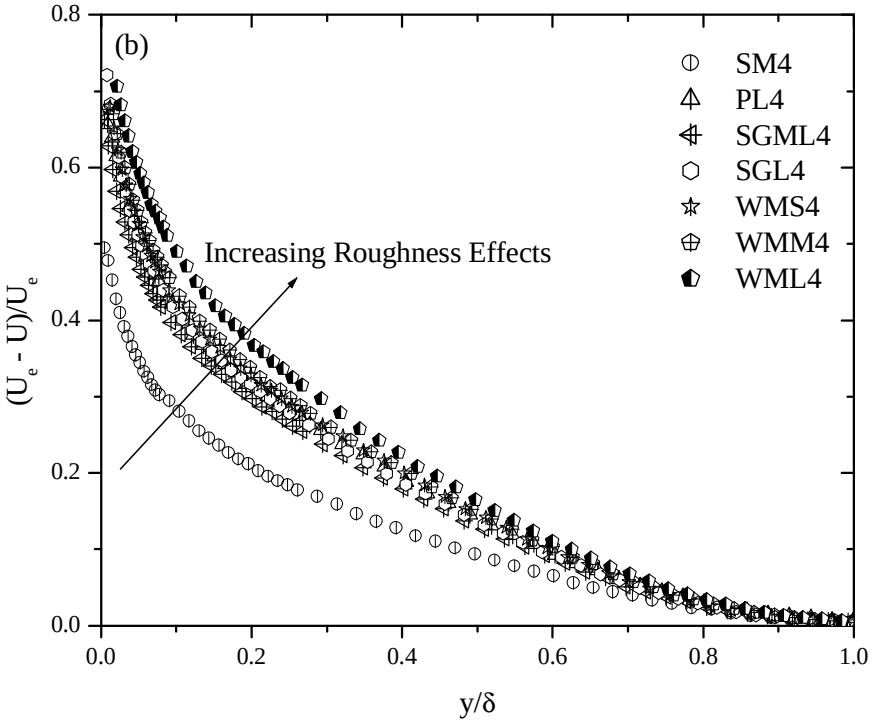

Figure 5.20: Mean velocity defect profiles using outer coordinates: (a) smooth and transitionally rough; (b) smooth and fully rough.

inferred directly from the velocity profiles shown in Figure 5.5. As the roughness shift increases the upward displacement of the mean velocity defect profile increases as indicated in Figure 5.20. The defect profile is somewhat higher for the rough surfaces, with a maximum deviation of approximately 38 % and 80 % obtained for the sand grain (SGM4) and wire mesh (WML4), respectively. Comparing Figure 5.20 to Figure 5.19, the effect of surface roughness on the defect profile is much more pronounced when the outer velocity scale is used to plot the data.

5.4.3 Scaling with Mixed Outer Scale

Figures 5.21a, and 5.21b compare the mean velocity defect profiles for the smooth and rough surfaces at the highest Reynolds number scaled with the mixed outer scale, $U_e\delta^*/\delta$. Unlike the previous velocity scales, the defect profile scaled with the mixed outer scale shows no effect of surface roughness and Reynolds number. All of the profiles collapse onto each other to form a single curve, and in this sense, use of the mixed outer scale identifies a self-similar flow condition for the defect profile irrespective of the surface condition. It is remarkable this scaling parameter is able to collapse all the mean velocity defect profiles irrespective of flow conditions, i.e., for hydraulically smooth, transitionally rough, and fully rough flows regimes.

5.5 Summary

In the previous sections in this chapter, scaling parameters advocated by different studies as the appropriate scaling parameter in the outer region were examined. These include

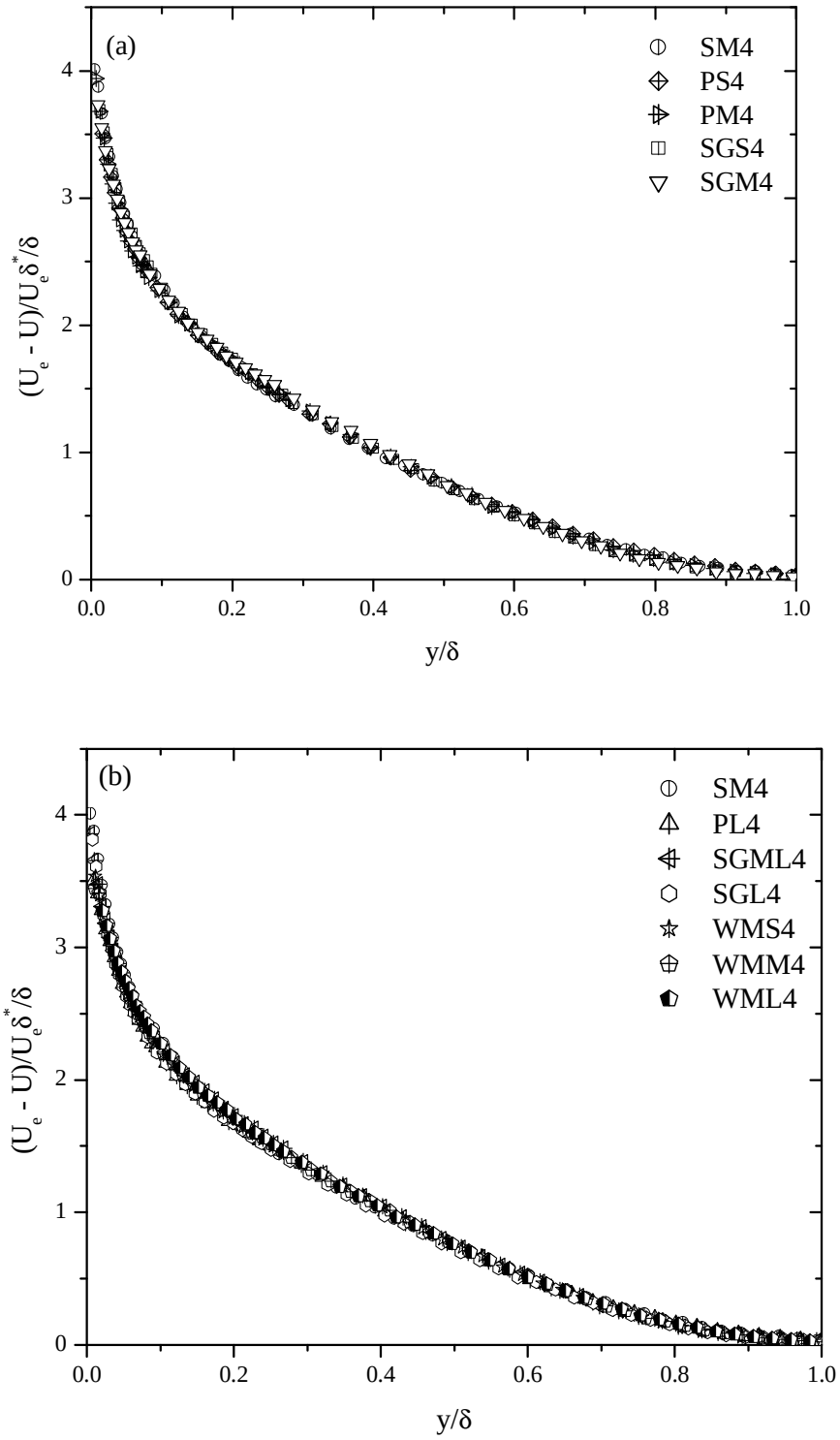

Figure 5.21: Mean velocity defect profiles using mixed outer scale: (a) smooth and transitionally rough; (b) smooth and fully rough.

the friction velocity, local freestream velocity, and mixed outer scale. Each of these scaling parameters using mean velocity profiles obtained for hydraulically smooth, transitionally rough and fully rough flow regimes using different surface roughness geometries was investigated. Based on the analysis of the results for different Reynolds numbers, it was shown that the defect profiles on certain roughness geometries support the principle of Reynolds number similarity when scaled with the friction velocity. The freestream velocity, U_e, was able to collapse the defect profiles for the perforated sheets (PS and PM) and wire mesh at different Reynolds number onto a single curve, but not for the smooth surface and sand grain roughness. The velocity defect profiles for the smooth surface and sand grain roughness both exhibit some Reynolds number dependence when scaled with the freestream velocity. Comparison of the mean velocity defect profiles on smooth and rough surfaces clearly shows that the effect of surface roughness is much more pronounced when the outer flow is scaled with the freestream velocity. When the mean defect profile is scaled with the mixed outer scale, $U_e\delta^*/\delta$, differences due to both Reynolds number and surface roughness are eliminated. For the mixed outer scale, the defect profiles all collapse on a single curve which then represents a self-similar profile.

Finally, the ability of the mixed scaling to collapse defect profiles on different surfaces does not of itself imply that the smooth and rough wall velocity profiles, when appropriately scaled, are similar. Some significant differences continue to exist between smooth – and rough – wall flows, e.g. the strength of the wake, even in the outer region.

CHAPTER 6

ROUGHNESS EFFECTS ON SECOND-ORDER MOMENTS OF THE VELOCITY FLUCTUATIONS

6.1 Introduction

In this chapter, experimental data for turbulence quantities obtained for hydraulically smooth, transitionally rough, and fully rough flow regimes are reported. The data presented include the streamwise and wall-normal fluctuating velocity components, as well as the Reynolds shear stress. Four different scaling parameters, i.e. the friction velocity, U_τ, freestream velocity, U_e, mixed scale, $U_\tau U_e$, as well as mixed outer scale, $U_e\delta^*/\delta$, are used for the purpose of achieving self-similar conditions for the streamwise turbulence intensity profiles in a turbulent boundary layer for hydraulically smooth, transitionally rough, and fully rough flow regimes. The effectiveness of each scaling is evaluated both with respect to Reynolds number and surface condition. Two different scaling parameters, namely, the friction velocity, U_τ, and freestream velocity, U_e, were used to assess the effect of the surface roughness on the wall-normal turbulence intensity and Reynolds shear stress.

6.2 Similarity Scaling of the Streamwise Turbulence Intensity

Figure 6.1 presents the streamwise turbulence intensity profiles scaled by the friction velocity, U_τ , for hydraulically smooth and transitionally rough flows at three different Reynolds numbers. Note that the transitionally rough flows were obtained on sand grain roughness (SGS) and perforated sheet (PM). For all three surfaces, the streamwise turbulence intensity profiles appear to collapse onto each other within the experimental uncertainty. Figure 6.2 shows the turbulence intensity profiles scaled with friction velocity for fully rough flows achieved on perforated sheet, sand grain roughness, and wire mesh at three different Reynolds numbers. For both PL and SGL (Figures 6.2a, b), the streamwise turbulence intensity profiles appear to be reasonably collapsed onto a single curve, indicating insignificant Reynolds number effects on the profiles. For the streamwise turbulence intensity profiles on wire mesh (WMM, Figure 6.2c), there is a maximum deviation of 2 % within the region $y/\delta < 0.3$, which still falls within the experimental uncertainty. In view of this, one can conclude that the streamwise turbulence intensity profiles obtained for the wire mesh surface are Reynolds number independent when scaled with the friction velocity. A similar observation was reported by Antonia and Krogstad (1993). This is not surprising since the fully rough flows are generally independent of Reynolds number.

Figure 6.3 presents the streamwise turbulence intensity profiles obtained for a hydraulically smooth surface normalized by the friction velocity. Also included for comparison (in Figure 6.3) are the smooth wall direct numerical simulation (DNS) data

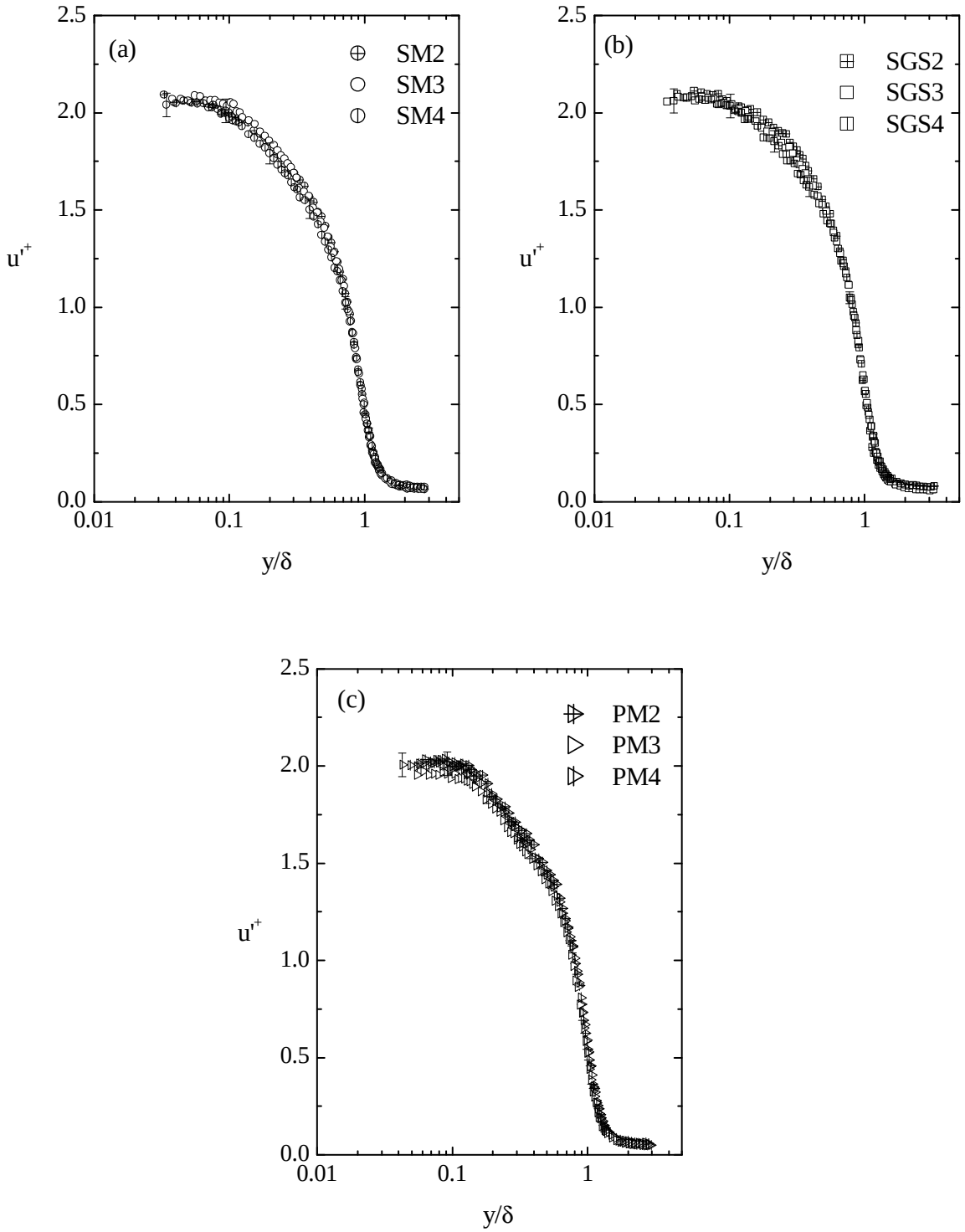

Figure 6.1: Streamwise turbulence intensity distributions for smooth and transitionally rough flows using inner coordinates: (a) smooth; (b) sand grain; (c) perforated sheet.

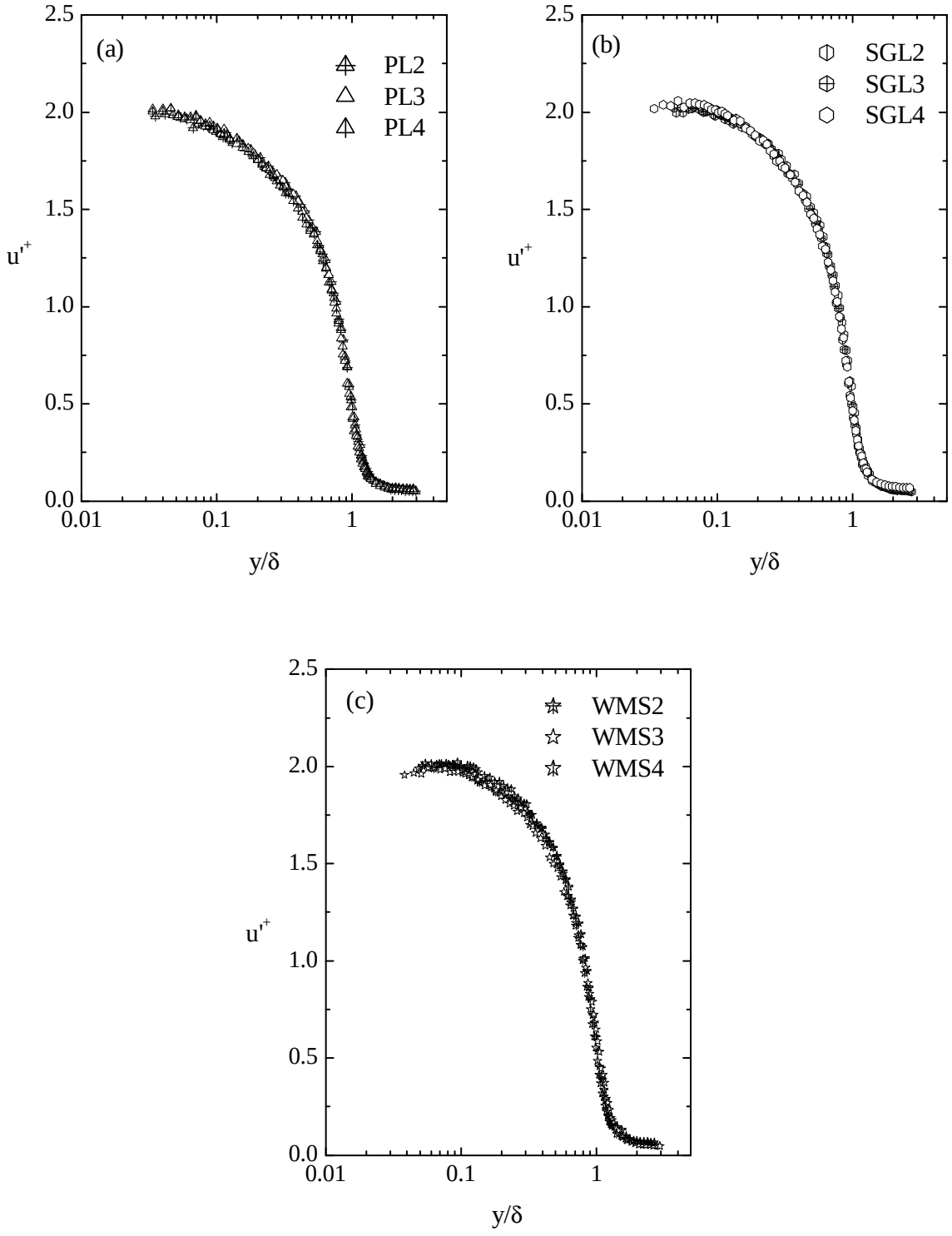

Figure 6.2: Streamwise turbulence intensity distributions on fully rough flows using inner coordinates: (a) perforated sheet; (b) sand grain; (c) wire mesh.

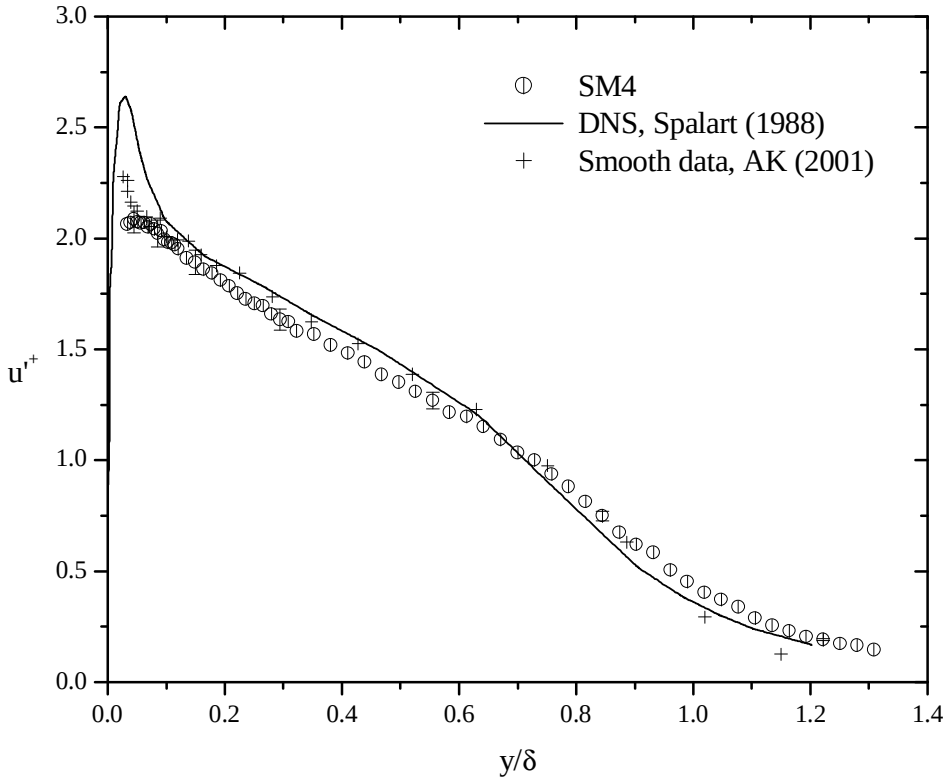

Figure 6.3: Streamwise turbulence intensity profiles for smooth wall scaled with friction velocity (AK denotes Antonia and Krogstad (2001))

of Spalart (1988) at Re_θ = 1410 and the smooth wall data of Antonia and Krogstad (2001) at Re_θ = 12,570. The present smooth wall (SM3) data are in good agreement with both the DNS data of Spalart (1988) and the smooth wall data of Antonia and Krogstad (2001) given the level of experimental uncertainty.

Figure 6.4 compares the streamwise turbulence intensity distributions for the smooth and rough surfaces at the highest Reynolds number normalized with the friction velocity. The streamwise turbulence intensity data for the smooth wall are compared with those obtained for transitionally rough flows, as indicated in Figure 6.4a. The comparison shows that the nominal transitionally rough flows exhibit minimal effect of surface roughness on the level of turbulence intensity profiles. Figure 6.4b compares the streamwise turbulence intensity profiles obtained for the hydraulically smooth and fully rough flows scaled by the friction velocity. We have also included for comparison the wire mesh data sets of Antonia and Krogstad (2001) at Re_θ = 12,800 in Figure 6.4b. As indicated in Figure 6.4b, the streamwise turbulence intensity data for all the rough surfaces considered are higher than that on a smooth wall in the region $y/\delta \geq 0.5$. These results support previous observations that the effect of surface roughness can extend into the outer region of the boundary layer (e.g. Krogstad et al., 1992; Antonia and Krogstad, 2001; Tachie et al., 2003). There is a reduction in the level of the streamwise turbulence intensity data for all three rough surfaces when compared to the smooth wall in the inner region ($y/\delta < 0.1$), as shown in Figure 6.4b. The disappearance of the near-wall peak of

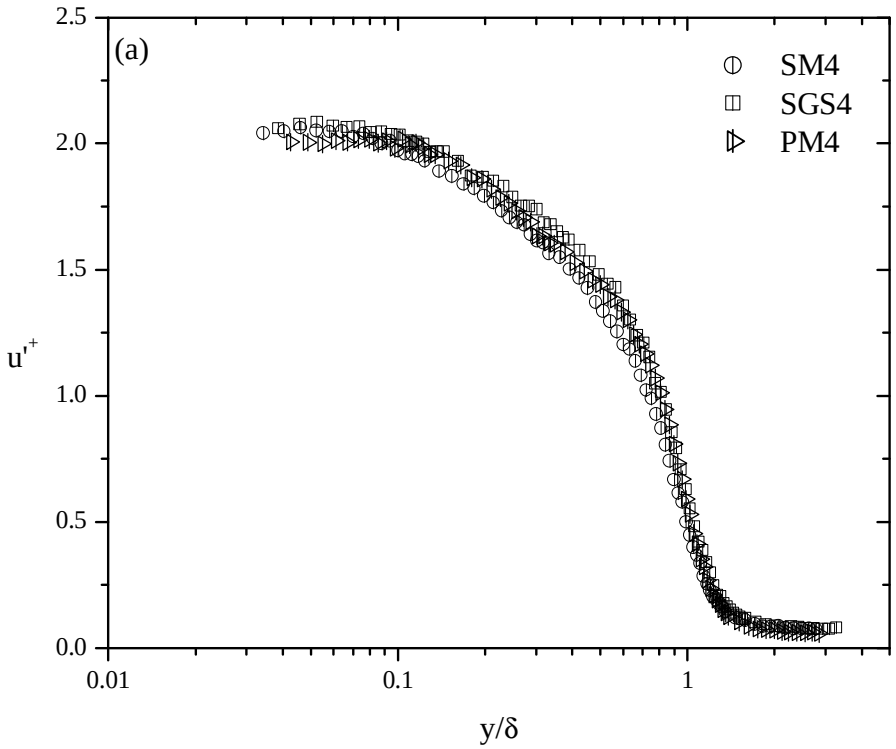

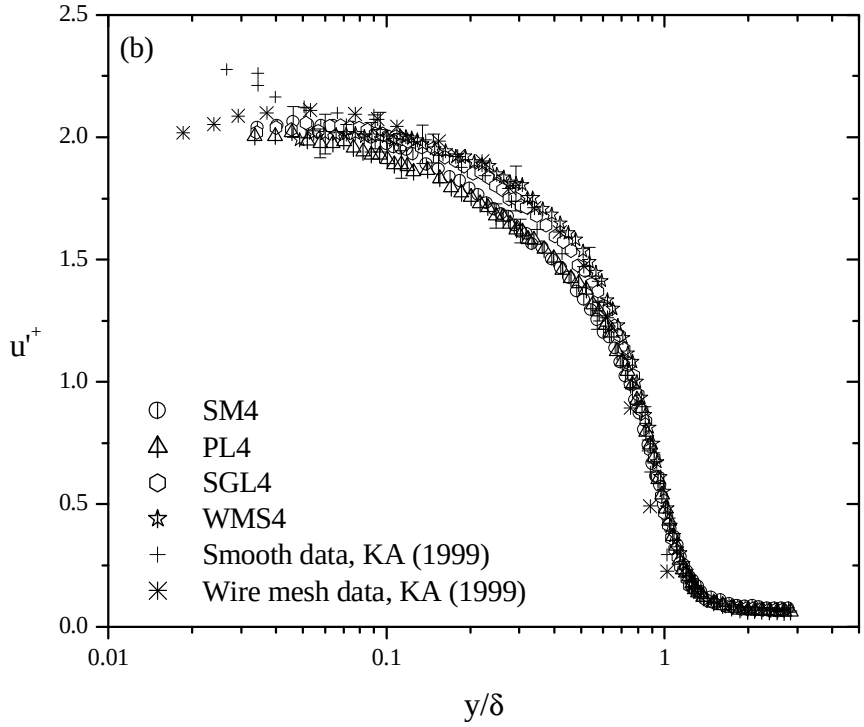

Figure 6.4: Streamwise turbulence intensity distributions surfaces using inner coordinates: (a) smooth and transitionally rough; (b) smooth and fully rough (KA denotes Krogstad and Antonia, 1999).

the streamwise turbulence intensity for a rough surface was shown also by Ligrani and Moffat (1985). The extent of the reduction in the values of the streamwise turbulence intensity for the perforated sheet (PL4) is greater than that for the sand grain (SGL4) and wire mesh (WMS4); furthermore, the data for the perforated sheet (PL4) drops below the smooth profile for $y/\delta \leq 0.3$. One possible explanation for this behaviour can be linked to the interaction between the flow within the cavities of the perforated sheet (PL4) and the bulk flow.

Figure 6.5 presents the distributions of the streamwise turbulence intensity normalized by the mixed scale, $U_\tau U_e$, for hydraulically smooth and nominal transitionally rough flows at three different Reynolds numbers. This scale was proposed by DeGraaf and Eaton (2000) as the appropriate scaling parameter for the streamwise fluctuating velocity component. The distributions of the streamwise turbulence intensity collapse onto each other in the region $y/\delta > 0.15$ for the smooth surface and $y/\delta > 0.2$ for both the sand grain (SGS) and perforated sheet (PM). Schultz and Flack (2003) reported a similar observation for the case of a smooth surface. Comparing Figures 6.1 and 6.5, it is obvious that scaling the streamwise turbulence intensity data with the mixed scale is useful for collapsing the profiles for different Reynolds numbers in the outer region of the flow. Figure 6.6 presents the distributions of the streamwise turbulence intensity normalized by the mixed scaling, $U_\tau U_e$, for fully rough flows at three different Reynolds numbers. The streamwise turbulence intensity data for all the fully flows considered appear to collapse onto each other in the region $y/\delta > 0.1$.

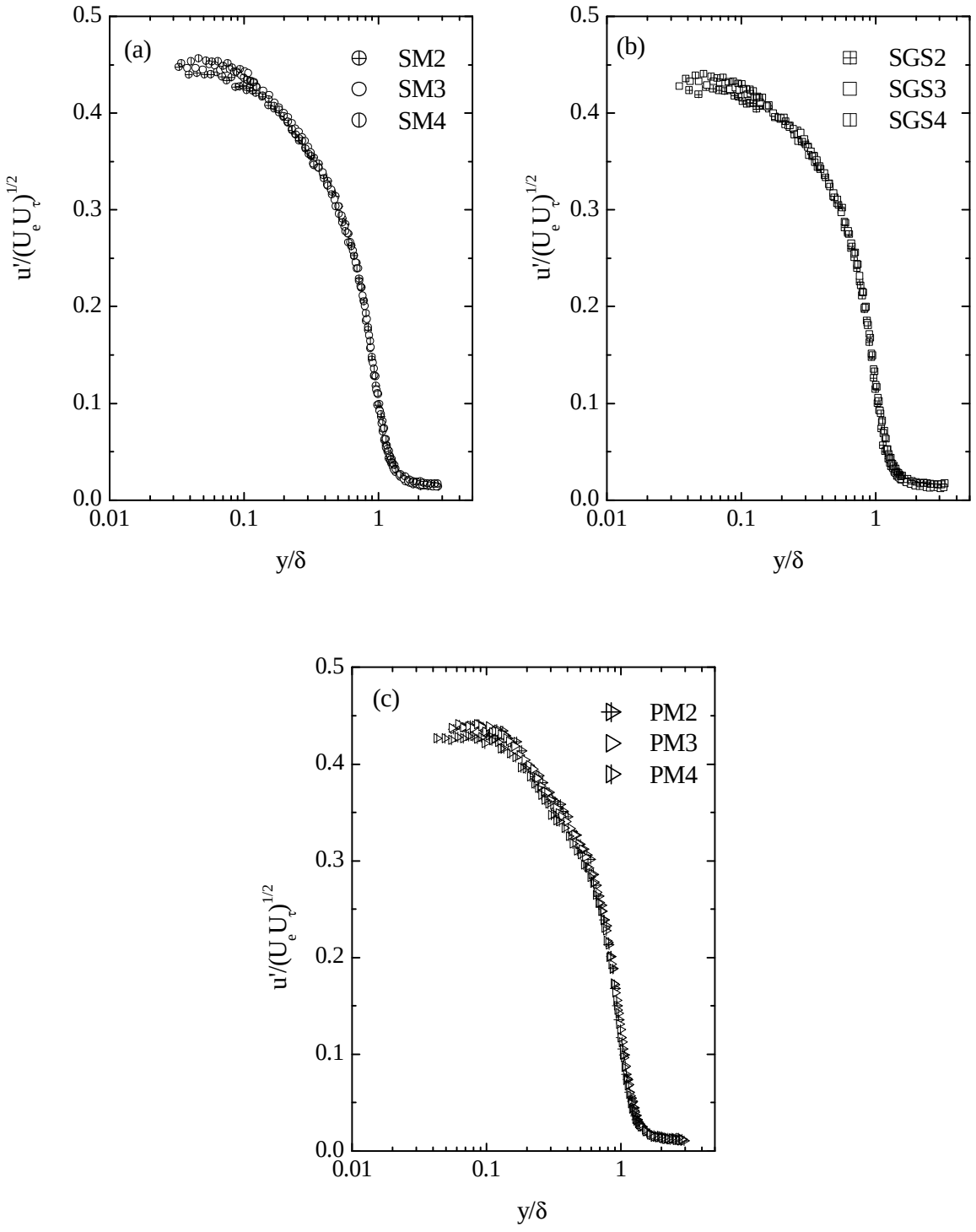

Figure 6.5: Streamwise turbulence intensity distributions for smooth and transitionally rough flows using mixed scale: (a) smooth; (b) sand grain; (c) perforated sheet.

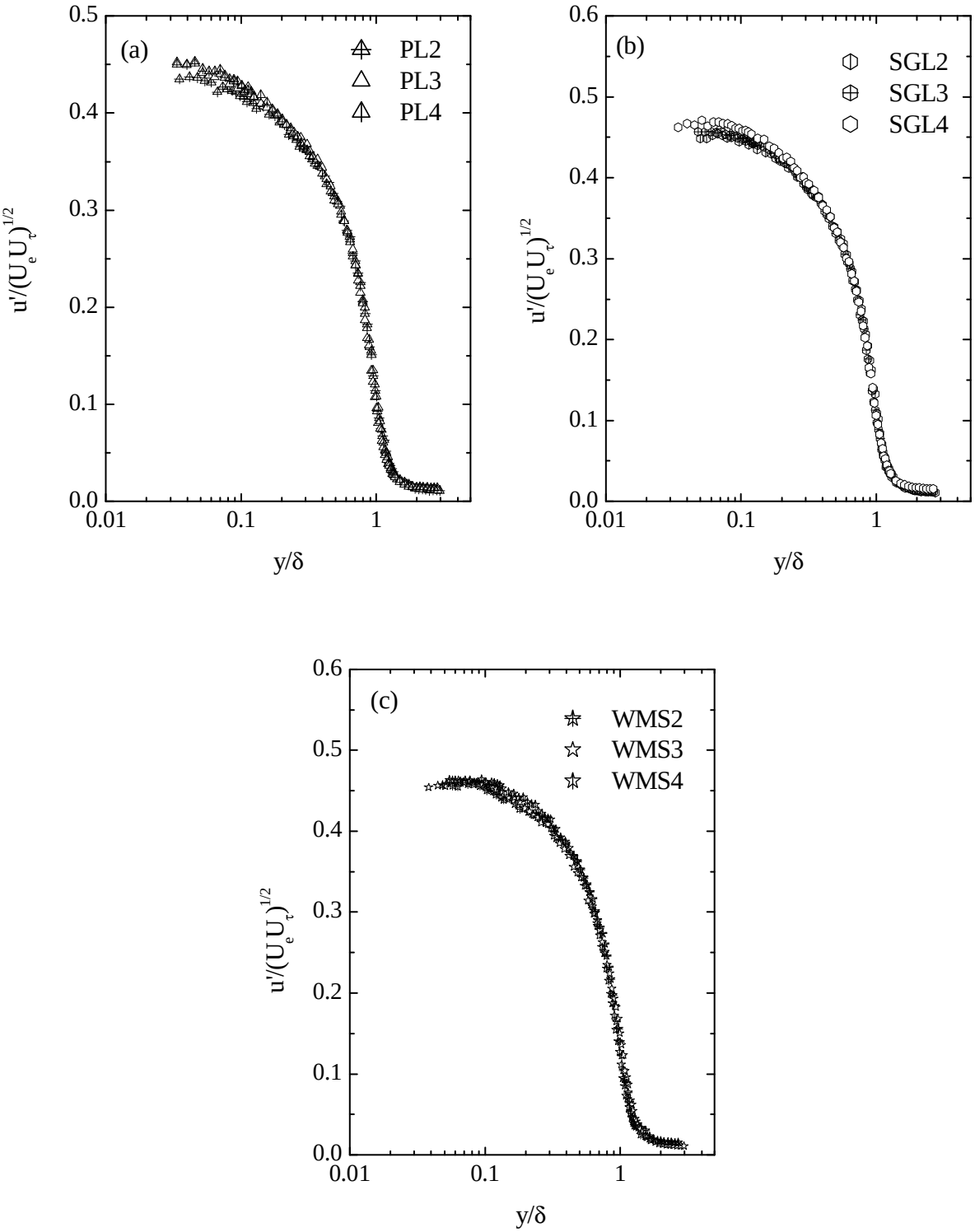

Figure 6.6: Streamwise turbulence intensity distributions on fully rough flows using mixed scale: (a) perforated sheet; (b) sand grain; (c) wire mesh.

Unlike Figure 6.1c, where a small effect of Reynolds number is observed on the wire mesh data, the mixed scale seems to perform better in collapsing the streamwise turbulence intensity profiles.

Figure 6.7a compares the distributions of the streamwise turbulence intensity for hydraulically smooth and transitionally rough flows scaled with mixed scale, $U_\tau U_e$, at the highest Reynolds numbers. The effect of surface roughness is observed to lower the level of streamwise turbulence intensity within the region $y/\delta < 0.1$. Beyond this region, no significant effect of surface roughness is noticed as the turbulence intensity data for the rough surfaces collapse on that of the smooth wall. It is clearly observed that scaling the turbulence intensity data with the mixed scale, $U_\tau U_e$, shows some appreciable improvement in collapsing the data in the outer region of the flow compared with that obtained for the friction velocity, U_τ, alone. Figure 6.7b compares the streamwise turbulence intensity profiles for hydraulically smooth and fully rough flows scaled with the mixed scale, $U_\tau U_e$, at the highest Reynolds numbers. Also included for comparison are the smooth wall of DeGraaf and Eaton (2000) at Re_θ = 13,000, and that of Krogstad and Antonia (1999). The wire mesh data of Krogstad and Antonia (1999) are also presented for comparison in Figure 6.7b. For the smooth and wire mesh surfaces, the present results and the experimental data of Krogstad and Antonia (1999) show good agreement outside the inner region. However, the mixed scaling did not collapse the streamwise turbulence intensity profiles on both smooth and rough surfaces

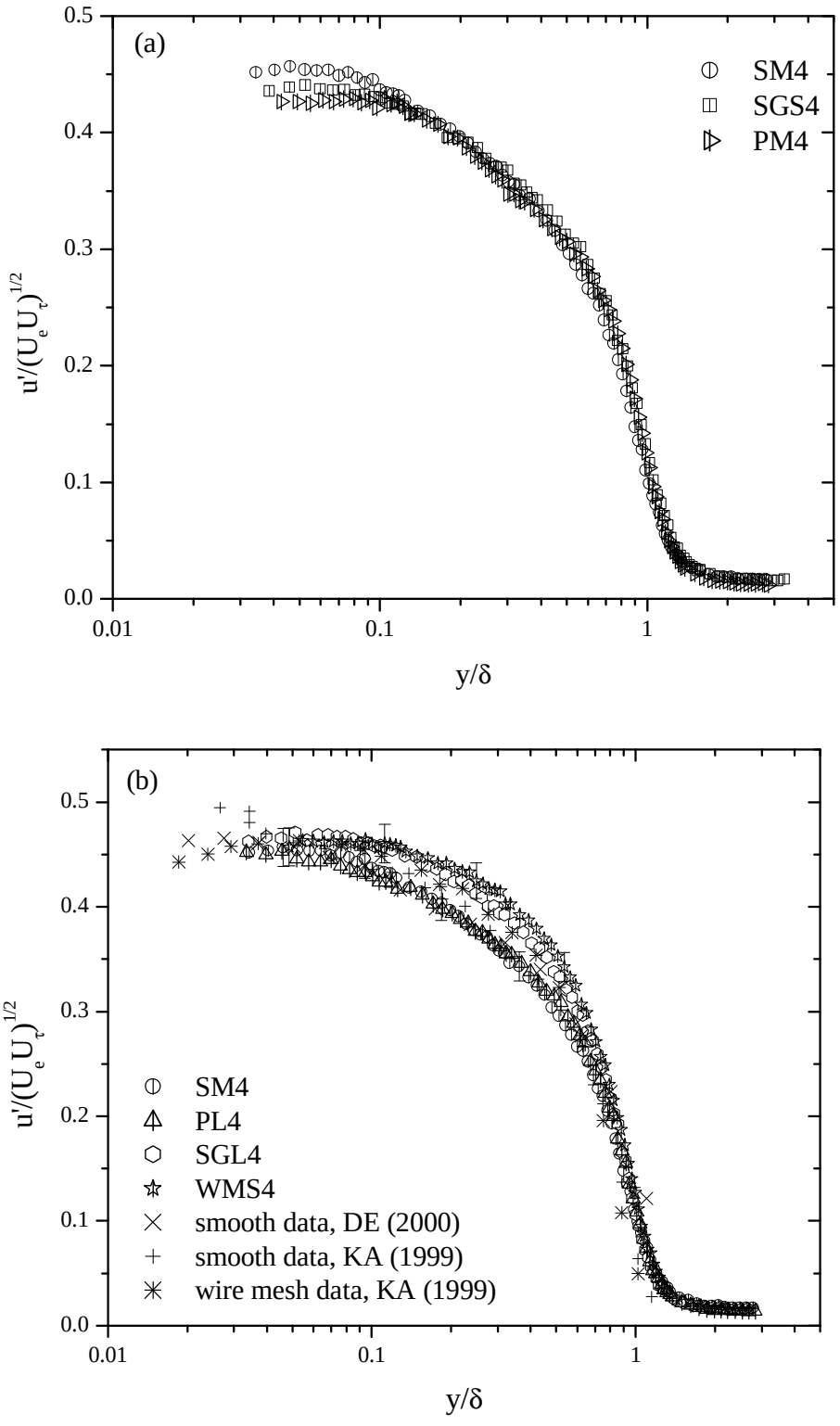

Figure 6.7: Streamwise turbulence intensity distributions surfaces using mixed scale: (a) smooth and transitionally rough; (b) smooth and fully rough (DE and KA denote DeGraaf and Eaton (2000) and Krogstad and Antonia (1999), respectively).

as effectively as did the friction velocity. A similar observation was noticed by Schultz and Flack (2003).

Figure 6.8 presents the streamwise turbulence intensity distributions normalised by the freestream velocity, U_e, for hydraulically smooth and transitionally rough flows at three different Reynolds numbers. This is the correct velocity scale according to the theory proposed by George and Castillo (1997). For the three surfaces considered, as indicated in Figures 6.8a, 6.8b, and 6.8c, the streamwise turbulence intensity profiles exhibit some Reynolds number dependence. For both the smooth and sand grain surfaces, the effect of Reynolds number is evident in the streamwise turbulence intensity profiles up to $y/\delta \approx 0.2$. Seo et al. (2004) reported a similar observation for the case of the smooth surface. For the perforated sheet, the effect of Reynolds number is much more pronounced, and this effect extends almost to $y/\delta \approx 0.6$. Figure 6.9 presents the streamwise turbulence intensity distributions normalised by the freestream velocity, U_e, for fully rough flows at three different Reynolds numbers. For all the fully rough flows, the effect of Reynolds number is observed to be limited within the region $y/\delta < 0.2$, as the turbulence intensity data beyond this region completely collapse onto single curve.

Figure 6.10a compares the streamwise turbulence intensity profiles for hydraulically smooth and transitionally rough flows at the highest Reynolds number using outer coordinates. Comparison between the streamwise turbulence intensity data for smooth and fully rough flows scaled with the freestream velocity is also shown in

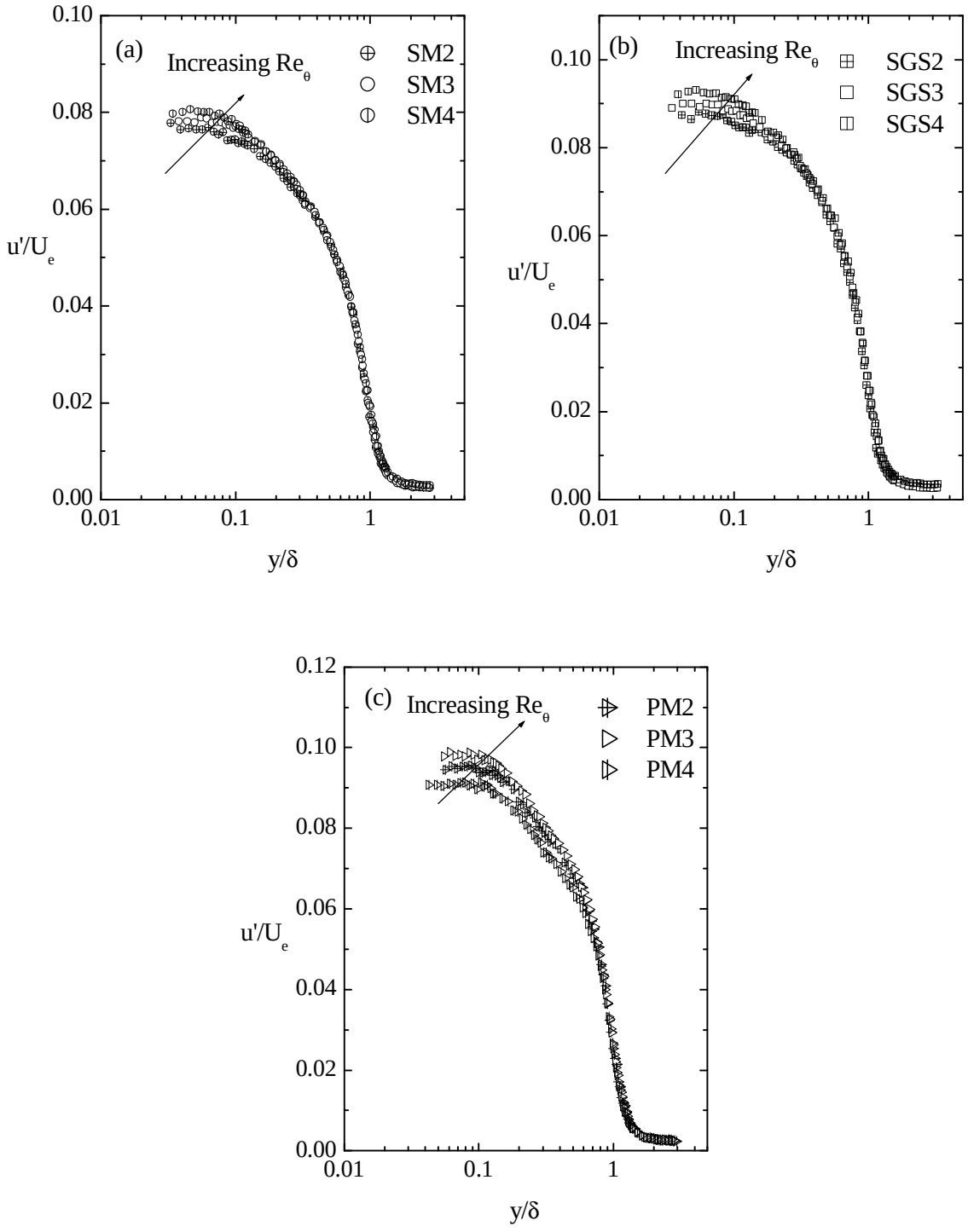

Figure 6.8: Streamwise turbulence intensity distributions for smooth and transitionally rough flows using freestream velocity scaling: (a) smooth; (b) sand grain; (c) perforated sheet.

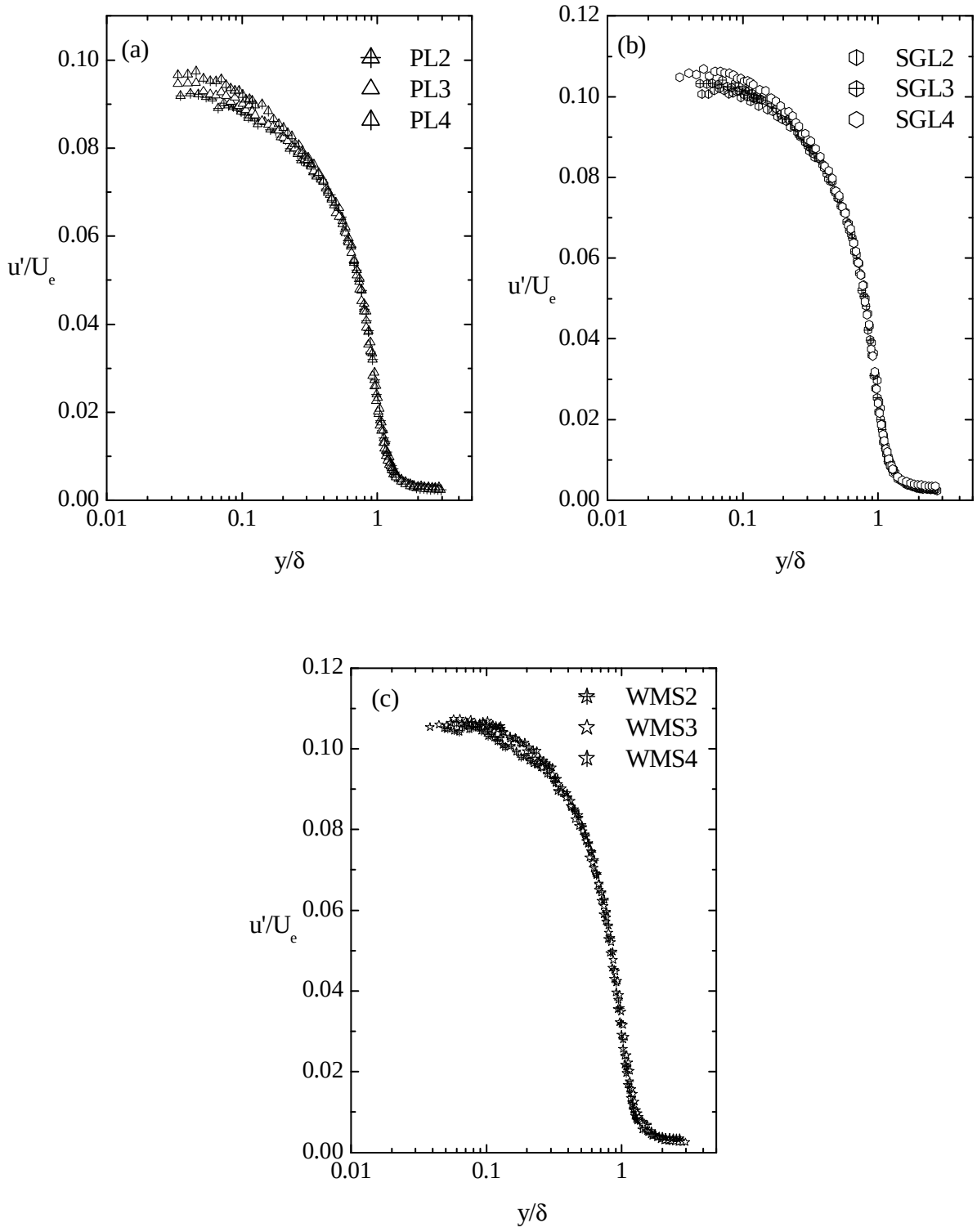

Figure 6.9: Streamwise turbulence intensity distributions on fully rough flows using outer coordinates: (a) perforated sheet; (b) sand grain; (c) wire mesh.

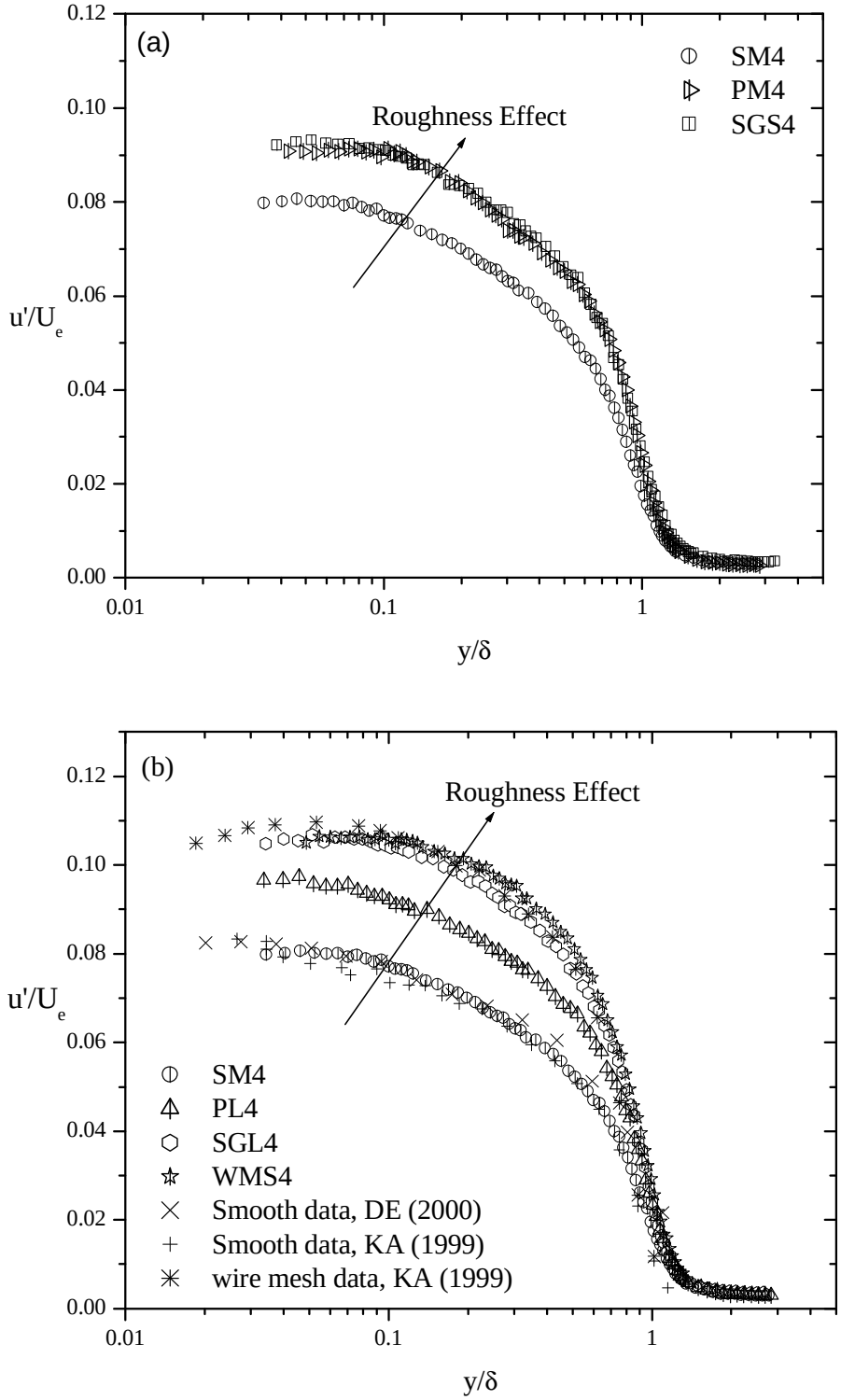

Figure 6.10: Streamwise turbulence intensity distributions surfaces using outer coordinates: (a) smooth and transitionally rough; (b) smooth and fully rough (DE and KA denote DeGraaf and Eaton (2000) and Krogstad and Antonia (1999), respectively).

Figure 6.10b. Also included for comparison are the smooth wall of DeGraaf and Eaton (2000) at Re_θ = 13, 000 and wire mesh data sets of Krogstad and Antonia (1999) at Re_θ = 12,800, respectively, in Figure 6.10b. The comparison shows that the present smooth and wire mesh surface data are in good agreement with the smooth data of DeGraaf and Eaton (2000) and wire mesh data of Krogstad and Antonia (1999), respectively, within the experimental uncertainty. It is observed that the effect of surface roughness is much more pronounced when the streamwise turbulence intensity is scaled with the freestream velocity, and this effect extends almost to the outer edge of the boundary layer. The strength of the roughness effect produced by each rough surface is reflected by the level of each profile compared to that for the smooth wall. For the transitionally rough flows, the streamwise turbulence intensity data for perforated sheet (PM4) and sand grain (SGS4) are 15 % and 16 % higher, respectively, than that on a smooth surface in the near-wall region ($y/\delta \approx 0.06$). As shown in Figure 6.10b, the streamwise turbulence intensity profile for perforated sheet (PL4) falls in between the smooth wall data and the data for the other two rough surfaces (SGL4 and WMS4). In the near-wall region ($y/\delta \approx 0.06$), the streamwise turbulence intensity data for PL4, SGL4, and WMS4 are 21%, 31%, and 33%, higher, respectively, than that on the smooth surface. Despite their different surface geometry characteristics, the magnitude of the roughness effect produced by both the sand grain and wire mesh on the streamwise turbulence intensity data is similar. Comparing Figures 6.4 and 6.10, it is obvious that scaling the streamwise turbulence intensity data with the freestream velocity is useful for illustrating the overall effect of the surface roughness. Similar to the conclusions of Tachie et al. (2003), the streamwise Reynolds stress profiles for the

different surfaces are distinct from each other not only in the wall region, but also over most of the outer region of the boundary layer.

Figure 6.11 shows the distributions of the streamwise turbulence intensity normalised with the mixed outer scale, $U_e\delta^*/\delta$, for hydraulically smooth and transitionally rough flows at different Reynolds numbers. The streamwise turbulence intensity data for fully rough flows scaled with the mixed outer scale, $U_e\delta^*/\delta$, are presented in Figure 6.12. The mixed outer scaling consistently collapses the streamwise turbulence intensity profiles for different Reynolds numbers on each surface considered within the region $y/\delta > 0.1$. This performance is comparable to some of the scaling parameters noted above.

Figures 6.13a and 6.13b compare the distributions of the streamwise turbulence intensity obtained for smooth and rough surfaces at the highest Reynolds number. Also included for comparison are the smooth wall data of DeGraaf and Eaton (2000) at Re_θ = 13,000, and the wire mesh data of Antonia and Krogstad (1993) at Re_θ = 13,040 in Figure 6.13b. Unlike the previous scaling parameters, the streamwise turbulence intensity data scaled with the mixed outer scale shows minimal effect of either surface roughness or Reynolds number in the outer region of the flow. All of the profiles collapse onto each other to form a single curve in the region $y/\delta > 0.2$. This observation suggests that the mixed outer scale can be used to obtain a self-similar

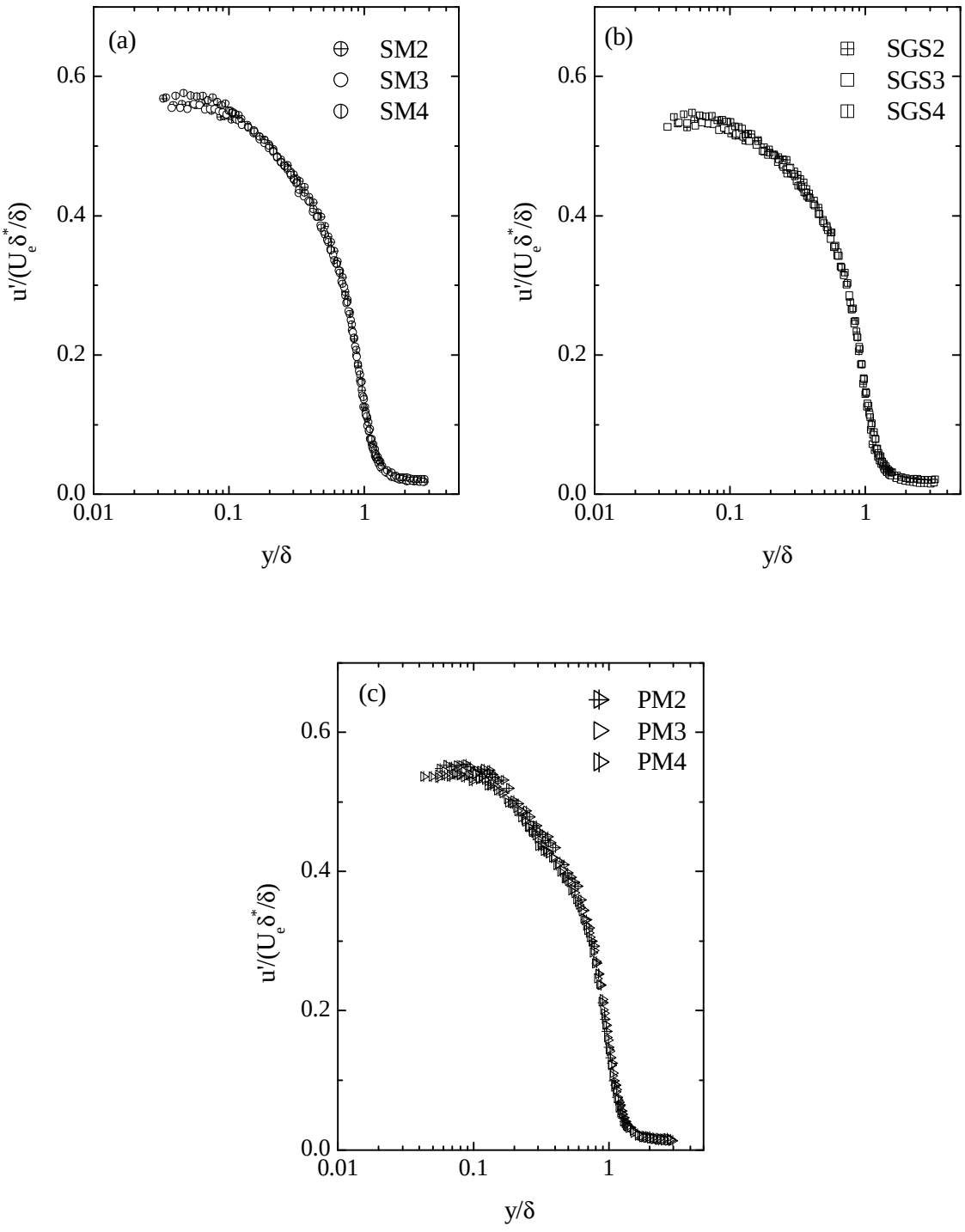

Figure 6.11: Streamwise turbulence intensity distributions for smooth and transitionally rough flows using outer mixed scale: (a) smooth; (b) sand grain; (c) perforated sheet.

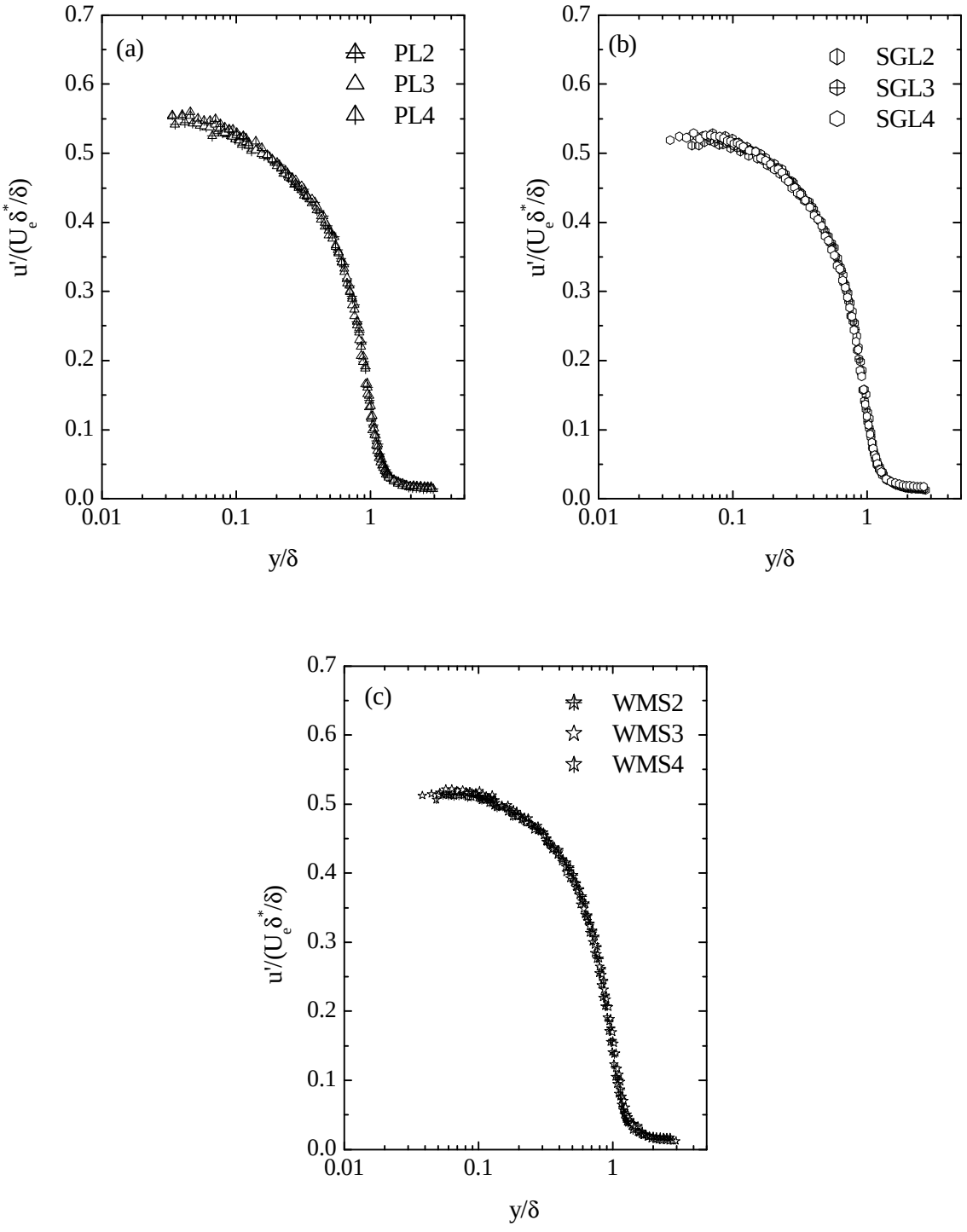

Figure 6.12: Streamwise turbulence intensity distributions on fully rough flows using outer mixed scale: (a) perforated sheet; (b) sand grain; (c) wire mesh.

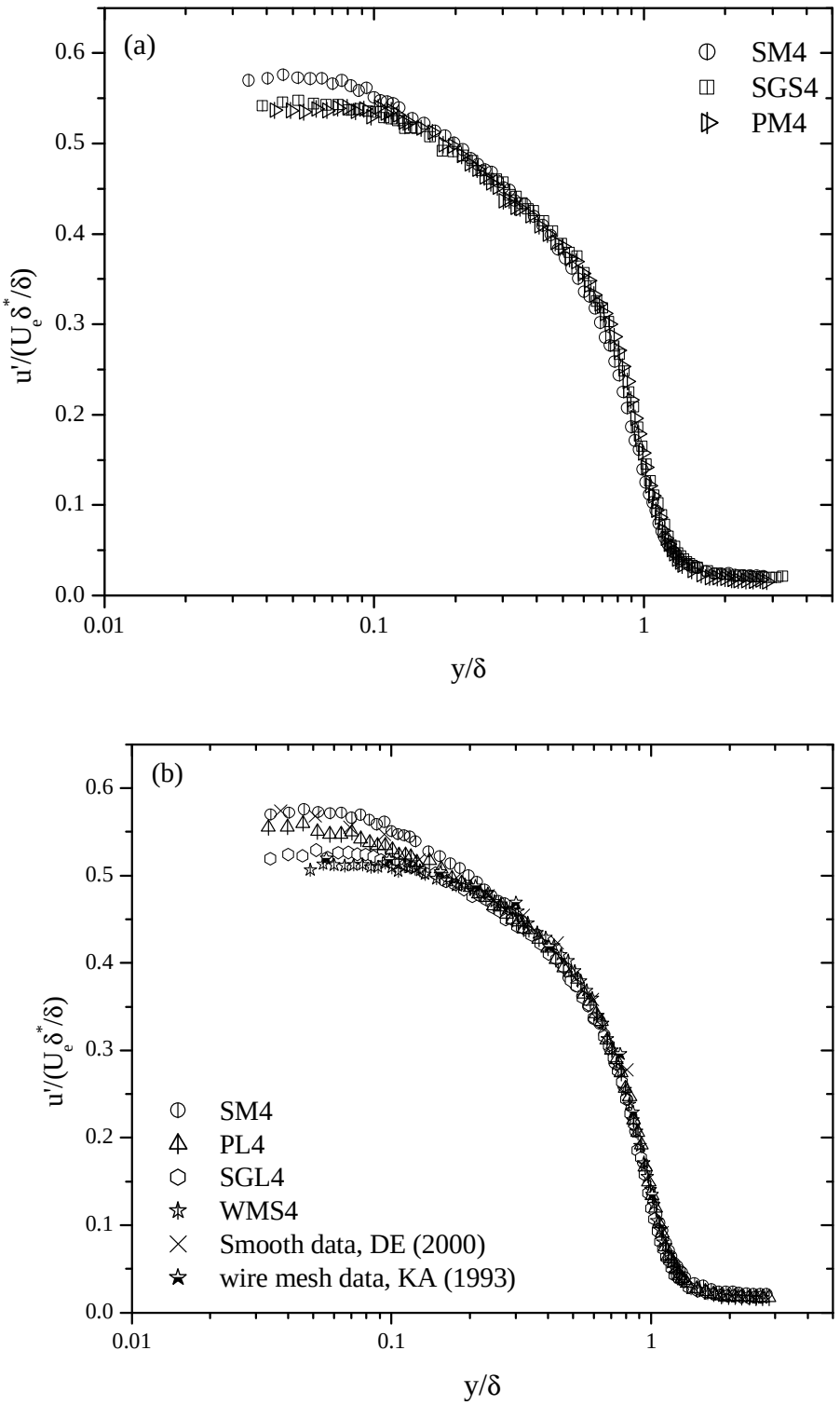

Figure 6.13: Streamwise turbulence intensity distributions surfaces using outer mixed scale: (a) smooth and transitionally rough; (b) smooth and fully rough (DE and KA denote DeGraaf and Eaton (2000) and Krogstad and Antonia (1993), respectively).

profile for the streamwise turbulence intensity profile irrespective of the surface condition in the outer region of the flow. The mixed outer scale fails to collapse the streamwise turbulence intensity data for the different surfaces in the inner region, however, the understanding of the failure of the mixed outer scale in this region still requires further investigation.

6.3 Wall-Normal Turbulence Intensity

Figure 6.14 presents the wall-normal turbulence intensity profiles normalized by the friction velocity for a hydraulically smooth surface. The wall-normal turbulence intensity data of the smooth wall data of Spalart (1988) at Re_θ = 1410 and smooth wall data of Antonia and Krogstad (2001) at Re_θ = 12,570 are also included for comparison in Figure 6.14. Comparison among the present smooth wall data, DNS data of Spalart (1988), and experimental data of Antonia and Krogstad (2001) shows reasonably good agreement.

Figure 6.15 compares the distributions of the wall-normal turbulence intensity scaled with friction velocity for smooth and rough surfaces. The wall-normal turbulence intensity data for the smooth wall compared with those of nominal transitionally rough flows, is indicated in Figure 6.15a. Also shown for comparison are the experimental data for a smooth wall of Antonia and Krogstad (2001) at Re_θ = 12,570. The present smooth wall data are observed to be in good agreement with those of Antonia and Krogstad (2001) within the experimental uncertainty. Near the wall $(y/\delta < 0.1)$, the wall-normal

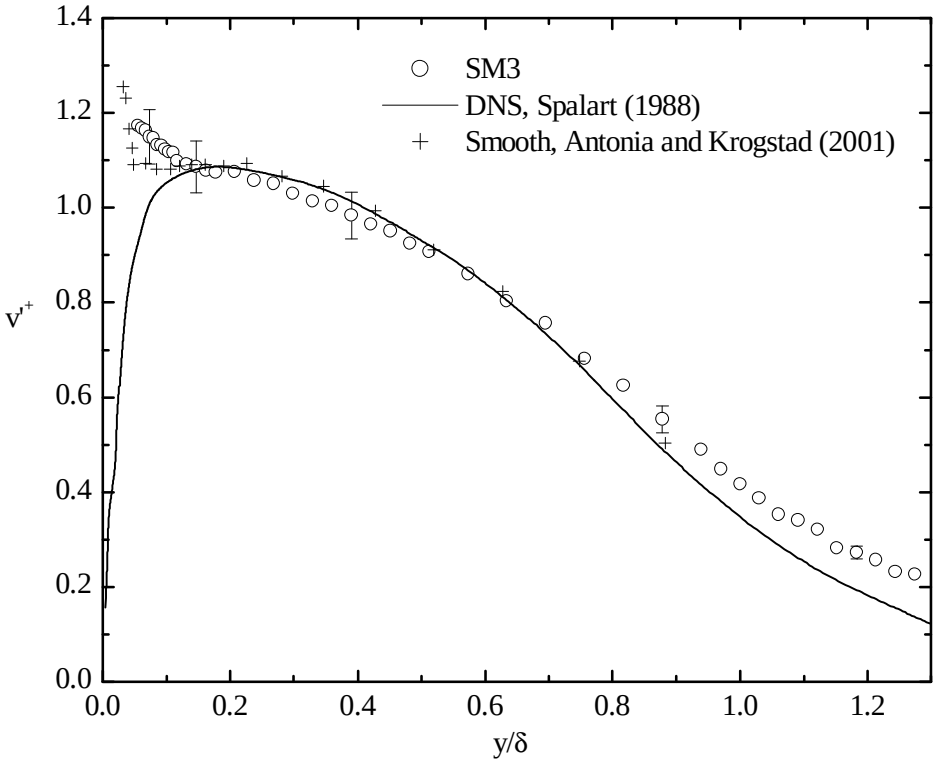

Figure 6.14: Wall-normal turbulence intensity profiles scaled by friction velocity for a smooth surface.

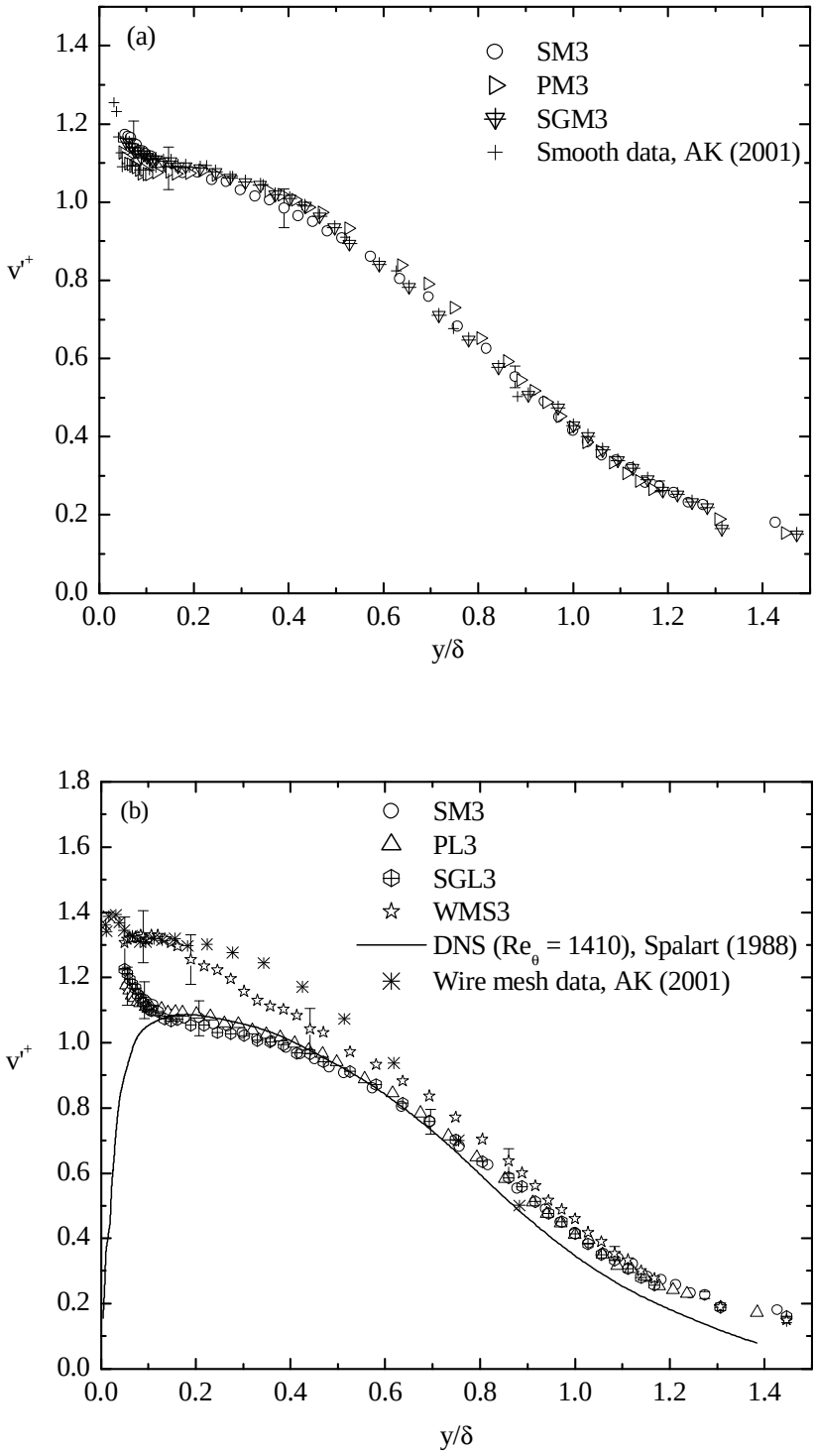

Figure 6.15: Wall-normal turbulence intensity profiles using inner coordinates: (a) smooth and transitionally rough; (b) smooth and fully rough (AK denotes Antonia and Krogstad (2001)).

turbulence intensity data for both PM3 and SGM3 are observed to be slightly lower than on a smooth surface. The wall-normal turbulence intensity profiles for the smooth and nominal transitionally rough flows are observed to achieve self-similar condition as the profiles collapse onto each other throughout the overlap and outer regions of the boundary layer.

Figure 6.15b compares the wall-normal turbulence intensity profiles for the smooth and fully rough flows normalized by the friction velocity. The wall-normal turbulence intensity data of the smooth wall direct numerical simulation (DNS) by Spalart (1988) at Re_θ = 1410 and wire mesh data of Antonia and Krogstad (2001) at Re_θ = 12,800 are also included for comparison in the Figure 6.14b. Except for the wire mesh roughness, the wall-normal turbulence intensity profiles for the smooth wall, perforated sheet, and sand grain roughness exhibit good collapse in both the overlap and outer regions of the boundary layer. Schultz and Flack (2003) reported a similar collapse of the wall-normal turbulence intensity profiles for sand grain and a surface roughness created by "surface painting" outside the roughness sublayer. In contrast, both wire mesh data show substantially higher values than the smooth data over a significant portion of the boundary layer. These results support recent observations that the effect of surface roughness can extend into the outer region of the boundary layer (e.g. Antonia and Krogstad, 2001; Keirsbulck et al., 2002; Tachie et al., 2003). However, the results of Flack et al. (2005) for the wall-normal turbulence intensity for a wire mesh surface disagree with the results in this thesis. They observed no effects of the surface roughness in both the overlap and outer region of the boundary layer. From the perspective of the

geometrical layout of the wire mesh, the upstream flow in the vicinity of the wall interacts with the cavities within the mesh. In addition, the wires at the point of interlacing also act as “local blockage” to the flow adjacent to the wall. Combination of these interactions can be linked to the behaviour observed for the wall-normal turbulence intensity on the wire-mesh roughness.

Figure 6.16 compares the distributions of the wall-normal turbulence intensity scaled by the freestream velocity for smooth and rough surfaces using outer coordinates. The theory of George and Castillo (1997) supported the use of the freestream velocity as the appropriate scaling parameter for the Reynolds stresses. The wall-normal turbulence intensity data for the smooth wall compared with those of nominal transitionally rough flows, is shown in Figure 6.16a. Comparison of the wall-normal turbulence intensity profiles for the smooth and fully rough flows are presented in Figure 6.16b. As shown in Figure 6.16, clear differences between the smooth- and rough-wall data are evident over most of the boundary layer. A similar conclusion was drawn by Tachie et al. (2003) in their study of the roughness effect in a low Reynolds number open-channel turbulent boundary layer. A distinct feature of this scaling parameter is that the effect of roughness on the wall-normal turbulence intensity follows the increase in the roughness shift, ΔU^+. For example, the wire mesh produced the largest roughness shift, and it also exhibits the highest dimensionless wall-normal turbulence level in Figure 6.16b. Even though of higher value, the shape of the wall-normal turbulence intensity profiles for both the perforated sheet (PM3) and sand grain (SGM3) for the transitionally rough, as well

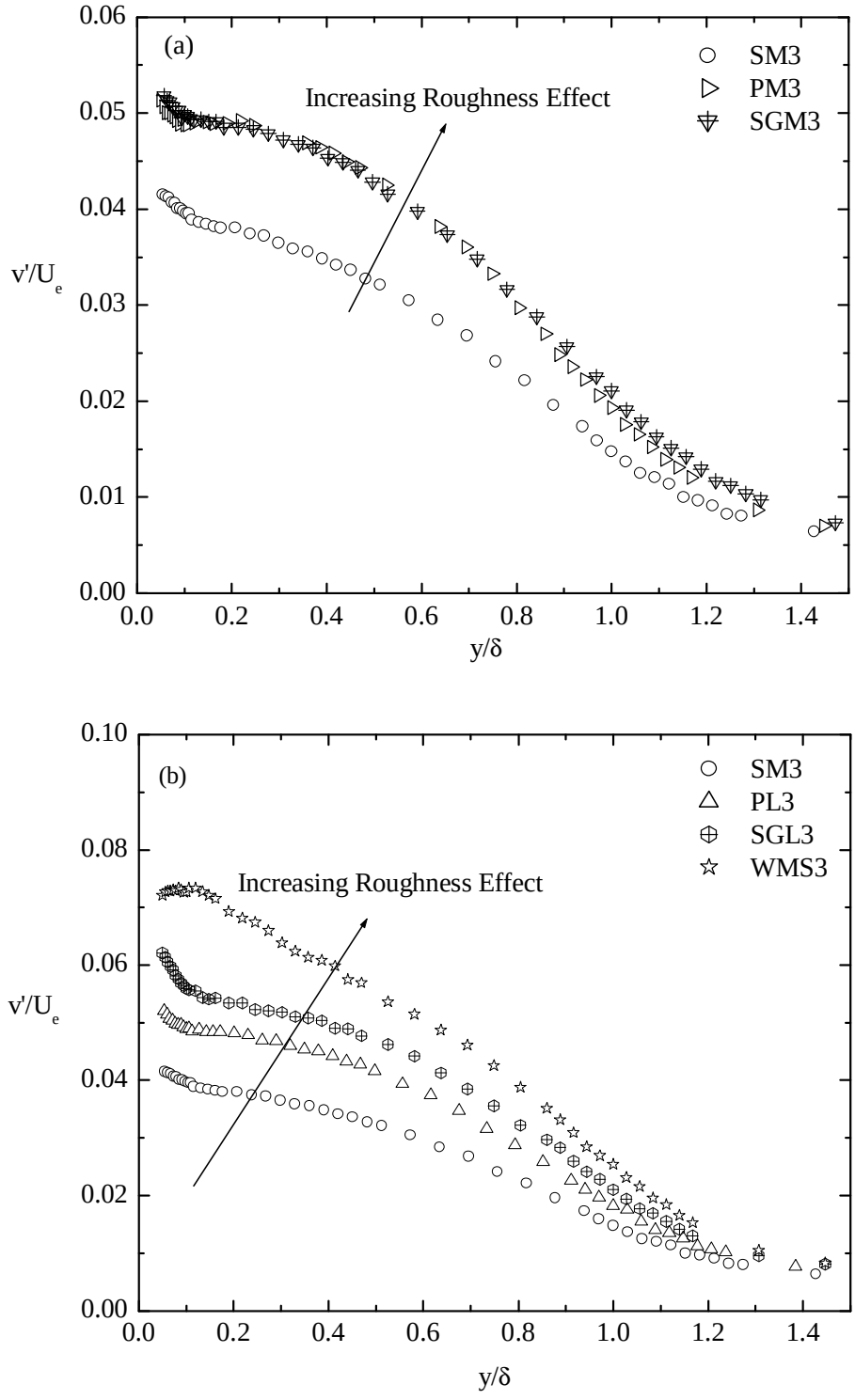

Figure 6.16: Wall-normal turbulence intensity profiles using outer coordinates: (a) smooth and transitionally rough; (b) smooth and fully rough.

as the perforated sheet (PL3) and to a lesser degree the sand grain (SGL3) for the fully rough are similar to that on the smooth wall. Recall that these two profiles collapsed with the smooth profile when scaled with the friction velocity, U_τ, in Figure 6.15.

Figure 6.17 presents the wall-normal turbulence intensity profiles obtained for the smooth and rough surfaces normalized by the mixed outer scale, $U_e\delta^*/\delta$. The effect of surface roughness on the wall-normal turbulence intensity profiles is observed to be less pronounced with this scaling compared to the freesream velocity. For the transitionally rough flow, the wall-normal turbulence intensity profiles for PM3 and SGM3 are generally close to each other. For the fully rough flow, except for the wire mesh (WMS3), the wall-normal turbulence intensity profiles for PL3 and SGL3 appear similar to each other and somewhat different than that of the smooth surface. Although, the mixed outer scale does not show a similar performance to that observed with the streamwise turbulence intensity profiles, it performs better than the freestream velocity in the context of collapsing the wall-normal turbulence intensity profiles obtained for smooth and rough surfaces.

6.4 Reynolds Shear Stress

Figure 6.18 presents the Reynolds shear stress profiles obtained for the hydraulically smooth wall normalized by the friction velocity. Also included for comparison are the smooth wall data of Spalart (1988) at Re_θ = 1410 and measurements of the experimental

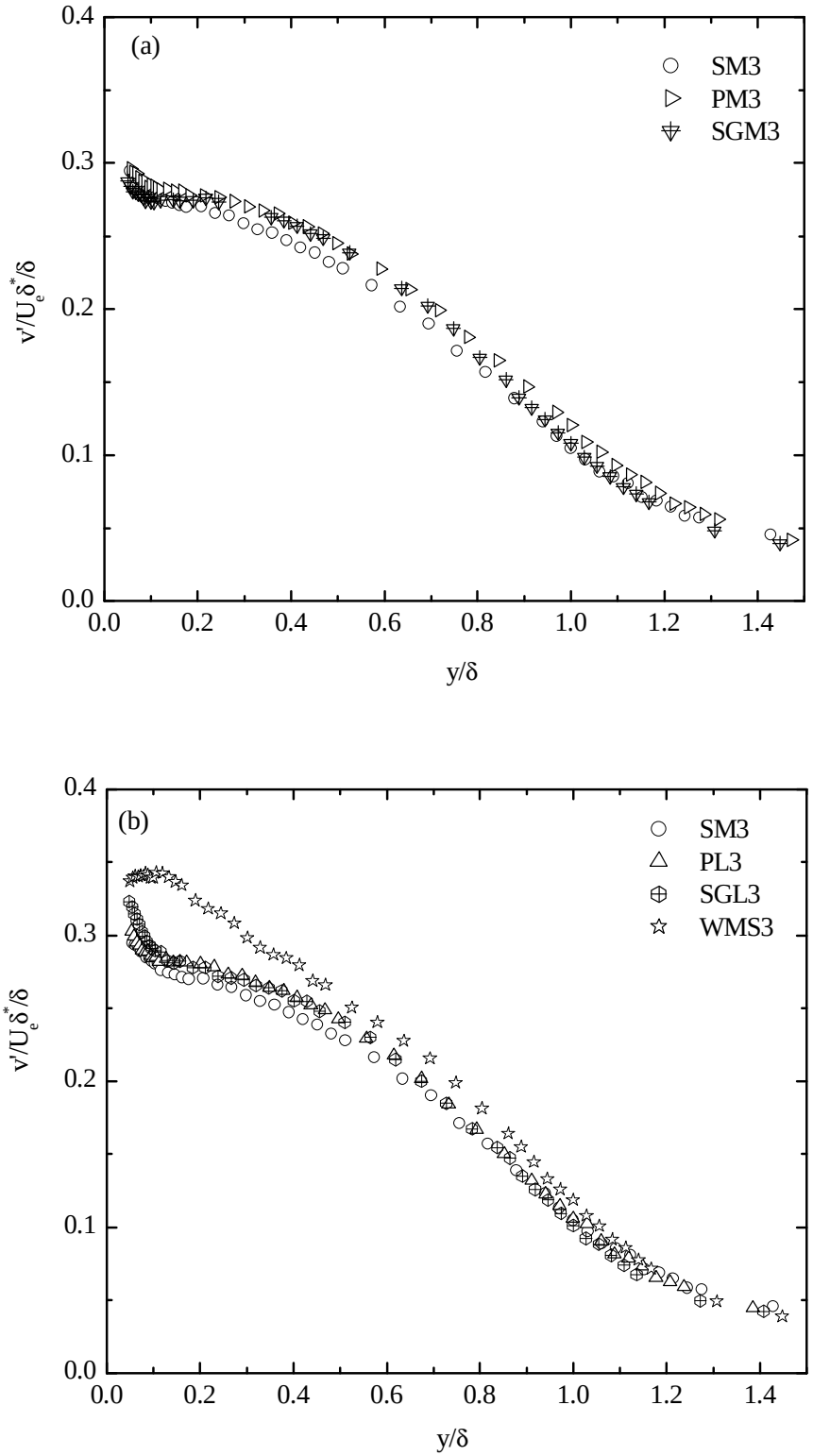

Figure 6.17: Wall-normal turbulence intensity profiles normalized by $U_e\delta^*/\delta$: (a) smooth and transitionally rough; (b) smooth and fully rough.

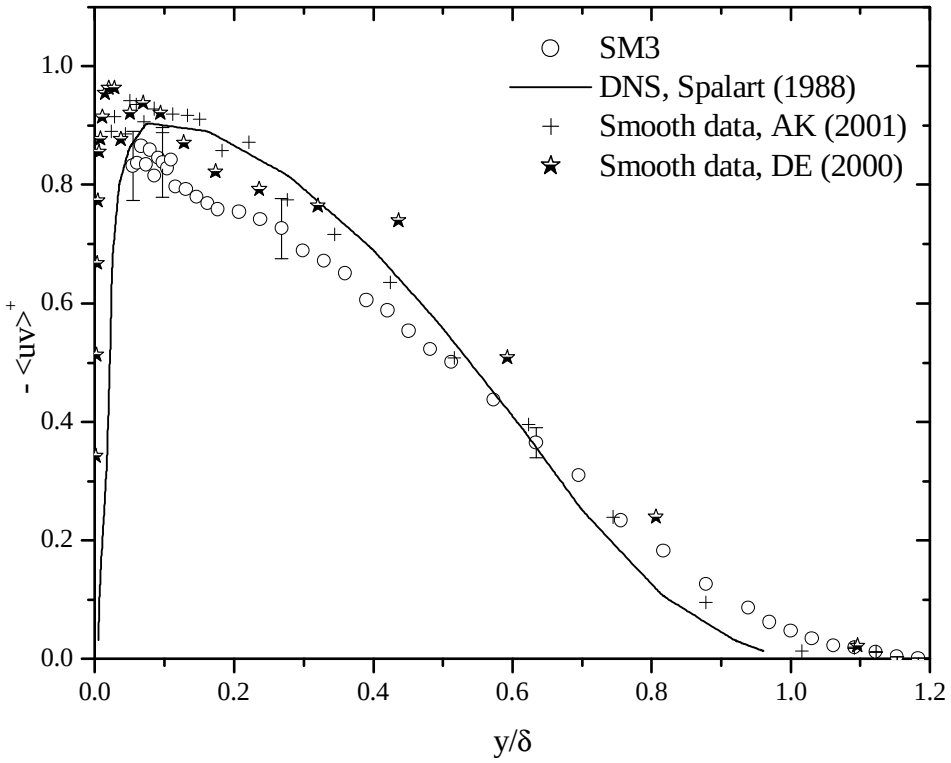

Figure 6.18: Reynolds shear stress profiles for a smooth surface using inner coordinates (AK and DE denote Antonia and Krogstad (2001) and DeGraaf and Eaton (2000)).

data of Antonia and Krogstad (2001) and DeGraaf and Eaton (2000) at Re_θ = 12,570 and 13,000, respectively. The peak value of the present smooth data is $-<uv>^+ \cong 0.86$ which is slightly lower than the values of 0.9, 0.94, and 0.96 for the DNS data, Krogstad and Antonia (2001), and DeGraaf and Eaton (2000), respectively. Fernholz and Finley (1997) reported that the peak value is between $-<uv>^+ = 0.8$ and 1.0 in their assessment of different Reynolds shear stress data obtained by different research groups.

Figure 6.19 presents the Reynolds shear stress profiles normalised by the friction velocity for the smooth and rough surfaces. The distributions of Reynolds shear stress for hydraulically smooth and transitionally rough flows are shown in the Figure 6.19a. For both the perforated sheet and sand grain surfaces, the effects of the surface roughness are observed to be less significant in the near-wall region ($y/\delta < 0.1$). Beyond this region, the effects of surface roughness slightly enhance the level of the Reynolds shear stress profiles, and this extends into the outer region of the flow.

Figure 6.19b compares the Reynolds shear stress profiles obtained for the hydraulically smooth and fully rough flows scaled by the friction velocity. Also included for comparison is the wire mesh data sets of Antonia and Krogstad (2001) at Re_θ = 12,800 in Figure 6.18b. The present wire mesh data generally follow the trend of the experimental data of Antonia and Krogstad (2001) within experimental uncertainty. The Reynolds shear stress data for all the rough surfaces considered are higher than those on

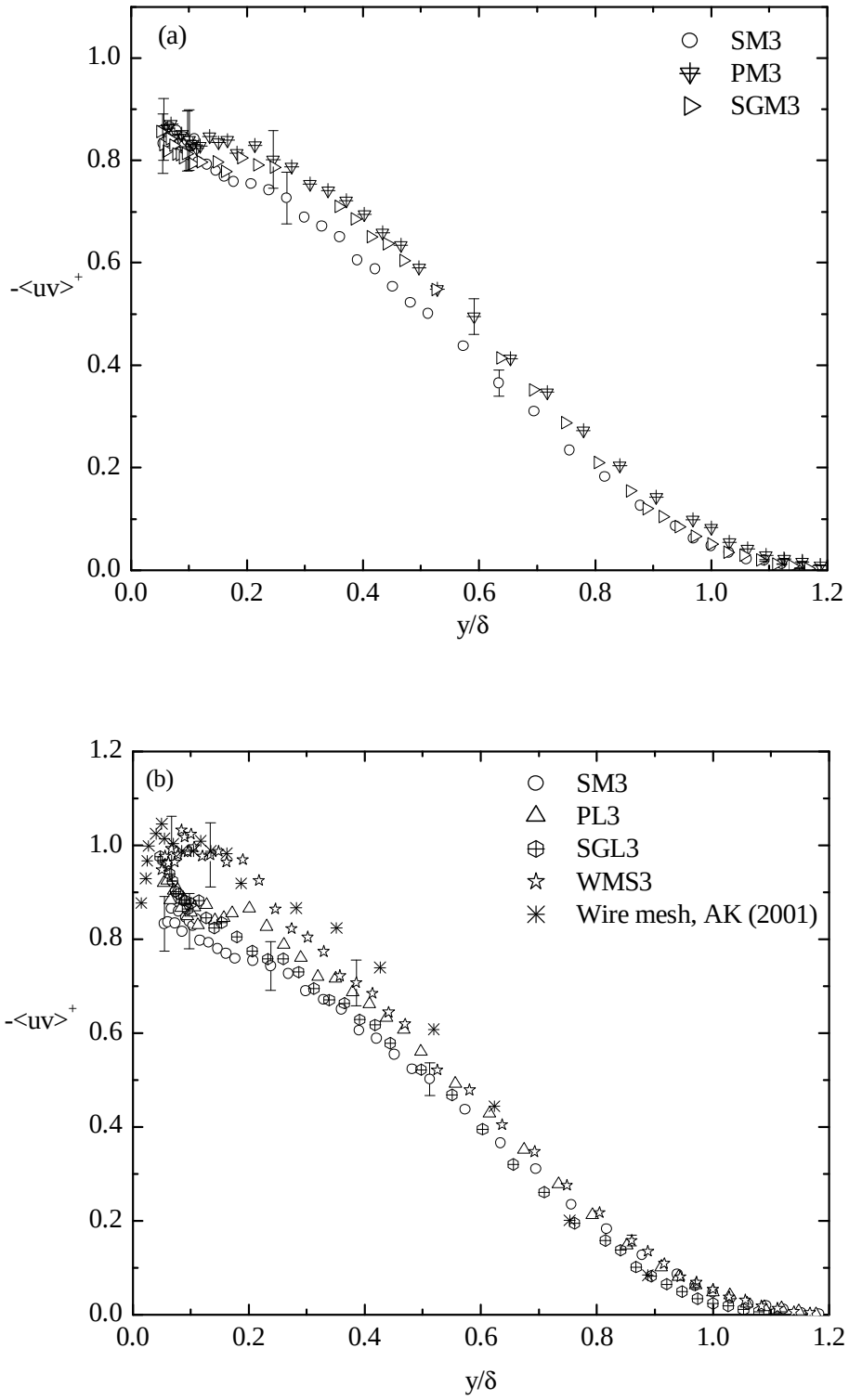

Figure 6.19: Reynolds shear stress profiles using inner coordinates: (a) smooth and transitionally rough; (b) smooth and fully rough.

the smooth surface in both the inner and lower part of the outer regions of the boundary layer. For instance, for the perforated sheet and sand grain roughness, noticeable surface roughness effects on the Reynolds shear stress are observed in the region $y/\delta \leq 0.4$, as indicated in Figure 6.19b. Finally, for the wire mesh, a plateau of $-<uv>^{+} \approx 1.0$ extends from $y/\delta \approx 0.07$ to 0.15. In addition, the effect of surface roughness is to dramatically enhance the level of the Reynolds shear stress in the near-wall region, and this extends into the outer region of the flow. The wire mesh results support the conclusions drawn by Krogstad et al. (1992), Antonia and Krogstad (2001), Keirsbulck et al. (2002), and Tachie et al. (2003), which are in disagreement with the wall similarity hypothesis.

Figure 6.20 presents the distributions of the Reynolds shear stress scaled by the freestream velocity for the smooth and rough surfaces using outer coordinates. Note that using this scaling, both the transitionally rough and fully rough surfaces produced a dramatic increase in the dimensionless Reynolds shear stress level. The wire mesh surface (fully rough) still produced the highest $<uv>^{+}$ values. Comparing Figures 6.19 and 6.20, the effect of surface roughness on the Reynolds shear stress is more pronounced when scaled by the freestream velocity.

Figure 6.21 presents the Reynolds shear stress profiles obtained for smooth and rough surfaces normalized by the mixed outer scale, $U_e\delta^*/\delta$. Although, the mixed

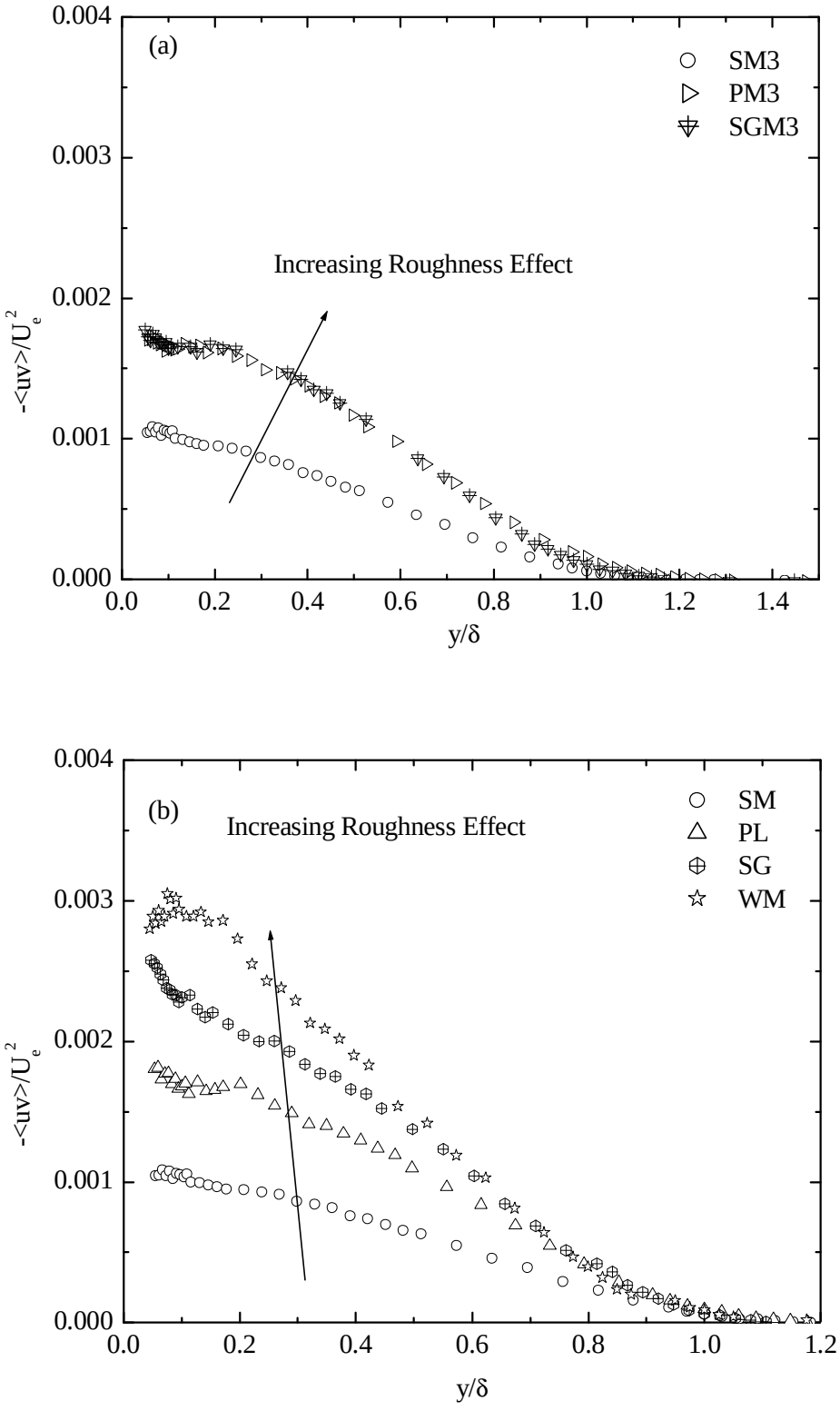

Figure 6.20: Reynolds shear stress profiles using outer coordinates: (a) smooth and transitionally rough; (b) smooth and fully rough.

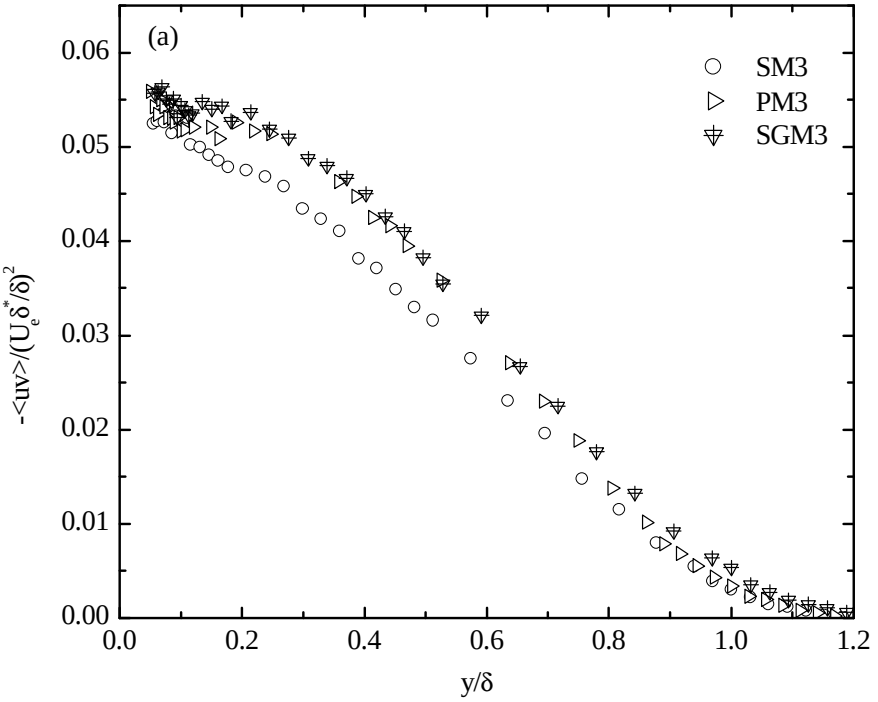

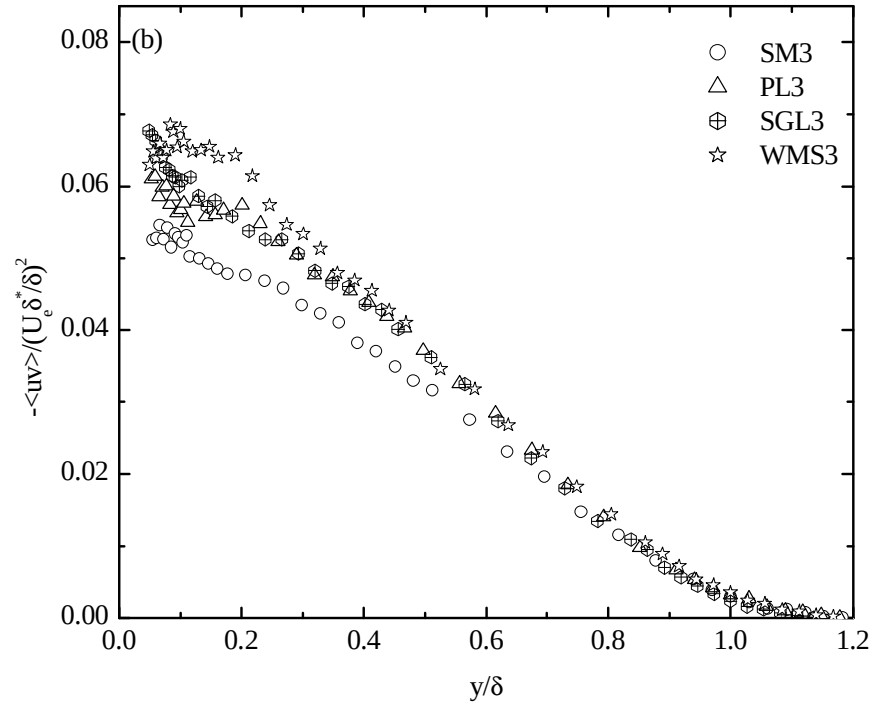

Figure 6.21: Reynolds shear stress profiles normalized by $U_e\delta^*/\delta$: (a) smooth and transitionally rough; (b) smooth and fully rough.

outer scale does not collapse the Reynolds shear stress profiles for both the smooth and rough surfaces, but the effect of the surface roughness is less pronounced on the Reynolds shear stress profiles when scaled with this parameter compared to the freestream velocity.

6.5 Summary

The results presented in this chapter carefully examine the streamwise turbulence intensity profile in a zero pressure gradient turbulent boundary layer using four different scaling parameters for four different surfaces at three different Reynolds numbers. The scaling parameters are: the friction velocity, U_τ; the freestream velocity, U_e; mixed scaling, $U_\tau U_e$; and the mixed outer scale, $U_e\delta^*/\delta$. The experimental results clearly show that the friction velocity, U_τ, does reasonably well in collapsing the streamwise turbulence intensity profiles obtained for the perforated sheet and sand paper roughness, but is unable to completely collapse the streamwise turbulence intensity profiles for the smooth surface and wire mesh. The streamwise turbulence intensity profiles for the smooth and rough surfaces all exhibit some Reynolds number dependence in the inner region when scaled with the freestream velocity. Furthermore the effect of surface roughness on the streamwise turbulence intensity profiles is much more pronounced when scaled with the freestream velocity. The mixed scaling of DeGraaf and Eaton(2000) does a fairly good job of collapsing the streamwise streamwise turbulence intensity profiles on the smooth surface, perforated sheet, sand paper, and wire mesh in the outer region of the flow. However, the mixed scaling was not able to collapse the streamwise turbulence intensity profiles on both the smooth and rough surfaces. Finally,

when the streamwise turbulence intensity profile is scaled with the mixed outer scale, $U_e\delta^*/\delta$, differences due to both Reynolds number and surface roughness are nearly eliminated. In this case, the streamwise turbulence intensity profiles in the outer region all collapse onto a single curve which then represents a self-similar profile.

When scaled with the friction velocity, surface roughness was generally found to modify the profile of the streamwise turbulence intensity and also the Reynolds shear stress throughout the extent of the boundary layer. The profiles on the rough surfaces were observed to be higher than those on a hydraulically smooth surface. For the Reynolds shear stress profile, the effect was most prominent in the inner region of the boundary layer. For the wall-normal turbulence intensity profile, a significant roughness effect was only observed for the wire-mesh roughness. When scaled with the freestream velocity, the profiles of all Reynolds stress components exhibited a clear and prominent effect of surface roughness, which was to increase the profile relative to the smooth wall case. Furthermore, the degree of enhancement of the turbulence profiles matched the effect of roughness as indicated by the magnitude of the roughness shift. From analysis using both scalings, one would conclude that the wire mesh surface produced the greatest roughness effect on the fluctuating velocity field. As summarized above, the present study offers experimental evidence, which contradicts the wall similarity hypothesis, except perhaps for the case of the wall-normal turbulence intensity on the perforated sheer and sand grain surfaces. As such, effect of surface roughness on the turbulence field depends on some degree on the specific characteristics of the roughness elements and also the component of the Reynolds stress tensor being considered.

CHAPTER 7

ROUGHNESS EFFECTS ON HIGHER-ORDER MOMENTS OF THE VELOCITY FLUCTUATIONS

7.1 Introduction

The higher-order moments contain valuable statistical information which relates to the turbulent flux of the Reynolds stress. Antonia and Krogstad (2001) noted that the velocity triple products are expected to be a more sensitive indicator of the effect of surface roughness than the second-order moments. The transport equation for the Reynolds stresses can be expressed as follows:

$$\frac{\partial \rho U_k \langle u_i u_j \rangle}{\partial x_k} = \frac{\partial}{\partial x_k}\left(\underbrace{\mu \frac{\partial \langle u_i u_j \rangle}{\partial x_k}}_{D_{ij}^{\nu}} \right) - \frac{\partial}{\partial x_k}\left(\underbrace{\rho \langle u_i u_j u_k \rangle}_{D_{ij}^{t}} + \underbrace{\langle p u_i \rangle \delta_{jk} + \langle p u_j \rangle \delta_{ik}}_{D_{ij}^{P}} \right)$$
$$- \left(\underbrace{\rho \langle u_i u_k \rangle \frac{\partial U_j}{\partial x_k} + \rho \langle u_j u_k \rangle \frac{\partial U_j}{\partial x_k}}_{P_{ij}} \right) + \underbrace{p\left\langle \frac{\partial u_i}{\partial x_j} + \frac{\partial u_j}{\partial x_i} \right\rangle}_{\Phi_{ij}} - \underbrace{2\mu \left\langle \frac{\partial u_i}{\partial x_k} \frac{\partial u_j}{\partial x_k} \right\rangle}_{\varepsilon_{ij}} \tag{7.1}$$

where D_{ij}^{ν} is the viscous diffusion of the turbulent fluxes, D_{ij}^{t} is the turbulent diffusion due to interaction between the fluctuating velocity components, D_{ij}^{P} is the pressure diffusion due to the interaction between the fluctuating pressure and fluctuating velocity

fields, P_{ij} is the production of the turbulent fluxes arising from the interaction between the fluctuating velocity and mean velocity gradient, Φ_{ij} is the pressure-strain correlation caused by the interaction between the fluctuating pressure and the fluctuating strain rates, and ε_{ij} is the dissipation rate of the turbulent fluxes. The triple correlation $<u_i u_j u_k>$ appears as $<u'^3>$, $<v'^3>$, $<u^2v>$, and $<uv^2>$ in the Reynolds stress transport equations. Their spatial gradients represent part of the turbulent diffusion of Reynolds stress components in the Reynolds stress transport equations. In this chapter, experimental data for the triple velocity correlations ($<u'^3>$, $<v'^3>$, $<u^2v>$, and $<uv^2>$), as well as skewness and flatness factors obtained for the smooth surface and five different rough surfaces are reported. Specifically, the higher-order moments of the velocity fluctuation data for both the nominal transitionally rough and fully rough flow regimes are discussed. The effects of surface roughness on the triple correlations are assessed using the friction velocity, U_τ, and the mixed scaling, $U_e U_\tau^2$, derived from the Asymptotic Invariance Principle (AIP) by George and Castillo (1997). The effects of the surface roughness on the skewness and flatness factors are also examined.

7.2 Triple Correlation

7.2.1 $<u'^3>$ profiles

Figure 7.1 presents the distributions of $<u'^3>$, which represents the average transport of $<u'^2>$by the turbulent motion in the streamwise direction, for smooth and rough surfaces, normalized by friction velocity. The distributions of $<u'^3>^+$ for smooth wall and nominal transitionally rough flows are shown in the Figure 7.1a. For both perforated sheet (PM3)

and sand grain (SGM3), the $\langle u'^3 \rangle^+$ data appear higher than that of a smooth surface in the near-wall region ($y/\delta < 0.2$). Beyond this region, the $\langle u'^3 \rangle^+$ profiles for the PM3 and SGM3 surfaces achieve reasonable collapse with the smooth wall. Figure 7.1b compares the $\langle u'^3 \rangle^+$ profiles for smooth wall and fully rough flows. There is little difference between the sand grain and smooth wall data for $\langle u'^3 \rangle^+$. However, the distributions of $\langle u'^3 \rangle^+$ for the perforated sheet and wire mesh roughness are observed to be higher than on a smooth surface within the region $y/\delta < 0.3$. Schultz and Flack (2005) reported similar observations for the $\langle u'^3 \rangle^+$ profile for flow over uniform spheres. The sign of $\langle u'^3 \rangle^+$ profile is negative for the smooth wall for $y/\delta > 0.06$, whereas, it is positive for the rough walls for $y/\delta < 0.1$. This behaviour can be attributed to the reduced frequency of sweep events (the occurrence of high-speed fluid from regions distant from the wall) for the smooth wall compared to the rough surfaces, resulting in an increase in the turbulent flux of streamwise Reynolds stress in the streamwise direction for the rough surfaces.

Figure 7.2 presents the distributions of $\langle u'^3 \rangle$ for the smooth and rough surfaces normalized by the mixed scaling, $U_e U_\tau^2$. The $\langle u'^3 \rangle$ data for the smooth wall and transitionally rough flows are presented in the Figure 7.1a. For both the perforated sheet (PM3) and sand grain roughness (SGM3), as indicated in Figure 7.2a, the effect of surface roughness enhances the level of the $\langle u'^3 \rangle$ profiles, and this effect is observed within the region $y/\delta < 0.2$. This observation is qualitatively similar to the $\langle u'^3 \rangle$ data scaled with the friction velocity shown in Figure 7.2a. The comparison of the $\langle u'^3 \rangle$ data for the smooth wall and fully rough flows is presented in Figure 7.2b. For the sand grain

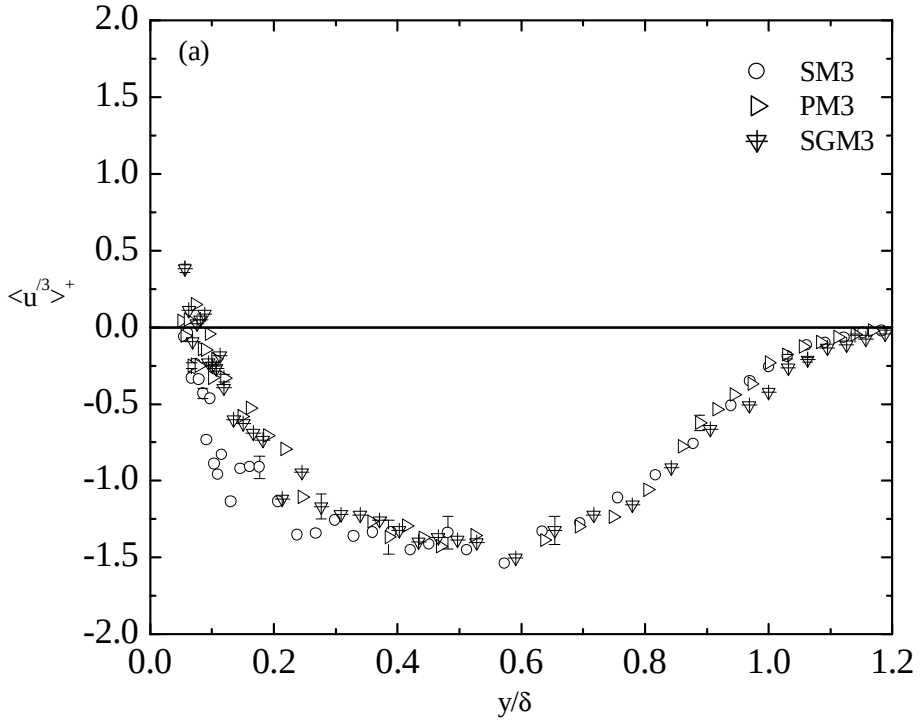

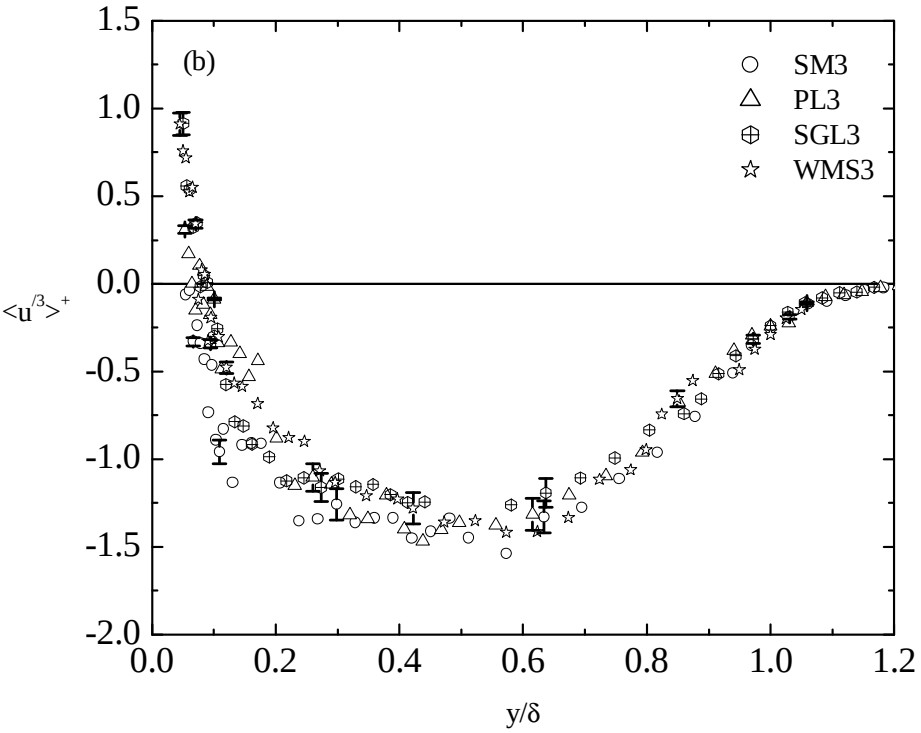

Figure 7.1: Distributions of triple correlation, $< u'^3 >$, using inner coordinates: (a) smooth and transitionally rough; (b) smooth and fully rough.

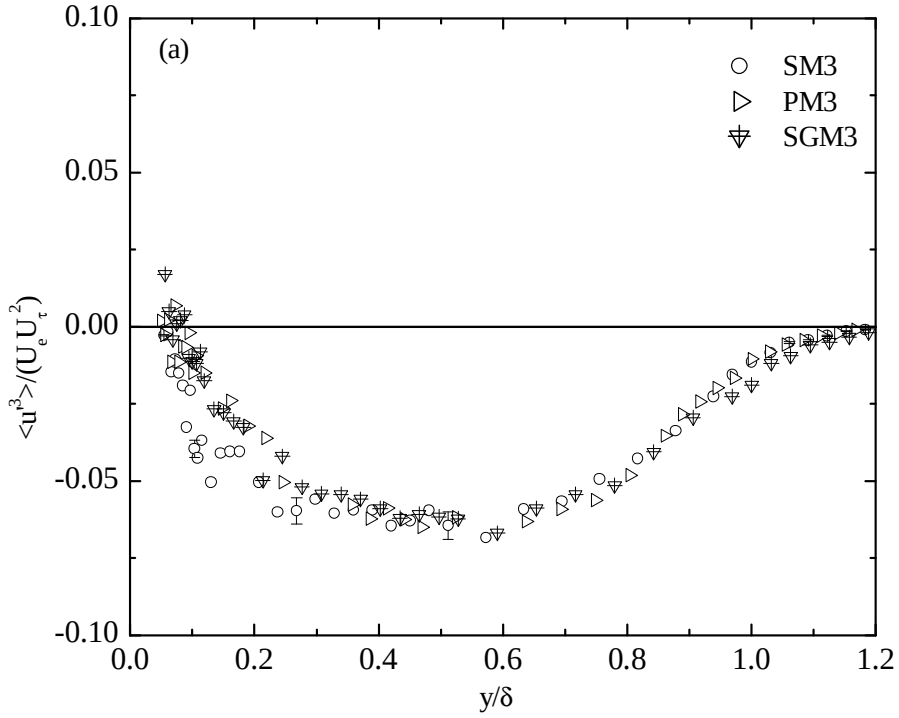

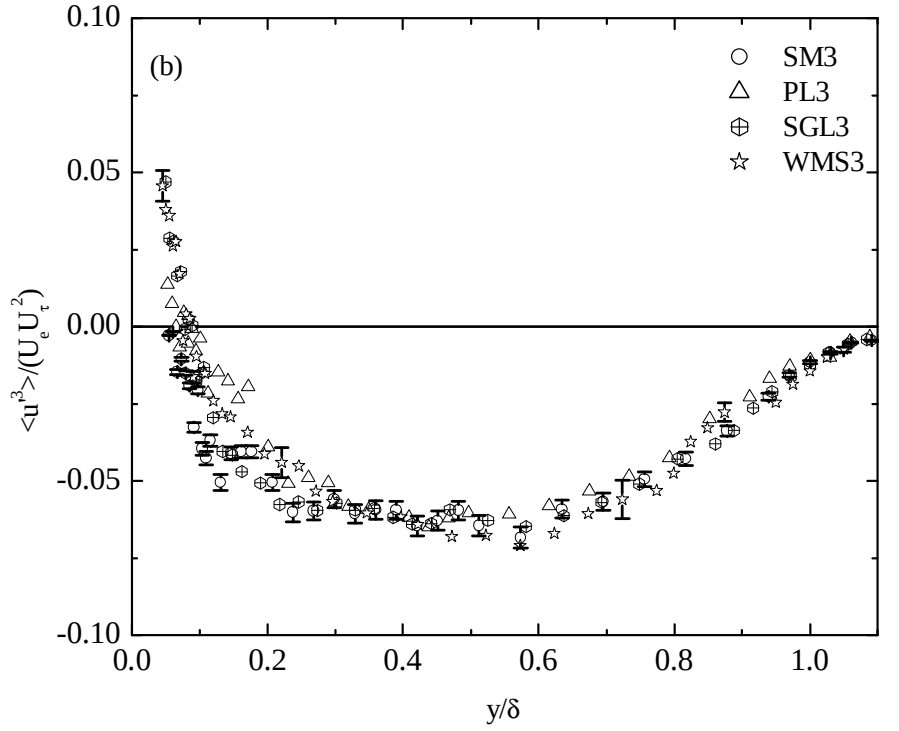

Figure 7.2: Distributions of triple correlation, $\langle u'^3 \rangle$, normalized by $U_e U_\tau^2$: (a) smooth and transitionally rough; (b) smooth and fully rough.

roughness (SGL3), the $\langle u'^3 \rangle$ data appears close to that of the smooth wall within the region $y/\delta < 0.1$. For both the perforated sheet (PL3) and wire mesh (WMS3), the $\langle u'^3 \rangle$ profiles are higher than on a smooth wall within the region $y/\delta < 0.2$. In the outer layer, the profiles are almost independent of surface conditions. Comparing Figures 7.1 and 7.2, the use of the friction velocity, U_τ, and mixed scaling, $U_e U_\tau^2$, as scaling parameters to assess the effects of the surface roughness on the $\langle u'^3 \rangle$ data indicate approximately the same behaviour.

7.2.2 $\langle v'^3 \rangle$ profiles

Figure 7.3 presents the distributions of $\langle v'^3 \rangle$, which represents the average transport of $\langle v'^2 \rangle$ by the turbulent motion in the wall-normal direction, for smooth and rough surfaces, normalized by the friction velocity. Figure 7.3a compares the $\langle v'^3 \rangle^+$ data for smooth wall and transitionally rough flows. The values of $\langle v'^3 \rangle^+$ for the perforated sheet (PM3) and sand grain roughness (SGM3) are significantly higher than on a smooth wall, $y/\delta < 0.3$. Beyond this region, the $\langle v'^3 \rangle^+$ data for PM3 and SGM3 appear to almost collapse onto the smooth wall data. The $\langle v'^3 \rangle^+$ data for the smooth wall and fully rough flows are compared in the Figure 7.3b. A dramatic increase in the level of the distribution of $\langle v'^3 \rangle^+$ for the wire mesh roughness is observed compared to the other surfaces, and this difference extends out to $y/\delta = 0.8$. Krogstad and Antonia (1999) reported a similar observation for a wall covered with wire mesh roughness. The value of $\langle v'^3 \rangle^+$ for SM3 is close to that for PL3 and SGL3, with the qualification that the values for the rough surfaces are slightly higher than the smooth wall, $y/\delta < 0.2$. The sign of the $\langle v'^3 \rangle^+$ profiles for both the smooth and rough surfaces are positive, indicating

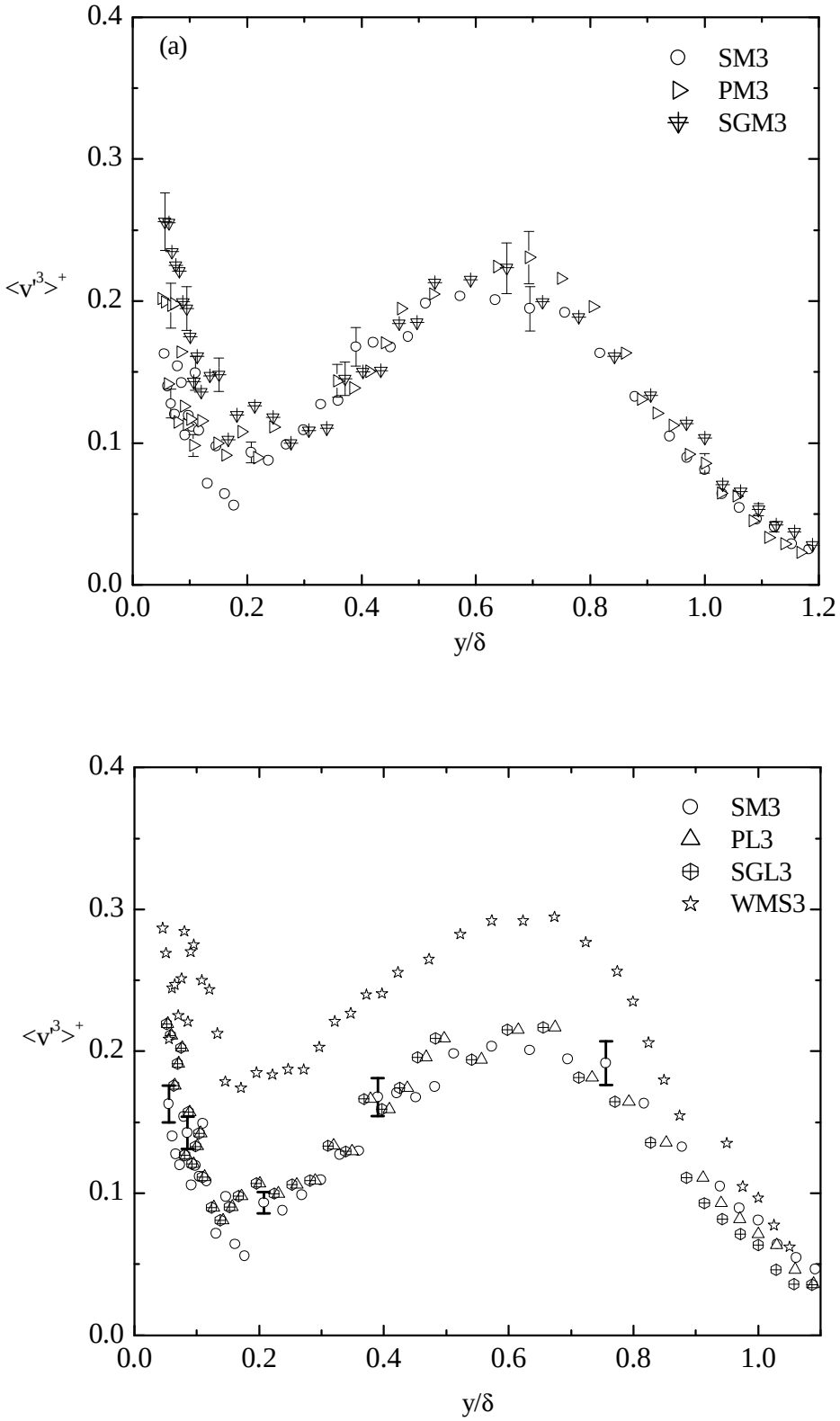

Figure 7.3: Distributions of triple correlation, $\langle v'^3 \rangle$, using inner coordinates: (a) smooth and transitionally rough; (b) smooth and fully rough.

transport of turbulence kinetic energy away from the wall. In contrast, the results of Antonia and Krogstad (2001) showed negative values of $\langle v'^3 \rangle^+$ for the flow over transverse rod roughness over a significant portion of the boundary layer, which suggests that the orientation of the transport of turbulence kinetic energy depends on the geometrical structure of the wall roughness.

Figure 7.4 presents the distributions of $\langle v'^3 \rangle$ for the smooth and rough surfaces normalized by the mixed scaling, $U_e U_\tau^2$. The $\langle v'^3 \rangle$ data for smooth wall and transitionally rough flows are compared in Figure 7.4a. Figure 7.4b compares the distributions of $\langle v'^3 \rangle$ for the smooth wall and fully rough flows. The effects of surface roughness appear to be more dramatic in the overlap and outer regions of the boundary layer as the magnitude of the data obtained for the rough surfaces is generally higher than for the smooth wall. With the exception of the wire mesh (WMS3), the mixed scaling tends to collapse the $\langle v'^3 \rangle$ data for the rough surfaces into a single curve within the region $0.3 < y/\delta < 0.8$, which is noticeably different from the smooth surface. One possible explanation for the behaviour of the wire mesh can be attributed to its geometrical orientation. This behaviour is similar to the wall-normal turbulence intensity data for wire mesh roughness. Figures 7.3 and 7.4 clearly show that scaling the $\langle v'^3 \rangle$ data with the mixed scaling, $U_e U_\tau^2$, is useful for illustrating the overall effect of the surface roughness.

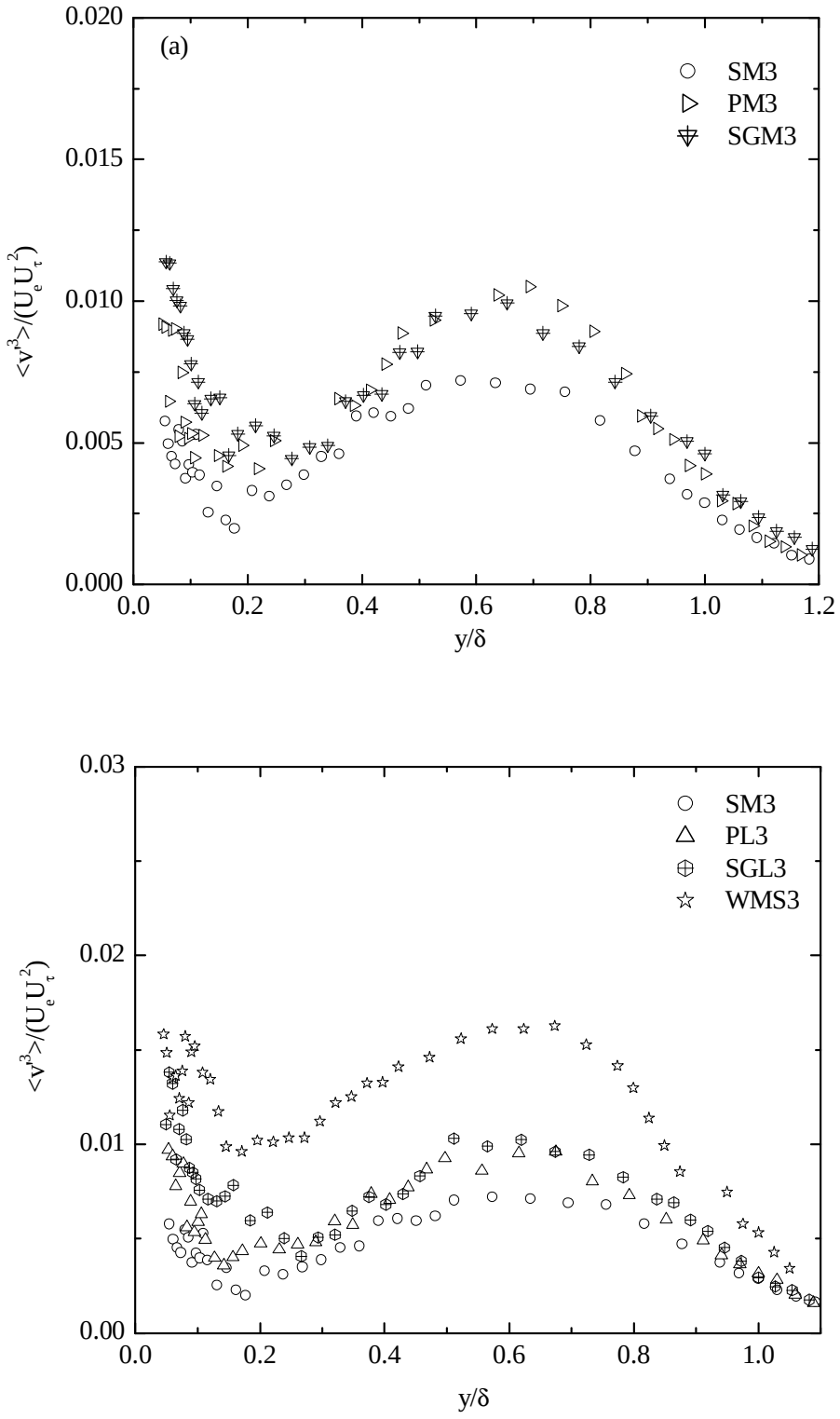

Figure 7.4: Distributions of triple correlation, $\langle v'^3 \rangle$, normalized by $U_e U_\tau^2$: (a) smooth and transitionally rough; (b) smooth and fully rough.

7.2.3 $\langle u^2v \rangle$ profiles

Figure 7.5 presents the distributions of $\langle u^2v \rangle$, which represents the streamwise flux of Reynolds shear stress for smooth and rough surfaces, normalized by the friction velocity. Figure 7.5a presents the $\langle u^2v \rangle^+$ data for a smooth wall and transitionally rough flows. The $\langle u^2v \rangle^+$ data for a smooth wall and fully rough flows are compared in Figure 7.5b. As indicated in both Figures 7.5a and 7.5b, the $\langle u^2v \rangle^+$ profiles for the rough walls drop below the smooth profile in the near-wall region. A similar trend was reported by Krogstad and Antonia (1999) for wire mesh roughness. The gradient of the triple product $\langle u^2v \rangle$ represents one component of the turbulent diffusion of the streamwise Reynolds stress, $\langle u^2 \rangle$, in the transport equation for the streamwise Reynolds stress, $\langle u^2 \rangle$. The present results suggest that the reduction in the level of the $\langle u^2v \rangle^+$ profiles for the rough walls results in a gain in the streamwise Reynolds stress, $\langle u^2 \rangle$, through turbulent diffusion, compare to a loss for the smooth wall.

Figure 7.6 presents the distributions of $\langle u^2v \rangle$ for the smooth and rough surfaces normalized by the mixed scaling, $U_e U_\tau^2$. Both transitionally rough and fully rough flows exhibit higher values of $\langle u^2v \rangle$ profiles in the overlap region, and this extends into the outer region of the flow. Tachie et al. (2003) reported a similar observation for sand grain and wire mesh roughnesses. A noticeable difference from the smooth surface within the region $0.2 < y/\delta < 0.8$ is observed as the mixed scaling tends to collapse the $\langle u^2v \rangle$ data for different rough surfaces into a single profile, as indicated in Figure 7.6. The mixed scaling $U_e U_\tau^2$ also provides information which distinguishes the effect of the surface roughness on the $\langle u^2v \rangle$ profiles.

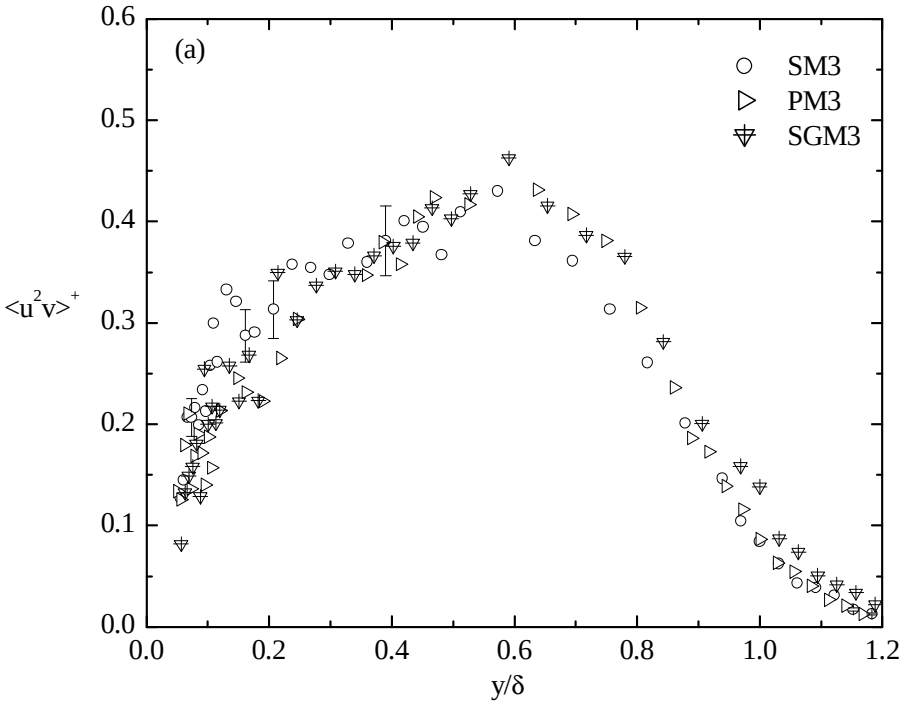

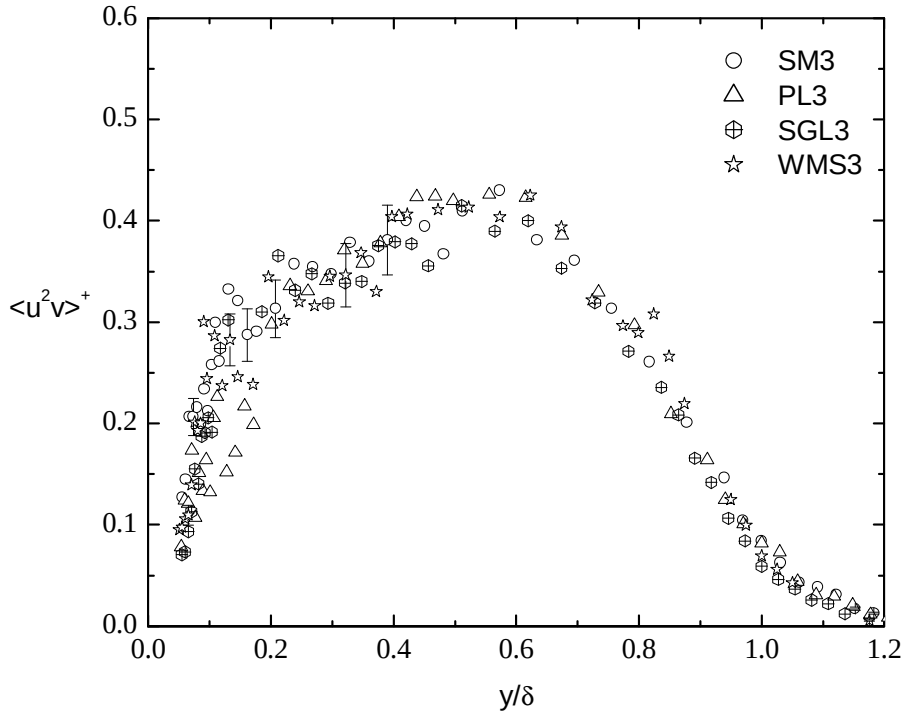

Figure 7.5: Distributions of triple correlation, $<u^2v>^+$, using inner coordinates: (a) smooth and transitionally rough; (b) smooth and fully rough.

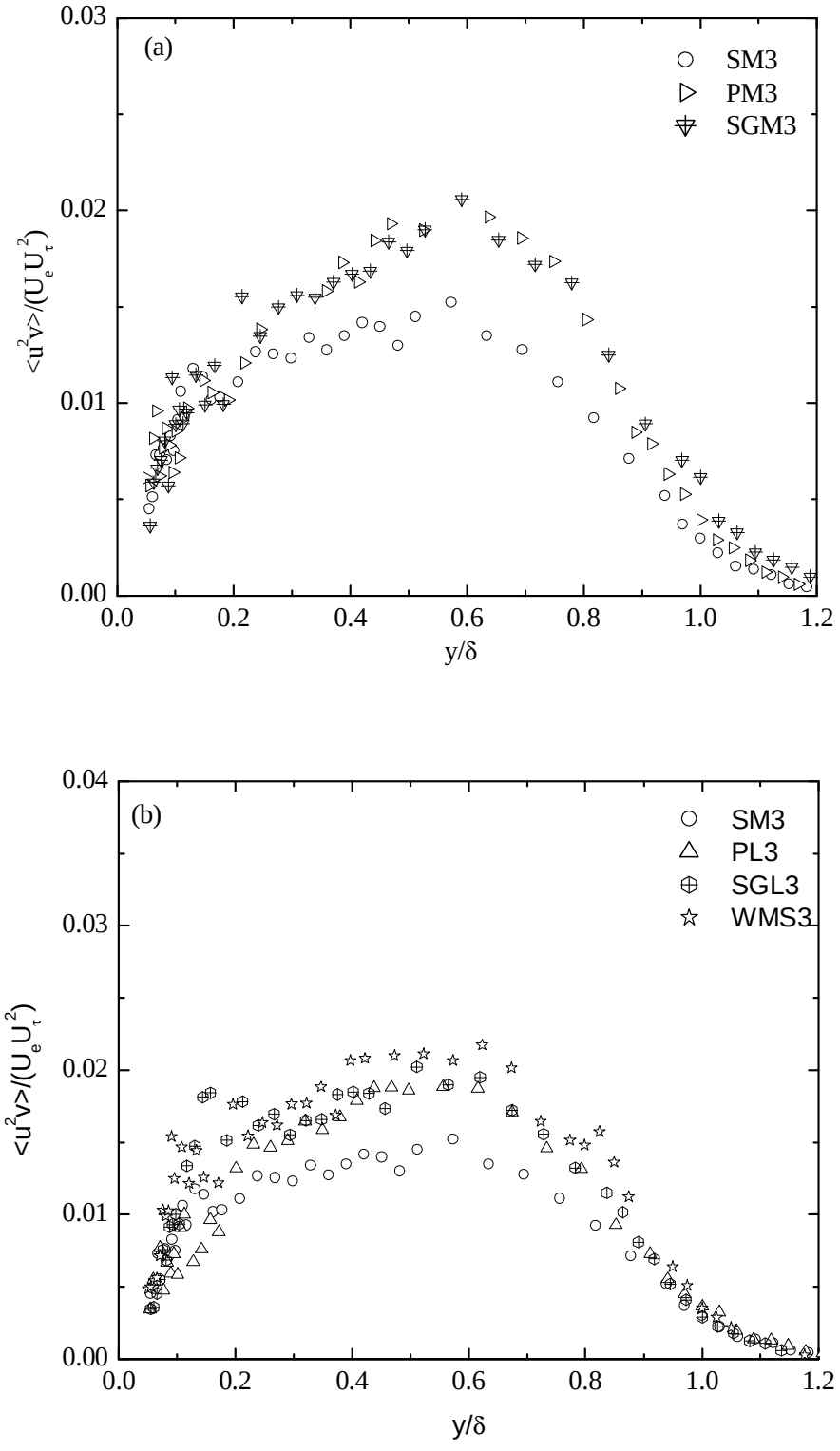

Figure 7.6: Distributions of triple correlation, $\langle u^2 v \rangle$, normalized by $U_e U_\tau^2$: (a) smooth and transitionally rough; (b) smooth and fully rough.

7.2.4 $\langle uv^2 \rangle$ profiles

Figures 7.7a and 7.7b present the distributions of $\langle uv^2 \rangle$, which represents the wall-normal turbulent transport of the Reynolds shear stress ($-\langle uv \rangle$) for hydraulically smooth, transitionally rough and fully rough flows, normalized by the friction velocity. For both transitionally rough and fully rough flows, the effect surface roughness significantly modifies the level of $\langle uv^2 \rangle^+$, and this extends out to $y/\delta \approx 0.3$, as indicated in Figures 7.7a and 7.7b. The derivatives of $\langle v^{+3} \rangle$ and $\langle uv^2 \rangle^+$ contribute to the term in the transport equation for turbulence kinetic energy, which represents the turbulent energy diffusion associated with wall-normal velocity fluctuating component.

Figure 7.8 presents the distributions of $\langle uv^2 \rangle$ for the smooth and rough surfaces normalized by mixed scaling, $U_e U_\tau^2$. For the transitionally rough flows, the $\langle uv^2 \rangle$ data scaled with mixed scaling tends to collapse into a single profile within the region $0.2 < y/\delta < 0.8$, as shown in Figure 7.8a. For the fully rough flows, the effects of surface roughness slightly lower the level of $\langle uv^2 \rangle$ data for both the sand grain roughness (SGL3) and wire mesh (WMS3) within the region $y/\delta < 0.1$. For the perforated sheet (PL3), the effect of surface roughness significantly enhanced the level of $\langle uv^2 \rangle$ data up until $y/\delta \approx 0.2$. Like SGL3 and WMS3, the effect of surface roughness on the $\langle uv^2 \rangle$ data for the perforated sheet (PL3) is noticed within the region $0.4 < y/\delta < 0.8$.

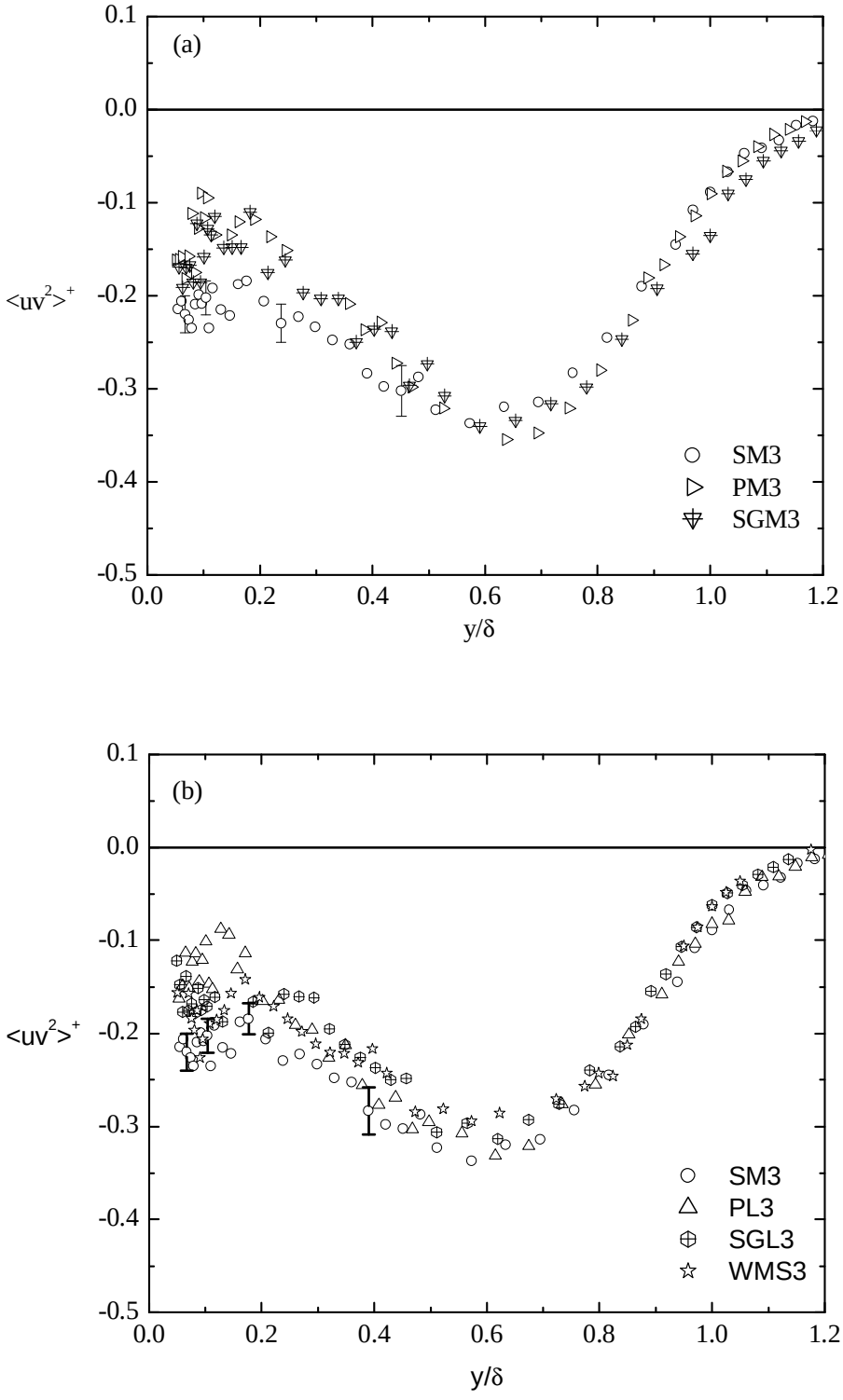

Figure 7.7: Distributions of triple correlation, $\langle uv^2 \rangle$, using inner coordinates: (a) smooth and transitionally rough; (b) smooth and fully rough.

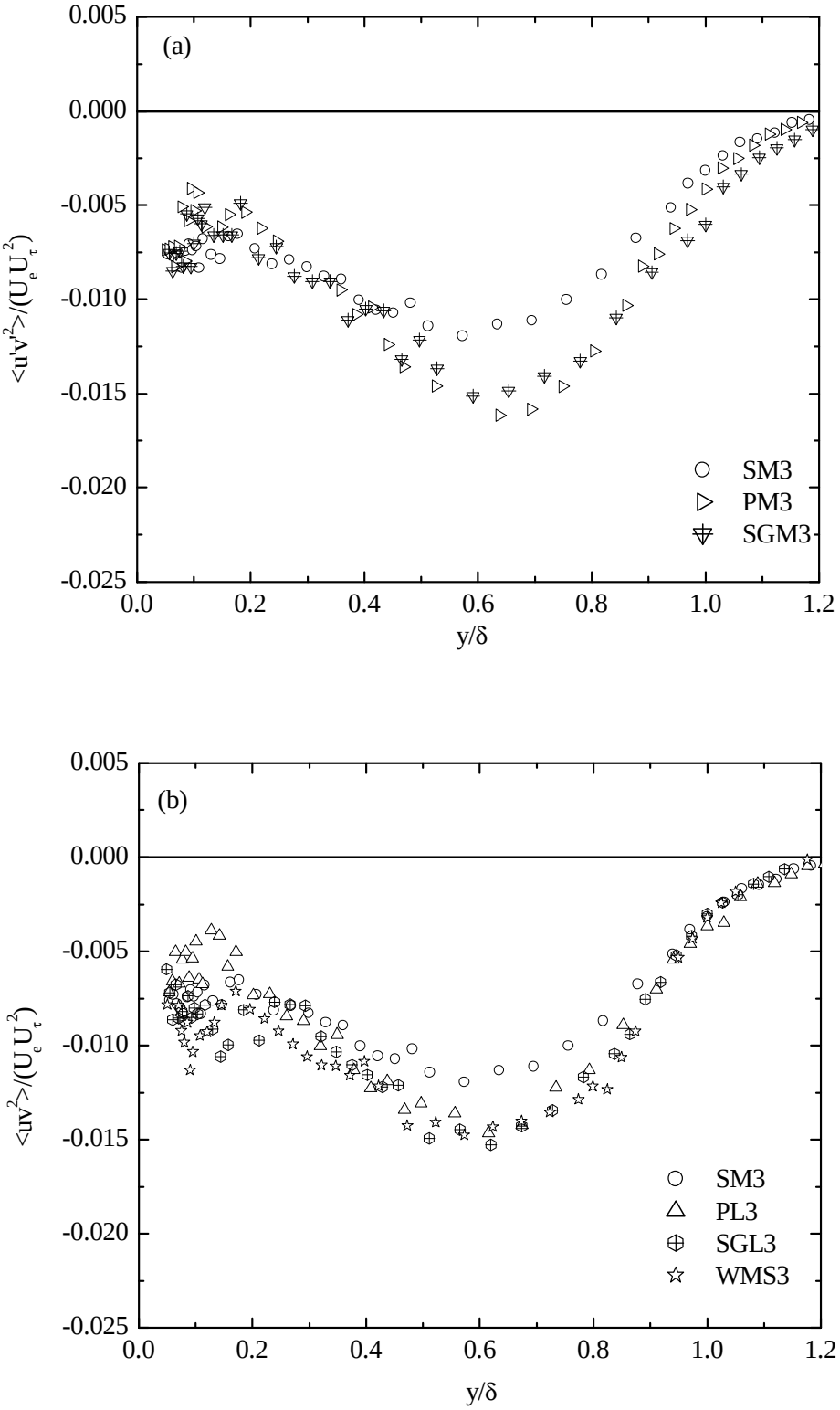

Figure 7.8: Distributions of triple correlation, $\langle uv^2 \rangle$, normalized by $U_e U_\tau^2$: (a) smooth and transitionally rough; (b) smooth and fully rough.

7.3 Skewness and Flatness Factors

The third and fourth velocity moments provide useful information on the sweep and ejection events. When non-dimensionalized using the root-mean-square value of the fluctuations, these become the skewness and flatness factors, respectively. The skewness factors of streamwise and wall-normal velocity fluctuations are defined as

$$S_u = \frac{< u'^3 >}{(u_{rms})^3} \quad \text{and} \quad S_v = \frac{< v'^3 >}{(v_{rms})^3} \tag{7.2}$$

The flatness factors streamwise and wall-normal velocity fluctuations are expressed as

$$F_u = \frac{< u'^4 >}{(u_{rms})^4} \quad \text{and} \quad F_v = \frac{< v'^4 >}{(v_{rms})^4} \tag{7.3}$$

Figures 7.9a and 7.9b present the distributions of the skewness of the longitudinal and vertical velocity fluctuations, S_u and S_v, for hydraulically smooth, transitionally rough, and fully rough flows versus y/δ. A non-zero skewness factor indicates the degree of temporal asymmetry of the random fluctuations, e.g. acceleration versus deceleration or sweep versus ejection. It is observed that S_u is independent of wall roughness, as the skewness profiles, S_u, for all the surfaces considered appear to collapse onto each other. Similar conclusions were drawn by Raupach et al. (1991) and Flack et al. (2005). The rough surfaces exhibit positive skewness, S_u, near the wall. As shown in Figure 7.9a, the effect of surface roughness appears to be diminishing as the wall-normal distance increases. It may be inferred from this observation that there is a likelihood of finding large positive streamwise velocity fluctuations, which is consistent with strong sweep events as observed by Grass (1971). The large negative values of S_u in the outer

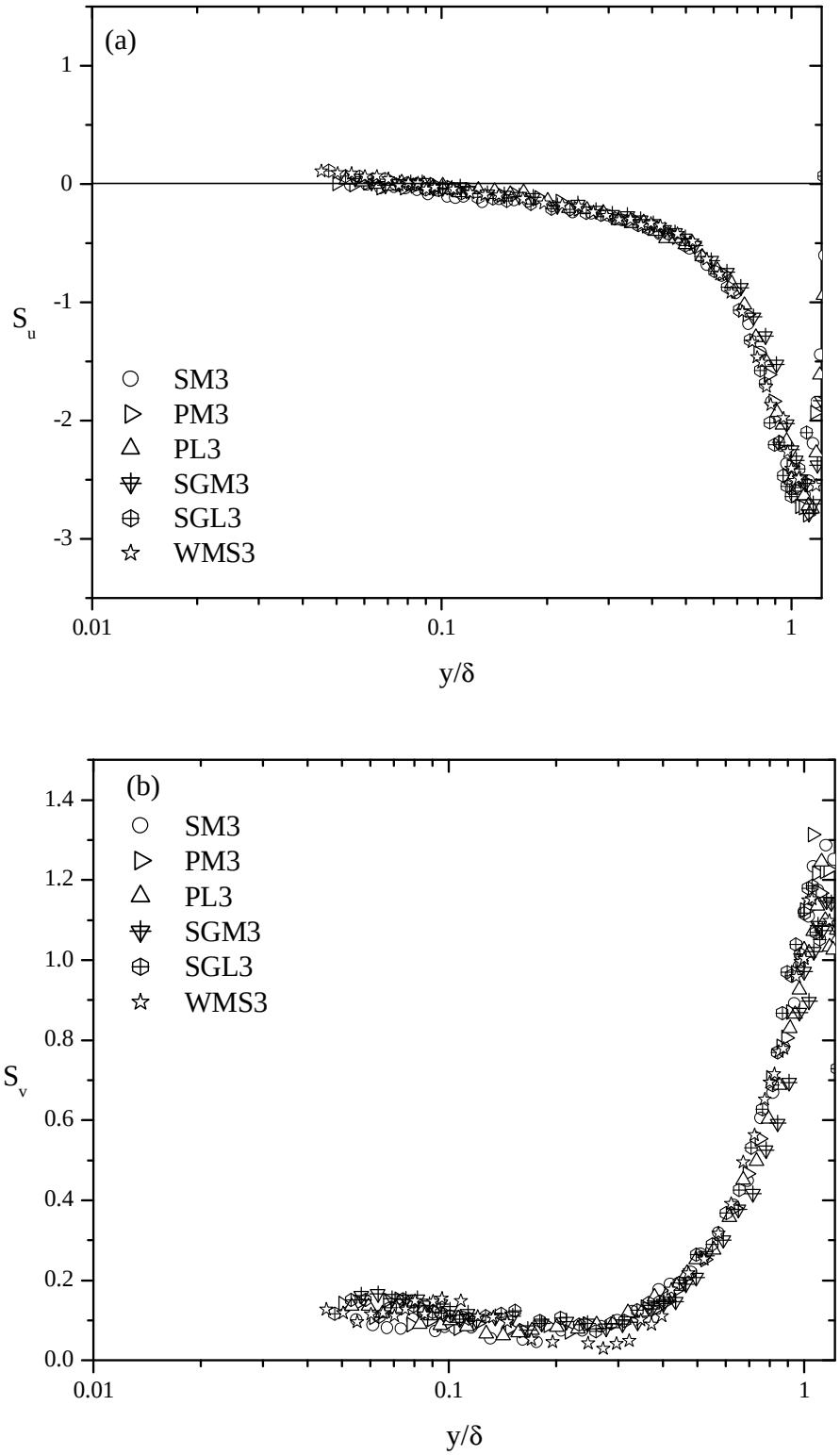

Figures 7.9: Distributions of skewness: (a) longitudinal velocity fluctuation; (b) vertical velocity fluctuation.

region indicate the occurrence of the arrival of low-speed fluids from the wall (deceleration-dominated ejection events). Although, v^{+2} exhibits sensitivity to wall roughness, S_v appears to be independent of wall roughness condition, as indicated in Figure 7.9b. This observation is similar to that of Mazouz et al. (1994) over smooth and grooved surfaces, and Flack et al. (2005) for sand grain roughness and a wire mesh surface. In contrast, Bandyopadhyay and Watson (1988), Antonia and Krogstad (2001), and Keirsbulck et al. (2002) observed significant differences in the values of S_v between the smooth and rough surfaces, which extended into the outer region of the flow. Bandyopadhyay and Watson (1988) attributed these differences to the hairpin vortices shape which induces different vertical motions and different vertical diffusion of turbulence in the rough wall compared to the smooth wall.

Figures 7.10a and 7.10b present the distributions of the flatness factor for the longitudinal and vertical velocity fluctuations, F_u and F_v, respectively, for hydraulically smooth, transitionally rough, and fully rough flows, versus y/δ. Flatness factor larger than 3 is associated with a signal that produced by intermittent turbulent events. As indicated in Figure 7.10a, the distributions of F_u data for both the smooth and rough walls appear to be slightly lower than the Gaussian value of 3. Comparison between the distributions of the flatness factors F_u for both smooth and rough surfaces shows that the profiles collapse onto each other, and no significant effect of surface roughness is observed. Flack et al. (2005) reported a similar observation. The distributions of F_v for both smooth and rough walls are higher than the Gaussian value of 3 over the entire boundary layer, as shown in Figure 7.10b. Similar to F_u, no effect of surface roughness

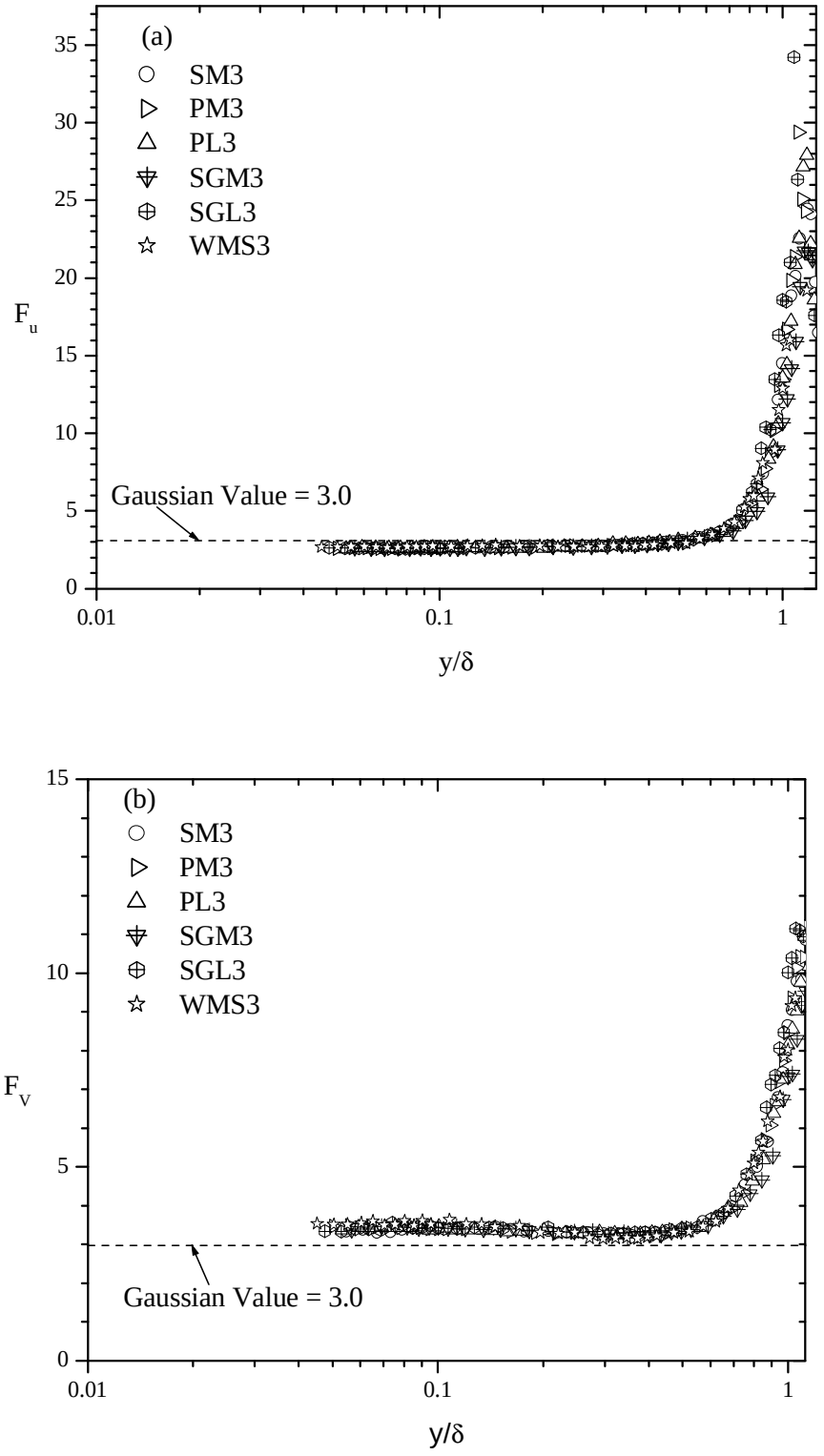

Figures 7.10: Distributions of Flatness factors: (a) longitudinal velocity fluctuation; (b) vertical velocity fluctuation.

on F_v is evident as all profiles collapse onto each other. Like S_u and S_v, the large values of F_u and F_v in the outer region signify the signatures of intermittent large-scale negative fluctuations which occur as a result of the large eddies driving the fluid from the low velocity region. The relatively larger values of F_u compared to F_v close to the freestream indicate that *u* signals are more intermittent that *v* near the freestream.

7.4 Summary

Profiles of the third moments of the fluctuating velocity field ($\langle u'^3 \rangle$, $\langle v'^3 \rangle$, $\langle u^2 v \rangle$, and $\langle uv^2 \rangle$) and distributions of the skewness of the longitudinal and wall-normal velocity fluctuations over smooth and different rough surfaces were measured in a zero pressure-gradient turbulent boundary layer. Two different scaling parameters, i.e. the friction velocity, U_τ , and a mixed scale, $U_e U_\tau^2$, proposed by George and Castillo (1997), were used to assess the effect of roughness on the triple velocity correlations. The experimental results indicate that surface roughness significantly alters some components of the third moment in the inner region, and this effect also extends into the outer region of the boundary layer. This observation is at variance with the wall similarity hypothesis. On the other hand, the distributions of the skewness for both the longitudinal and wall-normal velocity fluctuations are largely unaffected by surface roughness. The experimental results also show that there is a reduction in the arrived high-speed fluid from regions away from the wall (sweep events) for the smooth wall compared to the rough walls.

CHAPTER 8

NUMERICAL PREDICTION OF MEAN VELOCITY AND TURBULENCE QUANTITIES ON SMOOTH AND ROUGH WALLS

8.1 Introduction

In the previous chapters, the experimental results of the effect of surface roughness on the mean and turbulence fields have been discussed in great detail. One of the major conclusions from these results is that the validity of the wall similarity hypothesis depends to some degree on the specific characteristics of the roughness elements. This conclusion is at variance to some prior studies. The present experimental studies also suggest that the power law performs better than the logarithmic law in modelling the overlap region of the mean velocity profile in a wall-bounded flow. Most near-wall turbulence modellers have based their formulation on the classical logarithmic law. In this chapter, a new wall function formulation based on a power law, in contrast to the more traditional logarithmic law approach, is proposed. The new wall function formulation is used to predict the mean velocity profiles and friction factor for smooth and rough wall turbulent pipe flow. In addition, the validity of the wall similarity hypothesis is also investigated in the context of a numerical study. The two-layer k-ε

model of Durbin et al. (2001) is also used to simulate a zero pressure-gradient turbulent boundary layer flow over smooth and rough walls. Of special interest is the effect of surface roughness on the turbulence fields in both the inner and outer regions of the flow.

8.2 Governing Equations

The governing equations, which consist of the steady Reynolds-averaged equations for conservation of mass and momentum in incompressible turbulent flow, were given in Eqns. (1.1) and (1.2). The unknown Reynolds stresses are modeled using the eddy-viscosity concept, i.e.

$$-<u_i u_j> \; = 2\nu_t S_{ij} - \frac{2}{3}\delta_{ij} k \tag{8.1}$$

where S_{ij} (= $0.5(U_{i,j} + U_{j,i})$) is the strain rate tensor. The eddy viscosity is determined as follows:

$$\nu_t = C_\mu k T \; ; \qquad T = k/\varepsilon \tag{8.2}$$

where T is the turbulence time scale. The eddy viscosity then requires solution of the transport equation for the turbulence kinetic energy, k, and its dissipation rate, ε, given as follows:

$$U_j \frac{\partial k}{\partial xj} = \frac{\partial}{\partial x_j}\left[\left(\nu + \frac{\nu_t}{\sigma_k}\right)\frac{\partial k}{\partial x_j}\right] - <u_i u_j> U_{i,j} - \varepsilon \tag{8.3}$$

$$U_j \frac{\partial \varepsilon}{\partial x_j} = \frac{\partial}{\partial x_j}\left[\left(\nu + \frac{\nu_t}{\sigma_\varepsilon}\right)\frac{\partial \varepsilon}{\partial x_j}\right] - C_{\varepsilon 1}\frac{\varepsilon}{k}<u_i u_j> U_{i,j} - C_{\varepsilon 2}\frac{\varepsilon^2}{k} \tag{8.4}$$

The numerical values of the model constants of Durbin et al. (2001) are adopted: $C_\mu = 0.09$, $\sigma_k = 1.0$, $\sigma_\varepsilon = 1.3, C_{\varepsilon 1} = 1.44$ and $C_{\varepsilon 2} = 1.92$. Different near-wall treatments can be used in combination with $k-\varepsilon$ models. In the present study, both the wall function and two-layer formulations were used. Each of these formulations is further modified to account for the effect of surface roughness on the mean velocity and turbulence quantities.

8.3 New Wall Function Formulation

As stated in Chapter 2, a standard wall function is usually employed to treat the boundary conditions for velocity and other transported variables in near-wall flows at high Reynolds numbers. This approach enables the bridging of the viscous sublayer and blending region by employing empirical formulae to provide near-wall boundary conditions for the mean flow and turbulence transport equations. This allows placement of the first grid node in the overlap region in fully turbulent flow. In the new wall function formulation, the power law proposed by Barenblatt (1993) for turbulent pipe flow is adopted. The power law profile can be expressed as

$$U^+ = Cy^{+\gamma} \tag{8.5}$$

For a smooth surface, the coefficients proposed by Zagarola et al. (1997) are adopted and can be expressed by C = 0.7053ln(Re) + 0.3055, and γ = 1.085/ln(Re) + 6.535/ln(Re^2). In the case of a rough surface, the power law coefficients proposed by Porporato and Sordo (2001) are employed. Recall from Chapter 2 that the modified coefficients, C and γ, for fully rough flow are given as

$$\gamma_r = 0.455\left(\frac{D}{2k_s}\right)^{-0.225} \quad \text{and} \quad C_r = \frac{c}{\mathrm{Re}^{\gamma_r}} \tag{8.6}$$

For the new wall function formulation, the wall shear stress in the momentum equation is obtained from an algebraic (implicit) equation. At high Reynolds numbers, the turbulence energy balance in the overlap region reduces approximately to production equals dissipation, i.e. local equilibrium. Setting production equal to dissipation gives

$$-<uv>\frac{\partial U}{\partial y} = \frac{C_\mu k^2}{\nu_t} \tag{8.7a}$$

Eqn. (8.7a) can be re-arranged as follows:

$$-<uv>\nu_t \frac{\partial U}{\partial y} = C_\mu k^2 \tag{8.7b}$$

Recall that $-<uv> = \nu_t \frac{\partial U}{\partial y}$ and substituting into Eqn. (8.7b), this becomes

$$<uv><uv> = C_\mu k^2 \tag{8.7c}$$

Assuming a constant stress layer, i.e. $-<uv> \cong U_\tau^2$, the friction velocity is determined from Eqn. (8.7c) as follows:

$$U_\tau = C_\mu^{1/4} k_p^{1/2} \tag{8.8}$$

where p is the first node. From the definition for U_p^+, i.e.

$$U_p^+ = \frac{U_p}{\sqrt{\tau_w/\rho}} \tag{8.9}$$

the wall shear stress, τ_w, can then be expressed as

$$\tau_w = \frac{\rho U_p}{U_p^+} U_\tau \tag{8.10}$$

Substituting for U_τ from Eqn. (8.8), the expression for the wall shear stress and U_p^+ from Eqn. (8.5), becomes

$$\tau_w = \frac{\rho C_\mu^{1/4} k_p^{1/2} U_p}{C(y^+)^\gamma} \tag{8.11}$$

Assuming the shear stress to be nearly constant in the overlap region, the production in the wall region is determined as follows

$$P_K \approx \tau_w \left.\frac{\partial U}{\partial y}\right|_p \tag{8.12}$$

The turbulence kinetic energy is solved for at the first node from a simplified transport equation (with zero diffusion to the wall). This means that the net kinetic energy source is obtained as follows:

$$k_p = \tau_w \left.\frac{\partial U}{\partial y}\right|_p - \rho \varepsilon_p \tag{8.13}$$

The boundary condition for ε is also derived from the assumption of local equilibrium, i.e.

$$- < uv > \frac{\partial U}{\partial y} = \varepsilon_p \tag{8.14}$$

Eqn. (8.5) can also be expressed as follows:

$$U = U_\tau C \left(\frac{y U_\tau}{\nu} \right)^\gamma \tag{8.15}$$

Using Eqn. (8.15), the mean velocity gradient, $\partial U / \partial y$, becomes

$$\frac{\partial U}{\partial y} = \frac{\gamma U_\tau^2 C}{\nu}\left(\frac{yU^+}{\nu}\right)^{\gamma-1} \tag{8.16a}$$

$$\frac{\partial U}{\partial y} = \frac{\gamma U_\tau^2 C}{\nu}(y^+)^{\gamma-1} \tag{8.16b}$$

Recall that the assumption is based on the constant stress layer, i.e. $-<uv>\cong U_\tau^2$, then Eqn. (8.14) becomes

$$\varepsilon_p = \frac{\gamma U_\tau^4 C}{\nu}(y^+)^{\gamma-1} \tag{8.17}$$

Substituting for U_τ from Eqn. (8.8), the dissipation rate becomes

$$\varepsilon_p = \frac{\gamma C C_\mu k^2}{\nu}(y^+)^{\gamma-1} \tag{8.18}$$

Table 8.1 presents a summary of the new equations for the wall function compared with those obtained from the classic logarithmic law.

Table 8.1: A summary of new equations for the wall function and those obtained from the log-law

	New Formulation	Formulation based on Log-law
Wall shear stress	$\tau_w = \frac{\rho C_\mu^{1/4} k_p^{1/2} U_p}{C(y^+)^\gamma}$	$\tau_w = \frac{\kappa \rho C_\mu^{1/4} k_p^{1/2} U_p}{\ln(E y_p^+)}$
Turbulence kinetic energy	$k_p = \tau_w \left.\frac{\partial U}{\partial y}\right\|_p - \rho\varepsilon_p$	$k_p = \tau_w \left.\frac{\partial U}{\partial y}\right\|_p - \rho\varepsilon_p$
Dissipation rate	$\varepsilon_p = \frac{\gamma C C_\mu k^2}{\nu}(y^+)^{\gamma-1}$	$\varepsilon_p = \frac{u_\tau^3}{\kappa y_p}$

The implementation of the present wall function formulation, as the boundary conditions in the overlap region, is shown in Figure 8.1. The boundary condition for the momentum equation is implemented through the wall shear stress given by Eqn. (8.11). Both the turbulence kinetic energy and its dissipation rate, given by Eqns. (8.13) and (8.18), respectively, are calculated at the first node which should be located at $y^+ > 30$. At this location, the turbulent eddy viscosity used in the momentum and turbulence transport equations is also calculated from the values obtained for both turbulence kinetic energy and dissipation rate.

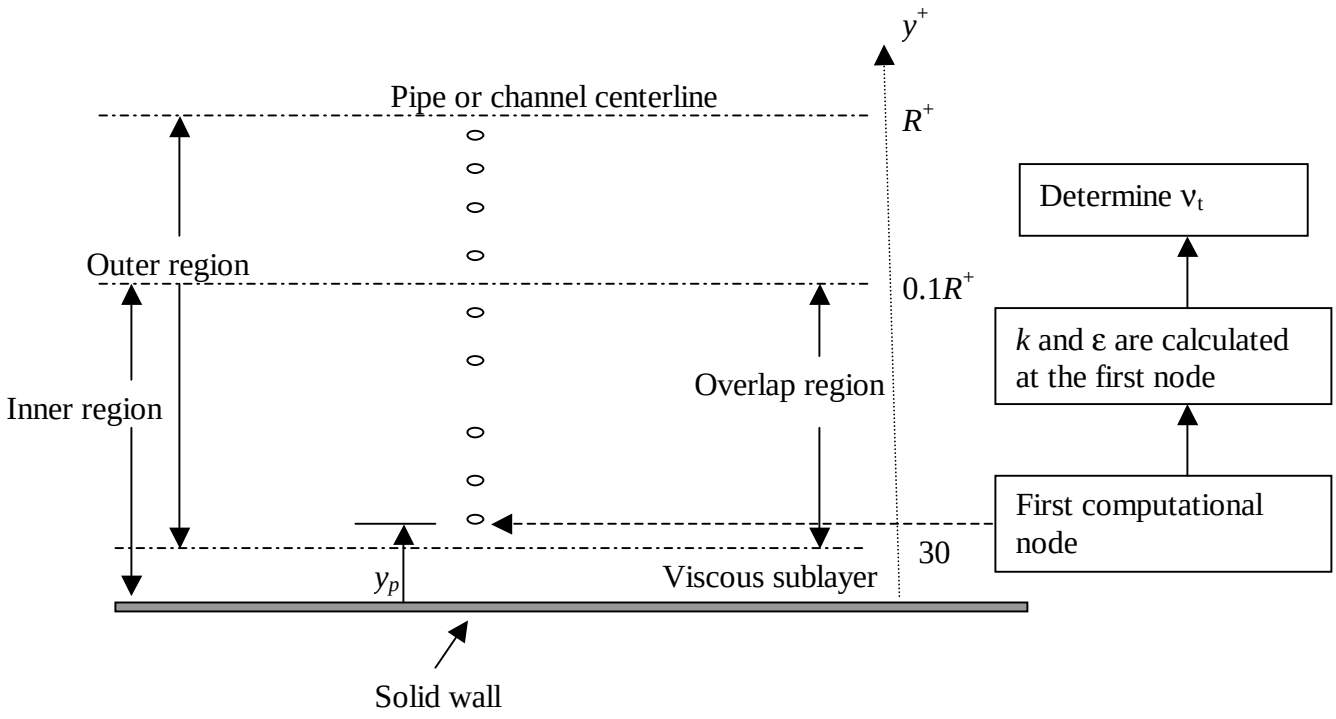

Figure 8.1: Schematic showing structure of pipe and channel flows.

8.4 Two-Layer Model Formulation

In this formulation, the eddy viscosity, ν_t, is obtained by employing a two-layer strategy, where the viscosity-affected region close to the wall is resolved with a one-equation model, while the outer region of the flow is resolved with the standard k-ε model.

In the $k-l$ model used in the inner region, the dissipation rate is given by an algebraic relation,

$$\varepsilon = \frac{k^{3/2}}{l_\varepsilon} \tag{8.20}$$

and the eddy viscosity is expressed as

$$\nu_t = C_\mu \sqrt{k} l_\nu \tag{8.21}$$

The length scales l_ν and l_ε are prescribed to model the wall-damping effects. Following Durbin et al. (2001), van Driest damping functions are implemented as follows:

$$l_\nu = C_l y[1-\exp(-R_y / A_\nu^o)] \quad \text{and} \quad l_\varepsilon = C_l y[1-\exp(-R_y / A_\varepsilon^o)] \tag{8.22}$$

where R_y $(= y\sqrt{k}/\nu)$ is the turbulent Reynolds number, $C_l = 2.5$, $A_\nu^o = 62.5$, and $A_\varepsilon^o = 5$. For a smooth wall, the boundary condition for k is as follows:

$$y = 0, \qquad k_w = 0 \tag{8.23}$$

In the two-layer formulation, at the location $y = \ln(20) A_\nu^o \nu / \sqrt{k}$ the model is abruptly switched from use of the length scale relation for ε to solving the dissipation rate equation. At the same time, the eddy viscosity relation given by (8.21) is replaced by (8.2).

8.4.1 Roughness Formulation

For a rough surface, the effective wall normal distance is expressed as, $y_{eff} = y + y_o$, where y is the wall-normal distance measured from a plane of 'apparent' zero velocity, and y_o is the hydrodynamic roughness length, as shown in Figure 8.3. The value specified for y_o will determine the effect of the surface roughness on the flow. As noted by Durbin et al. (2001) in their paper, "y_o is not a physical length; it is an artifice added to produce a suitable mean velocity."

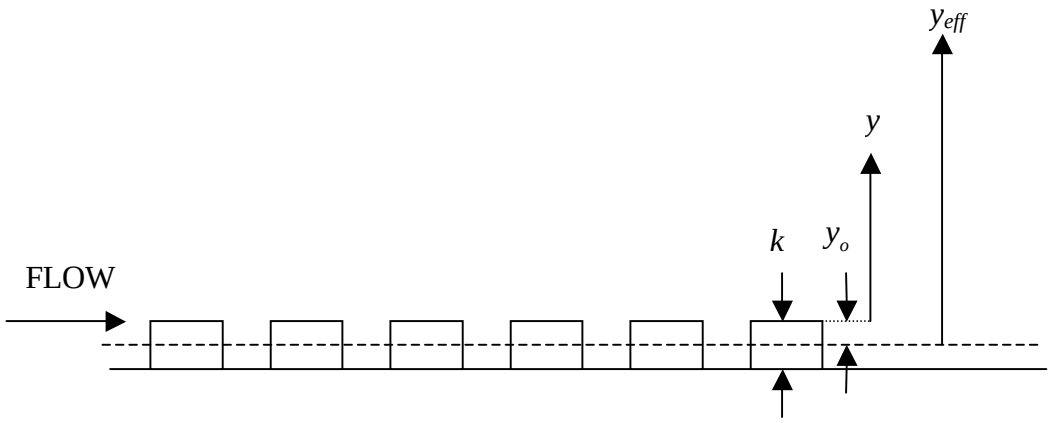

Figure 8.2: Schematic diagram indicating the location of y_{eff} on a 2-d generic rough surface.

In the present study, the case of a uniform sand grain roughness of height k_s is considered. The value of y_o^+ corresponding to a given k_{eq}^+ can be obtained from the calibration curve of Durbin et al. (2001). The damping functions for the length scales are

modified on a rough surface. The length scale, l_ν, becomes

$$l_\nu = C_l[y + y_o][1 - \exp(-R_{y_{eff}} / A_\nu)] \tag{8.24}$$

while l_ε becomes

$$l_\varepsilon = C_l[y + y_o][1 - \exp(-R_{y_{eff}} / A_\varepsilon)] \tag{8.25}$$

The value of A_ν is reduced for wall roughness according to the following linear interpolation,

$$A_\nu = \max[1; A_\nu^o(1.0 - k_s^+ / 90] \tag{8.26}$$

The constant A_ε is unchanged, i.e. $A_\varepsilon = A_\varepsilon^o$. A quadratic interpolation is adopted for the turbulence kinetic energy at $y = 0$, i.e.

$$k(0) = \frac{u_\tau^2}{\sqrt{C_\mu}} \min[1; (k_s^+ / 90)^2] \tag{8.27}$$

The friction velocity is determined from the following relation evaluated at $y = 0$

$$u_\tau^2 = (\nu + \nu_T) \left. \frac{\partial U}{\partial y} \right|_{y=0} \tag{8.28}$$

8.5 Numerical Procedure

8.5.1 Finite Volume Method

8.5.1.1 Pipe Flow

For a fully developed turbulent pipe flow, the transport equations for both the momentum and turbulence quantities can be written in general as follows:

$$\frac{\rho \partial \phi}{\partial t} = \frac{\partial}{\partial x_j} \left(\Gamma \frac{\partial \phi}{\partial x_j} \right) + S_\phi \tag{8.29}$$

where Γ is the diffusive coefficient and ϕ represents U, k, or ε. The first term of the left hand side represents the temporal change while the first and second terms of the right hand side denote the diffusive and source terms, respectively. Based on the finite volume method (FVM), the discrete equation is obtained by integrating the transport equation term by term in both space and time. Complete details of the derivation of the discrete equations are provided in Appendix B. The discrete equation for one-dimensional flow reduces to

$$a_P\phi = a_N\phi + a_S\phi + b_\phi \tag{8.30}$$

where a_N, a_S, and a_p are coefficients and b_ϕ is the source term.

The flow in the circular pipe is treated as symmetrical so that the calculations were made for one-half of the pipe cross section. The grid consisted of 100 control volumes distributed non-uniformly over the solution domain, which are sufficient to obtain a grid-independent solution. Reynolds numbers based on the mean velocity and diameter (d = 0.24 m) ranging from 5 x 10^4 to 2.5 x 10^6 were used in the simulations. The level of the bulk velocity was fixed by specifying the appropriate pressure gradient. Equivalent sand grain roughnesses with average diameters of 0.96 and 1.44 mm were used in the simulations. The transport equations were solved using an iterative solution procedure until the maximum normalized residuals were reduced below the value of 10^{-8}.

8.5.1.2 Boundary Layer

In the case of the fully developed turbulent pipe flow, the convective term in the Navier-Stokes' equation reduces to zero. For the boundary layer, the convective term is important and the general transport equation becomes

$$\frac{\rho\partial\phi}{\partial t}+\rho U_j\frac{\partial\phi}{\partial x_j}=\frac{\partial}{\partial x_j}\left(\Gamma\frac{\partial\phi}{\partial x_j}\right)+S_\phi \tag{8.31}$$

where ϕ represents U, V, k, or ε.

Based on FVM, the discrete equation is obtained by integrating the transport equation term by term in both space and time. Complete details of the derivation of the discrete equations are provided in Appendix B. The discrete equation for two-dimensional flow is given as follows:

$$a_P\phi=a_E\phi+a_W\phi+a_N\phi+a_S\phi+b_\phi \tag{8.32}$$

where a_E to a_W are coefficients and b_ϕ is the source term. A general nodal point is identified by P and its neighbours in a two-dimensional geometry, the nodes to east, west, north, and south, are identified by E, W, N, and S, respectively.

In the implementation of the discrete equation for the two-dimensional boundary layer flow, a in-house code originally developed by Prof. D. J. Bergstrom was modified to incorporate the two-layer model. A staggered grid was adopted, and the SIMPLEC algorithm was used to solve the pressure-velocity field. The discrete continuity equation is used to formulate a pressure correction field. The purpose of the correction field is to modify the pressure-velocity fields to better conserve mass. The complete details of the

pressure solver are provided in Appendix B. The grid used in the simulation consisted of 140×100 control volumes. The cross-stream nodes were distributed non-uniformly to obtain a grid independent solution, while a uniform node spacing was used for the streamwise direction. The solution domain was 2.5 m long and 0.25 m tall. The inlet condition in the simulations was a fully developed zero pressure gradient boundary layer. Approximately fully developed profiles for U, k, and ε were used as follows:

$$U_j = U_e\left(\frac{y}{\delta}\right)^{1/7} \quad ; \qquad k_j = 0.005U_j^2 \; ; \qquad \varepsilon_j = \frac{k_j^2}{1000\nu} \tag{8.33}$$

At the outlet boundary (exit) for both the smooth and rough surfaces, the flow was assumed to be fully developed and the transverse mean velocity component, V, was set to zero, i.e.,

$$\frac{\partial U}{\partial x_j} = \frac{\partial k}{\partial x_j} = \frac{\partial \varepsilon}{\partial x_j} = 0; \qquad V = 0 \tag{8.34}$$

Zero gradient boundary conditions are applied at the outer boundary. At the wall, the usual no-slip and no-penetration boundary conditions were applied to the velocity components for both smooth and rough surface, while the turbulence kinetic energy, k, was set to zero for the smooth surface and a finite value given by Eqn. (8.27) for the rough surface. Reynolds numbers ranging from 8,780 – 12,000, based on the momentum thickness, were used in the simulations for both smooth and rough walls. The sand grain roughness height used in the simulation ranged from 1.2 – 4.9 mm. For the smooth surface, the first grid point was located deep within the sublayer, i.e. $y^+ < 0.5$. In the case of the rough surface, the first grid point was placed above the hydrodynamic roughness y_o. The boundary conditions were implemented at $y = y_o$ for the flow over

the rough surface. The boundary conditions and switching of the model relations were efficiently implemented by modifying the coefficients in the discrete equations. No discontinuity was observed in the field variables at the point of patching.

8.6 Results and Discussion

8.6.1 Pipe Flow

Figure 8.3 presents the predicted mean velocity profiles for smooth and rough surfaces using inner coordinates. The present smooth wall result is compared with the experimental data of Zagarola et al. (1996) at Re = 10^6. The comparison shows the present result is within 1 % maximum deviation from the experimental data, indicating good agreement. As expected, the effect of surface roughness in the simulation shifts the mean velocity profile vertically downward and to the right due to an increase in the friction velocity. As indicated in Table 8.2, the values of the roughness shift, ΔU^+ = 8.4 and 10.5, which correspond to k_{eq}^+ = 144 and 287, respectively, which were calculated from the numerical results closely agree with the values predicted by the Prandtl-Schlichting relation given as,

$$\Delta U^+ = 3.5 - \frac{1}{\kappa}\ln(k_{eq}^+) \tag{8.35}$$

Table 8.2: Comparison of velocity shift for sand grain roughness

k_{eq}^+	Prandtl-Schlichting	Present	% Difference
144	8.6	8.4	2.3
257	10.3	10.5	1.9

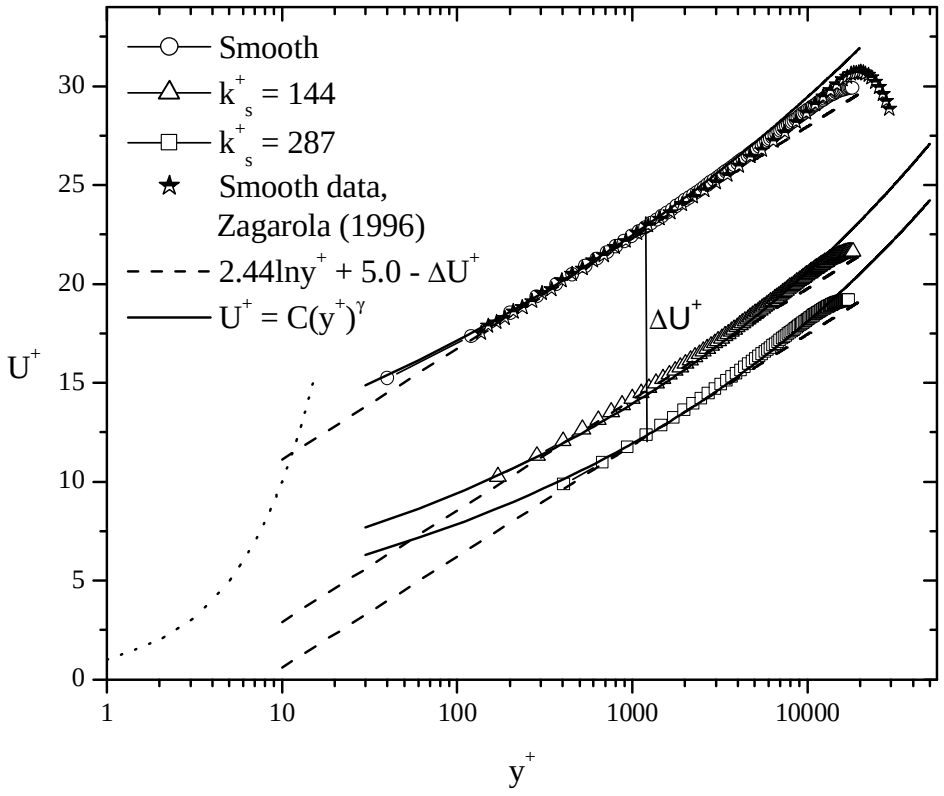

Figure 8.3: Mean velocity profiles for smooth and rough surfaces (predictions are represented by symbols:o, Δ, □).

Figure 8.4 shows the variation of friction factor with Reynolds number on smooth and rough walls. Included are the values of the friction factor obtained from smooth-pipe data of Zagarola (1996) and the correlation obtained by Colebrook (1939). Comparison shows that the values of the friction factor predicted by the present formulation agree well with both the experimental data and correlation; furthermore there is only a small difference from the value of the friction factor predicted using the standard wall function (SWF) approach. At the highest Reynolds number, the values of the friction factor for both the present formulation and standard wall function are 3% lower and 2.4 % higher, respectively, than that of the correlation, as indicated in Figure 8.4. Considering a level of the uncertainty of ± 15 % (White, 1972) for the correlation, it may be concluded that both formulations accurately predict the friction factor. In the case of the rough surface, the present formulation indicates that the fully rough flow is independent of Reynolds number, as expected. Comparison between the values predicted for the friction factor on the rough surface and the correlation of Colebrook (1939) again indicates good agreement. One weakness of the present wall function formulation is the inability to predict transitionally rough flows.

Summary

A new wall function formulation for the standard $k-\varepsilon$ model based on a power law profile has been proposed and used to simulate smooth and fully rough turbulent pipe flow. The new formulation correctly predicted the friction factors for smooth and fully rough flows. One of the shortcomings of the present formulation is that it is only valid

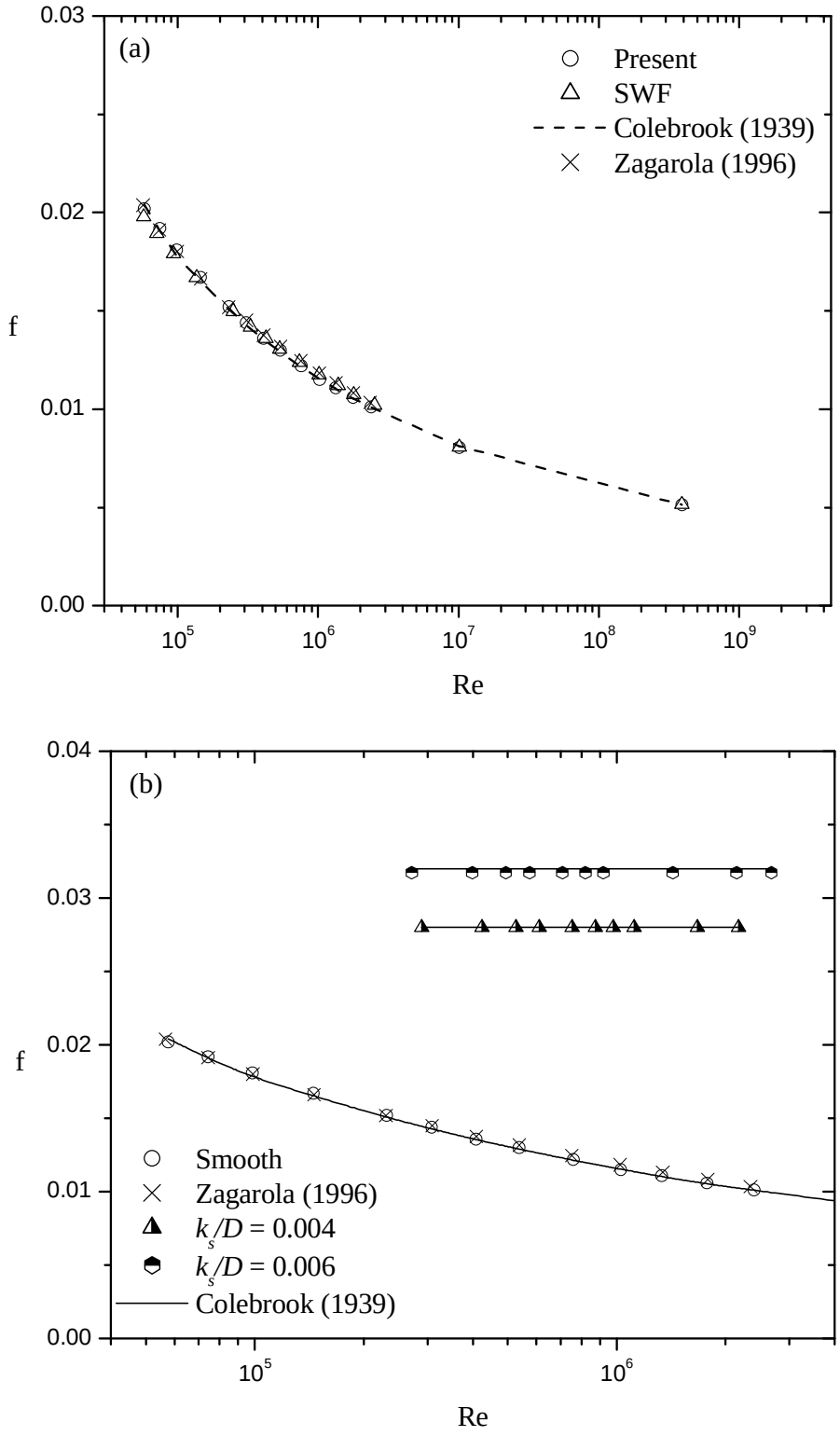

Figure 8.4: Variation of friction factor with Reynolds number: (a) smooth wall; (b) smooth and rough surfaces.

for smooth and fully rough flows. It remains to introduce an interpolation that accommodates the transitional flow regime.

8.6.2 Boundary Layer Flows

Figure 8.5 presents the mean velocity profiles for smooth and fully rough walls using inner coordinates. The effect of roughness in the present simulation shifts the mean velocity profile vertically downward and to the right due to the increase in the friction velocity. As shown in Figure 8.5, the log-layer is observed to extend to the origin of y under fully rough conditions. As the roughness Reynolds number, k_{eq}^{+}, increases, the velocity shift, ΔU^{+}, increases. For example (Table 8.3), the roughness Reynolds number, k_{eq}^{+} = 105 produces a velocity shift, ΔU^{+} = 8.0, while the roughness Reynolds number, k_{eq}^{+} = 310 gives the velocity shift, ΔU^{+} = 11.0. As indicated in Table 8.3, the effect of roughness appears to increase the strength of the wake in the simulation results, which is similar to observations noted in the previous rough-wall studies (e.g. Krogstad et al., 1992; Tachie et al., 2000; Bergstrom et al., 2005).

Table 8.3: Comparison of flow parameters for smooth and rough surfaces

	Re_{θ}	k_{eq}^{+}	Π	ΔU^{+}
Smooth	8800	-	0.52	-
Rough	9570	105	0.61	8.0
Rough	1180	310	0.62	11.0

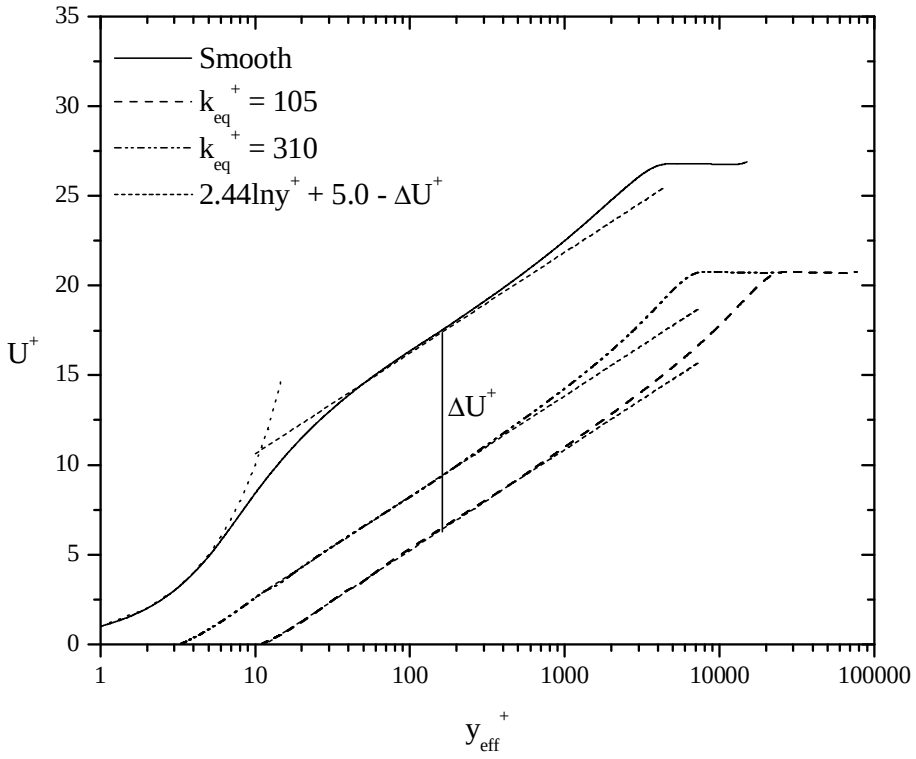

Figure 8.5: Mean velocity profiles for smooth and rough surfaces using inner coordinates.

Attention is now turned to the turbulence kinetic energy. In view of comparing the results obtained from the experimental study reported in the previous chapters with the present numerical results, the turbulence kinetic energy was calculated from the expression $k^+ \equiv 1/2(u'^{+2} + v'^{+2} + w'^{+2})$. Since the spanwise fluctuating velocity component was not measured, these values were approximated. Following earlier boundary layer results, the following approximation was used: $w'^{+2} = K(u'^{+2} + v'^{+2})$, where commonly used value of *K* for high Reynolds number boundary layers is 0.5 (see e.g., Antonia and Luxton, 1971). The more recent boundary layer measurements of Skare and Krogstad (1994) showed a preference for K = 0.4. In the analysis for the present experimental measurements, K = 0.4 was adopted.

Figures 8.6a and 8.6b give a comparison of the turbulence kinetic energy, k^+, on smooth and rough surfaces using inner and outer coordinates, respectively. The semi-log plot in Figure 8.6a using inner coordinates more clearly shows the near-wall peak values for k^+ on the smooth surface. In the case of the rough surface, it is observed that the two-layer model predicts a lower peak value near the wall, but a higher overall level for turbulence kinetic energy throughout the flow. Recently, Tachie et al. (2002) observed that the effect of surface roughness reduced the turbulence level in the immediate vicinity of the wall. This suggests that the behaviour predicted by the model in the vicinity of the wall appears to follow the experimental trend. As indicated in Figure 8.6b, the smooth wall prediction ($\mathrm{Re}_\theta = 8{,}800$) is compared with the smooth

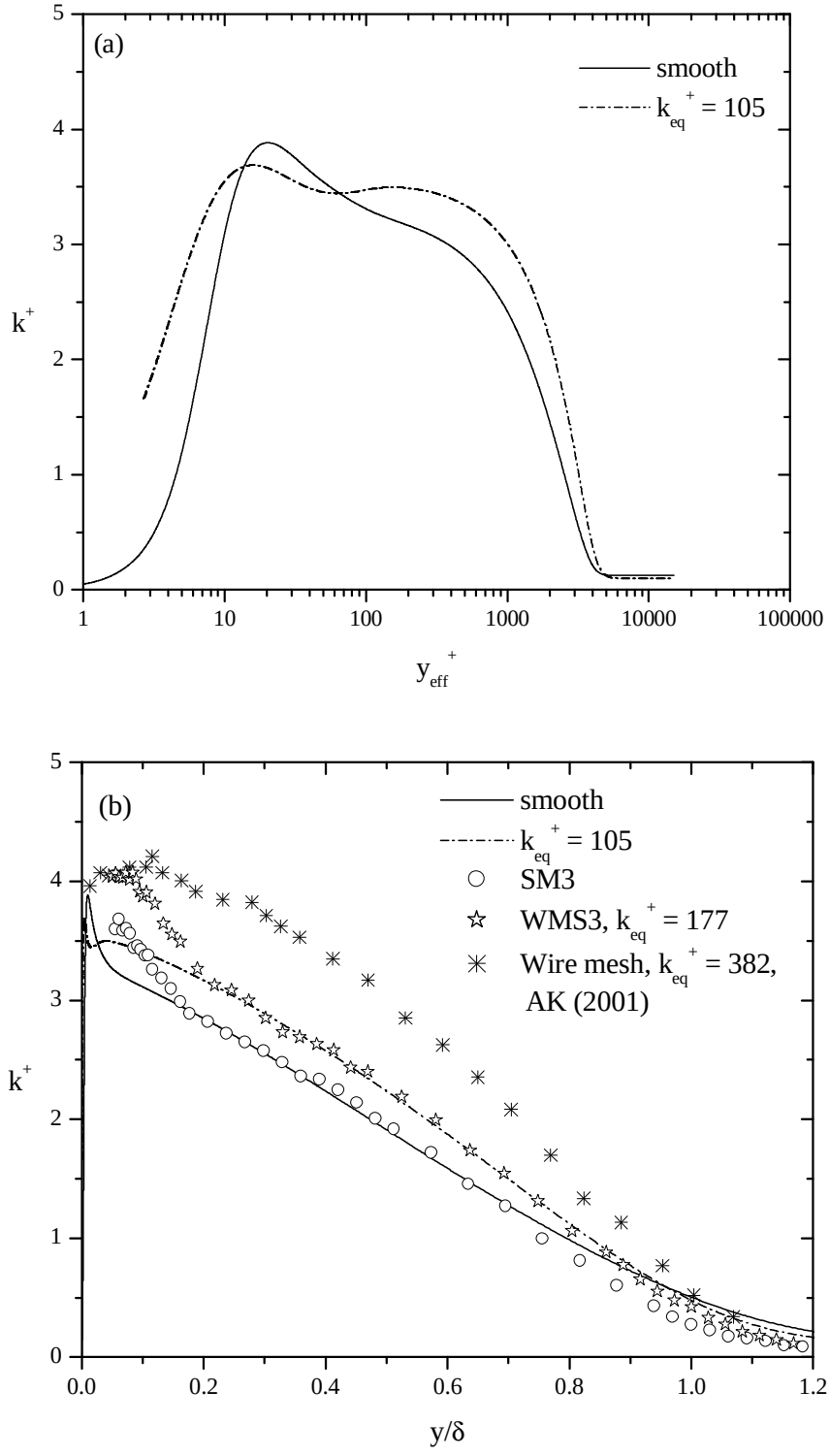

Figure 8.6: Distributions of turbulence kinetic energy on smooth and rough surfaces: (a) inner coordinates; (b) outer coordinates (AK denotes Antonia and Krogstad, 2001).

wall (SM3) data at Re_θ = 7720 obtained from the present experimental study. The comparison shows that both present numerical and experimental results are in good agreement in the overlap and outer regions of the boundary layer. In Figure 8.6b, the k^+ profile for wire mesh (WMS3) obtained from present experimental study at Re_θ = 9570 and the experimental data for wire mesh roughness obtained by Antonia and Krogstad (2001) at Re_θ = 12,800 are included for comparison. Comparison between the numerical results and WMS3 data shows that both are in good agreement in the region $y/\delta > 0.2$. Except in the near-wall region ($y/\delta \approx 0.06$), the WMS3 data for the turbulence kinetic energy is lower than the wire mesh data obtained by Antonia and Krogstad (2001). Both the predicted profile for the turbulence kinetic energy and experimental results evidently show that surface roughness significantly enhances the level of turbulence kinetic energy in the overlap and outer regions of the flow. The measurements of Tachie et al. (2000) for an open channel flow also show a higher level of turbulence kinetic energy in these regions. In this respect, the behaviour predicted by the model appears to follow the trend of recent experiments.

Figure 8.7 shows profiles for the Reynolds shear stress in the turbulent boundary layer for smooth and rough surfaces using outer coordinates. Comparison of the predicted Reynolds shear stress for the smooth surface (Re_θ = 8,800) to the experimental results reported in Chapter 6, as well as the experimental data of Antonia and Krogstad (2001) at Re_θ = 12,800 shows that the data are close to each other. The profile

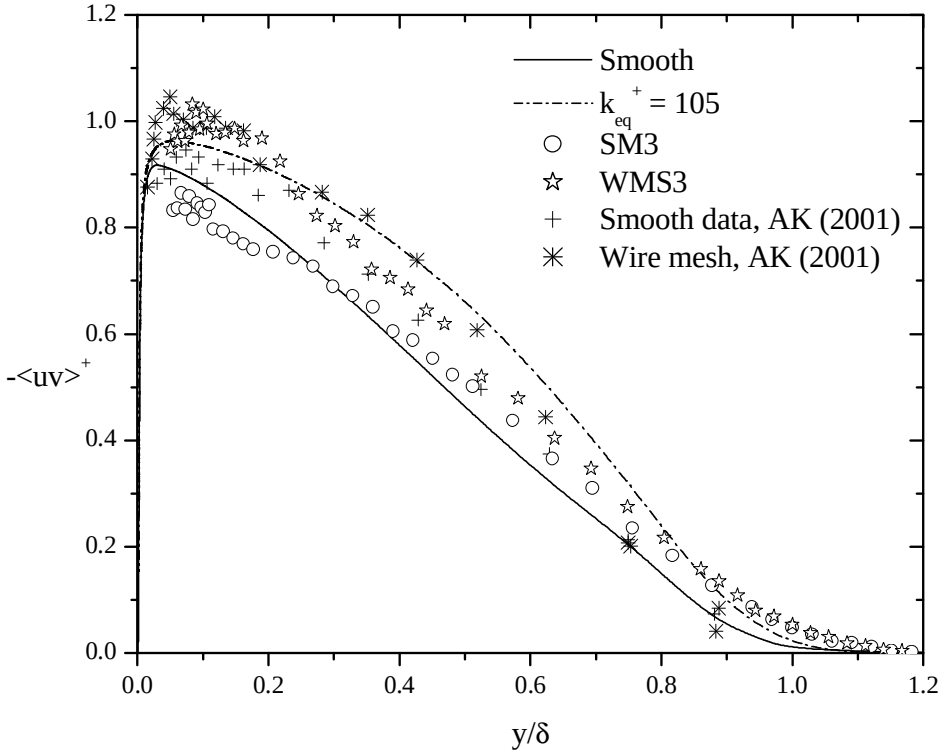

Figure 8.7: Reynolds shear stress profiles for smooth and rough surfaces (AK denotes Antonia and Krogstad, 2001).

predicted for the Reynolds shear stress is also compared with the wire mesh (WMS3) data obtained in the present experimental study and the experimental data obtained over a wire mesh roughness by Antonia and Krogstad (2001). For the case of a rough surface, the model predicts a higher level of Reynolds shear stress in both the inner and outer regions of the flow. Recent measurements of Tachie et al. (2002) showed that, irrespective of scaling, the effect of surface roughness increases the peak value of Reynolds shear stress when compared with that of smooth surface, which is similar to what the model predicted. For the wall boundary layer, the effect of surface roughness is to significantly enhance the level of the Reynolds stress profile and this effect extends almost to the outer edge of the boundary layer. Theses computational results therefore contradict the wall similarity hypothesis.

8.7 Summary

The two-layer $k-\varepsilon$ formulation of Durbin et al. (2001) has been used to simulate a zero pressure gradient turbulent boundary layer over smooth and rough surfaces. The numerical results show that the model correctly predicts the roughness shift of the mean velocity profile on a log-law plot for the fully rough flow regime. The model is also observed to predict an enhanced level for the turbulence kinetic energy and the Reynolds shear stress in the outer region of the flow. This is consistent with the present boundary layer measurements, which show that the effects of surface roughness can extend into the outer region of the flow for some specific roughness characteristics. This observation is at variance with the wall similarity hypothesis.

CHAPTER 9

SUMMARY, CONCLUSIONS, CONTRIBUTIONS, AND FUTURE WORK

A summary and conclusions, as well as the contributions of the study, are presented in this chapter. Recommendations for future work are also identified in the final section.

9.1 Summary

9.1.1 Experimental Study

Experimental measurements were obtained for two-dimensional zero pressure-gradient turbulent boundary layers over a smooth surface and ten different rough surfaces created from sand paper, perforated sheet, and woven wire mesh. The physical size and geometry of the roughness elements and freestream velocity were chosen to encompass both transitionally rough and fully rough flow regimes. Three different probes, namely, Pitot probe, single hot-wire, and cross hot-film, were used to measure the velocity fields in the turbulent boundary layer. A Pitot probe was used to measure the streamwise mean velocity, while the single hot-wire and cross hot-film probes were used to measure the fluctuating velocity components across the boundary layer. The flow Reynolds number

based on momentum thickness, Re_θ, ranged from 3730 to 13,550. In the present study, the data reported include the mean velocity, streamwise and wall-normal turbulence intensities, Reynolds shear stress, and triple correlations, as well as skewness and flatness factors. Different scaling parameters were used to interpret and assess both the smooth- and rough-wall data at different Reynolds numbers, for approximately the same freestream velocity.

For both the smooth- and rough-wall data, the friction velocity was obtained from fitting the defect profile to the experimental data. The defect profile assumes the existence of a log-law and a functional form of the wake, but it allows the strength of the wake to vary. The friction velocity was also obtained from the power law formulated by George and Castillo (1997) for the smooth and rough surfaces.

The present study examined the use of three velocity scales, i.e. the friction velocity, U_τ, freestream velocity, U_e, and mixed outer velocity scale, $U_e\delta^*/\delta$, to collapse the mean velocity data in the outer region of a turbulent boundary layer for hydraulically smooth, transitionally rough and fully rough flow regimes. The effect of each scaling was evaluated both with respect to Reynolds number and surface condition. The application of these scaling parameters gave different conclusions with regard to the effect of Reynolds number and surface roughness. The present results showed that application of the mixed outer scale, $U_e\delta^*/\delta$, caused the velocity profile in the outer region to collapse onto the same curve for different Reynolds numbers and roughness conditions.

Four different scaling parameters, i.e. the friction velocity, U_τ, freestream velocity, U_e, mixed scale, $U_\tau U_e$, as well as mixed outer scale, $U_e\delta^*/\delta$, were used to investigate self-similarity for the streamwise turbulence intensity profiles in a turbulent boundary layer for hydraulically smooth, transitionally rough, and fully rough flow regimes. The effectiveness of each scaling in collapsing the data was evaluated both with respect to Reynolds number and surface condition. The interpretation of the effect of roughness on the profile was shown to depend on the choice of scaling parameter. For the mixed outer scale, $U_e\delta^*/\delta$, the streamwise turbulence intensity profiles on smooth and rough surfaces tend to collapse in the outer region onto a single curve.

The characteristics of the fluctuating velocity field for transitionally rough and fully rough turbulent layers relative to that of the smooth-wall case were investigated. Two different scaling parameters, namely, the friction velocity and the freestream velocity, were used to assess the effect of surface roughness on the wall-normal turbulence intensity and the Reynolds shear stress in a zero pressure gradient turbulent boundary layer. In addition, profiles of the triple velocity products ($\langle u'^3\rangle$, $\langle v'^3\rangle$, $\langle u^2v\rangle$, and $\langle uv^2\rangle$), as well as skewness and flatness factors were also obtained for the smooth surface and five different rough surfaces. Two different scaling parameters, i.e. the friction velocity, U_τ, and a mixed scale, $U_eU_\tau^2$, proposed by George and Castillo (1997), were used to assess the effect of roughness on the triple velocity correlations. The present results show that the extent to which the turbulence quantities are modified in the inner and outer regions by surface roughness depends on the characteristics of the roughness elements.

9.1.2 Numerical Study

9.1.2.1 Pipe Flow

Time-averaged turbulence models were used to predict the mean velocity and turbulence quantities in smooth and rough pipes. Specifically, the use of a new proposed wall function formulation in the treatment of the boundary conditions for k-ε closures was employed. The new wall function formulation is based on power laws, opposed to the logarithmic law approach. The new wall function was used to predict the mean velocity profiles and friction factor for smooth and rough wall turbulent pipe flow.

9.1.2.2 Boundary layer

The two-layer k-ε model of Durbin et al. (2001) was used to simulate a zero pressure-gradient turbulent boundary layer flow over smooth and rough walls. The model was used to predict the mean velocity, turbulence kinetic energy, and Reynolds shear stress for smooth and rough surfaces. The numerical results show that the effect of surface roughness modifies the mean velocity and turbulence quantities both in the inner and outer regions of the boundary layer. This observation contradicts the wall similarity hypothesis.

9.2 Conclusions

The major conclusions of the present study are summarized as follows:

9.2.1 Experimental Study

1. Comparison between the values of the friction velocity obtained through the defect law and the power law profile fitting techniques for smooth and rough

surfaces gave values that are within ± 3% of each other. Comparison between the logarithmic law and power law profiles was used to identify a common region within the overlap region where both profiles adequately represent the flow. Based on this comparison, functional relationships between the roughness shift, ΔU^+, and the power law coefficients were developed for transitionally rough flows. For the fully rough flow, an envelope was established for the power law coefficient, C_i, and exponent, γ, at the lowest roughness shifts obtained for different rough surfaces.

2. A correlation that relates the skin friction, C_f, to the ratio of the displacement and boundary layer thicknesses, δ^*/δ, which is valid for both smooth- and rough-wall flows, was proposed (*Accepted for publication, ASME Journal of Fluids Engineering*).
3. It was found that use of a "mixed outer scale", $U_e\delta^*/\delta$, caused the velocity defect profile (*Published, Experiments in Fluids*), and streamwise turbulence intensity in the outer region to collapse onto the same curve, irrespective of Reynolds numbers and roughness conditions.
4. The surface roughness in general modifies the streamwise turbulence intensity and also the Reynolds shear stress in the inner layer for all rough surfaces considered, and the effects extend into the outer region of the boundary layer when scaled with the friction velocity. However, except for the wire mesh roughness, the effects of surface roughness on the wall-normal turbulence intensity are confined within the roughness sublayer. These observations at best

only lend partial support to the wall similarity hypothesis. The present results suggest that the effect of surface roughness on the turbulence field depends to some degree on the specific characteristics of the roughness elements and also the component of the Reynolds stress tensor being considered. Scaling the Reynolds stresses with the freestream velocity results in a more pronounced effect of surface roughness, which is to enhance the levels of all three Reynolds stress components.

5. The experimental results indicate that surface roughness significantly alters some components of the third moment in the inner region, and this effect also extends into the outer region of the boundary layer. This observation is at variance with the wall similarity hypothesis. On the other hand, the distributions of the skewness for both the longitudinal and wall-normal velocity fluctuations are largely unaffected by surface roughness.

9.2.2 Numerical Study

9.2.2.1 Pipe Flow

1. The new wall function formulation correctly predicted the friction factors for smooth and fully rough flows.

9.2.2.2 Boundary Layer

1. The two-layer $k-\varepsilon$ model realistically predicts the velocity shift on a log-law plot for the fully rough flow regime.

2. The effect of roughness is to enhance the level of turbulence kinetic energy compared to that on a smooth wall. This enhanced level extends into the outer region of the flow, which appears to be consistent with present experimental results for boundary layer.
3. The model predicts a higher level of Reynolds shear stress for the rough surface than that on a smooth surface in both inner and outer regions of the flow.
4. The computational results contradict Townsend's similarity hypothesis.

9.3 Contributions

The major contributions of this study are summarized as follows:

1. A complete and comprehensive data set for two-dimensional zero pressure-gradient rough wall turbulent boundary layers was obtained.
2. A novel skin friction correlation for a zero pressure gradient turbulent boundary layer over surfaces with different roughness characteristics was proposed.
3. Functional relationships between the roughness shift, ΔU^+, and the power law coefficients were developed for the transitionally rough flows was proposed.
4. The first study to incorporate a power law formulation into a wall function formulation which includes roughness effects.

9.4 Recommendations for Future Work

In view of the above conclusions and the current understanding of the effect arising from wall roughness elements on the turbulence structure, the following recommendations are relevant for future work:

1. A more comprehensive assessment of the validity of the novel skin friction correlation requires further investigation using other types of surface geometries and a wider range of Reynolds number based on boundary layer thickness.

2. Additional data for fully rough flow regimes are required to calibrate the power law coefficient and exponent, as well as to examine the effects of varying the blockage ratio, δ^* / δ, and the equivalent sand grain roughness Reynolds number, k_{eq}^+ .

3. In order to further investigate the flow dynamics on rough wall boundary layers, application of PIV or hot-wire rake to explore the coherent structure in the immediate vicinity of the roughness element is required. This will provide further insight into the interaction between the inner and outer layers.

REFERENCES

Acharya, M., Bornstein, J., and Escudier, M. P. 1986 Turbulent Boundary Layers on Rough Surfaces. *Experiments in Fluids*, **4**, pp. 33-47.

Afzal, N. 2001 Power Law and Log Law Velocity Profiles in Fully Developed Turbulent Boundary Layer Flow: Equivalent Relations at Large Reynolds Numbers. *Acta Mechanica*., **151,** pp. 195-216.

Andreopoulos, J. and Bradshaw, P. 1981 Measurements of Turbulence Structure in the Boundary Layer on a Rough Surface. *Boundary-Layer Meteorology*, **20**, pp. 201-213.

Antonia, R. A. and Krogstad, P. A. 2001 Effect of Different Surface Roughnesses on a Turbulent Boundary Layer. *Fluid Dynamics and Research*, **28**, pp. 139-157.

Antonia, R. A. and Krogstad, P-A. 1993 Scaling of the Bursting Period in Turbulent Rough Wall Boundary Layers. *Experiments in Fluids*, **15**, pp. 82-84.

Antonia, R. A. and Luxton, R. E. 1971 The Response of a Turbulent Boundary Layer to a Step Change in Surface Roughness, Part 1. Smooth to Rough. *Journal of Fluid Mechanics*, **48**, pp. 721-143.

Ashrafian, A., Andersson, H. I., and Manhart, M. 2004 DNS of Turbulent Flow in a Rod-Roughened Channel. *International Journal of Heat and Fluid Flow*, **25**, pp. 373-383.

Baldwin, B. S. and Barth, T. J. 1990 A One-Equation Turbulence Transport Model for High Reynolds Number Wall-Bounded Flows. NASA TM 102847.

Bandyopadhyay, P. R. and Watson, R. D. 1988 Structure of Rough-wall Turbulent Boundary Layers. *Physics of Fluids*, **31**, pp. 1877-1883.

Bandyopadhyay, P. R. 1987 Rough-Wall Turbulent Boundary Layers in the Transition Regime. *Journal Fluid Mechanics*, **180**, pp. 231-266.

Barenblatt, G. I. 1993 Scaling Laws for Fully Developed Shear Flow. Part 1. Basic Hypotheses and Analysis. *Journal of Fluid Mechanics*, **248**, pp. 513-520.

Barenblatt G. I., Chorin A. J., and Prostokishin V. M. 2000 A note on the overlap region in turbulent boundary layer. *Physics of Fluids*, **12,** pp. 2159-2161.

Bergstrom, D. J., Kotey, N. A. and Tachie, M. F. 2002 The Effect of Surface Roughness on the Mean Velocity Profile in a Turbulent Boundary Layer. *Transactions ASME Journal of Fluids Engineering*, **124**, pp. 664-670.

Bergstrom, D. J., Tachie, M. F., and Balachandar, R. 2001 Application of Power Laws to Low Reynolds Number Boundary Layers on Smooth and Rough surfaces. *Physics of Fluids*, **13**, pp. 3277-3284.

Bradshaw, P. 1970 *Experimental Fluid Mechanics*, Pergamon Press, Oxford.

Bradshaw, P. 1987 Wall Flows. *In Turbulent Shear Flows* 5, (eds. F. Durst, B. E. Launder, J. L. Lumley, F. W. Schmidt, and J. H. Whitelaw), pp. 171-175.

Buschmann M H and Gad-el-Hak M 2003 Debate Concerning the Mean-Velocity Profile of a Turbulent Boundary Layer. *AIAA Journal*., **41**, pp. 565-572.

Buschmann, M. H. and Meniert J. 1999 Power-Law or Logarithmic Law for Turbulent Boundary Layers with Low Reynolds Number? Colloquium Fluid Dynamics Prague, Germany, 8 pages.

Castillo, L. and Walker, D. J. 2002 Effect of Upstream Conditions on the Outer Flow of Turbulent Boundary Layers. *AIAA Journal*, **40**, pp. 1292-1299.

Cebeci, T. and Chang, K. C. 1978 Calculation of Incompressible Rough-Wall Boundary Layer Flows. *AIAA Journal*, **16**, pp. 730-735.

Chen C. J. and Patel V. C. 1988 Near-Wall Turbulence Models for Complex Flows Including Separation. *AIAA Journal*, **26**, 641-648.

Clauser, F. H. 1954 Turbulent Boundary Layers in Adverse Pressure Gradient. *J. Aeronaut. Sci*., **21**, pp. 91-108.

Colebrook, C. F. 1939 Turbulent Flow in Pipes, with Particular Reference to the Transition between the Smooth and Rough Pipes Laws. *J. Inst. Civ. Eng. Lond*., **11**, pp. 133-156.

Coleman, H. W. and Steele, W. G. 1999 *Experimentation and Uncertainty Analysis for Engineers*. 2nd Ed, Wiley, New York.

Coles, D. E. 1956 The Law of the Wake in the Turbulent Boundary Layer. *Journal of Fluid Mechanics*, **1**, pp. 191-226.

Coles, D. 1962 The Turbulent Layer in a Compressible Fluid. The Rand Corp., Rep. R-403-PR.

Craft, T. J., Launder, B. E., and Suga, K. 1996 Development and Application of a Cubic Eddy-Viscosity Model of Turbulence, *International Journal of Heat and Fluid Flow*, **17**, pp. 108-115.

DeGraaff, D. B. and Eaton, J. K. 2000 Reynolds-Number Scaling of the Flat-Plate Turbulent Boundary Layer. *Journal of Fluid Mechanics*, **422**, pp. 319-346.

Djenidi, L., Dubief, Y., and Antonia, R. A. 1997 Advantages of Using a Power Law in Low Re_θ Boundary Layers. *Experiments in Fluids,* **22,** pp. 348-350.

Durbin, P. A., Medic, G., Seo, J. M., Eaton, J. K., and Song, S. 2001 Rough Wall Modification of Two-Layer *k-ε*. *Transactions ASME Journal of Fluids Engineering,* **123**, pp. 16-21.

Fernholz, H. H. and Finley, P. J. 1996 The Incompressible Zero-Pressure Gradient Turbulent Boundary Layer: An Assessment of the Data. *Prog. Aerospace Sci.,* **32**, pp. 245-311.

Fernholz, H. H., Krause, E., Nockemann, M., and Schober, M. 1995 Comparative Measurements in the Canonical Boundary Layer at $Re_\theta \leq 6 \times 10^4$ on the Wall of the DNW, *Physics of Fluids A*, **7**, pp. 1275-1281.

Finley, P. J., Chong Phoe, Khoo., and Jeck Pohn, Chin. 1966 Velocity Measurements in a Thin Turbulent Wake Layer. *La Houille Blanche*, **21**, pp. 713-721.

Flack, K. A., Schultz, M. P., and Shapiro, T. A. 2005 Experimental Support for Townsend's Reynolds Number Similarity Hypothesis on Rough Walls. *Physics of Fluids*, **17**, pp. 035102.

Furuya, Y. and Fujita, H. 1967 Turbulent Boundary Layers on a Wire Screen. *Bull. JSME*, **10**, pp. 77-86.

Gad-el-Hak, M. and Bandyopadhyay, P. R. 1994 Reynolds Number Effects in Wall-Bounded Flows. *Applied Mechanics Review,* **47**, pp. 307-364.

George, J. and Simpson, R. L. 2000 Some Effects of Sparsely Distributed Three-Dimensional Roughness Elements on Two-Dimensional Turbulent Boundary Layers. 38th Aerospace Science Meeting and Exhibt, AIAA 2000-0915.

George, W. K. and Castillo, L. 1997 Zero Pressure Gradient Turbulent Boundary Layer. *Applied Mechanics Review,* **50**, pp. 689-729.

Granville, P. S. 1985 Mixing-Length Formulations for Turbulent Boundary Layers over Arbitrarily Rough Surfaces. *Journal of Ship Research*, **29**, pp. 223-233.

Granville, P. S. 1976 A Modified Law of the Wake for Turbulent Shear Layers. *Transactions ASME Journal of Fluids Engineering*, **29**, pp. 578-580.

Grass, A. J. 1971 Structural Features of Turbulent Flow Over Smooth and Rough Boundaries. *Journal of Fluid Mechanics*, **50**, pp. 233-255.

Hinze, J. O. 1975: *Turbulence*, 2nd edition, McGraw-Hill.

Hosni, M. H., Coleman, H. W., Gardner, J. W., and Taylor, R. P. 1993 Roughness Element Shape Effects on Heat Transfer and Skin Friction in Rough Wall Turbulent Boundary Layers. *International Journal of Heat and Mass Transfer*, **36**, pp. 147-153.

Iacovides, H. and Raise, M. 1999 Recent Progress in the Computation of Flow and Heat Transfer in Internal Cooling Passages of Turbine Blades, *International Journal of Heat and Fluid Flow,***20**, pp. 320-328.

Jayatillaka, C. L. V. 1969 The Influence of Prandtl Number and Surface Roughness on the Resistance of the Laminar Sublayer to Momentum and Heat Transfer. *Progress in Heat and Mass Transfer*, **1**, eds. U. Grigull and E. Hahne, Pergamon Press, New York, pp. 193-329.

Jimenez, J. 2004 Turbulent Flows over Rough Wall. *Annual Review of Fluid Mechanics*, **36**, pp. 173-196.

Keirsbulck, L., Labraga, L., Mazouz, A., and Tournier, C. 2002 Surface Roughness Effects on Turbulent Boundary Layer Structures. *Transactions ASME Journal of Fluids Engineering*, **124**, pp. 127-135.

Keirsbulck, L., Mazouz, A., Labraga, L., and Tournier, C. 2001 Influence of the Surface Roughness on the Third-Order Moments of Velocity Fluctuations. *Experiments in Fluids*, **30**, pp. 592-294.

Klebanoff P. S. 1954 Characteristics of Turbulence in a Boundary Layer with Zero Pressure Gradient. *NACA* TN-3178.

Klebanoff, P. S. and Diehl, Z. W. 1951 Some Features of Artificially Thickened Fully Developed Turbulent Boundary Layers with Zero Pressure Gradient. NACA Report 1110, NACA Technical Note 2475.

Kotey, N. A., Bergstrom, D. J., and Tachie, M. F. 2003 Power Laws for Rough Wall Turbulent Boundary Layers. *Physics of Fluids*, **15**, pp. 1396-1404.

Krogstad P. A. (1991). Modification of the van Driest Damping Function to Include the Effects of Surface Roughness. *AIAA Journal* **29**, 688-694.

Krogstad, P. A. and Antonia, R. A. 1999 Surface Roughness Effects in Turbulent Boundary Layers. *Experiments in Fluids*, **27**, pp. 450-460.

Krogstad, P. A., Antonia, R. A., and Browne, L. W. B. 1992 Comparison Between Rough and Smooth Wall Turbulent Boundary Layers. *Journal of Fluid Mechanics.*, **245**, pp. 599-617.

Launder, B. E. and Spalding, D. B. 1974 The Numerical Computation of Turbulent Flows. *Comp. Meth. Appl. Mech.*, **3**, pp. 269-298.

Ligrani, P. M. and Moffat, R. J. 1985 Structure of Transitionally Rough and Fully Rough Turbulent Boundary Layers. *Journal of Fluid Mechanics*, **162**, pp. 69-98.

Mazouz, A., Labraga, L., and Tournier, C. 1994 Behaviour of Reynolds Stress on Rough Wall. *Experiments in Fluids*, **120**, pp. 280-284.

Millikan, C. M. 1938 A Critical Discussion of Turbulent Flows in Channel and Circular Tubes. *In Proc. 5th International Congress on Applied Mechanics*, Wiley, New York, pp. 386-392.

Moretti, P. H. and Kays, V. M. 1965 Heat Transfer in Turbulent Boundary Layer with varying Freestream Velocity and Varying Surface Temperature--An Experimental Study *Int. J. Heat Mass Transfer*, **8**, pp. 1187-202

Nikuradse, J. 1933 Stromungsgesetze in rauhen rohen. ForschHft Ver. Dt. Ing 361.

Osaka, H., Kameda, T. and Mochizyki, S. 1998 Re-examination of the Reynolds Number Effects on the Mean Flow Quantities in a Smooth Wall Turbulent Boundary Layers. *JSME Int. J., Ser. B*, **41**, No. 5, pp. 802-811.

Österlund, J. M., 1999 Experimental Studies of Zero Pressure-Gradient Turbulent Boundary-Layer Flow. PhD Thesis, Royal Institute of Technology, Stockholm.

Österlund, J. M., Johansson A. V., Nagib, H. M., and Hites, M. H. 2000 A Note on the Overlap Region in Turbulent Boundary Layers. *Physics of Fluids*, **12** pp. 1-4.

Panton, R. L. 1990 Scaling Turbulent Wall Layers. *Transactions ASME Journal of Fluids Engineering*, **112**, pp. 425-432

Panton, R. L. 2000 Power Law or Log Law; That is Not the Question. *Bull. Am. Phys. Soc.*, **45**, pp. 160

Panton, R. L. 2002 Evaluation of the Barenblatt-Chorin-Prostokishin Power Law for Turbulent Boundary Layers. *Physics of Fluids*, **14**, pp. 1806-1808.

Patankar, S. V. 1980 *Numerical Heat Transfer and Fluid Flow*, McGraw-Hill, New York.

Patel, V. C. 1998 Perspective: Flow at High Reynolds Numbers and over Rough Surfaces- Achilles Heel of CFD. *Transactions ASME Journal of Fluids Engineering*, **120**, pp. 434-444.

Patel, V. C. and Yoon, J. Y. 1995 Application of Turbulence Models to Separated Flow over Rough Surfaces. *Transactions ASME Journal of Fluids Engineering*, **117**, pp. 234-241.

Perry, A. E. and Li, J. D. 1990 Experimental Support for the Attached Eddy Hypothesis in Zero-Pressure Gradient Turbulent Boundary Layers. *Journal of Fluid Mechanics*, **218**, pp. 405-438.

Perry, A. E., Lim, K. L., and Henbest, S. M. 1987 An Experimental Study of the Turbulence Structure in Smooth- and Rough-Wall Boundary Layers. *Journal of Fluid Mechanics*, **177**, pp. 437-466.

Perry, A. E., Schofield, W. H., and Joubert, P. N. 1969 Rough Wall Turbulent Boundary Layers. *Journal of Fluid Mechanics*, **37**, pp. 383-413.

Porporato, A. and Sordo, S. 2001 On the Incomplete Similarity for Turbulent Velocity Profiles in Rough Pipes. *Physics of Fluids*, **13**, pp. 2596-2601.

Prandtl, L. 1932 Zur Turbulenten Strömung in Roren und langs Plätten, Ergeb Aerod Versuch Gottingen, IV Lieferung, 18 (in German).

Purtell, L. P., Klebanoff, P. S., and Buckley, F. T. 1981 Turbulent Boundary Layer at Low Reynolds Number. *Physics of Fluids*, **24**, pp. 802-811.

Raupauch, M. R., Antonia, R. A., and Rajagopalan, S. 1991 Rough-Wall Turbulent Boundary Layers. *Applied Mechanics Review*, **44**, pp. 1-25

Rodi, W. and Mansour, N. N. 1990 One-Equation Near-Wall Turbulence Modeling with the Aid of Direct Simulation Data. *Proc. Summer Program 1990*, Center for Turbulence Research, Stanford.

Rotta, J. C. 1962 Turbulent Boundary Layers in Incompressible Flow. *Prog. Aeronaut. Sci.*, **2**, pp. 1-220.
Schlichting, H. 1968 *Boundary-Layer Theory*, 6th Edition, McGraw-Hill, New York.

Schlichting, H. 1979 *Boundary-Layer Theory*, 7th Edition, McGraw-Hill, New York.

Schultz, M. P. and Flack, K. A. 2005 Outer Layer Similarity in Fully Rough Turbulent Boundary Layers. *Experiments in Fluids*, **38**, pp. 328-340.

Schultz, M. P. and Flack, K. A. 2003 Turbulent Boundary Layers over Surface Smoothed by Sanding. *Transactions ASME Journal of Fluids Engineering*, **125**, pp. 863-870.

Schultz-Grunow, 1941 New Frictional Resistant Law for Smooth Plates. NACA TM 986.

Seo, J. 2003 Investigation of the Upstream Conditions and Surface Roughness in Turbulent Boundary Layer. Ph.D. thesis, Department of Mechanical and Aeronautical Engineering, Rensselaer Polytechnic Institute, NY.

Seo, J., Castillo, L., Johansson, T. G., and Hangan, H. 2004 Reynolds Stress in Turbulent Boundary Layers at High Reynolds Number. *Journal of Turbulence*, **5**, pp. 1-22.

Skare, P. E. and Krogstad, P. –A. 1994 A Turbulent Equilibrium Boundary Layer Near Separation. *Journal of Fluid Mechanics*, **272**, pp. 319-348.

Song, S. and Eaton, J. K. 2002 The Effects of Wall Roughness on the Separated Flow over a Smoothly Contoured Ramp. *Experiments in Fluids*, **33**, pp. 38-46.

Spalart R. 1988 Direct Simulation of a Turbulent Boundary Layer up to $Re_\theta = 1410$. *Journal of Fluid Mechanics*, **187**, pp. 61-98.

Spalart, P. R. and Allmaras, S. R. 1994 A One-Equation Turbulence Model for Aerodynamic Flows. *Recherche Aerospatiale*, **1**, 5-21.

Sumner, D. 2002 A Comparison of Data-Reduction Methods for a Seven-Hole Pressure Probe. *Transactions ASME Journal of Fluids Engineering*, **124**, pp. 523-527.

Tachie, M. F., Bergstrom, D. J., and Balachandar, R. 2000 Rough Wall Turbulent Boundary Layers in Shallow Open Channel Flow. *Transactions ASME Journal of Fluids Engineering*, **122**, pp. 533-541.

Tachie, M. F., Bergstrom, D. J., Balachandar, R., and Ramachandran, S. 2001 Skin Friction Correlation in Open Channel Boundary Layers. *Transactions ASME Journal of Fluids Engineering*, **123**, pp. 953-956.

Tachie M. F., Bergstrom D. J., and Balachandar R. 2002 The Effect of Wall Roughness on an Open Channel Boundary Layer. In *Proceedings of the 5th International Symposium on Engineering Turbulence Modelling and Measurements*, (eds.W. Rodi and Fueyo, N.), Mallorca, Spain, pp. 455-464.

Tachie, M. F., Bergstrom, D. J., and Balachandar, R. 2003 Roughness Effects in Low-Re_θ Open-Channel Turbulent Boundary Layers. *Experiments in Fluids*, **35**, pp. 338-346.

Tachie, M. F., Bergstrom, D. J., and Balachandar, R. 2004 Roughness Effects on the Mixing Properties in Open-Channel Turbulent Boundary Layers. *Transaction ASME Journal of Fluids Engineering*, **126**, pp. 1025-1032.

Tarada, F. 1990 Prediction of Rough-Wall Boundary Layers using a Low Reynolds Number k-ε Model. *International Journal of Heat and Fluid Flow*, **11**, pp. 331-354.

Taylor, R. P., Coleman, H. W., and Hodge, B. K. 1985 Prediction of Turbulent Rough-Wall Skin Friction Using a Discrete Element Approach. *Transactions ASME Journal of Fluids Engineering*, **107**, pp. 251-257.

Taylor, R. P., Scaggs, W. F., and Coleman, H. W. 1988 Measurement and Prediction of the Effects of Non-uniform Surface Roughness on Turbulent Flow Friction Coefficients. *Transactions ASME Journal of Fluids Engineering*, **110**, pp. 380-384.

Tennekes, H. and Lumley, J. L. 1972 *A First Course in Turbulence*. MIT Press, Cambridge, USA.

Townsend, A. A. 1976 *The Structure of Turbulent Shear Flow*. Cambridge University Press, Cambridge.

Van Driest, E. R. 1956 On Turbulent Flow Near a Wall. *Journal of Aerospace Science*, **7**, pp. 1-20.

White, F. M. 1974 *Viscous Fluid Flow*, McGraw-Hill, New York.

Zagarola, M. V. 1996 Mean Flow Scaling in Turbulent Pipe Flow. Ph.D Thesis, Princeton University.

Zagarola, M. V., Perry, A. E., and Smits, A. J. 1997 Log Laws or Power Law: The Scaling in the Overlap Region. *Physics of Fluids*, **9**, pp. 2094-2100.

Zagarola, M. V. and Smits, A. J. 1998 A New Mean Velocity Scale for Turbulent Boundary Layers. ASME paper FEDSM98-4950.

Zhang, H., Faghri, M. and White, F. M. 1996 A New Low-Reynolds Number $k-\varepsilon$ Model for Turbulent Flow Over Smooth and Rough Surfaces. *Transactions ASME Journal of Fluid Engineering* **118**, pp. 255-259.

APPENDIX A

THERMAL ANEMOMETER SYSTEM

Introduction

The thermal anemometer system is comprised of constant temperature anemometer (CTA) hardware, signal conditioner filter, and gain/offset adjustment. The overheat adjustment (static bridge balancing), a square wave test (dynamic bridge balancing), low-pass filter, and gain/offset settings are incorporated into the hardware set-up. The working temperature of the sensor is determined through the overheat adjustment. The use of overheat adjustment depends on how the temperature varies during set-up, calibration, and experiment. A value of 0.8 of the overheating ratio as recommended by TSI was adopted in the present experiment. This value was fixed throughout the experiment since the temperature correction was performed on the measured anemometer voltages before conversion and reduction.

Temperature Correction

The fluid temperature, T_a, with the CTA voltage, E_a, were acquired together in the present experiment. Due to the variation of the temperature during the calibration and experiment, the corrected CTA voltage, E_{corr}, following Bearman (1971), was calculated as follows:

$$E_{corr} = \left(\frac{T_w - T_o}{T_w - T_a} \right)^{0.5} E_a \tag{A1}$$

where E_a is the acquired voltage, T_w is the sensor hot temperature, T_o is the ambient reference temperature related to the last overheat set-up before calibration, and T_a is the ambient temperature during acquisition. The above Eqn. (A1) is valid for the temperature changes in air of $\pm 5^0$C.

Gain and Offset

The gain acts as the CTA signal amplifier, in which the signal is amplified in order to utilize an A/D board, while the offset is performed if the signal moves outside of the range of the A/D board, when a high amplification of the signal is needed prior to digitizing.

Sum and Difference Calibration Method for X-Probe and Error Analysis

Cheesewright (1972) introduced a look-up matrix method. In this method a (U_o, α) calibration was undertaken using different velocities and angular positions. For each velocity/yaw – angle pair (U_o, α), shown in Figure A1, a unique voltage pair (E_1, E_2) is obtained. A similar approach is also adopted in the present calibration. The probe is oriented such that the binormal velocity component (W), i.e. the velocity component perpendicular to both wires, equals zero. The angles α_1 and α_2 are both equal to 45^o. The streamwise and cross-stream velocities were obtained from the equations

$$U = U_o \cos\alpha \tag{A2}$$

$$V = U_o \sin\alpha \tag{A3}$$

where U and V are the streamwise and cross-stream velocity components, respectively, and α is the probe angle of attack. The reference values were selected for U_{or} in steps 5 m/s from 5 to 45 m/s and for α_r in steps 8.1^o from – 32.4 to + 32.4. For each set of reference values (U_{or}, α_r), the corresponding reference velocity components U_r and V_r are obtained using Eqns. (A2) and (A3). Two variables, x and y (not representing coordinates), denoting the streamwise and cross stream velocity components, are determined from the wire voltages E_1 and E_2 as follows

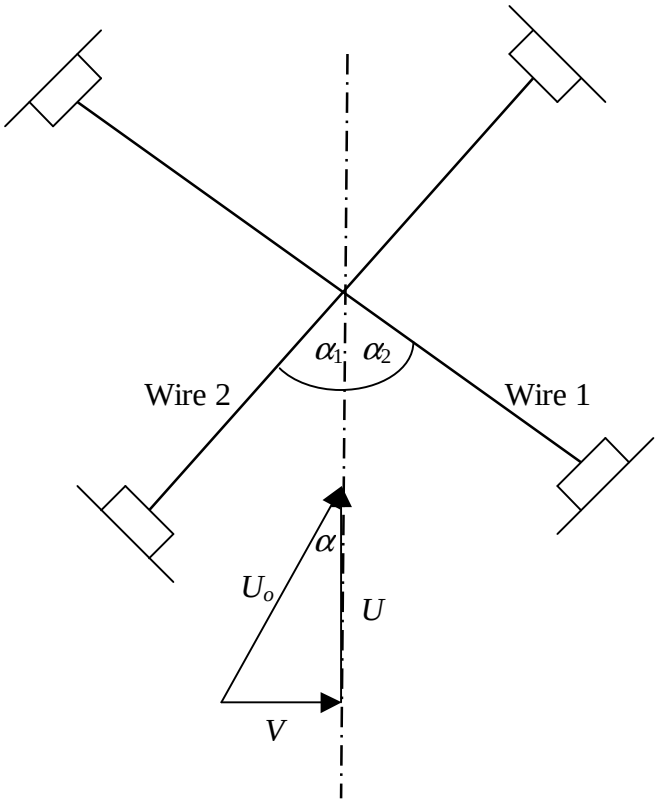

Figure A1: The definition of the yaw angle in the plane of the prong

$$x = E_1 + E_2 \tag{A4}$$

$$y = E_1 - E_2 \tag{A5}$$

The two variables are then used to obtain two two-dimensional third-order polynomials, given by Eqns. (3.9) and (3.10). The calibration data were curve-fitted using a least squares method. The accuracy of the curve-fit for the resultant velocity, U_o, and yaw angle, α, were determined from the related normalized standard error given in Eqn. A6 and A7, respectively

$$\varepsilon_{U_o} = \left(\frac{1}{N} \sum_{i=1}^{N} \left(1 - \frac{U_m}{U_c} \right)^2 \right)^{1/2} \tag{A6}$$

$$\varepsilon_{\alpha} = \left(\frac{1}{N} \sum \left(1 - \frac{\tilde{U}_m}{\tilde{U}_c} \right)^2 \right)^{1/2} \tag{A7}$$

where U_m is the measured velocity, $\tilde{U}_m$ is the measured magnitude of the velocity vector, U_c is the calculated velocity, and $\tilde{U}_m$ is the calculated magnitude of the velocity. Figures A2 and A3 demonstrate the accuracy of the calibration data and the curve-fit. The overall errors in the resultant velocity, U_o, and yaw angle, α, are 2.4 % and 4.4 %. By comparing the calculated values (U_c, V_c) with the reference values (U_r, V_r) in the form

$$\Delta U = \frac{U_c - U_r}{U_r} \% \tag{A8}$$

$$\Delta V = \frac{V_c - V_r}{V_r} \% \tag{A9}$$

The accuracy of the sum and difference calibration method was therefore established.

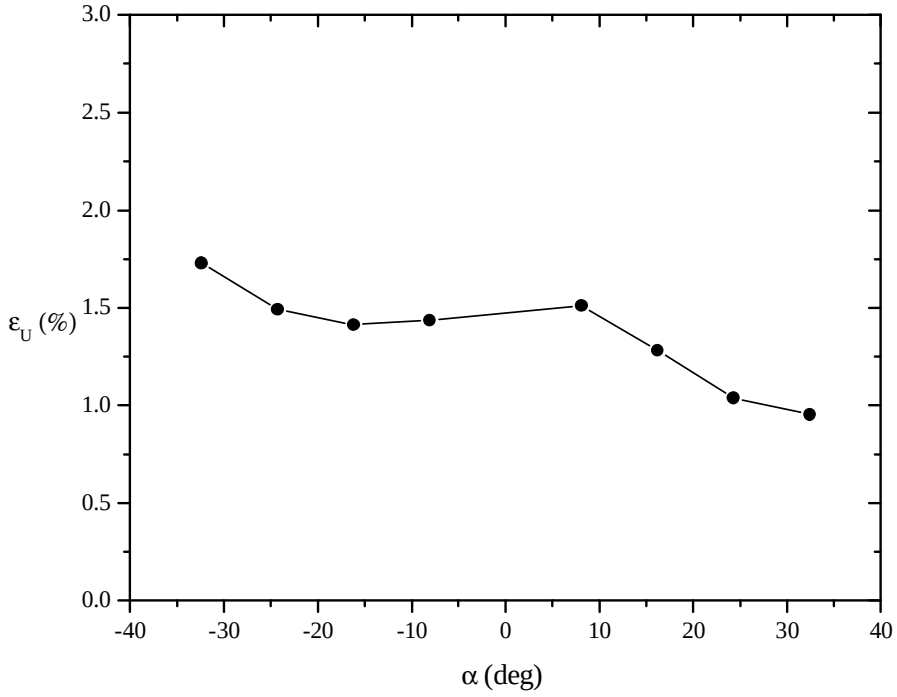

Figure A2: Calibration curve-fit accuracy for the effective velocity

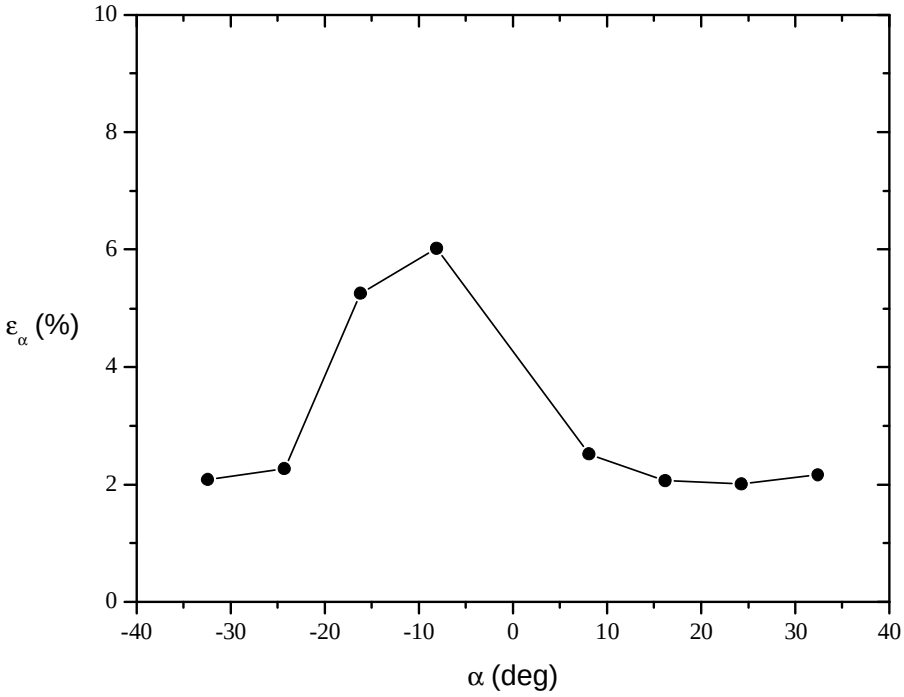

Figure A3: Calibration curve-fit accuracy for the flow angle

APPENDIX B

UNCERTAINTY ANALYSIS

General Background

Measurement systems consist of the instrumentation, the procedures for data acquisition and reduction, and the operational environment. Measurements are made of individual variables, x_i, to obtain a result, R, which is calculated by combining the data for various individual variables through data reduction equations as follows:

$$R = R(x_1, x_2, x_3, \ldots\ldots\ldots, x_n) \tag{B1}$$

Each of the measurement systems used to measure the value of an individual variable, x_i, is influenced by various elemental error sources. The effects of these elemental errors are manifested as bias errors, B_i, and precision errors, P_i, in the measured values of the variable, x_i. These errors in the measured values then propagate through the data reduction equation, thereby generating the bias and precision errors in the experimental results. The effect of an uncertainty on any individual variable on the experimental result, R, may be estimated by considering the derivative of the data reduction equation (Coleman and Steele, 1999). A variation δx_i (in x_i) would cause R to vary according to

$$\delta R_i = \frac{\partial R}{\partial x_i}\delta x_i \tag{B2}$$

Eqn. (B2) can be normalized by R to obtain

$$\frac{\delta R_i}{R} = \frac{1}{R}\frac{\partial R}{\partial x_i}\delta x_i \tag{B3}$$

where $\partial R / \partial x_i$ are the sensitivity coefficients. Eqn. (B3) can be re-written as follows:

$$\frac{\delta R_i}{R} = \frac{x_i}{R}\frac{\partial R}{\partial x_i}\frac{\delta x_i}{x_i} \tag{B4}$$

The estimation of the uncertainty interval in the experimental result due to any variation in x_i can be obtained using eqn. (B4) as follows:

$$\frac{U_{R_i}}{R} = \frac{x_i}{R}\frac{\partial R}{\partial x_i}\frac{U_{x_i}}{x_i} \tag{B5}$$

Applying Taylor's expansion to eqn. (B5) yields

$$\frac{U_R}{R} = \left[\left(\frac{x_1}{R}\frac{\partial R}{\partial x_1}\frac{U_{x_1}}{x_1}\right)^2 + \left(\frac{x_2}{R}\frac{\partial R}{\partial x_2}\frac{U_{x_2}}{x_2}\right)^2 + \ldots\ldots\ldots\ldots + \left(\frac{x_n}{R}\frac{\partial R}{\partial x_n}\frac{U_{x_n}}{x_n}\right)^2\right]^{\frac{1}{2}} \tag{B6}$$

For a measured variable, x_i, the uncertainty estimate is given by

$$U_{x_i} = \left[B_{x_i}^2 + P_{x_i}^2\right]^{1/2} \tag{B7}$$

Uncertainty Estimate in the Freestream Velocity

In order to estimate the 95% precision and bias confidence limits, the procedure given by Coleman and Steele (1999) was adopted. The uncertainty estimate in the freestream velocity is determined from its data reduction equation as follows:

$$U_e = \sqrt{\frac{2\Delta P}{\rho}} \tag{B8}$$

where ΔP is the dynamic pressure and ρ is the air density. The bias and precision errors of the dynamics pressure were given by the manufacturer in the pressure transducer manual as follows: $B_{\Delta P}^2$ = 0.35 % and $P_{\Delta P}^2$ = 0.98 %. The uncertainty estimate is the dynamic pressure is

$$U_{\Delta p}^c = \sqrt{B_{\Delta P}^2 + P_{\Delta P}^2} = \pm 1.04\ \%$$

Assuming the equation of state of an ideal gas holds for the measurement conditions, then the air density can be determined as

$$\rho = \frac{Pa}{RT} \tag{B9}$$

where Pa is the absolute pressure, R is the gas constant, and T is the temperature. The uncertainty estimate in the air density is calculated from

$$\frac{U_\rho}{\rho} = \left(\left(\frac{U_{Pa}}{Pa} \right)^2 + \left(\frac{U_T}{T} \right)^2 \right)^{1/2}$$

The uncertainty estimates in the absolute pressure and temperature are 0.99 % and 0.33 %, respectively. The uncertainty estimate in air density is

$$\frac{U_\rho}{\rho} = (0.99^2 + 0.33^2)^{1/2} = \pm 1.08\ \%$$

Using the values of the uncertainty estimates for the dynamic pressure and air density, the uncertainty estimate in U_e becomes

$$\frac{U_{U_e}^c}{U_e} = \left(\left(\frac{1}{2} \frac{U_{\Delta P}^c}{\Delta P} \right)^2 + \left(\frac{1}{2} \frac{U_\rho^c}{\rho} \right) \right)^{1/2} = \pm\ 0.75\ \%$$

Reynolds Number Uncertainty

The Reynolds number is defined as

$$\mathrm{Re}_\theta = \frac{\rho U_e \theta}{\mu}$$

The uncertainty in Reynolds number is determined as follows

$$\frac{\delta \mathrm{Re}_\theta}{\mathrm{Re}_\theta} = \left[\left(\frac{\delta\rho}{\rho} \right)^2 + \left(\frac{\delta U_e}{U_e} \right)^2 + \left(\frac{\delta\theta}{\theta} \right)^2 + \left(\frac{\delta\mu}{\mu} \right)^2 \right]^{\frac{1}{2}} = \pm 6.0\%$$

Uncertainty estimate in streamwise and wall-normal fluctuating velocity components (u′ and v′)

The bias errors associated with u′ and v′ are obtained from the independent calibration, and found to be 0.0415 and 0.085, respectively. In order to estimate the precision errors, three replicable velocity profiles were obtained on a smooth and a rough surface. The precision error is estimated using the expression given below:

$$P = t \times \frac{s.d}{\sqrt{N}}$$

where s.d is the standard deviation and *N* is the number of statistical independent samples. In order to determine the independent samples, the integral time scale, which measures the time interval over which u′ (t) is correlated with itself, is estimated using the equation given below:

$$\mathrm{T} = \int_0^\infty \rho(\tau)\, d\tau$$

where τ is the time delay and $\rho(\tau)$ is the autocorrelation coefficient and is defined as follows:

$$\rho(\tau) = \frac{u'(t)u'(t+\tau)}{(u')^2}$$

Figure B1 presents the autocorrelation coefficient plots obtained for smooth and rough surfaces. The figure suggests some degree of correlation between the fluctuating motion at time t and t + τ

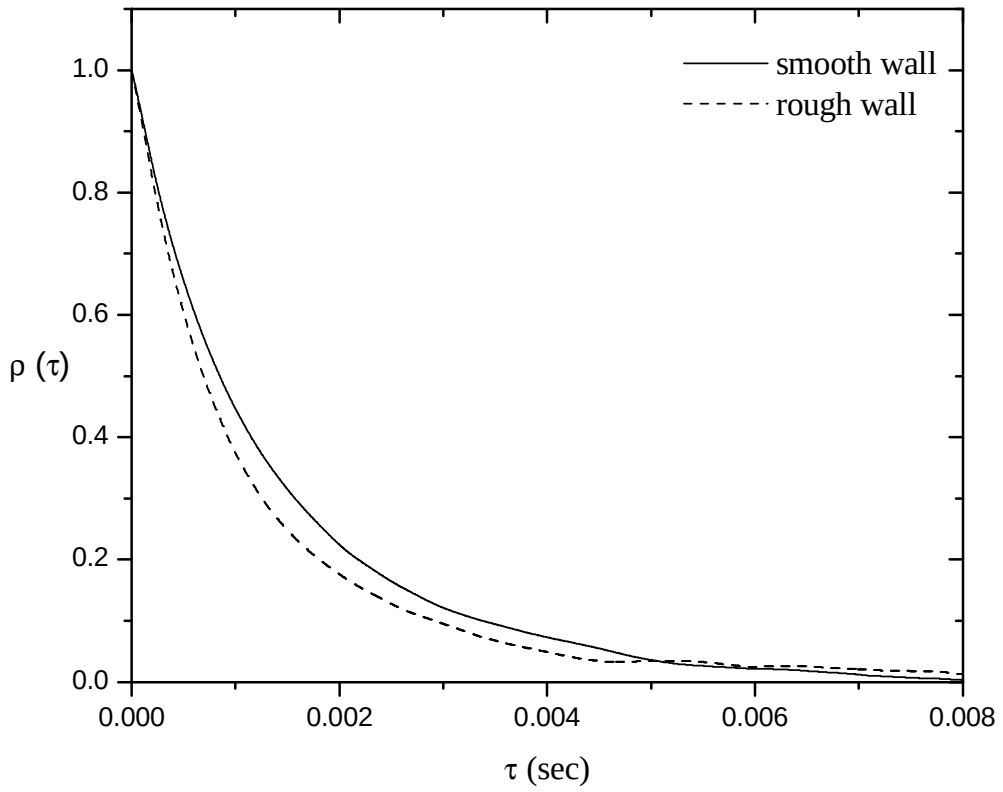

Figure B1: Autocorrelation coefficients obtained for smooth and rough surfaces

The estimated integral time scales for both the smooth and rough surfaces are 5.97×10^{-7} and 6.35×10^{-7} sec, respectively. From these results, the sample sets from the same experiment are separated by a time interval of approximately 17 integral time scales and 16 integral time scales for smooth and rough surface, respectively. The independent samples for both the smooth and rough surfaces are 5882 and 6250. Based on these information, the estimated precision errors for u' and v' are 0.00787 and 0.000253. The overall uncertainty estimates in u' and v' are 4 % and 8 %.

APPENDIX C

THE FINITE VOLUME METHOD

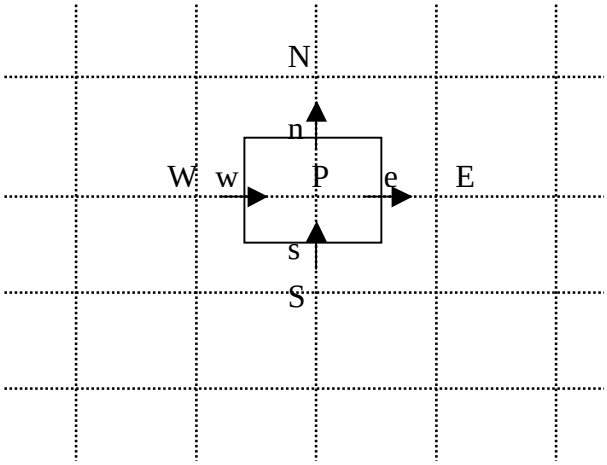

Figure C1: Control volume for discrete transport equation

As indicated in Figure C1, a general nodal point is identified by P and its neighbours in a two-dimensional geometry, the nodes to the east, west, north, and south, are identified by E, W, N, and S, respectively. The east side face of the control volume is referred to as ‘e’ and the west face of the control volume by ‘w’. Both n and s are the north and south faces of the control volume, respectively. The grid arrangement shown in Figure B1 is a staggered grid for the velocity components. This means that the scalar variables such as pressure, turbulence kinetic energy, and dissipation rate, are evaluated at ordinary nodal points, while the velocity components are calculated on staggered grids centred around the cell faces.

Discrete Transport Equations

For two-dimensional incompressible flow, the continuity and momentum equations can be written as follows:

Continuity: $$\frac{\partial(\rho U)}{\partial x}+\frac{\partial(\rho V)}{\partial y}=0 \quad \text{(C1)}$$

U – momentum: $$\rho\frac{\partial U}{\partial t}+\rho U\frac{\partial U}{\partial x}+\rho V\frac{\partial U}{\partial y}=-\frac{\partial P}{\partial x}+\frac{\partial}{\partial x}\left(\Gamma\frac{\partial U}{\partial x}\right)+\frac{\partial}{\partial y}\left(\Gamma\frac{\partial U}{\partial y}\right)+\rho g_x \quad \text{(C2)}$$

V – momentum: $$\rho\frac{\partial V}{\partial t}+\rho U\frac{\partial V}{\partial x}+\rho V\frac{\partial V}{\partial y}=-\frac{\partial P}{\partial x}+\frac{\partial}{\partial x}\left(\Gamma\frac{\partial V}{\partial x}\right)+\frac{\partial}{\partial y}\left(\Gamma\frac{\partial V}{\partial y}\right)+\rho g_y \quad \text{(c3)}$$

Each momentum equation is integrated over a control volume (CV) which is staggered, i.e. centred on the appropriate face, as shown in Figure C1.

Let ϕ represents the variables U and V, the momentum equations can be re-written as follows:

$$\underbrace{\rho\frac{\partial\phi}{\partial t}}_{Temporal}+\underbrace{\rho U\frac{\partial\phi}{\partial x}+\rho V\frac{\partial\phi}{\partial y}}_{Convection}=\underbrace{\frac{\partial}{\partial x}\left(\Gamma\frac{\partial\phi}{\partial x}\right)+\frac{\partial}{\partial y}\left(\Gamma\frac{\partial\phi}{\partial y}\right)}_{Diffusion}+S_\phi \quad \text{(C4)}$$

where S_ϕ is the source term. Integrating the momentum equation term by term as follows:

Temporal Term

$$\int_s^n \int_w^e \int_t^{t+\Delta t} \rho \frac{\partial \phi}{\partial t} dt dx dy = \int_s^n \int_w^e \rho(\phi - \phi^o)\, dx dy \doteq \rho v(\phi - \phi^o)$$

Convection Term

$$\int_t^{t+\Delta t} \int_s^n \int_w^e \left(\frac{\partial}{\partial x}(\rho U \phi) + \frac{\partial}{\partial y}(\rho V \phi) \right) dx dy dt =$$

$$\left[\underbrace{\int_s^n \int_w^e \frac{\partial}{\partial x}(\rho U \phi)\, dx dy}_{(1)} + \underbrace{\int_w^e \int_s^n \frac{\partial}{\partial y}(\rho V \phi)\, dy dx}_{(2)} \right] \Delta t$$

$$(1) = \int_s^n [(\rho U \phi)_e - (\rho U \phi)_w]\, dy = (\rho U A)_e \phi_e - (\rho U A)_w \phi_w$$

$$(2) = \int_w^e [(\rho V \phi)_n - (\rho V \phi)_s]\, dy = (\rho V A)_n \phi_n - (\rho V A)_s \phi_s$$

The mass flux is defined as $\dot{m} = \rho U A$, so that (1) and (2) become

$$(1) = \dot{m}_e \phi_e - \dot{m}_w \phi_w$$

$$(2) = \dot{m}_n \phi_n - \dot{m}_s \phi_s$$

Combining (1) and (2) together, yield

$$(\dot{m}_e \phi_e - \dot{m}_w \phi_w + \dot{m}_n \phi_n - \dot{m}_s \phi_s) \Delta t \qquad \text{(C5)}$$

Following Raithby and Schneider (1986), the interpolations for the $\phi_{i+1/2}$ and $\phi_{i-1/2}$ are given by

$$\phi_{i+1/2} = \left(\frac{1 + \alpha_{i+1/2}}{2} \right) \phi_i + \left(\frac{1 - \alpha_{i+1/2}}{2} \right) \phi_{i+1} \qquad \text{(C6)}$$

$$\phi_{i-1/2} = \left(\frac{1+\alpha_{i-1/2}}{2}\right)\phi_{i-1} + \left(\frac{1-\alpha_{i-1/2}}{2}\right)\phi_i \qquad \text{(C7)}$$

From the above interpolation, for example, the profile for ϕ_e at the CV face can be expressed as

$$\phi_e = \left(\frac{1+\alpha_e}{2}\right)\phi_P + \left(\frac{1-\alpha_e}{2}\right)\phi_E$$

The profiles for the CV faces are substituted into Eqn. (B5).

Diffusion Term

$$\int_t^{t+\Delta t}\int_s^n\int_w^e \left(\frac{\partial}{\partial x}\left(\Gamma\frac{\partial\phi}{\partial x}\right)+\frac{\partial}{\partial y}\left(\Gamma\frac{\partial\phi}{\partial y}\right)\right)dxdydt =$$

$$\left[\underbrace{\int_s^n\int_w^e \frac{\partial}{\partial x}\left(\Gamma\frac{\partial\phi}{\partial x}\right)dxdy}_{(3)} + \underbrace{\int_w^e\int_s^n \frac{\partial}{\partial y}\left(\Gamma\frac{\partial\phi}{\partial y}\right)dydx}_{(4)}\right]\Delta t$$

$$(3) = \int_s^n \left(\Gamma\frac{\partial\phi}{\partial x}\right)\Big|_w^e dy = A_e\left(\Gamma\frac{\partial\phi}{\partial x}\right)\Big|_w^e$$

$$= \left(\frac{\beta_e A_e\Gamma_e}{(\Delta x)_e}(\phi_E-\phi_P) + \frac{\beta_w A_w\Gamma_w}{(\Delta x)_w}(\phi_W-\phi_P)\right)\Delta t$$

The diffusion coefficient, D, given by

$$D = \frac{\Gamma A}{\Delta n}$$

$$(3) = \left(\beta_e D_e(\phi_E-\phi_P) + \beta_w D_w(\phi_W-\phi_P)\right)\Delta t$$

Similarly,

$$(4) = \left(\beta_n D_n(\phi_N-\phi_P) + \beta_s D_s(\phi_S-\phi_P)\right)\Delta t$$

Combining the temporal, convection, diffusion, and source terms together, yield the discrete equation

$$a_P\phi_P = a_E\phi_E + a_W\phi_W + a_N\phi_N + a_S\phi_S + b^{\phi} \qquad \text{(C8)}$$

where

$$a_E = \beta_e D_e - \frac{\dot{m}_e}{2} + \frac{\dot{m}_e}{2}|\alpha_e|$$

$$a_W = \beta_w D_w + \frac{\dot{m}_w}{2} + \frac{\dot{m}_w}{2}|\alpha_w|$$

$$a_N = \beta_n D_n - \frac{\dot{m}_n}{2} + \frac{\dot{m}_n}{2}|\alpha_n|$$

$$a_S = \beta_s D_s - \frac{\dot{m}_s}{2} + \frac{\dot{m}_s}{2}|\alpha_s|$$

$$a_P = a_E + a_W + a_N + a_S + a_P^o - S_P$$

$$a_P^o = \frac{\rho\upsilon}{\Delta t}$$

$$b^{\phi} = S_{\phi} + a_P^o\phi_P^o$$

For U – momentum

$$a_P^U U_P = a_E^U U_E + a_W^U U_W + a_N^U U_N + a_S^U U_S + b^U + C^U(P_P - P_E)$$

For V – momentum

$$a_P^V U_P = a_E^V V_E + a_W^V V_W + a_N^V V_N + a_S^V V_S + b^V + C^V(P_N - P_P)$$

where $C^U = A_e$ and $C^V = A_n$

Similarly, if the continuity equation is integrated over the scalar control volume, the following discrete relation is obtained

$$a_e^C U_e - a_w^C U_w + a_n^C U_n - a_s^C U_s$$

where

$$a_e^C = \rho A_e;\ a_w^C = \rho A_w;\ a_n^C = \rho A_n;\ \text{and}\ a_s^C = \rho A_s$$

The Pressure Equation

The discrete continuity equation is used as a pressure correction field, P', based on the following correction schemes for the velocity and pressure:

$$U_e = U_e^* + d_e^U (P_P' - P_E')$$

$$V_n = V_n^* + d_n^V (P_P' - P_N')$$

$$P = P^* + p'$$

The purpose of the correlations is to modify the pressure-velocity fields to better conserve mass.

If the velocity corrections are substituted into the continuity equation, the following discrete equation for P' is obtained:

$$a_P^P P_P' = a_E^P P_E' + a_W^P P_W' + a_N^P P_N' + a_S^P P_S' + b^P$$

where

$$a_E^P = a_e^C d_e^U$$

$$a_W^P = a_w^C d_w^U$$

$$a_N^P = a_n^C d_n^U$$

$$a_S^P = a_s^C d_s^U$$

$$a_P^P = a_E^P + a_W^P + a_N^P + a_S^P$$

$$b^P = a_w^C U_w^* - a_e^C U_e^* + a_s^C U_s^* - a_n^C U_n^*$$

The source term, b^P, represents the residual of the continuity equation based on the old (*) fields. The advantage of the source term is that it measures the degree to which U^* and V^* conserve mass.

Segregated Solution Method

Patankar (1980) proposed a specific pressure-velocity solution algorithm called SIMPLE (Semi-Implicit Method for Pressure-Linked Equations), while other researchers have advanced their own version. The general method followed by a number of SIMPLE-like segregated solution methods for the velocity and pressure fields in incompressible flow is as follows:

1. Calculate the coefficients of the momentum and continuity equations.
2. Solve the linearized U and V transport equations for a given P^* field to obtain U^* and V^*.
3. Calculate the coefficients, d_e^U and d_n^V for the velocity correction relations

$$U_e = U_e^* + d_e^U (P_P' - P_E')$$

$$V_n = V_n^* + d_n^V (P_P' - P_N')$$

4. Calculate the coefficients of the equation for P' and then solve the pressure equation for the P' field.
5. Correct/update the velocity and pressure fields based on the new P' field.
6. The new values of U and V will conserve mass, but not momentum. Therefore, iteration of the above solution process is required until a satisfactory convergence is obtained.

SIMPLEC Method

Raithby and co-workers proposed one of the more popular variant of Patankar's SIMPLE method known as SIMPLEC (Semi-Implicit Method for Pressure-Linked Equations Correction). The method uses the following relations for the coefficients in the pressure correction equations:

$$d_e^U = \frac{A_e}{a_P^U - \sum a_{nb}^U}$$

$$d_n^V = \frac{A_n}{a_P^V - \sum a_{nb}^V}$$